Structural and Electrochemical Characterisation of Transition Metal Doped Perovskite Related Structures $ABO_{3-\delta}$ (A = Ca/Sr/Ba; B = Fe/Si/In)

Thesis Submitted to AcSIR for the Award of the Degree of

DOCTOR OF PHILOSOPHY

In Chemical Sciences

By

Shibin T.

Enrollment Number: 10CC15J26005

Under the guidance of

Dr. R. Nandini Devi

Catalysis and Inorganic Chemistry Division
CSIR- National Chemical Laboratory, Pune - 411008, India

January 2020

CERTIFICATE

This is to certify that the work incorporated in this Ph.D. thesis entitled "**Structural and Electrochemical Characterisation of Transition Metal Doped Perovskite Related Structures $ABO_{3-\delta}$ (A = Ca/Sr/Ba; B = Fe/Si/In)**" submitted by **Mr. Shibin T.** to Academy of Scientific and Innovative Research (AcSIR) in fulfillment of the requirements for the award of the Degree of **Doctor of Philosophy in Chemistry,** embodies original research work under my supervision/guidance. I further certify that this work has not been submitted to any other University or Institution in part or full for the award of any degree or diploma. Research material obtained from other sources has been duly acknowledged in the thesis. Any text, illustration, table etc., used in the thesis from other sources, have been duly cited and acknowledged.

It is also certified that this work done by the student, under my supervision is, plagiarism free

Mr. Shibin T
(Student)

Research Guide
Dr. R. Nandini Devi
Principal Scientist, CSIR-NCL, Pune, India
Assistant Professor, AcSIR, New Delhi, India

Date: 06th January 2020
Place: CSIR-NCL, Pune

DECLARATION

I hereby declare that the thesis entitled "**Structural and Electrochemical Characterisation of Transition Metal Doped Perovskite Related Structures $ABO_{3-\delta}$ (A = Ca/Sr/Ba; B = Fe/SI/In)** " submitted for the award of the Degree of Doctor of Philosophy in Chemistry to the Academy of Scientific & Innovative Research (AcSIR), New Delhi, has been carried out by me at Catalysis & Inorganic Chemistry Division, CSIR-National Chemical Laboratory, Pune-411008, India, under the guidance of **Dr. R. Nandini Devi**. Research material obtained from other sources has been duly cited and acknowledged in the thesis. The work is original and has not been submitted as a part or full by me for any degree or diploma to this or any other university.

Shibin T.
Enrollment Number: 10CC12J26005

Date: 06th January 2020
Place: CSIR-NCL, Pune

Acknowledgement

There are many people that have earned my gratitude for their contribution to my PhD thesis. Foremost, I am indebted to my thesis advisor, Dr. R. Nandini Devi for her continued encouragement, scientific guidance, patience and trust which gave me total freedom throughout my research.

I would like to thank my lab mates for their continued support. This dissertation would not have been possible without the intellectual contribution of seniors Dr. Rajesh, Dr. Soumya, Dr. Jijil, Dr. Leena, Dr. Anupam and Dr. Ranjith. I would also like to thank my lab mates Sourik, Pavan, Anurag, Shunottara, Priyanka, Seema, Chinnu, Akshay, Mohsin, Deepak, Shubham, Deepali and all the project trainees for making my experience in and out of the lab exciting and fun.

I owe a very important debt to my collaborators from the institute Dr. K. Sreekumar, Dr. T. G. Ajith Kumar, Dr. C. P. Vinod and Dr. U. K. Kharul and DAC member Dr. P. A. Joy for insightful discussions. Also, I would like to express my gratitude to collaborators from University of Lille1, France Prof. Rose-Noelle Vannier, Dr. Aurelie Rolle and technical staff Dr. Eduoard Capoen for the warm hospitality and support during my stay at Lille. I acknowledge the coordinators of LIA Project (Indo-French project) Prof. Pascal Granger and Dr. Shubhangi for extending the funding opportunities to perform research work at Lille. I would like to offer my special thanks to Prof. Bernard Boukamp from University of Twente, Netherlands for the scientific discussions on solid state electrochemistry. I am thanking Dr. Sreekuttan, Rajith, Athulya, Prabu, Aswathy, Haris, Vidyanand and Dheerendra for experimental and data analysis assistance. I acknowledge S. S. Deo, P. Mane and C. R. Sangurde for the technical assistance.

I owe my deepest gratitude to the Director, CSIR-National Chemical Laboratory, for providing infrastructural facilities. I also thank DST-INSPIRE for research fellowship.

I am deeply grateful to my teachers who always motivated and guided towards research especially Dr. Uma Devi, and Dr. Sudheesh. I want to thank my friends, and well-wishers from the institute who has been greatly supportive throughout the period. I am particularly grateful for the constructive comments and warm atmosphere given by my G1 Family.

Last but not least I would like to say a heartfelt thank you to my family and friends for always believing in me and encouraging me to follow my dreams. I am in debt to their helps in whatever way they could during this challenging period.

Table of Contents

Abstract

Environmental problems associated with the extensive use of fossil fuels and their depletion necessitates research in alternative renewable sources of energy. Among the various energy generation technologies,fuel cells are promising on account of the efficiency and ease of operation. However,state of the art materials are expensive, which limits the wide spread deployment of fuel cells. The emission can be further reduced by the use of oxygen transport membranes (OTM), where pure oxygen allows complete utilization of fuel and maximum efficiency. In all these processes, material development balancing performance and cost is the key challenge.

Perovskite oxides are reported to possess stability over a wide potential range making them excellent candidates for electrochemical applications. These materials have gained considerable attention owing to their advantageous properties and low cost. Moreover, properties like conductivity, catalytic activity, and oxygen vacancy concentration can be tuned by proper doping strategy. These are the crucial parameters for the application of these materials in the fuel cell and OTM applications.

In the present thesis, perovskite related structures are selected to study the role of dopants in the room temperature and high temperature electrochemical properties. Structural and electrochemical characterisations of the doped perovskite and related brownmillerite type compounds are carried out. Based on the properties, the materials are projected as the candidates for OTM and SOFC applications in addition to their applicability in AFC and URFC.

The thesiscomprises of six chapter briefly described as follows

In the chapter 1, a broad introduction of the current energy scenario and need of the alternate energy generation is stated. Various types of fuel cells and rate limiting oxygen kinetics in the fuel cell are elaborated. Perovskite related structure and the electrochemical reaction pathways in the related oxides are explained. Finally the scope and objectives of the thesis are conveyed.

In the chapter 2,$Ca_2Fe_2O_5$, a well studiedbrownmillerite oxide has been selected as the parent material. The chapter is divided into two parts. In the first part, the role of first row transition metal (Mn/Co/Ni/Cu) doping on the structure and room temperature electrochemical properties areexamined.5atom% transition metal is incorporated in the lattice. The material has alternate layers of octahedra and tetrahedra in the structure, and the dopant material is observed to occupy tetrahedral sitespreferentially. Room temperature ORR and OER evaluation of the material suggest that the Ni doped material is a better practical catalyst on account of the better electron transfer mechanism and current response. In the second part of the chapter, role of increased concentration of Co dopant is studied for room temperature and high temperature electrochemistry. An interesting observation of inter and intra layer ordering phenomenon was observed with 50atom% Co doping in the lattice. The room temperature oxygen electrocatalysis and high temperature conductivity is improved by increased Co doping in the lattice.

Chapter 3 selects $Ba_2In_2O_5$ as the parent material. In the first part, first raw transition metal is doped in the In site of the compound in 12.5atom%,to have a stoichiometry of $Ba_2In_{1.75}M_{0.25}O_5$(M = Mn/Fe/Co/Ni/Cu) and its role in structure and electrochemical properties is studied. The parent material crystallises in the tetragonal system with disordered oxygen vacancy while on transition metal doping the material crystallises in the orthorhombic system with highly ordered oxygen vacancies.No considerable improvement in activity is observed on incorporating the transition metal centre in the structure. The role of incorporation of a Ce^{4+} redox centre and transition metal centre in the In site of the compound in the room temperature electrochemistry is examined in the second part of the chapter. Materials with stoichiometry $Ba_2InCe_{0.75}M_{0.25}O_5$ (M = Mn/Fe/Co/Ni/Cu) are synthesised by solid state method. The materials, except Fe doped material crystallises in the highly disordered cubic structure. The cubic form with complete disorder of vacancy is otherwise observed at high temperature only. The activity is found to be improved by the Ce and transition metal co-doping in the lattice. The synergistic effect of Co and Ce in varying concentrations on the structure and room temperature OER and ORR are analysed in the third part of the chapter. The ORR performance by the material improves by increased Co concentration and the best OER performance is exhibited by the compound with optimum Ce and Co content. High temperature phase stability and conductivity in different gas atmosphere also studied for the selected material in the chapter.

Chapter 4 describes the structure of Na and transition metal metal doped $SrSiO_3$. Na doping in 30atom% and transition metal in 5atom% has been carried out in the Sr and Si site respectively to get a final composition $Sr_{0.7}Na_{0.3}Si_{0.95}M_{0.05}O_{3-\delta}$ (M = Mn/Fe/Co/Ni/Cu). The structure consists of MO_4 units corner shared to form isolated M_3O_9 units. The detailed analysis by SEM-EDS, ^{29}Si MAS NMR and ^{23}Na MAS NMR points on the phase segregation of the material, which could not be observed from the PXRD. Room temperature electrochemical activity and high temperature conductivity is improved by transition metal incorporation in the lattice. The material exhibited excellent phase stability in oxidizing and reducing atmospheres at high temperatures, which is a crucial parameter for the high temperature application of the material.

Chapter 5 projects the material for OTM and SOFC applications. In the first part the dense hollow fiber fabrication of the selected materials are carried out. The material sintered as strong dense fiber at relatively lower temperatures in a single step reducing the cost of the overall process. A novel method of dense fiber fabrication directly from the precursor mixture is reported in the chapter, eliminating multiple steps of calcinations and sintering. The densification and phase stability on the fiber spinning process are analysed by SEM and PXRD analysis. The second part of the chapter projects the material as SOFC candidate. Stability of the material with conventional electrolyte material at operating conditions are analysed. The cathode ink is prepared and screen printed on the dense electrolyte membrane to make a dummy electrode. Lower temperature adhesion by the material is advantageous to the process. The conductivity of the electrode is compared with state of the art $La_{0.6}Sr_{0.4}Fe_{0.8}Co_{0.2}O_3$, the selected materials exhibited comparable conductivity with the latter show casing the applicability in SOFC.

Chapter 6 summarises and concludes the thesis.

List of Figures

List of Tables

List of Abbreviation

AFC	Alkaline Fuel Cell
URFC	Unitised Regenerative Fuel Cell
CV	Cyclic Voltammetry
LSV	Linear Sweep Voltammetry
ORR	Oxygen Reduction Reaction
OER	Oxygen Evolution Reaction
EIS	Electrochemical Impedance Spectroscopy
rds	Rate determining stp
GSAS	General Structure Analysis System
HTXRD	High Temperature X-ray Diffraction
ICSD	Inorganic Crystal Structure Database
JCPDS	Joint Committee on Powder Diffraction Standards
BET	Brunauer-Emmett-Teller
OTM	Oxygen Transport Membranes
MIEC	Mixed Ionic and Electronic Conduction
RDE	Rotating Disk Electrode
RRDE	Rotating Ring Disk Electrode
SOFC	Solid Oxide Fuel Cell
TGA	Thermo Gravimetric Analysis
PXRD	Powder X-ray Diffraction
XPS	X-ray Photoelectron Spectroscopy
UPS	Ultra-violet Photoelectron Spectroscopy
SEM	Scanning Electron Microscopy
EDS	Energy Dispersive X-ray Spectroscopy
NMR	Nuclear Magnetic Resonance spectroscopy
MAS	Magic Angle Spinning

Chapter 1

Introduction and Literature Survey

1.1. Introduction

Energy consumption in today's world is primarily dependent on fossil-based fuels. Population explosion and associated technological advances have led to excessive use of fossil fuels, due to which they are fast depleting. Fossil fuels such as coal, natural gas, petroleum etc. are considered as the back bone of industries; however, the environmental problems associated with spiralling consumption of these fuels are huge, resulting in global warming and green house effects. The exhaust gas after consumption of fossil fuels contains partial or complete oxides of C, S, and N as well as various hydrocarbons resulting in air pollution, and intake of such gases leads to serious health issues in living organisms.

These issues necessitate shifting to alternative renewable sources of energy, which are sustainable and with no hazardous emissions on operation. Such renewable limitless resources include biomass, solar energy, wind energy etc. Solar cell and wind turbine technologies have gained remarkable attention and development in the near past. However, the availability of solar energy and wind energy changes from hour to hour and depends on the seasons. This energy can be stored in batteries during availability and can be used when in need; the challenge is the cost associated with storage of appropriate capacity. One way to address this is to convert this electrical energy to chemical energy which can be stored, through hydrogen production by water electrolysers and reconversion to electricity by fuel cells.

Designing materials for catalysing the electrochemical processes in these devices is the main challenge in making this technology commercially competitive. State of the art catalysts for low temperature electrolysers and fuel cells are rare earth oxides and Pt based materials. Due to the scarcity of these materials, a wide deployment of these devices will be expensive; hence it is the need of the hour to develop catalysts which are cost effective yet with comparable performance, to reduce overall cost of the system.

1.2. Fuel Cell

Fuel cell is a device, which converts chemical energy to electrical energy, invented by Sir William Grove in 1839. The demand in the fuel cell research is mainly attributed to the lower emission and higher efficiency compared to other generating devices. Fuel cells are named on the basis of electrolytes involved, as alkaline fuel cells (AFCs), polymer-electrolyte fuel cells (PEFCs), molten carbonate fuel cells (MCFCs) and phosphoric acid fuel cells (PAFCs), which operate at lower temperatures below 100°C normally. Out of these, polymer electrolyte membrane fuel cells and phosphoric acid fuel cells work in acidic conditions. Precious metals like Pt, Pd, Ag etc. are currently used as catalysts to drive the electrode reactions in these fuel cells, which makes the technology expensive. Solid oxide fuel cells (SOFCs) form another class of fuel cells where the solid metal oxides are used as the electrolytes and electrodes and operate at high temperatures ~900°C. Details of a few fuel cells which are of interest to the current work are given in subsequent sections.

1.2.1. Alkaline Fuel Cell (AFC)

Alkaline fuel cells are the most efficient among different types of fuel cells and are the first practical working fuel cells. The historical work on the AFCs began by Sir Francis Bacon in 1933, to develop a hydrogen-oxygen cell that operates at moderate temperature. Originally, the cells had porous Ni electrodes and thin electrolyte layers in the pores, which gave large power density but the performance degraded eventually by the corrosion of the electrode[1]. The system was developed later to use in U. S. Apollo space program, with three 28V power plants, operated at 260°C, ~85% KOH concentration with Ni anode and lithiated Ni cathode[2].

The half-cell reaction and overall reaction can be written as follows.

Anode side: $2H_2 + 4OH^- \rightarrow 4H_2O + 4e$

Cathode side: $O_2 + 2H_2O + 4e \rightarrow 4OH^-$

Overall reaction: $O_2 + 2H_2 \rightarrow 2H_2O + \text{Heat} + \text{Electricity}$

Hydroxide ions produced at the cathode migrate to the anode where they react with H^+ ions to form H_2O. The overall process generates H_2O, heat and four electrons per mole of O_2, which passes through the external circuit to produce electricity.

Alkaline fuel cells have superior specific power and energy density even at lower operating temperatures, since the oxygen reduction kinetics is more facile in the alkaline media than the acidic media[3], normally employed in other types of low temperature fuel cells. Because of this, AFCs are flexible in terms of cathode material, where a number of combinations of non-noble metals can be potentially employed, which effectively brings down the cost of operation[4, 5]. However the main difficulty with the use of alkaline electrolyte is the CO_2 absorption or carbonate precipitation leading to reduced electrolyte conductivity, oxygen solubility and electrode activity. This is addressed to a large extent by recent research on anion exchange membranes allowing the use of even low-purity feed gases[6, 7]. KOH has higher ionic conductivity than NaOH, and the corresponding carbonate has higher solubility product than that of Na, making KOH the preferred electrolyte in AFC[6]. A schematic representation of AFC is shown in figure 1.1.

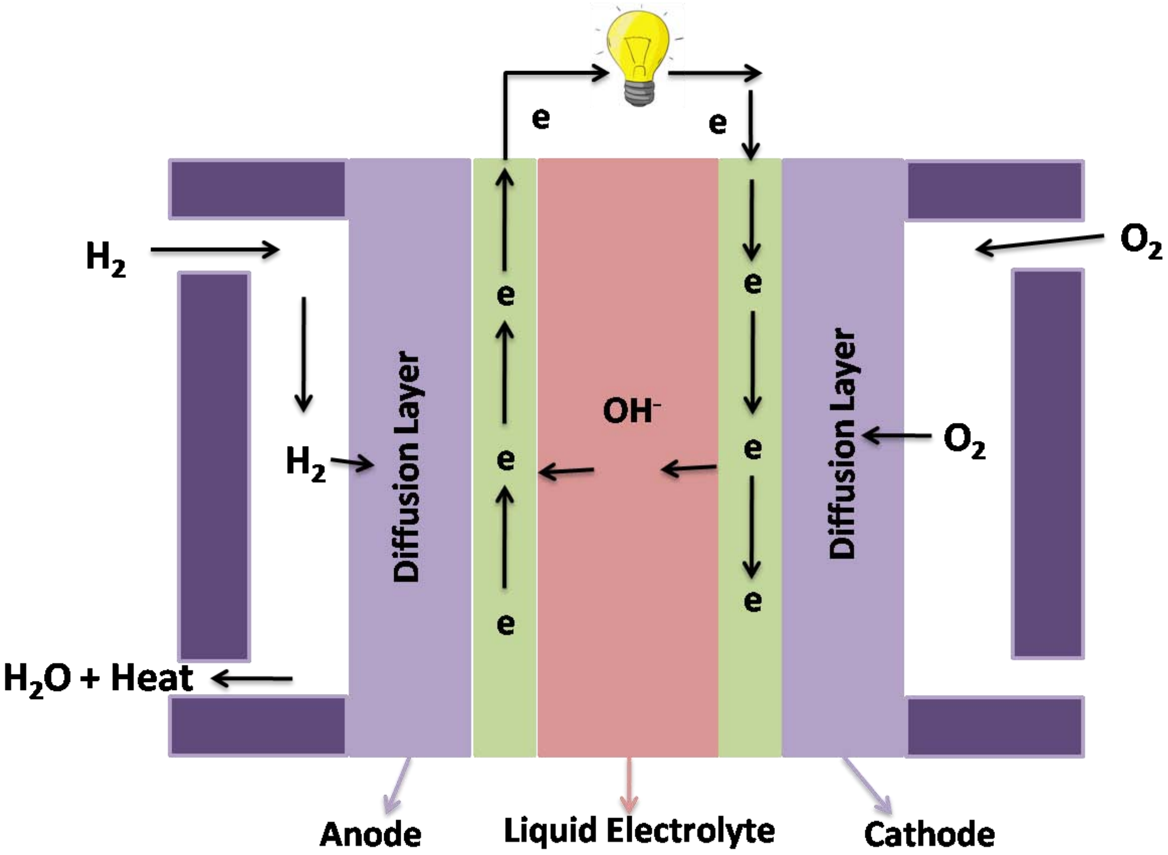

Figure 1.1: Schematic representation of alkaline fuel cell

1.2.2. Unitised Regenerative Fuel Cell (URFC)

URFC is the most advanced and highly developed fuel cell technology[8-10], combining fuel cell and electrolyser. Hydrogen and oxygen are produced in the electrolyser and used in the fuel cell to generate energy. Attempts to develop URFC technology had begun by 1960s; however, due to issues with catalysts and membranes, performance was poor in the initial stages. Further development was done by 1972 at General Electric Co, and by 1990s, prototype development and testing of a device with a specific power density of ~450Wh/kg was carried out at Lawrence Livermore National Laboratory. The first commercial product was developed by Proton Energy Systems with a production electric power up to 5kW in fuel cell mode and the consumption of 15kW in the electrolyser mode. [11, 12]

Overall reaction can be represented as,

In fuel cell mode: $4H^+ + O_2 + 4e \rightarrow 2H_2O$

In electrolyser mode: $2H_2O \rightarrow 4H^+ + O_2 + 4e$

There are several advantages for URFC than a conventional fuel cell system on account of the cyclic energy conversion. The system offers high specific energy density (~ 400-1000Wh/Kg) and uses the abundant source H_2O as the energy carrier. Since the feedstock and the product formed are H_2O, it is a renewable, sustainable and emissionless energy system. The fact that the overall system is light weight and durable also adds to the advantage of the technology[13, 14]. Figure1.2 shows the schematic representation of the URFC system and assembly. The central part of the system is polymer electrolyte membrane followed by nafion layer stacked with electrode containing electrocatalyst with support, gas diffusion backing composed of mesoporous layer and gas diffusion layer followed by bipolar plate on both sides.

In order to use a single catalyst in both the modes, the catalyst has to be active for both oxygen reduction and oxygen evolution reactions and also stable over a wide potential range, it should be resistant to anodic corrosion during the process of electrolysis[9]. The main difficulty associated with the URFC system is that, to operate as electrolyser it requires higher resistant material than in comparison with fuel cell function. In addition to the difficulty, the high cost of Pt based catalyst, cost effectiveness, aggregation and migration of the catalyst, dissolution and cracking of the nafion membrane, low proton conductivity of the membrane and dimension change on operation, are the main challenges of the URFC system[15-20]. Recently, there is some development in the solid oxide regenerative fuel cells (SORFC), with much lower overpotential and faster kinetics compared to the low temperature systems, where some of these issues are addressed.

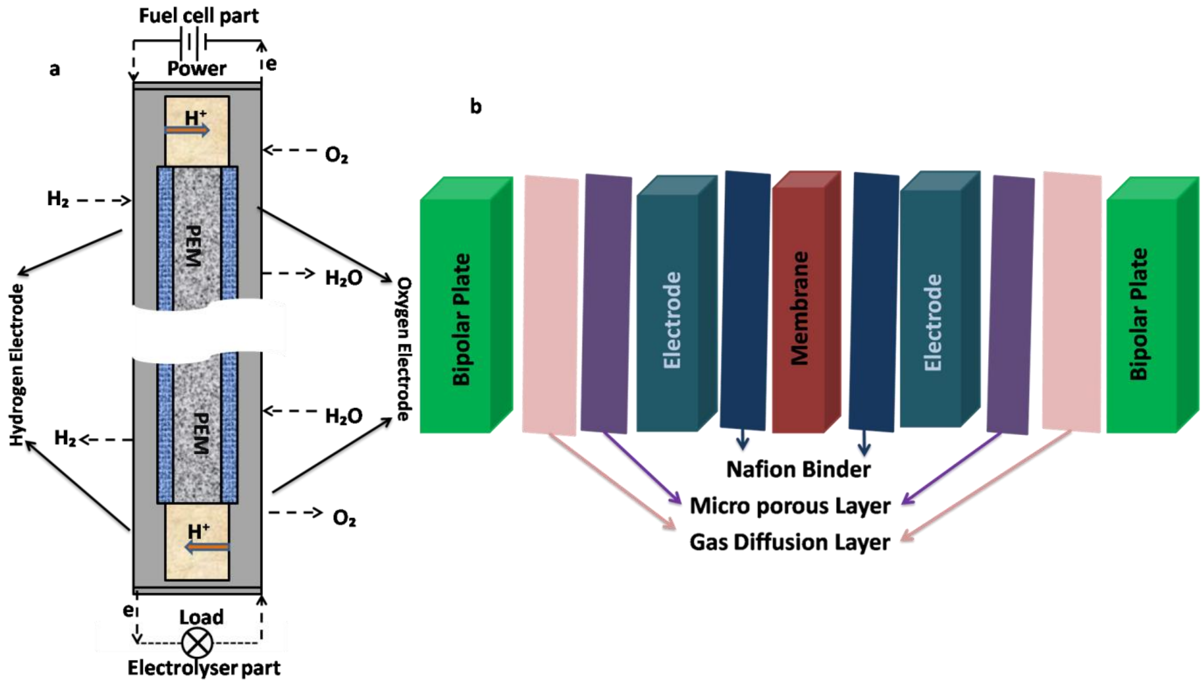

Figure 1.2: Schematic representation of a) URFC system, where the top part represents the fuel cell function and the bottom part represents the electrolyser part b) URFC assembly, where the central part consists of electrolyte membrane, followed by nafion layer, electrode containing electrocatalyst, gas diffusion layer and bipolar plate on both the sides

1.2.2. Solid Oxide Fuel Cell (SOFC)

Solid Oxide Fuel Cells (SOFCs) generate electrical energy by separating the redox reactions at cathode and anode by means of a solid oxide ion conducting electrolyte, and is a potentially durable, reliable and inexpensive fuel cell technology [21]. State of the art material used as electrolyte is mostly Yttria stabilised Zirconia (YSZ), and electrodes are porous $LaMnO_3$ cathode and Ni-YSZ cermet anode, all of which are relatively abundant and cheap. The function of the electrolyte is to transport the oxygen ions from the cathode to the anode and it has to be pure oxide ion conductor. The flexibility in terms of the fuels adds to the advantages of the fuel cells. Variety of fuels like reformed gases, impure hydrogen from coal and hydrocarbons can be used[22-25]. The schematic of the SOFC is shown in figure1.3.

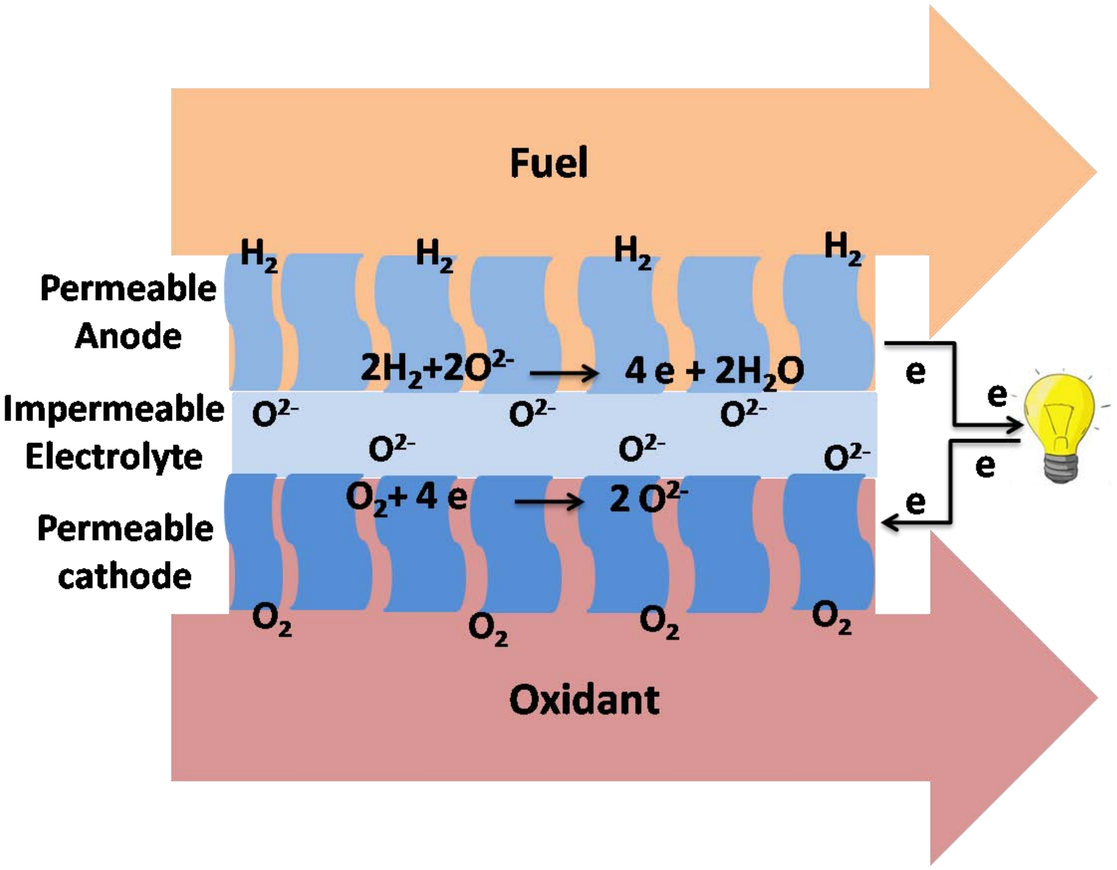

Figure 1.3: Schematic representation of SOFC, fuel is passed through permeable anode and oxidant from permeable cathode, electrolyte is the oxide ion conducting dense membrane made up of metal oxide

The development of SOFC began in 19th century with Nerst Glower, who demonstrated the solid ionic conduction, further explanation to the conduction process was given by Carl Wagner and the first SOFC was reported by Baur and Pries in 1937[2, 26-28]. The electrolyte handling problem as in the other types of fuel cells is no longer a concern with the solid oxide fuel cells, as the electrolytes are solid oxides. Each component should possess proper stability in oxidising and reducing atmospheres, compatibility with other components and excellent conductivity at higher temperatures. The high operating temperature makes the SOFC much more tolerant of reformed gases and results in much faster reaction kinetics. However, this leads to durability issues of the components and limited number of sealants can be employed at higher temperatures. Another major difficulty is the thermal coefficient mismatch between electrodes and electrolytes, and also with inter-connects, generally stainless steel.

Lowering the operation temperature from around 1000°C to 500°C offers various technical advantages such as improved durability, suppression of degradation of components and ultimately lower cost. Stacking and durability of inter-connects also improve by reduction in temperature. Lowering of temperature could be achieved by improving the electrolyte conductivity and catalysis by the electrodes. As the conductivity is strongly affected by the temperature, development of the low temperature conducting materials is crucial in developing low or intermediate temperature fuel cells.

Perovskite oxides are the best-known cathodes in SOFC. Doped $LaMnO_3$ (LMO) is one of the widely studied cathode materials. It has good match of thermal expansion with the YSZ electrolyte. LMO is a p type semiconductor and undergoes atomic distortions leading to orthorhombic crystal structure. The material exhibits oxygen excess or oxygen deficiency in the oxidising and reducing atmospheres respectively and at extreme reducing atmosphere, it decomposes to La_2O_3 and MnO reversibly. Significant changes in the oxygen non-stoichiometry is not preferred for SOFC application, hence appropriate doping strategies have been employed to stabilise the phase during operation[29-31]. The solid solution $LaCrO_3$-$LaMnO_3$ is also widely investigated for SOFC and exhibits better morphological stability and durability against reduction[32]. Early SOFC studies explored the use of $LaCoO_3$, Sn doped In_2O_3, combination of oxides such as In_2O_3-PrO_2-HfO_2, In_2O_3-PrO_2-ZrO_2,Sr doped LMO and $LaCoO_3$ etc. as the cathode materials[33-37].

Reduction in operating temperature adversely affects the kinetics of the oxygen reduction reaction at the cathode, a sharp increase in the polarisation resistance results in the depletion of the SOFC performance[38, 39]. For high-temperature oxygen reduction in SOFC, oxygen transport dominates the reaction kinetics. Increasing covalency leads to enhanced oxygen surface exchange kinetics at higher temperatures, also the oxygen vacancy concentration reduces the barrier for the rate-limiting steps. Oxygen vacancies enhance the mobility of oxygen ion through the lattice and catalytic activity of the material[40, 41].

The materials for the above-mentioned applications are monitored by their electrochemical activities in room temperature or high temperatures depending on the type of fuel cell application. Oxygen reduction reaction and oxygen evolution reactions are the rate limiting reactions in these processes, since both the reactions involve four electron processes to either create or break a strong double bond compared to the counterpart hydrogen evolution reaction and hydrogen oxidation reaction.

1.3. Oxygen Reduction Reaction (ORR)

Oxygen Reduction Reaction (ORR) is a fundamental reaction in electrochemistry and is the cathodic branch of the reactions in fuel cells. A strong double bond has to be broken for the oxygen to get reduced to the hydroxide or peroxide ion and thus the reaction is sluggish in kinetics compared to its anodic counterpart, hydrogen oxidation. State of the art catalysts for ORR in low temperature fuel cells are Pt and Pt based alloys, which are highly active and efficient. However, scarcity and cost of Pt has driven research towards reducing its use and developing alternate materials. Various types of carbon morphologies and doped carbons are studied as alternative catalysts. Metal oxides are also well studied as ORR catalysts, but they are limited by the bulk conductivity.

ORR is a highly irreversible reaction with multiple adsorption and desorption steps, and it is important to attain as much reversibility as possible, ie., overpotential as close to zero, for achieving high energy efficiency. The mechanism of ORR has not been completely understood, due to the involvement of complicated electron-charge transfer and adsorption-desorption steps. It is more desirable to perform the reaction in alkaline medium due to the fact that it confers reduced adsorption energies to the anions. Also, kinetics is more rapid in alkaline medium in comparison with acidic and provides lesser corrosive atmosphere to the catalyst. The oxygen reduction reaction can either take place through direct four electron mechanism or 2+2 indirect mechanism. The favoured reaction is the direct mechanism, where the oxygen is converted directly to the hydroxide ion at the expense of four electrons, whereas in the other case, the O_2 is first converted to peroxide ion by two electrons and further reduced by another two electrons to the final hydroxide ions or disproportionation of the peroxide to water and oxygen. Peroxide formed in the indirect mechanism is detrimental to the fuel cell components and thus direct mechanism is preferred. The two-electron mechanism is preferred for the electrochemical synthesis of peroxide. The mechanism in alkaline medium can be represented as[42]

$$O_2 + H_2O + 4e \leftrightarrow 4OH^- \, ; E^0 = 0.401 \text{ V vs SHE}$$

Two electron pathway:

$$O_2 + H_2O + 2e \leftrightarrow HO_2^- + OH^-; E^0 = -0.076 \text{ V vs SHE}$$

$$HO_2^- + OH^- + 2e \leftrightarrow 3OH^- \, ; E^0 = 0.878 \text{ V vs SHE}$$

Disproportionation

$$2HO_2^- \leftrightarrow 2OH^- + O_2$$

1.4. Oxygen Evolution Reaction (OER)

Oxygen evolution reaction is the most common anodic reaction coupled with most of the cathodic processes occurring in aqueous medium. OER is a four-electron reaction and involves the formation of strong double bond and thus requires higher energy to overcome the kinetic barrier.

OER is exploited in energy storage devices, such as metal air batteries and electrolysers. Metal Air Battery (MAB) was first invented by Leclanche in 1868 and commercialized in 1932 by Hiese and Schumacher[43]. Ambient air is used as the reactant in the MAB and the device consists of metal anode, where the OER takes place.

Overall oxygen evolution reaction can be represented as follows

$$H_2O \rightarrow H_2 + O_2$$

And the mechanism in alkaline media can be represented as[44]

$$M + OH^- \rightarrow MOH$$

$$MOH + OH^- \rightarrow MO + H_2O_{(l)}$$

$$2MO + OH^- \rightarrow MOOH + e$$

$$MOOH + OH^- \rightarrow M + O_{2(g)} + H_2O_{(l)}$$

Rutile type RuO_2 exhibits excellent activity in both acidic and alkaline media, however suffers from the instability in highly anodic conditions. At higher potentials, the phase RuO_4 is formed and gets dissolved in solution[45]. Another state of the art material IrO_2 also suffers from the same problem of oxidation to IrO_3[46, 47], however it is more stable than RuO_2 in high oxidising potentials[48]. The large scale deployment of the catalyst is limited by the cost and scarcity of these precious metals.[44]

Requisite properties for materials to be used in the devices mentioned in sections 1.2 vary considerably due to certain unique features. For eg., electrode materials for the application in unitised regenerative fuel cells should possess stability in a wide potential window since bifunctionality in terms of activity in both ORR and OER is required. State of the art materials for the room temperature ORR and OER reactions are Pt based materials and RuO_2 or IrO_2 respectively. However, there are inherent issues of stability when either of these catalysts is used in the other condition. Oxide layer formation on platinum surface under OER conditions affects its durability. Moreover, any combinations or alloys of these noble metals would render the catalyst prohibitively expensive. Carbon based morphologies are the other cheap and abundant alternatives suggested for bifunctionality, but they corrode in the OER experimental conditions due to rapid oxidation of carbon to CO_2.

On the other hand, for SOFC applications, materials should possess higher conductivity, catalytic activity and thermal stability. Electrolytes used are pure oxide ion conductors, which allow only the conduction of oxide ions through them and the porous electrode layer should be mixed electronic and ionic conductor allowing the conduction of ions and electrons. Oxygen conduction in such materials is explained by hoping mechanism of oxide ions from one lattice position to the other. In order to exhibit good oxide ion conductivity, the material should have requisite oxygen vacancy concentration.

In the above mentioned applications, perovskite and related structured oxides are potential candidates due to their advantageous catalytic properties and stability in oxidising and reducing conditions. Moreover, catalytic activity and conductivity can be tuned by proper doping strategy without altering the structure.

1.5. Perovskites

Gustav Rose discovered the mineral perovskite ($CaTiO_3$) in 1839 from samples found in the Ural mountains and named them after Russian mineralogist Count Lev Alekesvich von Perovski as perovskites. The group of compounds with stoichiometry and connectivity as in $CaTiO_3$ was defined as Perovskites by Goldschmidt who prepared the first synthetic perovskite during 1924-26. He has synthesised large number of ABX_3 composition and studied the crystal structure of each phase far before the invention of the x-ray crystallography[49]. He has also postulated some basic principles of perovskite synthesis, viz., (i) the radius of cation is fundamental to the structure, (ii) the radius ratio determines the coordination number, and (iii) packing of polyhedra follows simple rules. The research and development in the perovskite chemistry accelerated during World war-II (1941-44). Doping studies on BaO and TiO_2 in search of alternatives to commonly used dielectric mica, resulted in $BaTiO_3$, with enhanced dielectric permittivity. The ferroelectric property of the composite BaO-TiO_2 was also significant and gave an insight that simple oxides can also be ferroelectric materials. Helen. D. Megaw was the first one to study the crystal structure and high-temperature ferroelectric properties of orthorhombic perovskite $BaTiO_3$ in 1945[50, 51],which was confirmed soon in 1946 by Miyake and Ueda[52, 53]. The cubic type structure of perovskite class is explained by $SrTiO_3$ model as shown in figure 1.4 and can be viewed as oxygen at the centre of the cube faces and Ti atom at the centre forming TiO_6 octahedra. Each Sr atom is surrounded by twelve equidistant oxygens and each TiO bond is at perfect 90° angle to each other. The structure can also be viewed as the cubic close packed arrangement in which O and Sr are close packed along the [111] direction. Muller and Roy[54, 55] suggested the representation of the structure with coordination number and local symmetry as shown below.

$$Sr^{XII}Ti^{VI}O_3^{XII}\{Sr_{m3m}^{XII}Ti_{m3m}^{VI}O_{3_{(4/mm)}}^{VI}$$

The perovskites are characterised by high thermal and chemical stability and hence is applied for various types of reactions, viz., gas-solid reactions, liquid reactions and those with irradiation[56-58]. The conductivity of the perovskite oxides are also well studied and is used in various fields of energy-related technologies such as fuel cells, solar cells, oxygen sensors, transport membranes etc. The superconductivity, magnetism, and catalysis of these materials are also well studied[59-62].

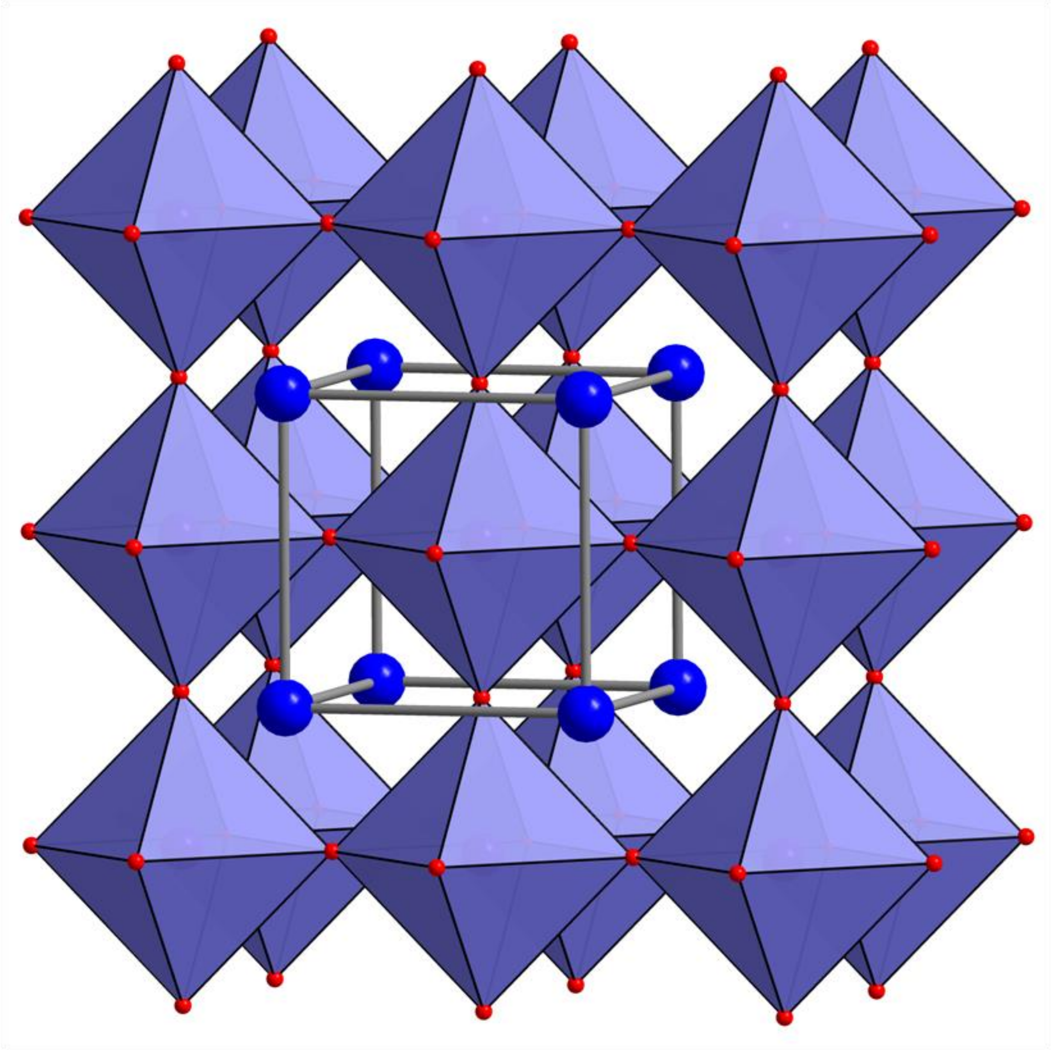

Figure 1.4: Extended cubic unit cell representation of $SrTiO_3$, where the red balls represent the oxygen atom. Sr atom (Blue) forms corners of the cubic unit cell, body centre is occupied by Ti atom, which forms octahedra with six oxygens

The advantage of perovskite structure lies in the fact that, it has two metal positions and more than 90% of metallic elements including rare-earths in the periodic table could be stabilised in the perovskite structure giving vast variety of properties and applications. In general, perovskite structure ABO_3 has 'A' site occupied by larger cation and 'B' site by smaller cation. Based on the valence of the cation and charge neutrality of the compound, various distributions of compositions viz., $A^{I}B^{V}O_3$, $A^{II}B^{IV}O_3$, $A^{III}B^{III}O_3$, $A^{IV}B^{III}O_3$ are possible. It is also possible to introduce or tune properties in these materials by partial substitution with cations of similar size having same or different charges. The partial aliovalent substitution also results in the mixed oxidation states of cation or even unusual oxidation states in the lattice. The oxygen vacancies are created in the lattice to maintain the charge neutrality in the structure. The resultant structure can be expressed by the formula $A_{1-x}A'_{x}B_{1-y}B'_{y}O_{3\pm\delta}$, where δ denotes oxygen non-stoichiometry which can be either oxygen deficiency or excess. In 1989, J. H. Kuo et al[30], analysed the oxygen excess and oxygen deficiency in Sr doped $LaMnO_3$ perovskite in different oxygen partial pressures. Oxygen excess structure occurs in higher partial pressures of oxygen and it can be expressed by the Kroger-Vink notation[63]

$$La_{1-y}Sr_{y}^{'}V_{La_{x/3}}^{'''}Mn_{1-y-2x}^{x}Mn_{y+2x}^{\cdot}V_{Mn_{x/3}}^{'''}O_{3+x} \leftrightarrow La_{1-y}Sr_{y}^{'}Mn_{1-y}^{x}Mn_{y}^{\cdot}O_{3} + \frac{x}{2}O_{2}$$

Where y represents dopant and x represents oxygen excess concentration. In terms of reactants, the equation can be simplified as

$$V_{La}^{'''} + V_{Mn}^{'''} + 6Mn_{Mn}^{\cdot} + 3O_{O} \leftrightarrow 6Mn_{Mn}^{x} + \frac{3}{2}O_{2}$$

The oxygen vacancy in the same material in low P_{O2} can be represented as

$$La_{1-y}Sr_{y}^{'}Mn_{1-y}^{x}Mn_{y}^{\cdot}O_{3} \leftrightarrow La_{1-y}Sr_{y}^{'}Mn_{1-y+2x}^{x}Mn_{y-2x}^{\cdot}V_{\ddot{O}_{x}}O_{3-x} + \frac{x}{2}O_{2}$$

Or,

$$2Mn_{Mn}^{\cdot} + O_{O} \leftrightarrow 2Mn_{Mn}^{x} + V_{\ddot{O}} + \frac{1}{2}O_{2}$$

Where O_O is the lattice oxygen,$V_{\ddot{O}x}$ is the oxygen vacancy and O_2 is the gaseous oxygen. Thus, oxygen vacancy/excess concentration in a perovskite oxide depends mainly on oxygen partial pressure, other components which affect the concentration are temperature, aliovalent dopant concentration etc.

The unit cell of an ideal perovskite structure with cubic Pm3m space group is explained for $SrTiO_3$ earlier. If the edge length is (unit cell parameter) "a", the A-O bond distance is a/√2 and B-O distance is a/2, then

$$r_A + r_O = \sqrt{2}(r_B + r_O)$$

Where r_A is the ionic radii of 'A' cation r_B that of 'B' and r_O that of Oxygen. Many compounds exhibit perovskite structure even when the above equation is not obeyed, deviating from the ideal structure. The extent of deviation is usually assessed by Goldschimdt tolerance factor[64] (t) which indicates the geometric stability and distortion in a perovskite crystal structure and is defined by the equation,

$$t = \frac{r_A + r_O}{\sqrt{2}(r_B + r_O)}$$

For an ideal cubic structure, the tolerance factor, "t" is unity; nevertheless the cubic structure is maintained if the tolerance factor lies between 0.9 to 1[57]. However lower symmetry structures (e.g. orthorhombic structure of $CaTiO_3$ and $GdFeO_3$) are formed if the value is in between 0.71 to 0.9. If the value of t further drops below 0.71, the compound adopts a trigonal ilmenite structure ($FeTiO_3$). On the other hand, for higher t values ($1.00 < t < 1.13$), the structure exhibits a hexagonal symmetry.

1.6. Brownmillerites

Brownmillerite oxides are named after the mineral Ca_2FeAlO_5 and its crystal structure was first suggested by Bussem in 1937-38 to be crystallised in Imma space group with corner shared AlO_6 octahedra and alternate layers of FeO_4 tetrahedra[65]. Structure of the end member $Ca_2Fe_2O_5$ was solved in 1959 by Bertaut, Blum and Sagnieres[66], the atomic arrangement was similar to that of Ca_2FeAlO_5 with alternate layers of octahedra and tetrahedra and crystallised in Pcmn space group. They have concluded that the Ca_2FeAlO_5 crystallises in Pnma rather than Imma space group by the help of x-ray crystallography. By different studies it is also found that $Ca_2Fe_{2-x}Al_xO_5$ is not isostructural throughout the series of varying *x* values, but exhibits a higher-order phase transition[67, 68]. The general structure of brownmillerite $ABO_{2.5}$ or $A_2B_2O_5$ can be regarded as derived from the perovskite structure by removing 1/6th of the oxygen from the structure to maintain charge neutrality. Relation between the perovskite structure and brownmillerite is represented in figure 1.5. The brownmillerite structure is more accurately described as $A_2BB'O_5$, where B/B' is in +3 oxidation state generally (eg: Al, Ga, In, Fe, Mn, Cr, Co), but also can be in a mixed state of +2, +3 or +4 when a rare earth metal is substituted in the A site. Thus, a perfect brownmillerite structure has alternate layers of BO_6 octahedra and $B'O_4$ tetrahdra. The presence of additional tetrahedral layer makes the understanding of the structure and properties more complex. The variation in structure and space group can be attributed to the ordering of the layers relative to each other by twisting and elongation. The common space group observed when there is no rotation of octahdra and tetrahedra is Imma, and the commonly observed space groups are I2bm, Pbcm, Pnma, Icmm etc. Also, the disorder in the brownmillerite oxides increases as a function of temperature, where it undergoes transition from orthorhombic to tetragonal and further to cubic, associated with sudden changes in the properties.

$Ba_2In_2O_5$ is a well studied system among the family of brownmillerites on account of its structure and interesting properties. The protonic and oxide ion conductivity by the material is well studied and the oxide ion conductivity was even higher than the conventionally used YSZ at higher temperatures. J. B. Goodenough et al.,[69] had observed the sudden enhancement in conductivity at around 925°C in $Ba_2In_2O_5$. The reason was later found to be due to the phase transition at 925°C from orthorhombic to tetragonal crystal system involving oxygen vacancies; further at 1040°C, it changes to the cubic form. The conductivity improvement was actually due to the order-disorder transition of oxygen vacancies. The structure of the brownmillerite family and defect chemistry is well explained by $Ba_2In_2O_5$ model. Frenkel defect formation in the lattice is favoured due to the ease of formation of oxygen vacancies ($V_{\ddot{O}}$) and interstitial oxygens (O_i''). The structure below transition temperature consists of a perovskite layer $(A^{2+}B^{3+}O_3)^-$ where the 'B' cation is in octahedral coordination and $(A^{2+}B^{3+}O_2)^+$ layer with tetrahedral 'B' site coordination. The positive layer is in tension due to the loss of oxygen and the B cation occupies the tetrahedral geometry whereas the negative perovskite layer is in compression resulting in a stress-free microstructure, here the 'B' cation occupies the octahedral site. The perovskite layer prefers to have vacancy type defect $V_{\ddot{O}}$ and the other layer prefers to have interstitial type vacancy O_i''. Above the disorder temperatures, the oxygen vacancies randomly distribute over 1/6th of the oxygen anion sites. The structural explanation is more suitable for the brownmillerites with fixed cation oxidation state and for the one with transition metals, the situation may be different due to the presence of higher intrinsic electronic defect concentration[70, 71].

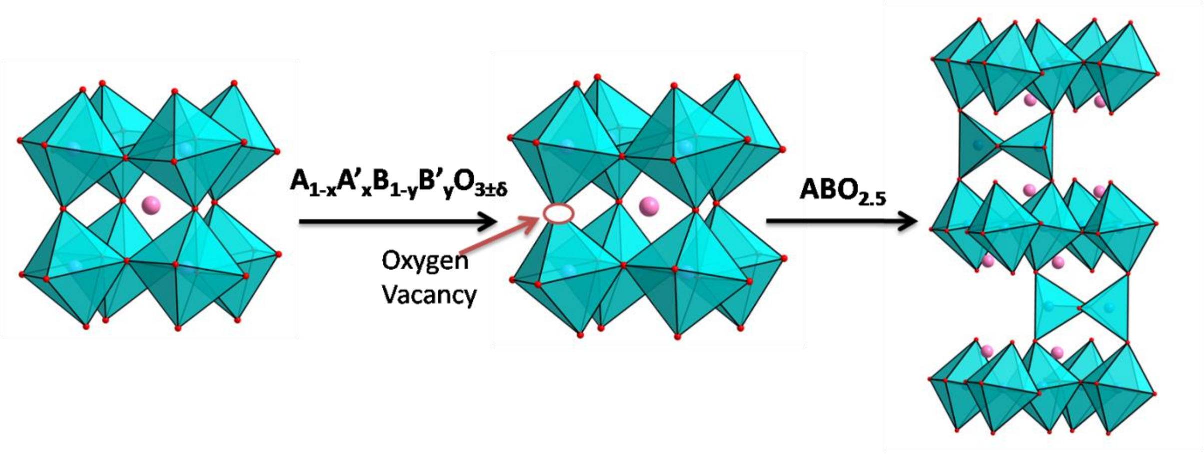

Figure 1.5: Structural relation between perovskite and brownmillerite oxide

1.7. Reaction Pathways on Transition Metal Oxides

1.7.1. ORR by Transition Metal Oxides

The reaction mechanism on transition metal oxide surface is different from that on the precious metal catalyst. The oxygenated species coordinate to the surface cations with coordinative unsaturation, and then undergoes redox reactions for the sake of charge compensation. The surface cation of the transition metal adjacent to oxygen vacancy (or coordinative unsaturation) coordinates with the oxygen atom of H_2O to fulfil the coordination. The surface metal cation undergoes reduction to charge compensate the surface oxygen ligand to create surface OH^- species. And this M- OH^- interacts with the incoming O_2 in either side-on or end-on configuration. The reaction pathway in a transition metal oxide surface would be[42]

$$2M^{m+} - O^{2-} + 2H_2O + 2e \rightarrow 2M^{(m-1)+} - OH^- + 2OH^-$$

$$2O_2 + e \rightarrow O^-_{2,ads}$$

$$2M^{(m-1)+} - OH^- + O^-_{2,ads} + e \rightarrow 2M^{m+} - O^{2-} + 2OH^-$$

Or,

$$2M^{m+} - O^{2-} + H_2O + e \rightarrow 2M^{(m-1)+} - OH^- + OH^-$$

$$2O_2 + e \rightarrow O^-_{2,ads}$$

$$M^{(m-1)+} - OH^- + O^-_{2,ads} \rightarrow M^{m+} - O - O^{2-} + OH^-$$

$$M^{m+} - O - O^{2-} + H_2O + e \rightarrow M^{(m-1)+} - O - OH^- + OH^-$$

$$\mathrm{M^{(m-1)+} - O - OH^- + e \rightarrow M^{m+} - O^{2-} + OH^-}$$

$$\mathrm{M^{m+} - O - O^{2-} + H_2O + e \rightarrow M^{(m-1)+} - OH^- + HO_2^-}$$

Molecular orbital theory, crystal field theory and inorganic chemistry principles govern the interaction of O_2 with the transition metal oxides. The kinetics of reaction is determined by the surface oxygen binding; if it is too strong, the step O-to-OH formation will be rate limiting and if the binding is too weak, OH-to-OO displacement will be the rate limiting step. The orbital overlap integral between the e_g orbital of the transition metal and the 2pσ orbital of the O_2 greatly affects the catalytic activity of the oxide. For e.g., with the lowest e_g electron count of zero, the B-O_2 bonding is very strong in $LaCrO_3$ whereas O_2 interaction with the BO_5 is very poor in $LaFeO_3$ with high e_g electron of two. The e_g electron count *vs* ORR activity can be represented as a volcano plot as represented in figure 1.6a, where the maximum activity is observed for near unity filling of e_g electrons, even comparable with the state of the art materials[72]. The correlation of the 'A' site metal on the ORR activity was studied in $LnMnO_3$ perovskite by Hyodo et al[73] with Ln= La, Pr, Nd, Sm, Gd, Dy, Yb, or Y in 8M KOH, and found that the activity reduced with the decrease in ionic size of the A cation. As the size of the A cation increases, tolerance factor and symmetry increases and more symmetric cubic phase is more likely to form with the largest La^{3+}, while, as the radius decreases the phase is stabilised in the orthorhombic or tetragonal phase. The orientation and distortion of the BO_6 octahedra can be altered by the doping at B site and that in turn affects the activity of the perovskite oxide[74, 75]. A site cations with 4f electrons limit[76] the electronic conductivity of the material, and thus lowering the activity; this observation was consistent with the resistivity values studied for the $Ln_xSr_{1-x}CoO_{3-\delta}$ with various Ln cation[77]. Partial substitution to the A site with lower valent cations introduces the oxygen vacancies and the large proportion of the B site cations shifts to the unstable oxidation state, increasing the mobility and kinetics and thus the electrocatalytic activity. The B site, regarded as the center of reaction and its role in the reaction is well studied by many groups. In the bulk $LaMO_3$ with M = Cr/Mn/Fe/Co/Ni, the highest current density and positive onset was observed for Co[78], and the current density decreased in the order Mn, Ni, Fe and Cr. Though, in the nano $LaMO_3$ the best activity was observed for Mn[79].

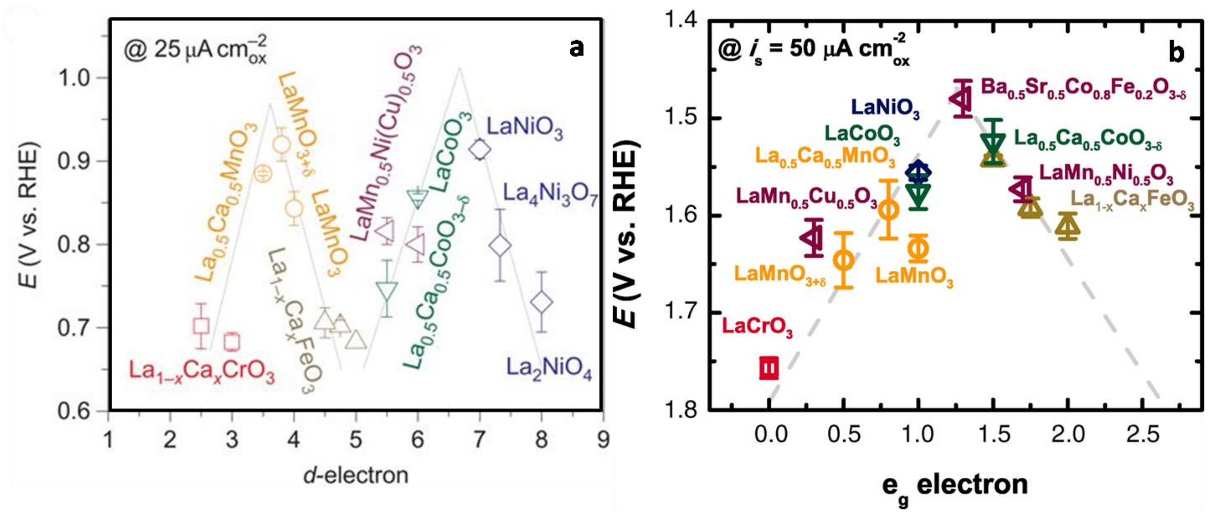

Figure 1.6: a) Relation of ORR activity of catalyst with d electron count of metal ion and b) volcano plot of OER activity with e_g electron count in perovskite oxides (adapted from references 72 and 85)

1.7.2. OER by Transition Metal Oxides

The OER pathway in transition metal-based perovskite oxides is well also studied. OER activity in perovskite oxides are greatly affected by the electrons in the *d* band of the transition metal B ions as suggested by the studies in $La_{1-x}Sr_xFe_{1-y}Co_yO_3$ by Matsumoto et al[80]. Activity is enhanced by increasing *x* and *y*, due to the band distribution of the d character and higher oxidation state of Co. This was a pioneering work to correlate the bonding interaction of the catalyst with the OER activity. B-OH bond strength also greatly influences the reaction kinetics, which is dominated by the population in σ^* level decreasing from Ni to Fe[81]. Systematic study on the transition metal based perovskite oxides by Bockris and Otagawa[82, 83] concluded that the trend on OER overpotential inversely varies with number of d electrons.

The e_g orbital of transition metal cation coordinates with the p orbital of oxygenated species and ultimately influences the OER kinetics[84]. OER activity in perovskites also follows a volcano relationship with the e_g electron count as represented in figure 1.6b, where the maximum activity was observed with the material $Ba_{0.5}Sr_{0.5}Co_{0.8}Fe_{0.2}O_{3-\delta}$, with e_g electron count of ~1.2[85]. This approach has led to the discovery of highly active materials $SrNb_{0.1}Co_{0.7}Fe_{0.2}O_3$ and $CaCu_3Fe_4O_{12}$ with e_g electron count of ~1.2[86-88]. It is observed that the bulk strain breaks the BO_6 octahedral symmetry, leading to the asymmetric d-electron occupation. In $LaNiO_3$, the e_g filling changes to the desired ~1.2

from the nominal 1, due to the compressive strain, increasing the occupancy of dz^2 orbital[89]. The unity electron configuration of the e_g electron is a good indicator for OER activity which was further explained by the example of $BaNiO_3$ and $BaNi_{0.83}O_{2.5}$, where the e_g electron is zero and one respectively, and corresponding improvement in the OER activity of the latter[90]. Further Yagi et al[91] found that increasing Fe^{4+} population in $La_{1-x}FeO_{3-\delta}$ by increasing the oxygen vacancy concentration enhances the reaction as the molecular orbital of the $[Fe^{4+}O_6]$ has single electron in the e_g orbital. The covalency, as measured by the O2p band center determines the stability and activity in the OER conditions. Increasing the covalency increases the stability and activity as observed from $LaCoO_3$ to $Pr_{0.5}Ba_{0.5}CoO_{3-\delta}$[92]. Further increase to have a maximum covalency reduces the stability of the material converting to amorphous oxyhydroxides as observed with $Ba_{0.5}Sr_{0.5}Co_{0.8}Fe_{0.2}O_{3-\delta}$. This is explained by the correlation of oxygen covalency and vacancy formation. Too high driving force to make oxygen vacancy can destroy the perovskite structure leading to surface amorphisation[93]. Higher covalency and reduced oxygen binding on the surface leads to higher OER activity. Greater covalency could reduce the charge transfer gap between the metal cation and the oxygenated species. Then during the reaction, covalent mixing of metal 3d orbital and O2p orbital can occur due to the similarity in energy and spatial overlap[72]. DFT calculation suggests that the electrons in both t_{2g} and e_g orbitals contribute to the adsorption energy; too weak or too high adsorption energy is not appropriate for the catalysis reactions. This observation was in accordance with the maximum activity observed with Ni and Co based oxides[94]. The position of metal d orbital and O p orbital relative to the Fermi level is also crucial in the activity, as understood by the DFT calculations. The calculation of metal d band position may lead to large correlation error and therefore, the delocalised nature of O2p is exploited more to obtain the electronic structure, reflecting the metal d-character through hybridised density states[88].

1.8. Other Applications of Perovskite Related Oxides

In addition to the above mentioned applications in various fuel cells, oxygen nonstoichiometric perovskite related structures are also employed as oxygen transport materials, exploiting the oxygen vacancies and B site activity. Oxygen transport materials have potential to be used in fields such as oxy-fuel combustion and also in various fields of catalysis such as partial oxidation of light hydrocarbons[95-98], methane to ethane and syngas conversion[99, 100], steam reforming[101] etc. In oxy-fuel combustion, only pure oxygen is supplied to the fossil fuel thus increasing the efficiency of the fuel. Also the emission product consists of only pure CO_2 vapour which can be sequestrated for other applications after drying[102-104], ensuring the use of fuel to maximum efficiency. Here, the material is fashioned as a membrane stable at high temperatures and uses pressurised air on one side of the membrane and pure oxygen is swept through the other side. Oxygen transport membrane is one of the most potential applications of oxygen deficient materials.

1.8.1. Oxygen Transport Membranes

Oxygen permeation membranes selectively separate or permeate oxygen from a mixture with other gases. OTM functions either by a chemical potential gradient or electrical potential gradient. Chemical potential gradient is provided by oxygen partial pressure difference. OTM materials can be of two types[105], pure ionic conductor or mixed ionic electronic conductors (MIEC)[106]. Oxygen is reduced at the surface to oxide ion and diffuses by the vacancy hopping mechanism, as the oxide ion diffuses in one direction through bulk, in order to maintain charge neutrality electrons should flow in the opposite direction. Pure ionic conductors like YSZ allow only ionic conduction and to maintain charge neutrality an external circuit must be connected to provide the electron flow. Whereas MIEC materials allow both electron and ions to pass through, in opposite directions[107]. Separation of ultrapure oxygen from air is possible by means of dense ceramic membranes. Oxygen is separated in the industries by conventional cryogenic separation, which occupies more than 40% of the total capital. Ceramic based oxygen separation membranes can reduce the cost by 30-50%[108-111]

US based companies Praxair and Air Products and chemicals Inc. commercialised the oxygen production by ceramic technique and have production of more than 5 tons per day. A number of perovskite related materials are examined for the separation application in various membrane geometries, of which hollow fiber geometry is of great interest on account of the higher area to volume ratio in comparison with other geometries[112, 113].

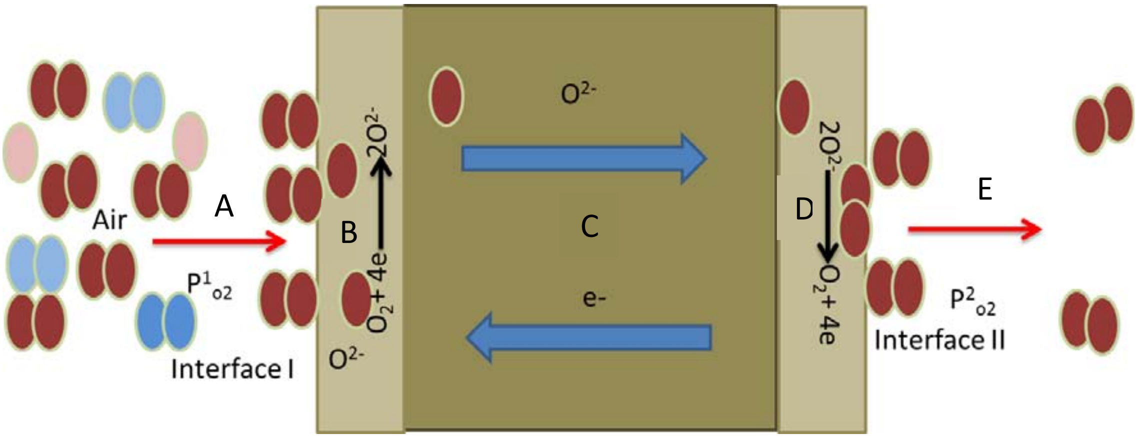

Figure 1.7: Schematic representation of oxygen transport membrane

The mechanism of transport of oxygen through ceramic membrane is complicated and mainly driven by the oxygen vacancy. In mixed electronic ionic conducting material, the oxide conduction occurs through the partial pressure gradient. Figure 1.7 represents the schematic of oxygen transport membrane. The conduction of oxygen through the material consists of five steps represented by A to E in the schematic diagram[114, 115].

(A) Air is in contact with the interface I, where the oxygen molecules undergo surface adsorption to the interface of the membrane.

(B) The adsorbed gas molecule undergoes charge transfer to form oxide ions. The vacancy on the material plays an important role in the step, the oxygen molecule undergoes reduction by interacting with the vacancy in the material

(C) The oxide ions formed as a result of surface reactions are conducted through the bulk of the material. Electron flow in the opposite direction takes place to charge balance the overall conduction. As the thickness of the membrane increases more will be the distance it needs to travel to reach the surface.

(D) Once the oxide ion reaches the oxygen lean surface, itundergoesa charge transfer reaction. Holes can interact with the oxide ion at the surface to produce oxygen molecule

(E) Mass transfer of oxygen molecules in the oxygen lean surface takes place at the oxygen lean interface. Oxygen is liberated at the interface II which are collected by the sweep gas.

The reaction can be summarised as follows[116]:

$$O_{2(g)} \rightarrow 2O_{(w')}$$

$$O_{(w')} + V_{\ddot{O}(w')} \rightarrow O^{X}_{(w')} + 2h_{(w')}$$

$$O^{X}_{(w')} \rightarrow 2O^{X}_{(w")}$$

$$h_{(w')} \rightarrow 2h_{(w")}$$

$$O^{X}_{(w")} + h_{(w')} \rightarrow O_{(w")} + V_{\ddot{O}(w")}$$

$$2O_{(w")} \rightarrow O_{2(g)}$$

Where, w’ and w” indicates interface I and II respectively, x stands for valance state V for vacancy and h for holes.

There are two main reactions in the overall process, surface reaction and bulk conduction[117-119]. One of these can be the rate determining step in the overall reaction. If surface reaction takes place faster, the bulk conduction can be slower and vice versa. Oxygen vacancy, electron and hole can also play a role in determining the rate determining step in the overall reaction.

The surface reaction at the Interface I is the reduction of molecular oxygen and at the Interface II, is the oxidation of oxide ions to molecular oxygen. The reaction is identical to the electrochemical oxygen reduction and oxygen evolution. The third reaction is the oxygen conduction through the bulk. So, it is proposed here that the development of material with oxygen reduction and oxygen evolution catalytic activity and higher bulk conductivity would result in a better membrane material for the defined application. Hence potential candidates for oxygen transport membranes can be identified through ORR and OER studies.

1.9. Scope and Objective of the Thesis

Based on the literature survey carried out in the previous sections, it is clear that perovskite type oxides are potential candidates for fuel cells and transport membrane applications possessing electrochemical ORR and OER activity as well as high conductivity. Owing to their relatively low price when compared to noble metal based catalysts, stability under harsh operating conditions (high temperatures, highly oxidizing and reducing atmosphere etc.) and the ability to tune properties by doping in the lattice by more than 90% of the elements present in the periodic table, perovskite based oxides have gained considerable attention in research community. Further research has proved that oxygen vacancies in these types of oxides play a pivotal role in all these applications. Hence oxide systems with properties similar to that of perovskite type compounds and with inherent oxygen vacancies in the lattice can be envisaged as better candidates for these applications.

Brownmillerite ($A_2B_2O_5$) type oxides which have alternate layers of octahedra and tetrahedra with oxygen vacancies orderly distributed in the two-dimensional tetrahedral layers are selected as the parent material for the work carried out in this thesis. Proper doping strategies at the cationic sites are employed to tune the properties of the parent brownmillerite. The cationic substitution at the B-site with elements exhibiting redox properties will help in inducing disorder in the orderly distributed two-dimensional oxygen vacancies. The randomly distributed oxygen vacancies along the lattice will enhance the catalytic activity of the compound as it will facilitate isotropic conduction through the sample.

Similarly, $Sr_{0.7}Na_{0.3}SiO_3$ is a recently reported compound with same compositional formula that of perovskite but with different structure. The structure consists of corner shared SiO_4 units to form Si_3O_9 type units. Due to the structural features and presence of Si, the material is anticipated to have better stability at oxidising and reducing atmospheres. And the conductivity can be tuned by proper doping strategy.

Based on these, the following works have been carried out in the present thesis

1. Synthesis, characterisation and room temperature electrocatalytic monitoring of $Ca_2Fe_{1-x}M_xO_{5\pm\delta}$, where M= Mn, Co, Ni and Cu and *x* is fixed to 0.1 for the studies. In the second part of the work, room temperature electrocatalytic activity of $Ca_2Fe_{1-x}Co_xO_{5\pm\delta}$, where *x* = 0, 0.25 and 1 is analysed. The high temperature activity analysis of the $Ca_2FeCoO_{5+\delta}$is also conducted.
2. Synthesis and characterisation of first row transition metal doping in $Ba_2In_2O_{5+\delta}$ viz. $Ba_2In_{1.75}M_{0.25}O_{5\pm\delta}$ (where M= Mn, Fe, Co, Ni, Cu) is done to study the role of dopant towards ORR and OER under alkaline medium. In the second part, the doping strategy is continued with the base metal oxide $Ba_2InCeO_{5\pm\delta}$, viz. $Ba_2CeIn_{0.75}M_{0.25}O_{5\pm\delta}$, with the same metals and analysed for ORR and OER activity. The third part of the work focuses on Co doping at both In and Ce positions to yield $Ba_2In_{2-x+y}Ce_xCo_yM_{0.25}O_{5\pm\delta}$ with different

x and *y*. The high temperature electrochemical analysis of $Ba_2InCe_{0.5}Co_{0.5}O_{5\pm\delta}$ is also performed in the third part.

3. A site and B site doping in $SrSiO_3$ viz, $Sr_{0.7}Na_{0.3}Si_{0.95}M_{0.05}O_{3-\delta}$, where M= Mn, Fe, Co, Ni, Cu. Room temperature ORR and OER activity as well as high temperature activity are monitored
4. The materials are projected as candidates for application as cathode material in SOFC and OTM membrane materials. Hollow fiber membrane fabrication and sintering analysis of $Ca_2FeCoO_{5\pm\delta}$, and $Sr_{0.7}Na_{0.3}Si_{0.95}Co_{0.05}O_{3-\delta}$ are conducted to evaluate the potential in OTM application. Electrodes with the selected materials are prepared and their conductivity in O_2 atmosphere is measured to test the feasibility in SOFC application.

1.10. References

1. Bacon, F. T., Fuel cells, past, present and future. *Electrochimica Acta* **1969,** *14* (7), 569-585.
2. Perry, M. L.; Fuller, T. F., A Historical Perspective of Fuel Cell Technology in the 20th Century. *Journal of The Electrochemical Society* **2002,** *149* (7), S59-S67.
3. Yeager, E., Electrocatalysts for O2 reduction. *Electrochimica Acta* **1984,** *29* (11), 1527-1537.
4. Kordesch, K.; Hacker, V.; Gsellmann, J.; Cifrain, M.; Faleschini, G.; Enzinger, P.; Fankhauser, R.; Ortner, M.; Muhr, M.; Aronson, R. R., Alkaline fuel cells applications. *Journal of Power Sources* **2000,** *86* (1), 162-165.
5. Zhang, Z.; Liu, J.; Gu, J.; Su, L.; Cheng, L., An overview of metal oxide materials as electrocatalysts and supports for polymer electrolyte fuel cells. *Energy & Environmental Science* **2014,** *7* (8), 2535-2558.
6. Bidault, F.; Brett, D. J. L.; Middleton, P. H.; Brandon, N. P., Review of gas diffusion cathodes for alkaline fuel cells. *Journal of Power Sources* **2009,** *187* (1), 39-48.
7. Deavin, O. I.; Murphy, S.; Ong, A. L.; Poynton, S. D.; Zeng, R.; Herman, H.; Varcoe, J. R., Anion-exchange membranes for alkaline polymer electrolyte fuel cells: comparison of pendent benzyltrimethylammonium- and benzylmethylimidazolium-head-groups. *Energy & Environmental Science* **2012,** *5* (9), 8584-8597.

8. Wittstadt, U.; Wagner, E.; Jungmann, T., Membrane electrode assemblies for unitised regenerative polymer electrolyte fuel cells. *Journal of Power Sources* **2005,** *145* (2), 555-562.

9. Pettersson, J.; Ramsey, B.; Harrison, D., A review of the latest developments in electrodes for unitised regenerative polymer electrolyte fuel cells. *Journal of Power Sources* **2006,** *157* (1), 28-34.

10. Gabbasa, M.; Sopian, K.; Fudholi, A.; Asim, N., A review of unitized regenerative fuel cell stack: Material, design and research achievements. *International Journal of Hydrogen Energy* **2014,** *39* (31), 17765-17778.

11. Grigoriev, S. A.; Millet, P.; Porembsky, V. I.; Fateev, V. N., Development and preliminary testing of a unitized regenerative fuel cell based on PEM technology. *International Journal of Hydrogen Energy* **2011,** *36* (6), 4164-4168.

12. Mitlitsky, F.; Myers, B.; Weisberg, A. H.; Molter, T. M.; Smith, W. F., Reversible (unitised) PEM fuel cell devices. *Fuel Cells Bulletin* **1999,** *2* (11), 6-11.

13. Mitlitsky, F.; Myers, B.; Weisberg, A. H., Regenerative Fuel Cell Systems. *Energy & Fuels* **1998,** *12* (1), 56-71.

14. Huang, S.-Y.; Ganesan, P.; Jung, H.-Y.; Popov, B. N., Development of supported bifunctional oxygen electrocatalysts and corrosion-resistant gas diffusion layer for unitized regenerative fuel cell applications. *Journal of Power Sources* **2012,** *198*, 23-29.

15. Vesborg, P. C. K.; Jaramillo, T. F., Addressing the terawatt challenge: scalability in the supply of chemical elements for renewable energy. *RSC Advances* **2012,** *2* (21), 7933-7947.

16. Jung, H.-Y.; Choi, J.-H., The effect of a modified Nafion binder on the performance of a unitized regenerative fuel cell (URFC). *Journal of Solid State Electrochemistry* **2012,** *16* (4), 1571-1576.

17. Lee, H.; Kim, J.; Park, J.; Joe, Y.; Lee, T., Performance of polypyrrole-impregnated composite electrode for unitized regenerative fuel cell. *Journal of Power Sources* **2004,** *131* (1), 188-193.

18. Song, S.; Zhang, H.; Ma, X.; Shao, Z.-G.; Zhang, Y.; Yi, B., Bifunctional oxygen electrode with corrosion-resistive gas diffusion layer for unitized regenerative fuel cell. *Electrochemistry Communications* **2006,** *8* (3), 399-405.

19. Hermann, A.; Chaudhuri, T.; Spagnol, P., Bipolar plates for PEM fuel cells: A review. *International Journal of Hydrogen Energy* **2005,** *30* (12), 1297-1302.

20. Dihrab, S. S.; Sopian, K.; Alghoul, M. A.; Sulaiman, M. Y., Review of the membrane and bipolar plates materials for conventional and unitized regenerative fuel cells. *Renewable and Sustainable Energy Reviews* **2009,** *13* (6), 1663-1668.

21. Ralph, J. M.; Schoeler, A. C.; Krumpelt, M., Materials for lower temperature solid oxide fuel cells. *Journal of Materials Science* **2001,** *36* (5), 1161-1172.

22. Sengodan, S.; Choi, S.; Jun, A.; Shin, T. H.; Ju, Y.-W.; Jeong, H. Y.; Shin, J.; Irvine, J. T. S.; Kim, G., Layered oxygen-deficient double perovskite as an efficient and stable anode for direct hydrocarbon solid oxide fuel cells. *Nature Materials* **2014,** *14*, 205.

23. Liu, M.; Lynch, M. E.; Blinn, K.; Alamgir, F. M.; Choi, Y., Rational SOFC material design: new advances and tools. *Materials Today* **2011,** *14* (11), 534-546.

24. Wachsman, E. D.; Lee, K. T., Lowering the Temperature of Solid Oxide Fuel Cells. *Science* **2011,** *334* (6058), 935-939.

25. Mogensen, M.; Jensen, K. V.; Jørgensen, M. J.; Primdahl, S., Progress in understanding SOFC electrodes. *Solid State Ionics* **2002,** *150* (1), 123-129.

26. Heraeus, W. C., Über die elektrolytische Leitung fester Körper bei sehr hohen Temperaturen. *Zeitschrift für Elektrochemie* **1899,** *6* (2), 41-43.

27. Weissbart, J.; Ruka, R., A Solid Electrolyte Fuel Cell. *Journal of The Electrochemical Society* **1962,** *109* (8), 723-726.

28. Baur, E.; Preis, H., Über Brennstoff-Ketten mit Festleitern. *Zeitschrift für Elektrochemie und angewandte physikalische Chemie* **1937,** *43* (9), 727-732.

29. Kamata, K.; Nakajima, T.; Hayashi, T.; Nakamura, T., Nonstoichiometric behavior and phase stability of rare earth manganites at 1200°C: (1). $LaMnO_3$. *Materials Research Bulletin* **1978,** *13* (1), 49-54.

30. Kuo, J. H.; Anderson, H. U.; Sparlin, D. M., Oxidation-reduction behavior of undoped and Sr-doped LaMnO3 nonstoichiometry and defect structure. *Journal of Solid State Chemistry* **1989,** *83* (1), 52-60.

31. Kuo, J. H.; Anderson, H. U.; Sparlin, D. M., Oxidation-reduction behavior of undoped and Sr-doped $LaMnO_3$: Defect structure, electrical conductivity, and thermoelectric power. *Journal of Solid State Chemistry* **1990,** *87* (1), 55-63.

32. Koc, R.; Anderson, H. U.; Howard, S. A., Structural, Sintering and Electrical Properties of the Perovskite-Type $(La,Sr)(Cr,Mn)O_3$. *ECS Proceedings Volumes* **1989,** *1989-11*, 220-241.

33. Ohno, Y.; Nagata, S.; Sato, H., Effect of electrode materials on the properties of high-temperature solid electrolyte fuel cells. *Solid State Ionics* **1981,** *3-4*, 439-442.

34. Gray, T. J., Strontium ceramics for chemical applications. *Journal of Power Sources* **1981,** *6* (2), 121-142.

35. Mizusaki, J.; Mima, Y.; Yamauchi, S.; Fueki, K.; Tagawa, H., Nonstoichiometry of the perovskite-type oxides $La_{1-x}Sr_xCoO_{3-\delta}$. *Journal of Solid State Chemistry* **1989,** *80* (1), 102-111.

36. Ohno, Y.; Nagata, S.; Sato, H., Properties of oxides for high temperature solid electrolyte fuel cell. *Solid State Ionics* **1983,** *9-10*, 1001-1007.

37. Minh, N. Q., Ceramic Fuel Cells. *Journal of the American Ceramic Society* **1993,** *76* (3), 563-588.

38. Doshi, R.; Richards, V. L.; Carter, J. D.; Wang, X.; Krumpelt, M., Development of Solid-Oxide Fuel Cells That Operate at 500°C. *Journal of The Electrochemical Society* **1999,** *146* (4), 1273-1278.

39. Colomer, M. T.; Steele, B. C. H.; Kilner, J. A., Structural and electrochemical properties of the $Sr_{0.8}Ce_{0.1}Fe_{0.7}Co_{0.3}O_{3-\delta}$ perovskite as cathode material for ITSOFCs. *Solid State Ionics* **2002,** *147* (1), 41-48.

40. Kim, G.; Wang, S.; Jacobson, A. J.; Reimus, L.; Brodersen, P.; Mims, C. A., Rapid oxygen ion diffusion and surface exchange kinetics in $PrBaCo_2O_{5+x}$ with a perovskite related structure and ordered A cations. *Journal of Materials Chemistry* **2007,** *17* (24), 2500-2505.

41. Ried, P.; Holtappels, P.; Wichser, A.; Ulrich, A.; Graule, T., Synthesis and Characterization of $La_{0.6}Sr_{0.4}Co_{0.2}Fe_{0.8}O_{3-\delta}$ and $Ba_{0.5}Sr_{0.5}Co_{0.8}Fe_{0.2}O_{3-\delta}$. *Journal of The Electrochemical Society* **2008,** *155* (10), B1029-B1035.

42. Ge, X.; Sumboja, A.; Wuu, D.; An, T.; Li, B.; Goh, F. W. T.; Hor, T. S. A.; Zong, Y.; Liu, Z., Oxygen Reduction in Alkaline Media: From Mechanisms to Recent Advances of Catalysts. *ACS Catalysis* **2015,** *5* (8), 4643-4667.

43. Neburchilov, V.; Wang, H.; Martin, J. J.; Qu, W., A review on air cathodes for zinc–air fuel cells. *Journal of Power Sources* **2010,** *195* (5), 1271-1291.

44. Suen, N.-T.; Hung, S.-F.; Quan, Q.; Zhang, N.; Xu, Y.-J.; Chen, H. M., Electrocatalysis for the oxygen evolution reaction: recent development and future perspectives. *Chemical Society Reviews* **2017,** *46* (2), 337-365.

45. Kötz, R.; Lewerenz, H. J.; Stucki, S., XPS Studies of Oxygen Evolution on Ru and RuO2 Anodes. *Journal of The Electrochemical Society* **1983,** *130* (4), 825-829.

46. Antolini, E., Iridium As Catalyst and Cocatalyst for Oxygen Evolution/Reduction in Acidic Polymer Electrolyte Membrane Electrolyzers and Fuel Cells. *ACS Catalysis* **2014,** *4* (5), 1426-1440.

47. Kötz, R.; Neff, H.; Stucki, S., Anodic Iridium Oxide Films: XPS-Studies of Oxidation State Changes and. *Journal of The Electrochemical Society* **1984,** *131* (1), 72-77.

48. Cherevko, S.; Geiger, S.; Kasian, O.; Kulyk, N.; Grote, J.-P.; Savan, A.; Shrestha, B. R.; Merzlikin, S.; Breitbach, B.; Ludwig, A.; Mayrhofer, K. J. J., Oxygen and hydrogen evolution reactions on Ru, RuO_2, Ir, and IrO_2 thin film electrodes in acidic and alkaline electrolytes: A comparative study on activity and stability. *Catalysis Today* **2016,** *262*, 170-180.

49. Beskow, G., V. M. Goldschmidt: Geochemische Verteilungsgesetze der Elemente. *Geologiska Föreningen i Stockholm Förhandlingar* **1924,** *46* (6-7), 738-743.

50. Forrester, W. F.; Hinde, R. M., Crystal Structure of Barium Titanate. *Nature* **1945,** *156* (3954), 177-177.

51. Megaw, H. D., Crystal structure of barium titanate. *Nature* **1945,** *155* (3938), 484-485.

52. Miyake, S.; Ueda, R., On Polymorphic Change of $BaTiO_3$. *J. Phys. Soc. Jpn.* **1946,** *1* (1), 32-33.

53. Ueda, R., On the Phase Transition of Barium Titanate (II). *J. Phys. Soc. Jpn.* **1948,** *3* (5-6), 333-337.

54. Müller, O.; Roy, R., *The major ternary structural families*. Springer-Verlag: 1974.

55. Bhalla, A. S.; Guo, R.; Roy, R., The perovskite structure – a review of its role in ceramic science and technology. *Mater. Res. Innovat.* **2000,** *4* (1), 3-26.

56. Maegli, A. E.; Hisatomi, T.; Otal, E. H.; Yoon, S.; Pokrant, S.; Grätzelb, M.; Weidenkaff, A., Structural and photocatalytic properties of perovskite-type $(La,Ca)Ti(O,N)_3$ prepared from A-site deficient precursors. *J. Mater. Chem.* **2012,** *22* (34), 17906-17913.

57. Wei, Z.-X.; Wang, Y.; Liu, J.-P.; Xiao, C.-M.; Zeng, W.-W., Synthesis, magnetization and photocatalytic activity of $LaFeO_3$ and $LaFe_{0.5}Mn_{0.5-x}O_{3-\delta}$. *Mater. Chem. Phys.* **2012,** *136* (2-3), 755-761.

58. Su, H.; Jing, L.; Shi, K.; Yao, C.; Fu, H., Synthesis of large surface area $LaFeO_3$ nanoparticles by SBA-16 template method as high active visible photocatalysts. *J. Nanopart. Res.* **2010,** *12* (3), 967-974.

59. Murphy, D. W.; Sunshine, S.; van Dover, R. B.; Cava, R. J.; Batlogg, B.; Zahurak, S. M.; Schneemeyer, L. F., New superconducting cuprate perovskites. *Physical Review Letters* **1987,** *58* (18), 1888-1890.

60. Maeno, Y.; Hashimoto, H.; Yoshida, K.; Nishizaki, S.; Fujita, T.; Bednorz, J. G.; Lichtenberg, F., Superconductivity in a layered perovskite without copper. *Nature* **1994,** *372* (6506), 532-534.

61. Filippetti, A.; Hill, N. A., Coexistence of magnetism and ferroelectricity in perovskites. *Physical Review B* **2002,** *65* (19), 195120.

62. Mazin, I. I.; Singh, D. J., Electronic structure and magnetism in Ru-based perovskites. *Physical Review B* **1997,** *56* (5), 2556-2571.

63. Kröger, F. A.; Vink, H. J., Relations between the Concentrations of Imperfections in Crystalline Solids. In *Solid State Physics*, Seitz, F.; Turnbull, D., Eds. Academic Press: 1956; Vol. 3, pp 307-435.

64. Goldschmidt, V. M., Die Gesetze der Krystallochemie. *Naturwissenschaften* **1926,** *14* (21), 477-485.

65. Colville, A. A.; Geller, S., The crystal structure of brownmillerite, Ca_2FeAlO_5. *Acta Crystallographica Section B* **1971,** *27* (12), 2311-2315.

66. Bertaut, E. F.; Blum, P.; Sagnières, A., Structure du ferrite bicalcique et de la brownmillerite. *Acta Crystallographica* **1959,** *12* (2), 149-159.

67. Smith, D., Crystallographic changes with the substitution of aluminum for iron in dicalcium ferrite. *Acta Crystallographica* **1962,** *15* (11), 1146-1152.

68. Geller, S.; Grant, R. W.; Fullmer, L. D., Magnetic structures in the $Ca_2Fe_{2-x}Al_xO_5$ system. *Journal of Physics and Chemistry of Solids* **1970,** *31* (4), 793-803.

69. Goodenough, J. B.; Ruiz-Diaz, J. E.; Zhen, Y. S., Oxide-ion conduction in Ba2In2O5 and $Ba_3In_2MO_8$ (M=Ce, Hf, or Zr). *Solid State Ionics* **1990,** *44* (1), 21-31.

70. Zhang, G. B.; Smyth, D. M., Defects and transport of the brownmillerite oxides with high oxygen ion conductivity — $Ba_2In_2O_5$. *Solid State Ionics* **1995,** *82* (3), 161-172.

71. Fisher, C. A. J.; Islam, M. S.; Brook, R. J., A Computer Simulation Investigation of Brownmillerite-Structured Ba2In2O5. *Journal of Solid State Chemistry* **1997,** *128* (1), 137-141.

72. Suntivich, J.; Gasteiger, H. A.; Yabuuchi, N.; Nakanishi, H.; Goodenough, J. B.; Shao-Horn, Y., Design principles for oxygen-reduction activity on perovskite oxide catalysts for fuel cells and metal–air batteries. *Nature Chemistry* **2011,** *3* (7), 546-550.

73. Hyodo, T.; Hayashi, M.; Miura, N.; Yamazoe, N., Catalytic Activities of Rare-Earth Manganites for Cathodic Reduction of Oxygen in Alkaline Solution. *J. Electrochem. Soc* **1996,** *143* (11), L266-L267.

74. Wang, Y.; Cheng, H.-P., Oxygen Reduction Activity on Perovskite Oxide Surfaces: A Comparative First-Principles Study of $LaMnO_3$, $LaFeO_3$, and $LaCrO_3$. *The Journal of Physical Chemistry C* **2013,** *117* (5), 2106-2112.

75. Yadav, K.; Singh, M. P.; Razavi, F. S.; Varma, G. D., Effect of A-site cation size on magnetic and charge-ordering properties of $Ln_{0.5}Sr_{0.5}Mn_{0.9}Cu_{0.1}O_3$ (Ln=La, Pr, Nd, or Ho). *Materials Science and Engineering: B* **2012,** *177* (14), 1225-1231.

76. Kozuka, H.; Ohbayashi, K.; Koumoto, K., Electronic conduction in La-based perovskite-type oxides. *Science and Technology of Advanced Materials* **2015,** *16* (2), 026001.

77. Obayashi, H.; Kudo, T., Perovskite-type compounds as electrode catalysts for cathodic reduction of oxygen. *Materials Research Bulletin* **1978,** *13* (12), 1409-1413.

78. Sunarso, J.; Torriero, A. A. J.; Zhou, W.; Howlett, P. C.; Forsyth, M., Oxygen Reduction Reaction Activity of La-Based Perovskite Oxides in Alkaline Medium: A Thin-Film Rotating Ring-Disk Electrode Study. *The Journal of Physical Chemistry C* **2012,** *116* (9), 5827-5834.

79. Zhu, C.; Nobuta, A.; Nakatsugawa, I.; Akiyama, T., Solution combustion synthesis of $LaMO_3$ (M = Fe, Co, Mn) perovskite nanoparticles and the measurement of their electrocatalytic properties for air cathode. *International Journal of Hydrogen Energy* **2013,** *38* (30), 13238-13248.

80. Matsumoto, Y.; Yamada, S.; Nishida, T.; Sato, E., Oxygen Evolution on $La_{1-x}Sr_xFe_{1-y}Co_yO_3$ Series Oxides. *Journal of The Electrochemical Society* **1980,** *127* (11), 2360-2364.

81. Liu, Y.; Wang, H.; Lin, D.; Liu, C.; Hsu, P.-C.; Liu, W.; Chen, W.; Cui, Y., Electrochemical tuning of olivine-type lithium transition-metal phosphates as efficient water oxidation catalysts. *Energy & Environmental Science* **2015,** *8* (6), 1719-1724.

82. Bockris, J. O. M.; Otagawa, T., Mechanism of oxygen evolution on perovskites. *The Journal of Physical Chemistry* **1983,** *87* (15), 2960-2971.

83. Bockris, J. O. M.; Otagawa, T., The Electrocatalysis of Oxygen Evolution on Perovskites. *Journal of The Electrochemical Society* **1984,** *131* (2), 290-302.

84. Hong, W. T.; Risch, M.; Stoerzinger, K. A.; Grimaud, A.; Suntivich, J.; Shao-Horn, Y., Toward the rational design of non-precious transition metal oxides for oxygen electrocatalysis. *Energy & Environmental Science* **2015,** *8* (5), 1404-1427.

85. Suntivich, J.; May, K. J.; Gasteiger, H. A.; Goodenough, J. B.; Shao-Horn, Y., A Perovskite Oxide Optimized for Oxygen Evolution Catalysis from Molecular Orbital Principles. *Science* **2011,** *334* (6061), 1383-1385.

86. Zhu, Y.; Zhou, W.; Chen, Z.-G.; Chen, Y.; Su, C.; Tadé, M. O.; Shao, Z., $SrNb_{0.1}Co_{0.7}Fe_{0.2}O_{3-\delta}$ Perovskite as a Next-Generation Electrocatalyst for Oxygen Evolution in Alkaline Solution. *Angewandte Chemie International Edition* **2015,** *54* (13), 3897-3901.

87. Yagi, S.; Yamada, I.; Tsukasaki, H.; Seno, A.; Murakami, M.; Fujii, H.; Chen, H.; Umezawa, N.; Abe, H.; Nishiyama, N.; Mori, S., Covalency-reinforced oxygen evolution reaction catalyst. *Nature Communications* **2015,** *6* (1), 8249.

88. Grimaud, A.; May, K. J.; Carlton, C. E.; Lee, Y.-L.; Risch, M.; Hong, W. T.; Zhou, J.; Shao-Horn, Y., Double perovskites as a family of highly active catalysts for oxygen evolution in alkaline solution. *Nature Communications* **2013,** *4* (1), 2439.

89. Rong, X.; Parolin, J.; Kolpak, A. M., A Fundamental Relationship between Reaction Mechanism and Stability in Metal Oxide Catalysts for Oxygen Evolution. *ACS Catalysis* **2016,** *6* (2), 1153-1158.

90. Lee, J. G.; Hwang, J.; Hwang, H. J.; Jeon, O. S.; Jang, J.; Kwon, O.; Lee, Y.; Han, B.; Shul, Y.-G., A New Family of Perovskite Catalysts for Oxygen-Evolution Reaction in Alkaline Media: $BaNiO_3$ and $BaNi_{0.83}O_{2.5}$. *Journal of the American Chemical Society* **2016,** *138* (10), 3541-3547.

91. Zhao, B.; Zhang, L.; Zhen, D.; Yoo, S.; Ding, Y.; Chen, D.; Chen, Y.; Zhang, Q.; Doyle, B.; Xiong, X.; Liu, M., A tailored double perovskite nanofiber catalyst enables ultrafast oxygen evolution. *Nature Communications* **2017,** *8* (1), 14586.

92. Grimaud, A.; Diaz-Morales, O.; Han, B.; Hong, W. T.; Lee, Y.-L.; Giordano, L.; Stoerzinger, K. A.; Koper, M. T. M.; Shao-Horn, Y., Activating lattice oxygen redox reactions in metal oxides to catalyse oxygen evolution. *Nature Chemistry* **2017,** *9* (5), 457-465.

93. Hu, C.; Zhang, L.; Gong, J., Recent progress made in the mechanism comprehension and design of electrocatalysts for alkaline water splitting. *Energy & Environmental Science* **2019,** *12* (9), 2620-2645.

94. Vojvodic, A.; Nørskov, J. K., Optimizing Perovskites for the Water-Splitting Reaction. *Science* **2011,** *334* (6061), 1355.

95. Wu, X.-Y.; Ghoniem, A. F.; Uddi, M., Enhancing co-production of H_2 and syngas via water splitting and POM on surface-modified oxygen permeable membranes. *AIChE Journal* **2016,** *62* (12), 4427-4435.

96. Yang, W.; Wang, H.; Zhu, X.; Lin, L., Development and Application of Oxygen Permeable Membrane in Selective Oxidation of Light Alkanes. *Topics in Catalysis* **2005,** *35* (1), 155-167.

97. Wang, H.; Cong, Y.; Yang, W., High selectivity of oxidative dehydrogenation of ethane to ethylene in an oxygen permeable membrane reactor. *Chemical Communications* **2002,** (14), 1468-1469.

98. Lu, Y.; Dixon, A. G.; Moser, W. R.; Ma, Y. H.; Balachandran, U., Oxygen-permeable dense membrane reactor for the oxidative coupling of methane. *Journal of Membrane Science* **2000,** *170* (1), 27-34.

99. Shao, Z.; Dong, H.; Xiong, G.; Cong, Y.; Yang, W., Performance of a mixed-conducting ceramic membrane reactor with high oxygen permeability for methane conversion. *Journal of Membrane Science* **2001,** *183* (2), 181-192.

100. Bouwmeester, H. J. M., Dense ceramic membranes for methane conversion. *Catalysis Today* **2003,** *82* (1), 141-150.

101. Wang, Z.; Oemar, U.; Ang, M. L.; Kawi, S., Oxidative steam reforming of biomass tar model compound via catalytic $BaBi_{0.05}Co_{0.8}Nb_{0.15}O_{3-\delta}$ hollow fiber membrane reactor. *Journal of Membrane Science* **2016,** *510*, 417-425.

102. Liu, T.; Chen, Y.; Fang, S.; Lei, L.; Wang, Y.; Ren, C.; Chen, F., A dual-phase bilayer oxygen permeable membrane with hierarchically porous structure fabricated by freeze-drying tape-casting method. *Journal of Membrane Science* **2016,** *520*, 354-363.

103. Wall, T.; Liu, Y.; Spero, C.; Elliott, L.; Khare, S.; Rathnam, R.; Zeenathal, F.; Moghtaderi, B.; Buhre, B.; Sheng, C.; Gupta, R.; Yamada, T.; Makino, K.; Yu, J., An overview on oxyfuel coal combustion—State of the art research and technology development. *Chemical Engineering Research and Design* **2009,** *87* (8), 1003-1016.

104. Mezghani, K.; Hamza, A., Application of $Ba_{0.5}Sr_{0.5}Co_{0.8}Fe_{0.2}O_{3-\delta}$ membranes in an oxy-fuel combustion reactor. *Journal of Membrane Science* **2016,** *518*, 254-262.

105. Goodenough, J. B., Oxide-ion conductors by design. *Nature* **2000,** *404* (6780), 821-823.

106. Sunarso, J.; Baumann, S.; Serra, J. M.; Meulenberg, W. A.; Liu, S.; Lin, Y. S.; Diniz da Costa, J. C., Mixed ionic–electronic conducting (MIEC) ceramic-based membranes for oxygen separation. *Journal of Membrane Science* **2008,** *320* (1), 13-41.

107. Badwal, S. P. S.; Ciacchi, F. T., Ceramic Membrane Technologies for Oxygen Separation. *Advanced Materials* **2001,** *13* (12-13), 993-996.

108. Wang, B.; Song, J.; Tan, X.; Meng, B.; Liu, J.; Liu, S., Reinforced perovskite hollow fiber membranes with stainless steel as the reactive sintering aid for oxygen separation. *Journal of Membrane Science* **2016,** *502*, 151-157.

109. Wei, Y.; Yang, W.; Caro, J.; Wang, H., Dense ceramic oxygen permeable membranes and catalytic membrane reactors. *Chemical Engineering Journal* **2013,** *220*, 185-203.

110. Sun, M.; Chen, X.; Hong, L., Leveraging the A-site Ba^{2+}–Sr^{2+} ratio in the designated perovskite to enhance oxygen transport and structural/interfacial stability. *RSC Advances* **2014,** *4* (11), 5618-5625.

111. Liu, Y.; Zhu, X.; Li, M.; Liu, H.; Cong, Y.; Yang, W., Stabilization of Low-Temperature Degradation in Mixed Ionic and Electronic Conducting Perovskite Oxygen Permeation Membranes. *Angewandte Chemie International Edition* **2013,** *52* (11), 3232-3236.

112. Armor, J. N., Applications of catalytic inorganic membrane reactors to refinery products. *Journal of Membrane Science* **1998,** *147* (2), 217-233.

113. Zaman, J.; Chakma, A., Inorganic membrane reactors. *Journal of Membrane Science* **1994,** *92* (1), 1-28.

114. Kusaba, H.; Shibata, Y.; Sasaki, K.; Teraoka, Y., Surface effect on oxygen permeation through dense membrane of mixed-conductive LSCF perovskite-type oxide. *Solid State Ionics* **2006,** *177* (26), 2249-2253.

115. Bouwmeester, H. J. M.; Kruidhof, H.; Burggraaf, A. J., Importance of the surface exchange kinetics as rate limiting step in oxygen permeation through mixed-conducting oxides. *Solid State Ionics* **1994,** *72*, 185-194.

116. Dou, S.; Masson, C. R.; Pacey, P. D., Mechanism of Oxygen Permeation Through Lime-Stabilized Zirconia. *Journal of The Electrochemical Society* **1985,** *132* (8), 1843-1849.

117. Lin, Y.-S.; Wang, W.; Han, J., Oxygen permeation through thin mixed-conducting solid oxide membranes. *AIChE Journal* **1994,** *40* (5), 786-798.

118. Lee, T. H.; Yang, Y. L.; Jacobson, A. J.; Abeles, B.; Zhou, M., Oxygen permeation in dense $SrCo_{0.8}Fe_{0.2}O_{3-\delta}$ membranes: Surface exchange kinetics versus bulk diffusion. *Solid State Ionics* **1997,** *100* (1), 77-85.

119. van Hassel, B. A.; Kawada, T.; Sakai, N.; Yokokawa, H.; Dokiya, M.; Bouwmeester, H. J. M., Oxygen permeation modelling of perovskites. *Solid State Ionics* **1993,** *66* (3), 295-305.

Chapter 2

The $Ca_2Fe_2O_5$ system

Part A

Role of Transition Metal Doping in the Structure and Room Temperature Electrochemical Activity of $Ca_2Fe_2O_5$

2A.1. Introduction

$Ca_2Fe_2O_5$ crystallises in the brownmillerite structure with alternate layers of octahedra and tetrahedra. A fraction of Fe^{3+} can get associated with holes to form Fe^{4+} resulting in a stoichiometry of $Ca_2Fe_2O_{5+\delta}$, and the loss of oxygen can restore the stoichiometry by the reduction of IV state to III state. $Ca_2Fe_2O_5$ is a well studied system for its structure and various properties with applications in catalysis like photocatalysis, biodiesel production, anode material in Li ion battery, propylene combustion, etc[1-7].

Aliovalent doping strategy results in the oxygen vacancy formation and it is having a crucial role in the adsorption reactions. Oxygenated species coordinate to oxygen vacant sites during the reaction, since the coordinative unsaturation facilitates ion transport[8]. DFT studies show the reduction of kinetic barrier with oxygen vacancy[9]. Also, it is reported to enhance coulombic efficiency of electrochemical reaction by incorporating coordinative unsaturation in the lattice[10]. Oxygen vacant sites enhance the bifunctional ORR-OER activity by improved mobility of hopping vacancies among various oxidation states[11, 12].

The design of a bifunctional catalyst is a difficult task without understanding the contribution of the dopant metal towards the structure and property. $Ca_2Fe_2O_5$, a well studied brownmillerite system has been selected to study the effect of dopants in the structure and resulting electrochemical properties. The size and the crystal field effect of the transition metal dopant plays an important role in the site occupancy. Fe in +3 oxidation state and high spin d^5 configuration can occupy both the tetrahedral and octahedral positions. In this chapter, first row transition metals such as Mn, Co, Ni and Cu are substituted for Fe in $Ca_2Fe_2O_5$ and their structure property correlation is studied.

2A.2. Experimental Section

2A.2.1. Synthesis of $Ca_2Fe_{1.9}M_{0.1}O_{5\pm\delta}$ (M = Mn/Fe/Co/Ni/Cu)

$Ca_2Fe_2O_{5\pm\delta}$ and doped $Ca_2Fe_{1.9}M_{0.1}O_{5\pm\delta}$ (M = Mn, Co, Ni and Cu) are synthesised by citrate gel route. The precursors $Ca(NO_3)_2.4H_2O$ (Alfa-Aeser, 99%), $Fe(NO_3)_3.9H_2O$ (Alfa-Aeser, 98%), $Mn(NO_3)_2.6H_2O$ (Alfa-Aeser, 98%), $Co(NO_3)_2.6H_2O$ (Merck, 98%), $Ni(NO_3)_2.6H_2O$ (Sigma-Aldrich) and $Cu(NO_3)_2.4H_2O$ (Merck, 99.5%) are weighed in stoichiometric proportions and dissolved in Milli-Q-Ultrapure water. Twice mole proportion of citric acid monohydrate is added to the solution and made into gel at 80-90°C. Ethylene glycol is added to the gel and stirred for homogeneity. Decarbonation is carried out at 400°C followed by calcination at 1000°C for 6 h.

2A.2.2. Characterisation

Phase purity and structure is analysed with powder X-ray diffraction (PXRD) in PANaylitical X'pert Pro dual goniometer diffractometer with Ni as filter and Cu Kα source operating at 40kV and 30mA. Room temperature diffraction patterns are recorded with X'celerator solid state detector with step size 0.008° and time per step 96.52s. Rietveld refinement of resulted PXRD patterns is carried out using GSAS-EXPGUI suit of programs[13] through a least square approach and all the parameters including occupancy of metal sites are refined to get a good fit. Agilent made Microwave Plasma Atomic Emission Spectrometer (MP-AES) is used for the bulk composition analysis. The materials are digested with aqua regia and diluted with milli Q ultrapure water for analysis. Morphology and surface composition are analysed by SEM-EDAX in FEI Quanta 200 3D Elite Plus instrument, EDS analysis is carried out in the same instrument with Octane Elite plus detector. Surface area analysis of the samples are done by N_2 adsorption at the liquid nitrogen temperature using the Autosorb iQ Quantachrome system, initially samples are degassed at 300°C under vacuum for 6 h to remove the moisture and adsorbed gases. Surface states of the cations are analysed by X-ray photoelectron spectroscopy (XPS) analysis in K-Apha+ model Thermo Fischer Scientific (UK) make XPS instrument with Al Kα source. XPS data of the compounds are fitted with Shirley type background subtraction method using XPS PEAK41 software. The data is corrected by standardised peak for carbon at 284.8eV. Work function calculations are carried out with the Ultra Violet Photoelectron spectroscopy (UPS) experiment in the same instrument. Oxygen vacancy concentration is estimated by SDT Q600 DSC-TDA Thermogravimetric instrument from 100°C to 500°C in He and O_2 atmosphere. The material is pretreated at 125°C in He atmosphere to remove the volatile matters. The pretreated material is heated to 500°C in 5°C/min ramp rate with 30mL/min flow rate of He and weight loss associated with the treatment is noted. After cooling down at a rate of 10°C/minute, weight gain is noted with O_2 flow of 30mL/min from 27°C to 500°C with ramp rate of 5°C/min. The difference in weight in both the atmospheres is noted as the oxygen uptake and the number of moles of oxygen taken up is calculated from the weight gain.

2A.2.3. Electrochemical Analysis

Electrochemical oxygen reduction and evolution activity are monitored by Biologic SP-300 equipped with Pine electrode speed control. The system is configured with conventional 3-electrode system with Hg/HgO as the reference electrode and graphite rod as the counter electrode. The glassy carbon coated with the catalyst acted as the working electrode. Data collection is carried out in EC lab software and cyclic voltammetry (CV) and linear sweep voltammetry (LSV) experiments are conducted.

The catalyst oxide is mixed with carbon for the catalyst ink preparation by ball milling the oxide material and activated carbon (3:2) at 400rpm for 2h. Catalyst ink is prepared by weighing 5mg of this mixture and dispersing in 40μL of 5 wt% nafion solution and 960μL of 3:1 IPA-water mixture. 10μL of the catalyst ink is applied to the glassy carbon surface for electrochemical analysis. Experiments are conducted in 0.1M KOH solution. For monitoring ORR, CV experiments are conducted with 50 mV/s scan rate and LSV profiles are recorded in 10mV/s scan rate with 400, 900, 1200, 1600, 2000, and 2500 rpm rotations of the working electrode in the potential window 0.2 to -0.9V with respect to Hg/HgO. Rotating Ring Disk Electrode (RRDE) technique is used to determine the electron transfer number associated with the reduction reaction. 40 wt% Pt/C ink prepared in the same manner is used as a standard for the reaction; the sample is scanned in the same potential window at 10mV/s at 1600rpm in O_2 saturation.

Oxygen Evolution Reaction (OER) studies are conducted with the same catalyst ink separately in N_2 saturation at 1600rpm rotation with 10mV/s scan rate, where the potential window applied is maintained from 0 to 1V with respect to Hg/HgO.

2A.3. Results and Discussion

2A.3.1. Synthesis and Structural Characterisation

The brownmillerite structures $Ca_2Fe_{1.9}M_{0.1}O_{5\pm\delta}$ are synthesised successfully by citrate gel method. The phase purity analysis by powder x-ray diffraction suggests that all the materials are formed phase pure, matching with the reference pattern with JCPDS reference code: 47-1744. Substitution of more than 5% resulted in the formation of impurity phases in case of Ni and Cu, hence for the sake of comparison, the composition is fixed to be $Ca_2Fe_{1.9}M_{0.1}O_{5\pm\delta}$. The PXRD patterns are represented in figure 2A.1.

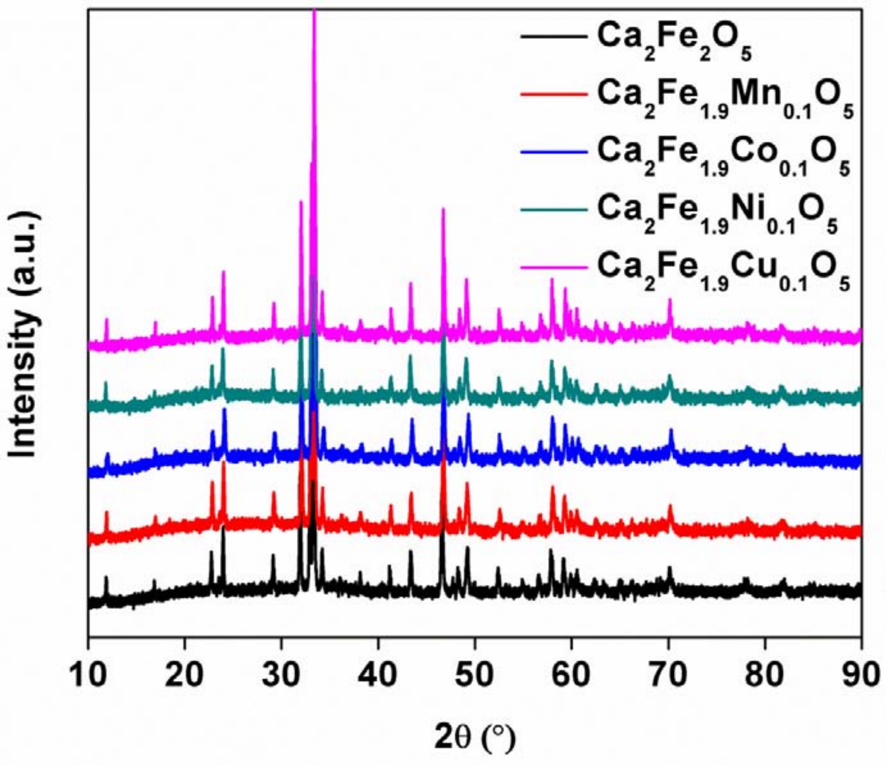

Figure 2A.1: Powder XRD patterns of the 5 atom% transition metal doped $Ca_2Fe_2O_{5\pm\delta}$

Detailed structural studies are conducted by Rietveld refinement of PXRD patterns by GSAS-EXPGUI suit of software[13]. Refinement proceeded smoothly with $Ca_2Fe_2O_5$ model with ICSD reference number: 15059 crystallising in Pnma space group. The parent structure $Ca_2Fe_2O_5$ consists of alternate layers of tetrahedra and octahdra. Alternate layers of tetrahedra and octahedra are connected by O2 atoms, O1 atom connects the octahedra within a layer and O3 is the connecting atom within the tetrahedral layer. The Rietveld refinement of the doped materials are conducted by stoichiometrically substituting the Fe position in three ways, metal dopant in both octahedral and tetrahedral sites equally, octahdedral sites alone, and tetrahedral sites alone. While refining with the mixed occupancy of both tetrahedral and octahedral sites, the occupancy at the octahedral site is observed to decrease tremendously, and when the occupancy is restricted to octahedral position, the fit was not acceptable showing a tetrahedral site preference of the dopant metals. The profiles after refinement are represented in figure 2A.2 and the data is represented in table 2A.1.

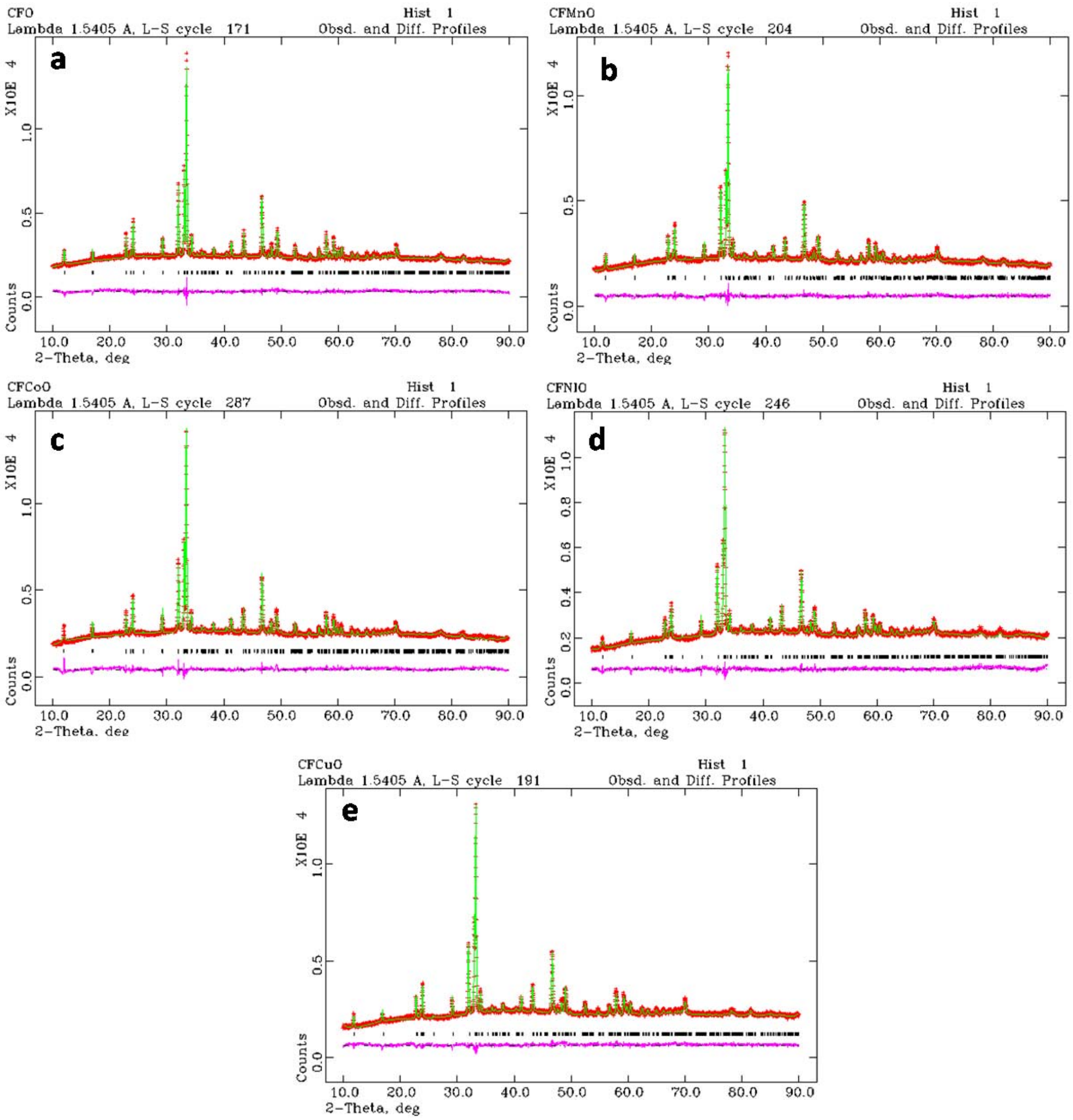

Figure 2A.2: Rietveld refined patterns of a) $Ca_2Fe_2O_{5\pm\delta}$ b) $Ca_2Fe_{1.9}Mn_{0.1}O_{5\pm\delta}$ c) $Ca_2Fe_{1.9}Co_{0.1}O_{5\pm\delta}$ d) $Ca_2Fe_{1.9}Ni_{0.1}O_{5\pm\delta}$ and e) $Ca_2Fe_{1.9}Cu_{0.1}O_{5\pm\delta}$

The surface composition and morphology are analysed by SEM-EDS technique. The materials are found to be agglomerated on account of the high temperature synthesis method as represented in figure 2A.3. The surface composition observed by the EDS analysis is in accordance with the sample stoichiometry, and is tabulated in table 2A.2. Surface area analysed by BET analysis suggests that the materials exhibit low surface area on account of the high temperature synthesis route. The details are given in table 2A.2.

Table 2A.1: Structural parameters obtained after Rietveld refinement of $Ca_2Fe_{1.9}M_{0.1}O_{5\pm\delta}$

	$Ca_2Fe_2O_{5\pm\delta}$	$Ca_2Fe_{1.9}Mn_{0.1}O_{5\pm\delta}$	$Ca_2Fe_{1.9}Co_{0.1}O_{5\pm\delta}$	$Ca_2Fe_{1.9}Ni_{0.1}O_{5\pm\delta}$	$Ca_2Fe_{1.9}Cu_{0.1}O_{5\pm\delta}$
χ^2	1.609	1.247	2.361	1.835	1.770
Rp	2.02	1.86	2.33	2.25	2.21
wRp	2.57	2.35	3.03	2.87	2.75
a b c	5.42217(6) 14.7679(2) 5.59259(7)	5.41420(7) 14.8097(2) 5.57402(8)	5.42069(9) 14.8064(3) 5.5908(1)	5.3975(1) 14.8176(3) 5.5736(1)	5.4002(4) 14.833(12) 5.5730(5)
Ca^{2+}	0.482324 0.108876 0.023243	0.483100 0.109084 0.022546	0.483480 0.108097 0.021602	0.482632 0.108726 0.022990	0.482269 0.108949 0.022860
Fe1 Occupancy	0.9789	0.9790	0.9736	0.9723	0.9708
Fe2	-0.053743 0.2500 -0.065482	-0.052250 0.2500 -0.064512	-0.051891 0.25 -0.066503	-0.053758 0.2500 -0.065936	-0.052862 0.2500 -0.065869
Occupancy	1.0143	0.9139	0.9080	0.9062	0.9126
O1	0.257460 -0.015580 0.237850	0.258874 -0.015282 0.235868	0.265844 -0.015244 0.233989	0.260449 -0.016437 0.232030	0.264121 -0.016478 0.235397
Occupancy	0.9823	0.9828	0.9678	0.9804	0.9829
O2	0.020601 0.142685 0.071458	0.019580 0.142192 0.071671	0.025005 0.14124 0.065634	0.026880 0.142767 0.068482	0.023014 0.143026 0.070514
Occupancy	1.0162	1.0051	1.0327	1.0372	1.0243

O3	0.598711 0.2500 -0.124172	0.596608 0.25 -0.125477	0.591290 0.2500 -0.117393	0.594150 0.2500 -0.118098	0.594306 0.2500 -0.122587
Occupancy	1.0143	1.0128	1.0368	1.0313	1.0262
Mn/Co/Ni/Cu		-0.044325 0.2500 -0.057149	-0.043773 0.2500 -0.074534	-0.050691 0.2500 -0.066098	-0.042945 0.2500 -0.065248
Occupancy		0.1078	0.1017	0.1083	0.1155

*Fe1 (0,0,0) **$\chi2 = \frac{M}{\text{Nobs}-\text{Nvar}}$ where N_{obs} is the total number of observations in all the histograms and N_{var} is the number of variables in the least square refinement *** The residual factors R_p and wRp are defined as $R_p = \frac{\Sigma|\text{Io}-\text{Ic}|}{\Sigma\text{Io}}$ and $wR_p = \sqrt{\frac{\text{Mp}}{\Sigma w I o^2}}$ where I_o and I_c are observed and calculated intensities M_p is the minimisation powder diffraction function

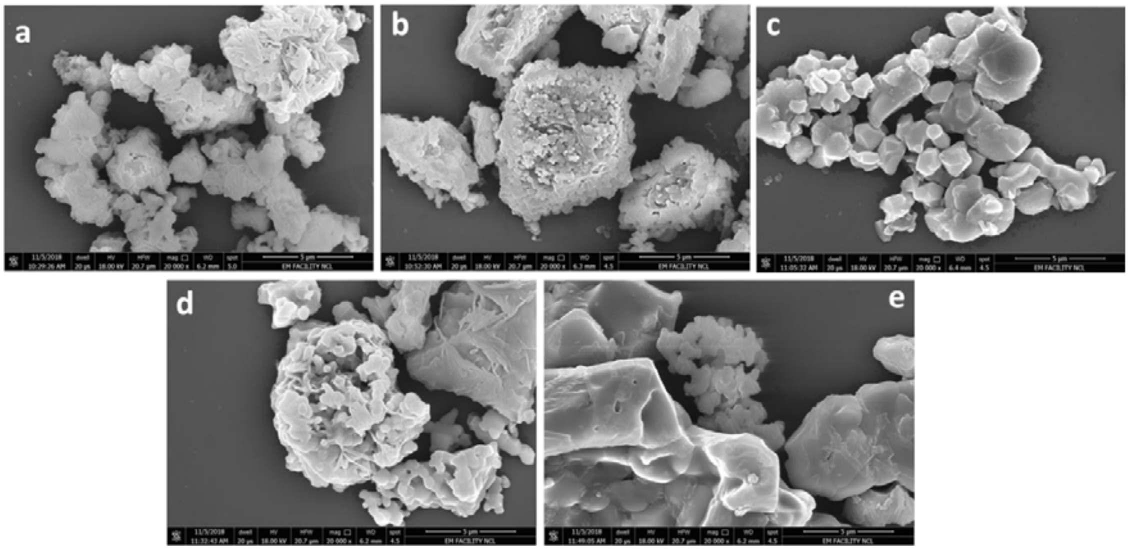

Figure 2A.3: SEM images of Figure of a) $Ca_2Fe_2O_{5\pm\delta}$ b) $Ca_2Fe_{1.9}Mn_{0.1}O_{5\pm\delta}$ c) $Ca_2Fe_{1.9}Co_{0.1}O_{5\pm\delta}$ d) $Ca_2Fe_{1.9}Ni_{0.1}O_5$e) $Ca_2Fe_{1.9}Cu_{0.1}O_{5\pm\delta}$

The surface states of the metals are analysed by XPS. The $Fe2p_{3/2}$ spectrum, deconvoluted into five peaks and is represented in figure 2A.4, proves the existence of Fe in +3 oxidation state alone[14, 15]. The details of the deconvoluted spectra are given in table 2A.3. Mn spectrum consists of $2p_{3/2}$ and $2p_{1/2}$ contributions, upon deconvolution the spectrum is fitted with two peaks corresponding to +2 and +3 states, $2p_{3/2}$ spectra is fitted with peaks at 639.5eV and 641.4eV corresponding to +2 and +3 states respectively. $2p_{1/2}$ peak situated at 12eV higher binding energy than the $2p_{3/2}$, is fitted with peaks at 651.5eV and 653.4eV corresponding to the Mn(II) and Mn(III) respectively[16, 17]. Similarly Co2p spectrum is also resolved with contribution from +2 and +3 states, $2p_{3/2}$ and $2p_{1/2}$ peaks has a coupling constant of ~15eV, and a satellite peak at 6eV higher, confirming the presence of Co(II) and Co(III) states. The peaks at 781.1eV, 796.1eV and intense satellite peaks at 787.5eV and 802.4eV correspond to Co (III) state. Those at 784.5eV, 798.9eV, and satellite peaks at 790.5eV and 805.8eV correspond to the Co(II) state[14, 15, 18]. Ni $2p_{3/2}$ XP spectrum is resolved with peak at 855.4eV and an intense satellite peak at a binding energy 6eV higher which confirms the presence of only Ni(II) state[19, 20]. Similarly Cu$2p_{3/2}$ spectrum is also fitted with peak at 934.2eV and a satellite peak at 941.3eV confirming the presence of Cu in +2 state[21, 22]. The detailed marked XP spectra of the samples are represented in figure 2A.5. The surface weight percentage of different oxidation states of Mn and Co are calculated from the deconvoluted area of XP spectrum. The +3 state of both the metals are in majority, Mn(III) confines ~65% and Co(III) contributes ~60% of the total composition in respective compounds.

Workfunctions of the materials are calculated by Ultraviolet Photoelectron Spectroscopy (UPS), which is a powerful technique to analyse the molecular orbital energies in the valence band region. The work function calculations are performed from the spectrum collected with -10eV bias, where the cut-off regions are clearly observed. The value of work function can be regarded as the easiness of electron transfer from the surface of the material. The calculation is performed by the equation 2A.1[23]

$$E_B + E_K + \phi = 21.2 \text{ eV} \tag{2A.1}$$

where E_B is the binding energy measured from the Fermi level, E_K is the kinetic energy of the electron and ϕ the work function, which is measured as the difference in value from the cut off region to Fermi level position. The vacuum energy level is located above 21.2eV from the cut off energy point. The work function values are calculated by correcting the bias, and subtracting the cut-off value from 21.2eV. The UP spectra are represented in figure 2A.6. The values obtained for secondary electron cut-off, width of the spectrum and work function are tabulated in table 2A.4. The valence band in the

Table 2A.2: Surface composition of the materials from EDS analysis, surface area of the materials from BET analysis and bulk composition obtained by MP-AES analysis

Materials	Elements	EDS Data (weight %)		MP-AES Data (ppm)		Surface area (m^2/g)
		Calculated	Observed	Calculated	Observed	
$Ca_2Fe_2O_{5\pm\delta}$	Ca	29.48	21.51	--	--	--
	Fe	41.08	32.33	--	--	
	O	29.47	46.16	--	--	
$Ca_2Fe_{1.9}Mn_{0.1}O_{5\pm\delta}$	Ca	29.49	26.56	53.1	53.7	4.44
	Fe	39.05	40.64	70.3	63.7	
	Mn	2.02	2.01	3.6	3.03	
	O	29.43	31.10	--	--	
$Ca_2Fe_{1.9}Co_{0.1}O_{5\pm\delta}$	Ca	29.45	28.76	90.72	107.9	0.89
	Fe	38.99	44.09	112.3	119.6	
	Co	2.17	3.61	6.24	6.37	
	O	29.39	23.53	--	--	
$Ca_2Fe_{1.9}Ni_{0.1}O_{5\pm\delta}$	Ca	29.45	25.04	90.72	100.3	4.23
	Fe	38.99	36.81	120.1	118.2	
	Ni	2.16	2.74	6.64	5.9	
	O	29.39	35.41	--	--	
$Ca_2Fe_{1.9}Cu_{0.1}O_{5\pm\delta}$	Ca	29.4	23.97	57.63	69.6	8.14
	Fe	38.92	36.43	76.3	83.7	
	Cu	2.33	2.31	4.57	4.9	
	O	29.34	37.3	--	--	

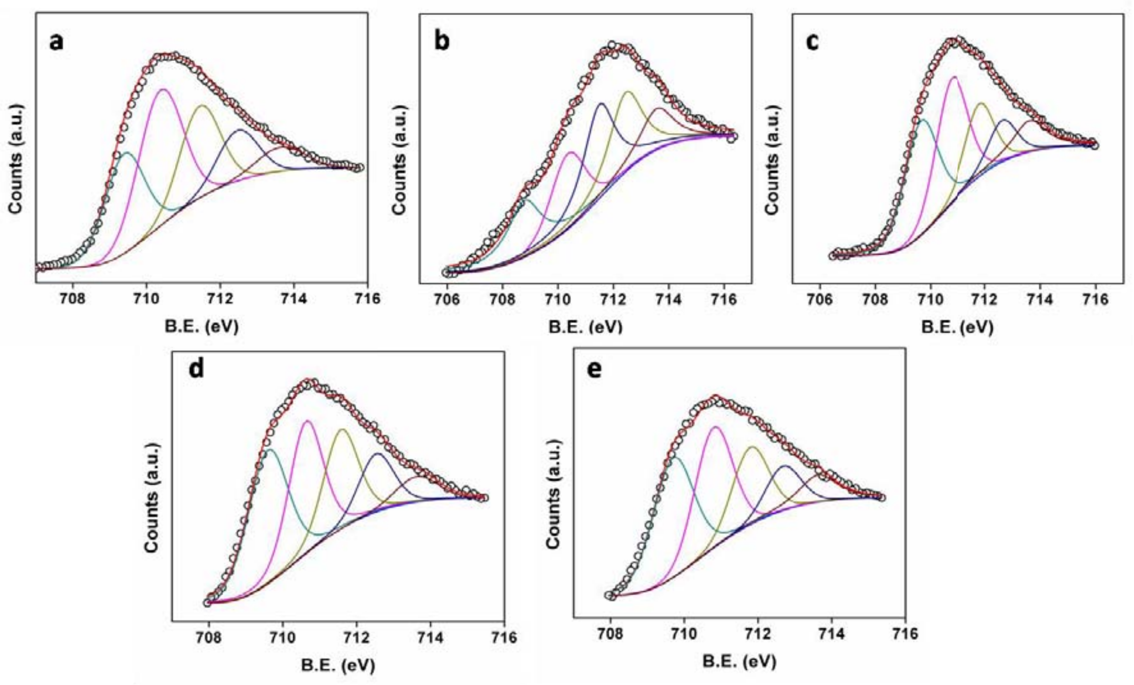

Figure 2A.4: Deconvoluted Fe2p XPS of a) $Ca_2Fe_2O_{5\pm\delta}$ b) $Ca_2Fe_{1.9}Mn_{0.1}O_{5\pm\delta}$ c) $Ca_2Fe_{1.9}Co_{0.1}O_{5\pm\delta}$ d) $Ca_2Fe_{1.9}Ni_{0.1}O_{5\pm\delta}$ e) $Ca_2Fe_{1.9}Cu_{0.1}O_{5\pm\delta}$

Table 2A.3: Peak positions of Fe2p deconvoluted XPS spectra

Material	Peaks (eV)				
	1	2	3	4	5
$Ca_2Fe_2O_5$	709.4	710.4	711.4	712.5	713.6
$Ca_2Fe_{1.9}Mn_{0.1}O_5$	708.8	710.4	711.5	712.5	713.6
$Ca_2Fe_{1.9}Co_{0.1}O_5$	709.7	710.8	711.8	712.6	713.6
$Ca_2Fe_{1.9}Ni_{0.1}O_5$	709.6	710.4	711.6	712.6	713.6
$Ca_2Fe_{1.9}Cu_{0.1}O_5$	709.7	710.8	711.8	712.7	713.6

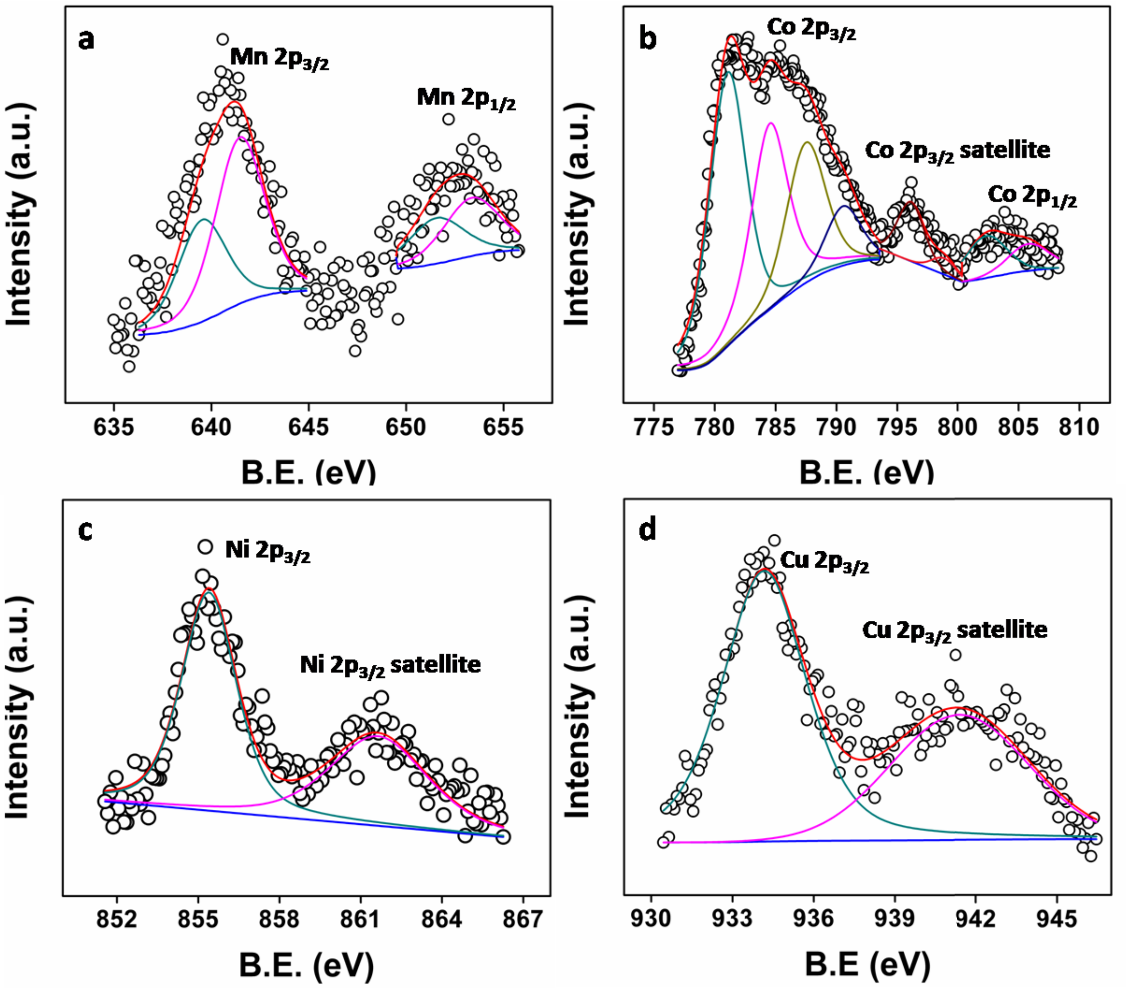

Figure 2A.5: Deconvoluted 2p XP spectra of a) Mn in $Ca_2Fe_{1.9}Mn_{0.1}O_{5\pm\delta}$ c) Co in $Ca_2Fe_{1.9}Co_{0.1}O_{5\pm\delta}$ d) Ni in $Ca_2Fe_{1.9}Ni_{0.1}O_{5\pm\delta}$ e) Cu in $Ca_2Fe_{1.9}Cu_{0.1}O_{5\pm\delta}$

mixed metal oxide constitutes of O2p orbitals and the workfunction implies the extent of electron donating capability of the catalyst. The calculated work function is in the order $Ca_2Fe_{1.9}Mn_{0.1}O_{5\pm\delta}$ < $Ca_2Fe_{1.9}Cu_{0.1}O_{5\pm\delta}$ < $Ca_2Fe_{1.9}Co_{0.1}O_{5\pm\delta}$ < $Ca_2Fe_2O_{5\pm\delta}$ < $Ca_2Fe_{1.9}Ni_{0.1}O_{5\pm\delta}$. In the case of molecules the UPS analysis is complicated due to a number of reasons such as charge transfer across the interface, multi-electron excitation, redistribution of electron cloud and interfacial chemical reactions. Here in $Ca_2Fe_{1.9}Mn_{0.1}O_{5\pm\delta}$, the observed work function is lower in comparison with the other system, probable reason is the presence of Mn^{+3} state, which is more likely to abstract an electron to form more degenerate Mn^{+2} form and can be regarded as a case of strong acceptor low work-function material.

Oxygen uptake studies to get an insight on the oxygen vacancy concentration of the materials are conducted by thermo gravimetric experiments. The sample is treated in He to remove all the loosely bound oxygen to get maximum oxygen vacancy followed by treatment in O_2 atmosphere till 500°C, the weight gain associated with the process corresponds to the oxygen uptake capability of the material and is tabulated in table 2A.5. Ni doped material exhibits maximum oxygen uptake and least by Cu doped and parent brownmillerite. The oxygen vacancy concentration is estimated by combining

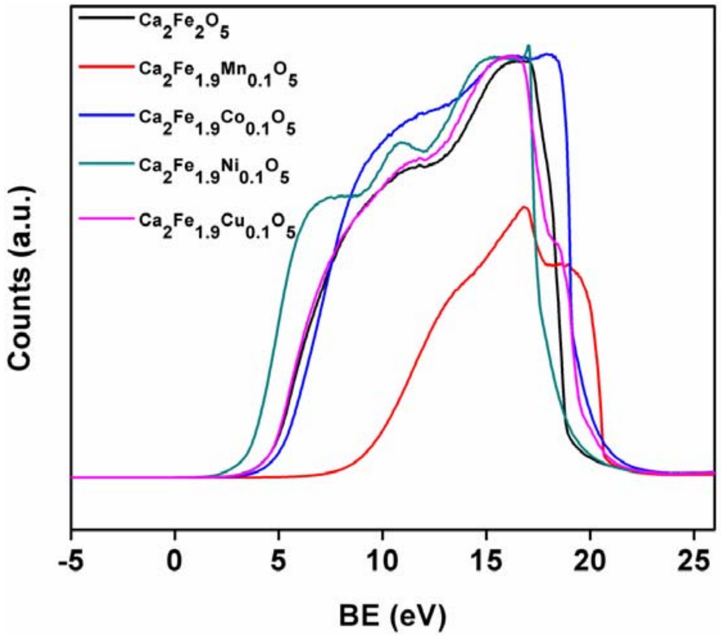

Figure 2A.6: Ultraviolet photoelectron spectra of the samples with respect to various energy levels at -10eV bias

Table 2A.4: Work function and secondary electron cut-off calculated from UPS data

Material	Secondary electron cutoff	Width	Work function
$Ca_2Fe_2O_{5\pm\delta}$	18.52	14.37	2.68
$Ca_2Fe_{1.9}Mn_{0.1}O_{5\pm\delta}$	20.37	12.45	0.83
$Ca_2Fe_{1.9}Co_{0.1}O_{5\pm\delta}$	19.02	14.43	2.18
$Ca_2Fe_{1.9}Ni_{0.1}O_{5\pm\delta}$	17.47	14.64	3.73
$Ca_2Fe_{1.9}Cu_{0.1}O_{5\pm\delta}$	19.12	15.04	2.08

data and the Rietveld refined occupancy parameter of the metals. The details are incorporated in table 2A.5. Ni doped material exhibited maximum theoretical oxygen vacancy, followed by Cu and the least by Co doped material.

Table 2A.5: Oxygen uptake calculated from TG analysis and oxygen vacancy concentration calculated from combined XPS and Rietveld data

Material	Weight gain (mg)	Oxygen uptake (mmol)	δ
$Ca_2Fe_2O_{5\pm\delta}$	0.001598	49.9301	0.0102
$Ca_2Fe_{1.9}Mn_{0.1}O_{5\pm\delta}$	0.003544	110.7583	0.01076
$Ca_2Fe_{1.9}Co_{0.1}O_{5\pm\delta}$	0.002323	72.58825	0.0897
$Ca_2Fe_{1.9}Ni_{0.1}O_{5\pm\delta}$	0.004247	132.7201	0.1479
$Ca_2Fe_{1.9}Cu_{0.1}O_{5\pm\delta}$	0.00153	47.8125	0.1188

2A.3.2. Electrochemical Characterisation

Detailed electrochemical studies of the compounds are carried out by CV and LSV method under alkaline medium at room temperature

2A.3.2.1. ORR Activity in Alkaline Medium

ORR is monitored in 0.1M KOH solution with N_2 and O_2 saturation with varying rotation speeds. The cyclic voltammogram recorded at 900 rpm in N_2 and O_2 saturation indicates a clear reduction peak in the O_2 saturation. CV of samples is represented in figure 2A.7. A clear image of reduction behaviour is received by LSV in the same potential window. Individual LSVs of the samples with rotation speed 400, 900, 1200, 1600, 2000, and 2500rpm in O_2 saturation is represented in figure 2A.8, where the blank run is conducted in N_2 saturated solution without rotating the working electrode.

LSVs of materials recorded at 1600rpm are compared in figure 2A.9. A close analysis of the profile clearly indicates an improvement in activity on metal doping in the Fe position. The zoomed image of the onset (given in the inset of the figure), clearly depicts the improvement in onset values on doping. The Co doped material exhibits better onset value of 0.86V *vs* RHE, Ni and Cu doped variety have a similar onset value of 0.84V *vs* RHE, Mn doped material exhibits onset value of 0.82V *vs* RHE, and the parent structure

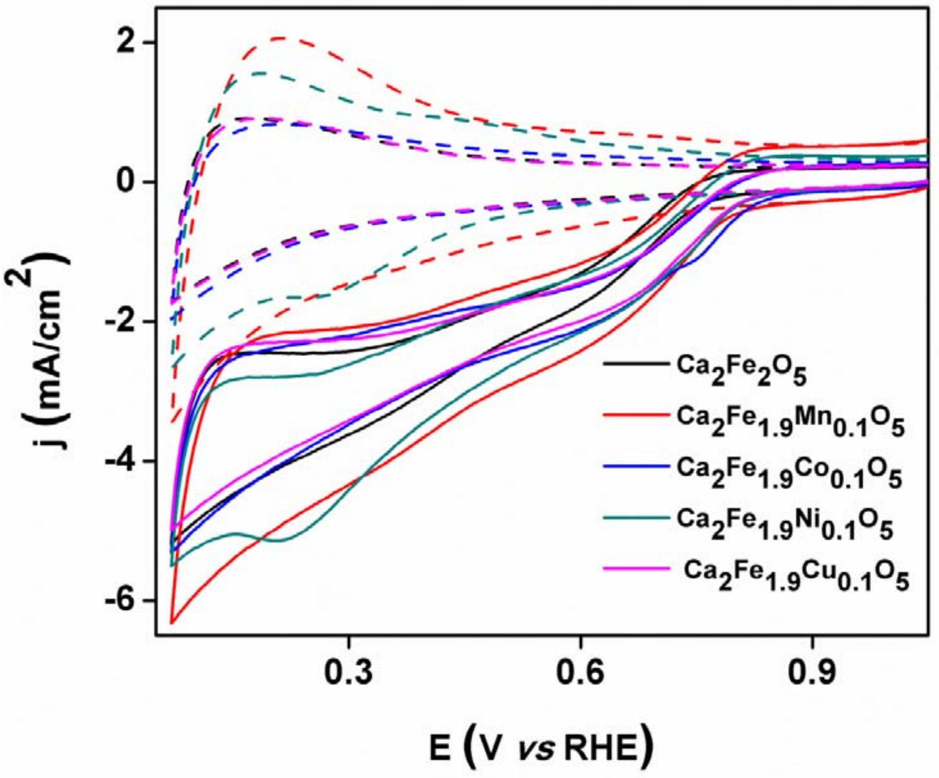

Figure 2A.7: Cyclic voltammogram of the materials recorded at 900 rpm in 0.1M KOH solution with a scan rate of 50mV/s. The dotted profile indicates the scan in N_2 saturation and solid line represents the scan in O_2 saturation

exhibits an onset of 0.76V *vs* RHE. The parent material exhibits an overpotential of 100mV compared to the material with best onset potential, while the onsets of doped varieties differ by 20-40mV only. Better current response is shown by Ni and Mn based materials, at a constant potential of 0.6V *vs* RHE current densities are noted, the order of the current density values are $Ca_2Fe_{1.9}Mn_{0.1}O_{5\pm\delta}$ (-2.39mA/cm^2) > $Ca_2Fe_{1.9}Ni_{0.1}O_{5\pm\delta}$ (-2.29mA/cm^2) > $Ca_2Fe_{1.9}Co_{0.1}O_{5\pm\delta}$ (-2.16mA/cm^2) > $Ca_2Fe_{1.9}Cu_{0.1}O_{5\pm\delta}$ (-2.02mA/cm^2) > $Ca_2Fe_2O_{5\pm\delta}$ (-1.66mA/cm^2).

Koutechy-Levich plot gives a primary idea on the electron transfer mechanism of the catalysts[24, 25]. It is desirable to follow a direct 4 electron mechanism, with no peroxide formation. The peroxide formed in the indirect path way can poison the fuel cell component and hence the path way is not desirable. This is one of the most important

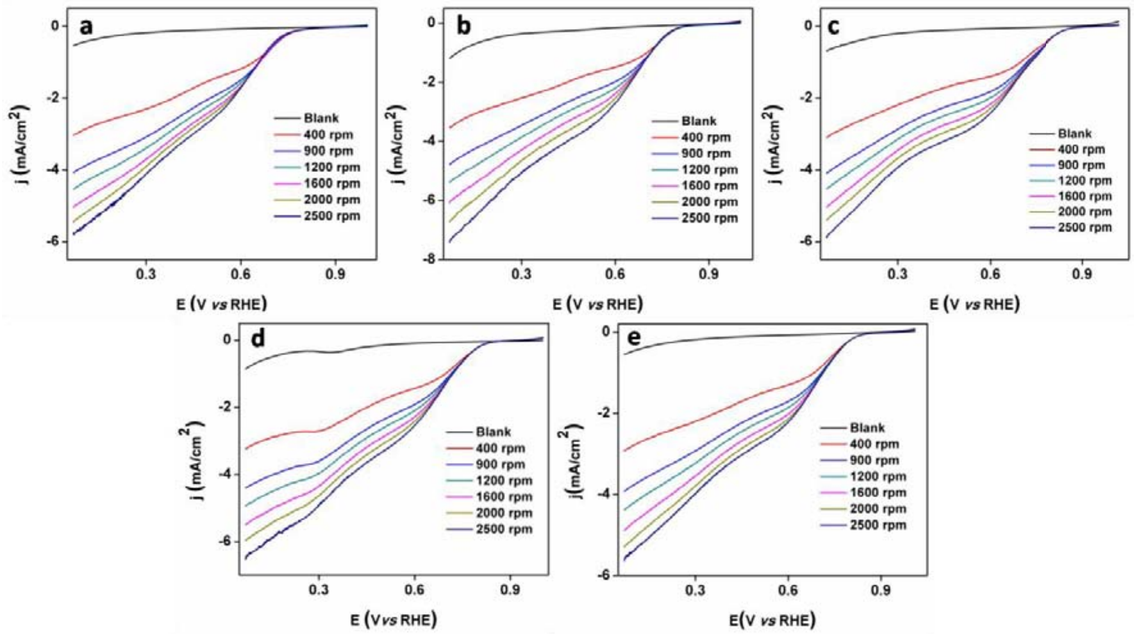

Figure 2A.8: LSVs of samples at various rotation speeds in O_2 saturation recorded with 10mV/s scan rate, the blank data is the scan in N_2 saturation without rotation of a) $Ca_2Fe_2O_{5\pm\delta}$ b) $Ca_2Fe_{1.9}Mn_{0.1}O_{5\pm\delta}$ c) $Ca_2Fe_{1.9}Co_{0.1}O_{5\pm\delta}$ d) $Ca_2Fe_{1.9}Ni_{0.1}O_{5\pm\delta}$ e) $Ca_2Fe_{1.9}Cu_{0.1}O_{5\pm\delta}$

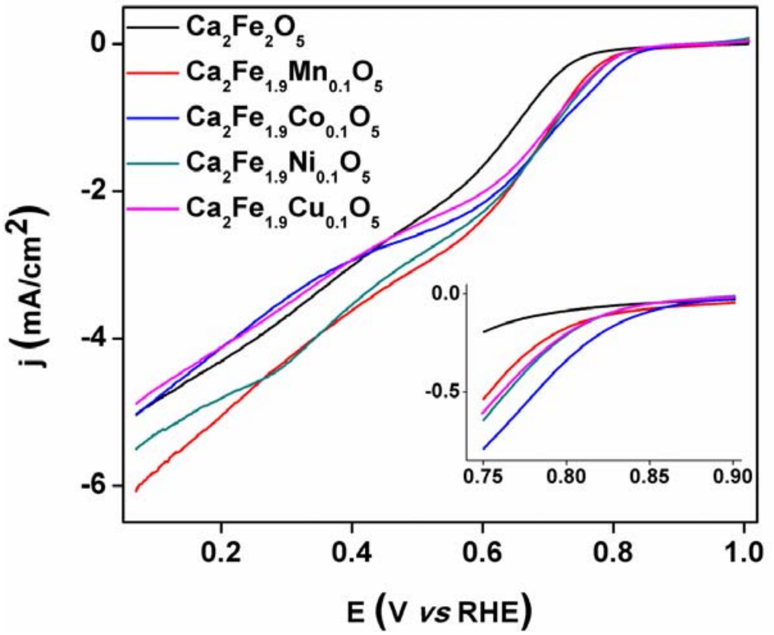

Figure 2A.9: Comparison of LSV of the materials recorded with scan rate 10mV/s in O_2 saturation with rotation speed of 1600 rpm, the inset image is the zoomed portion of the onset region

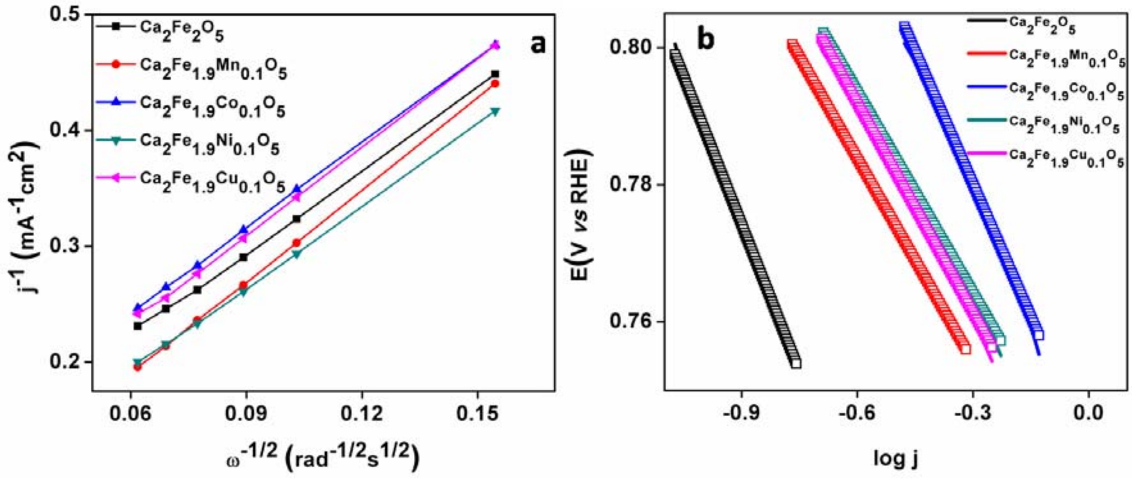

Figure 2A.10: a) K-L plot calculated from LSV data at various rotation speeds at 0.25V *vs* RHE, the points represents the calculated data, and the line represents the linear fit b) Tafel plot, calculated from LSV data at 1600rpm with scan rate 10mV/s in O_2 saturation, the empty symbols represents the calculated data and the line represents the linear fit of the data

parameters for the practical applicability of catalysts in fuel cells. The K-L calculation has been performed at 0.25V *vs* RHE from the LSV at various rotation speeds and represented in figure 2A.10a. The slope values obtained are $Ca_2Fe_{1.9}Ni_{0.1}O_5$ (0.427)> $Ca_2Fe_2O_{5\pm\delta}$ (0.426)> $Ca_2Fe_{1.9}Co_{0.1}O_{5\pm\delta}$ (0.408)> $Ca_2Fe_{1.9}Cu_{0.1}O_{5\pm\delta}$ (0.400)> $Ca_2Fe_{1.9}Mn_{0.1}O_{5\pm\delta}$ (0.379). Materials exhibit similar characteristics with similar slope value of ~0.4, indicating mechanism near 4 electron mechanism.

Details regarding the kinetics are studied by Tafel plot represented in figure 2A.10b. ORR expected to proceed through a number of steps as represented in the annexure, the *rds* in the mechanism of the reaction can be predicted by the Tafel slope values. Tafel slopes calculated from the LSV at 1600rpm in O_2 saturation with 10mV/s scan rate follows the order: $Ca_2Fe_2O_5$ (-143mV/d) > $Ca_2Fe_{1.9}Co_{0.1}O_5$ (-129mV/d) > $Ca_2Fe_{1.9}Cu_{0.1}O_5$ (-101mV/d) > $Ca_2Fe_{1.9}Mn_{0.1}O_5$ (-98mV/d) > $Ca_2Fe_{1.9}Ni_{0.1}O_5$ (-97mV/d). From the order it is clear that, there is a clear shift of the *rds* of the mechanism from the first electron transfer to the surface migration of the reduced species, which in turn indicate the better catalytic activity of the material with Ni and Mn substitution in comparison to the rest of the materials[25, 26].

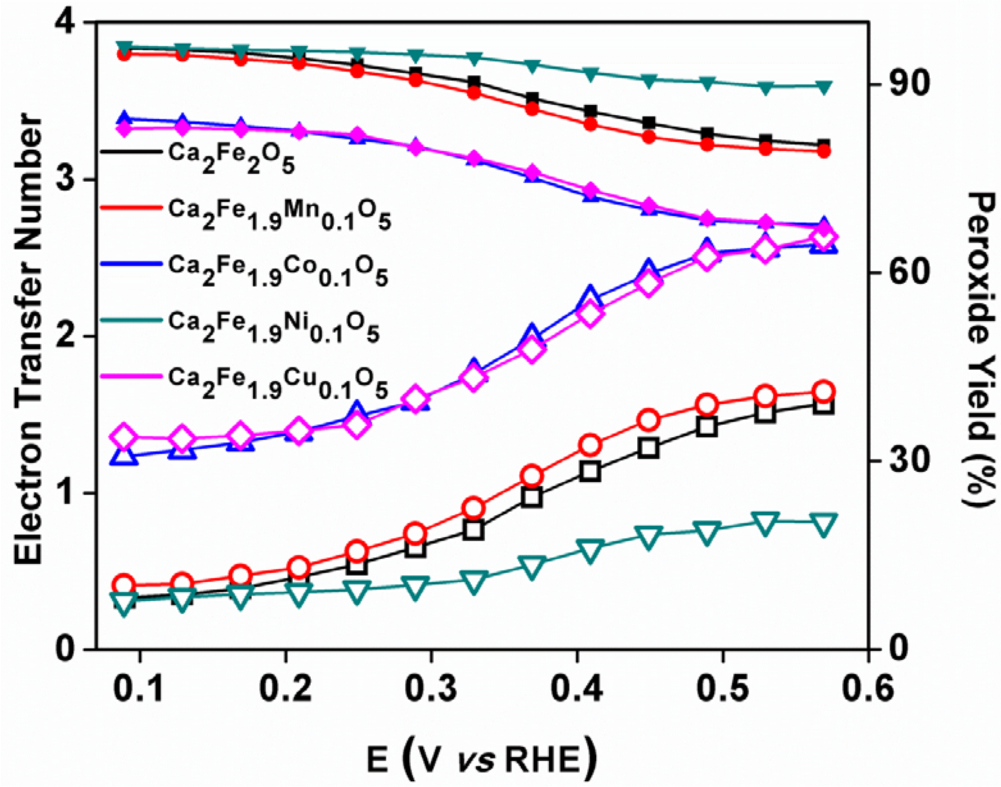

Figure 2A.11: Combined E-n (filled symbols) and E-peroxide yield (empty symbols) plot calculated from RRDE experiments conducted with 1600 rpm rotation speed, 10mV/s scan rate in O_2 saturated 0.1M KOH

Direct experimental data on the electron transfer number is obtained by RRDE experiments. The peroxide yield and electron transfer number is calculated by the equation represented in the annexure[27]. Figure 2A.11 represents the combined E-n and E-Peroxide yield relation. The electron transfer number is very low for Cu and Co doped materials compared to parent and other varieties; in parallel the peroxide yield is also as high as 60% by these materials, indicating an intermediate electron transfer mechanism by these materials. The best performance is observed with Ni doped materials, where the material shows a stable, near 4 electron transfer mechanism over a wide potential range studied and a lesser peroxide yield of 5- 17%.

Considering current response, onset values, Tafel slope values and stable electron transfer number and lower peroxide yield, Ni doped material can be considered as a best practical catalyst for the ORR applications.

2A.3.2.2. OER Activity in Alkaline Medium

Oxygen Evolution reaction is monitored in 0.1M KOH with N_2 saturation. Figure 2A.12a represents the OER LSV of the materials, recorded at 10 mV/s scan rate. The inset shows a zoomed image of the onset region for the reaction. Ni doped material, distinctly better onset in comparison with rest of the materials. Activity of materials are compared by the potential required to reach a common current density of 0.15 mA/cm^2. Ni doped material exhibited a considerably higher activity than the rest of the samples. $Ca_2Fe_{1.9}Ni_{0.1}O_{5\pm\delta}$ reached the current value at 1.522V *vs* RHE, while the materials $Ca_2Fe_2O_{5\pm\delta}$, $Ca_2Fe_{1.9}Mn_{0.1}O_{5\pm\delta}$, $Ca_2Fe_{1.9}Co_{0.1}O_{5\pm\delta}$ and $Ca_2Fe_{1.9}Cu_{0.1}O_{5\pm\delta}$ exhibited an overpotential of 95.6mV, 64.3mV, 65.2mV, and 61.5mV respectively with respect to the Ni doped material. Further current density at a potential of 1.62V *vs* RHE as plotted in figure 2A.12b clearly suggests an improvement in current density value of around 16 times, on Ni doping.

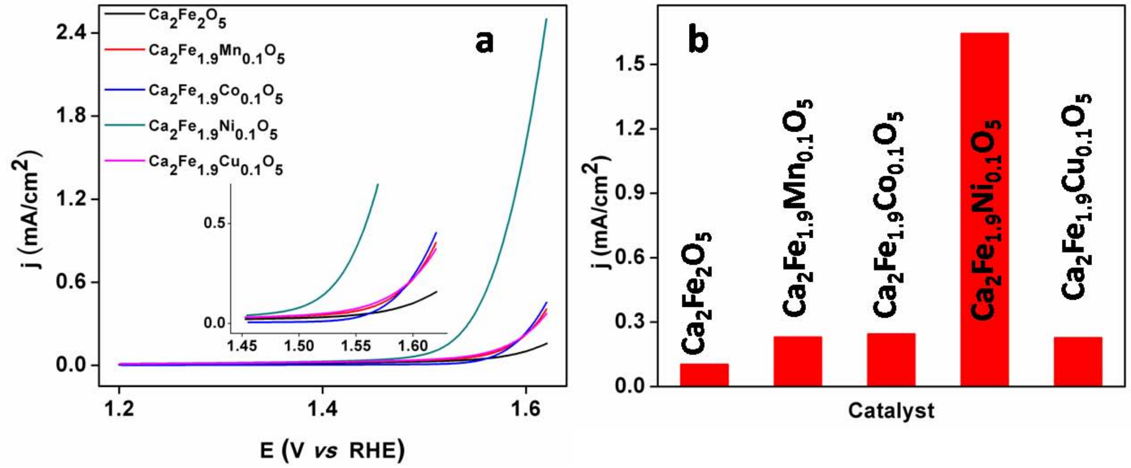

Figure 2A.12: a) OER LSV recorded at 1600 rpm rotation speed and 10mV/s scan rate in N_2 saturated 0.1M KOH b) comparison of current density at 1.62V *vs* RHE from LSV

A detailed study to find out the *rds* of the mechanism is conducted by the Tafel plot analysis. The OER is expected to proceed through a number of steps as suggested by De Faria represented in annexure[28]. The Tafel calculations are performed from the LSV data and plotted in figure 2A.13. The parent brownmillerite $Ca_2Fe_2O_{5\pm\delta}$ exhibited a slope value of 120mV/d indicating the first electron transfer step as the *rds*. There is a clear transition of mechanism from the first electron transfer to surface migration on metal doping in Fe position. The order of Tafel slope values are $Ca_2Fe_2O_{5\pm\delta}$ (120mV/d) >

$Ca_2Fe_{1.9}Cu_{0.1}O_{5\pm\delta}$ (97mV/d)> $Ca_2Fe_{1.9}Ni_{0.1}O_{5\pm\delta}$ (86mV/d) > $Ca_2Fe_{1.9}Mn_{0.1}O_{5\pm\delta}$ (82mV/d)> $Ca_2Fe_{1.9}Co_{0.1}O_{5\pm\delta}$ (59mV/d). The Tafel slope values indicate that the catalytic activity of the material improves by the doping in the Fe site.

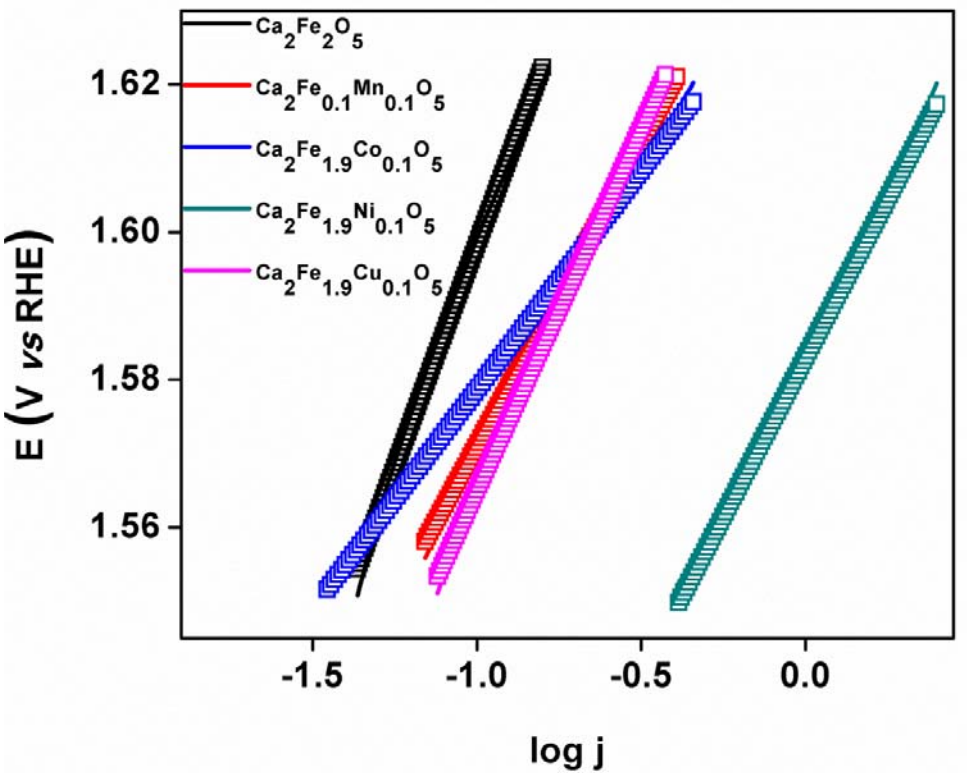

Figure 2A.13: OER Tafel plots calculated from LSV at 1600rpm

2A.4 Activity Correlation

A number of descriptors have been suggested for the electrochemical ORR and OER separately, but has not been successful in suggesting a joint descriptor for bifunctional activity of the materials. e_g electron count is the most accepted descriptor for the activity of perovskite metal based oxides[29-31]. The oxygenated species coordinate to the e_g orbital of the active metal. The σ bond formed has better overlap than the π bond formed between the t_{2g} orbitals. Hence e_g electron count has a significant role in the activity of the oxides. Calculation of e_g electron count is performed theoretically by combining the results of Rietveld refinement and XPS data. The order is found to be

$Ca_2Fe_{1.9}Mn_{0.1}O_{5\pm\delta} < Ca_2Fe_{1.9}Co_{0.1}O_{5\pm\delta} = Ca_2Fe_{1.9}Ni_{0.1}O_{5\pm\delta} = Ca_2Fe_2O_{5\pm\delta} < Ca_2Fe_{1.9}Cu_{0.1}O_{5\pm\delta}$. However there is no direct correlation on the activity with the e_g electron in our case. The order of oxygen vacancy calculated could be correlated to the overall activity of the material. Calculated oxygen vacancy is in favor of $Ca_2Fe_{1.9}Cu_{0.1}O_{5\pm\delta}$ but experimentally the oxygen uptake exhibited by the sample is very low and thus the activity of the material is lower than expected on the basis of theoretical calculation. O2p position also had an influence in the overall activity, correlated to the work function can be regarded as the easiness of electron transfer in a process. Lower work function of $Ca_2Fe_{1.9}Mn_{0.1}O_{5\pm\delta}$ compared to the other materials can be correlated to the Tafel slope values for ORR and OER reactions of the material. The poor performance by the parent brownmillerite and $Ca_2Fe_{1.9}Cu_{0.1}O_{5\pm\delta}$ can be primarily due to the lower concentration of oxygen vacancies as evidenced from the TG analysis.

2A.5. Summary and Conclusion

The main goal of the chapter was to compare the role of the transition metal dopants in the brownmillerite $Ca_2Fe_2O_{5\pm\delta}$ towards the electrochemical ORR and OER at room temperature. The materials synthesised by the citrate gel route crystallised in the orthorhombic Pnma space group. The structure consists of alternate layers of tetrahedral and octahedral layers and the dopant metala are found to occupy preferentially tetrahedral site evidenced from the Rietveld refinement results. The surface state analysis by XPS confirms the presence of Fe, Ni and Cu in single oxidation state, whereas Co and Mn exist in multiple states. The electrochemical activity analysis of the materials suggests that the Ni doped material shows a better activity towards ORR and OER, on account of the current response, Tafel slope values, electron count, and OER onset-current response. The calculated e_g electron count does not show any direct correlation on the activity. The oxygen vacancy concentration analysed by thermo gravimetry gives a clear indication on the activity trend. The parent brownmillerite and the Cu doped material exhibited relatively low activity on account of lower oxygen vacancy concentration. The work function calculated also has a role in the activity. However a single parameter cannot be suggested as a collective descriptor to express bifunctionality. All the parameters come in to play for the overall activity of the material.

2A.6. References

1. Asenath-Smith, E.; Lokuhewa, I. N.; Misture, S. T.; Edwards, D. D., p-Type thermoelectric properties of the oxygen-deficient perovskite $Ca_2Fe_2O_5$ in the brownmillerite structure. *Journal of Solid State Chemistry* 2010, *183* (7), 1670-1677.

2. Takeda, T.; Yamaguchi, Y.; Tomiyoshi, S.; Fukase, M.; Sugimoto, M.; Watanabe, H., Magnetic Structure of $Ca_2Fe_2O_5$. *Journal of the Physical Society of Japan* 1968, *24* (3), 446-452.

3. Shin, S.; Hatakeyama, Y.; Ogawa, K.; Shimomura, K. y., Catalytic decomposition of NO over brownmillerite-like compounds, $Ca_2Fe_2O_5$ and $Sr_2Fe_2O_5$. *Materials Research Bulletin* 1979, *14* (1), 133-136.

4. Xue, B.-j.; Luo, J.; Zhang, F.; Fang, Z., Biodiesel production from soybean and Jatropha oils by magnetic $CaFe_2O_4$–$Ca_2Fe_2O_5$-based catalyst. *Energy* 2014, *68*, 584-591.

5. Xu, X.; Li, S.; Wang, X.; Ma, Y.; Wang, X.; Gao, K., Fabrication and characterization of $Ca_2Fe_2O_5$ nanofibers photocatalyst by sol-gel assisted electrospinning at low-temperature. *Materials Letters* 2015, *143*, 75-79.

6. Sharma, N.; Shaju, K. M.; Subba Rao, G. V.; Chowdari, B. V. R., Mixed oxides $Ca_2Fe_2O_5$ and $Ca_2Co_2O_5$ as anode materials for Li-ion batteries. *Electrochimica Acta* 2004, *49* (7), 1035-1043.

7. Li, Q.; Sun, L.; Huo, L.; Zhao, H.; Grenier, J.-C., Electrode properties of Co-doped $Ca_2Fe_2O_5$ as new cathode materials for intermediate-temperature SOFCs. *International Journal of Hydrogen Energy* 2010, *35* (17), 9151-9157.

8. Kim, J.; Yin, X.; Tsao, K.-C.; Fang, S.; Yang, H., $Ca_2Mn_2O_5$ as Oxygen-Deficient Perovskite Electrocatalyst for Oxygen Evolution Reaction. *J. Am. Chem. Soc* 2014, *136*, 14646-14649.

9. Cheng, F.; Zhang, T.; Zhang, Y.; Du, J.; Han, X.; Chen, J., Enhancing Electrocatalytic Oxygen Reduction on MnO_2 with Vacancies. *Angewandte Chemie International Edition* 2013, *52* (9), 2474-2477.

10. Lee, J.-H.; Black, R.; Popov, G.; Pomerantseva, E.; Nan, F.; Botton, G. A.; Nazar, L. F., The role of vacancies and defects in $Na_{0.44}MnO_2$ nanowire catalysts for lithium–oxygen batteries. *Energy & Environmental Science* 2012, *5* (11), 9558-9565.

11. Pan, X.; Yang, M.-Q.; Fu, X.; Zhang, N.; Xu, Y.-J., Defective TiO_2 with oxygen vacancies: synthesis, properties and photocatalytic applications. *Nanoscale* 2013, *5* (9), 3601-3614.

12. Sadighi, Z.; Huang, J.; Qin, L.; Yao, S.; Cui, J.; Kim, J.-K., Positive role of oxygen vacancy in electrochemical performance of $CoMn_2O_4$ cathodes for Li-O_2 batteries. *Journal of Power Sources* 2017, *365*, 134-147.

13. Toby, B., EXPGUI, a graphical user interface for GSAS. *Journal of Applied Crystallography* 2001, *34* (2), 210-213.

14. Thundiyil, S.; Kurungot, S.; Devi, R. N., Bifunctional Oxygen Reduction and Evolution Activity in Brownmillerites $Ca_2Fe_{(1-x)}Co_xO_5$. *ACS Omega* 2019, *4* (1), 31-38.

15. Biesinger, M. C.; Payne, B. P.; Grosvenor, A. P.; Lau, L. W. M.; Gerson, A. R.; Smart, R. S. C., Resolving surface chemical states in XPS analysis of first row transition metals, oxides and hydroxides: Cr, Mn, Fe, Co and Ni. *Applied Surface Science* 2011, *257* (7), 2717-2730.

16. Guo, D.; Wu, Z.; An, Y.; Li, X.; Guo, X.; Chu, X.; Sun, C.; Lei, M.; Li, L.; Cao, L.; Li, P.; Tang, W., Room temperature ferromagnetism in $(Ga_{1-x}Mn_x)_2O_3$ epitaxial thin films. *Journal of Materials Chemistry C* 2015, *3* (8), 1830-1834.

17. Si, C.; Zhang, J.; Wang, Y.; Ma, W.; Gao, H.; Lv, L.; Zhang, Z., Nanoporous Platinum/$(Mn,Al)_3O_4$ Nanosheet Nanocomposites with Synergistically Enhanced Ultrahigh Oxygen Reduction Activity and Excellent Methanol Tolerance. *ACS Applied Materials & Interfaces* 2017, *9* (3), 2485-2494.

18. Baird, T.; Campbell, K. C.; Holliman, P. J.; W. Hoyle, R.; Stirling, D.; Williams, B. P.; Morris, M., Characterisation of cobalt–zinc hydroxycarbonates and their products of decomposition. *Journal of Materials Chemistry* 1997, *7* (2), 319-330.

19. Zhou, T.; Cao, Z.; Zhang, P.; Ma, H.; Gao, Z.; Wang, H.; Lu, Y.; He, J.; Zhao, Y., Transition metal ions regulated oxygen evolution reaction performance of Ni-based hydroxides hierarchical nanoarrays. *Scientific Reports* 2017, *7* (1), 46154.

20. Sun, T.; Xu, L.; Yan, Y.; Zakhidov, A. A.; Baughman, R. H.; Chen, J., Ordered Mesoporous Nickel Sphere Arrays for Highly Efficient Electrocatalytic Water Oxidation. *ACS Catalysis* 2016, *6* (3), 1446-1450.

21. Shuai, M.; Liao, L.; Lu, H. B.; Zhang, L.; Li, J. C.; Fu, D. J., Room-temperature ferromagnetism in Cu+implanted ZnO nanowires. *Journal of Physics D: Applied Physics* 2008, *41* (13), 135010.

22. Wu, C.-K.; Yin, M.; O'Brien, S.; Koberstein, J. T., Quantitative Analysis of Copper Oxide Nanoparticle Composition and Structure by X-ray Photoelectron Spectroscopy. *Chemistry of Materials* 2006, *18* (25), 6054-6058.

23. Chun, W.-J.; Ishikawa, A.; Fujisawa, H.; Takata, T.; Kondo, J. N.; Hara, M.; Kawai, M.; Matsumoto, Y.; Domen, K., Conduction and Valence Band Positions of Ta_2O_5, TaON, and Ta_3N_5 by UPS and Electrochemical Methods. *J. Phys. Chem. B* 2003, *107*, 1798-1803.

24. Hu, P.; Song, Y.; Chen, L.; Chen, S., Electrocatalytic activity of alkyne-functionalized AgAu alloy nanoparticles for oxygen reduction in alkaline media. *Nanoscale* 2015, *7* (21), 9627-9636.

25. Ge, X.; Sumboja, A.; Wuu, D.; An, T.; Li, B.; Goh, F. W. T.; Hor, T. S. A.; Zong, Y.; Liu, Z., Oxygen Reduction in Alkaline Media: From Mechanisms to Recent Advances of Catalysts. *ACS Catalysis* 2015, *5* (8), 4643-4667.

26. Taylor, R. J.; Humffray, A. A., Electrochemical studies on glassy carbon electrodes: II. Oxygen reduction in solutions of high pH (pH>10). *Journal of Electroanalytical Chemistry and Interfacial Electrochemistry* 1975, *64* (1), 63-84.

27. Zhou, R.; Zheng, Y.; Jaroniec, M.; Qiao, S.-Z., Determination of the Electron Transfer Number for the Oxygen Reduction Reaction: From Theory to Experiment. *ACS Catalysis* 2016, *6* (7), 4720-4728.

28. De Faria, L. A.; Boodts, J. F. C.; Trasatti, S., Electrocatalytic properties of ternary oxide mixtures of composition $Ru_{0.3}Ti_{(0.7-x)}Ce_xO_2$: oxygen evolution from acidic solution. *Journal of Applied Electrochemistry* 1996, *26* (11), 1195-1199.

29. Hong, W. T.; Risch, M.; Stoerzinger, K. A.; Grimaud, A.; Suntivich, J.; Shao-Horn, Y., Toward the rational design of non-precious transition metal oxides for oxygen electrocatalysis. *Energy Environ. Sci* 2015, *8* (5), 1404-1427.

30. Suntivich, J.; May, K. J.; Gasteiger, H. A.; Goodenough, J. B.; Shao-Horn, Y., A Perovskite Oxide Optimized for Oxygen Evolution Catalysis from Molecular Orbital Principles. *Science* 2011, *334* (6061), 1383-1385.

31. Suntivich, J.; Gasteiger, H. A.; Yabuuchi, N.; Nakanishi, H.; Goodenough, J. B.; Shao-Horn, Y., Design principles for oxygen-reduction activity on perovskite oxide catalysts for fuel cells and metal–air batteries. *Nature Chemistry* **2011,** *3* (7), 546-550.

Part B

Role Of Co Doping in Structure , Room Temperature Electrochemical Activity Activity and High Temperature Conductivity of $Ca_2Fe_2O_5$

2B.1. Introduction

Proper doping strategy in the B site in perovskite related structures results in improved room temperature electrochemistry of the material. In order to develop a single catalyst applicable for various energy systems like, Alkaline fuel cell, URFC, SOFC and OTM applications, the conductivity part also has to be taken care of. In the design of a material which can act as a promising candidate in all the applications, selection of the dopant metal and its proportion is crucial. Cobalt is selected as the dopant in Fe site in $Ca_2Fe_2O_5$ on account of its ability to improve the conductivity and room temperature electrochemical properties.

Our aim is to see the effect of increased concentration of the transition metal in B site. Ni substitution resulted in better bifunctional activity by the material, but the higher substitution of Ni resulted in the impurity phase of NiO, hence we have focused on the substitution with Co.

2B.2. Experimental Section

2B.2.1. Synthesis of $Ca_2Fe_{2-x}Co_xO_{5\pm\delta}$ (x = 0, 0.25, 1)

The compounds are synthesised by solid state method using $CaCO_3$ (Sigma Aldrich,≥ 99.0%), Fe_2O_3 (Sigma Aldrich, 99.98%), $CoCO_3.xH_2O$ (Sigma Aldrich, Co= 43-47%) as the starting materials. The precursors in stoichiometric proportions are weighed and ball milled at 150 rpm for 2 h for homogeneity. Precalcination is carried out at 900°C for 6h, for decarbonisation followed by calcinations at 1100°C for 12h.

2B.2.2. Characterisation

Phase formation is confirmed with powder x-ray diffraction (PXRD) in PANalytical X'pert Pro dual goniometer diffractometer as explained in the chapter 2A. Rietveld refinement is carried out to study the structural changes on doping by GSAS-EXPGUI software. Surface state of the metals are analysed by XPS as explained in chapter 2A. Surface area analysis of the samples is done by BET analysis using the Autosorb iQ Quantachrome system. Morphology and surface composition analysis is performed in E-SEM-EDAX.

2B.2.3. Electrochemical Analysis

Room temperature electrochemical activity is monitored in alkaline solution with BioLogic SP-300 electrochemical work station as explained in chapter 2A.

High temperature electrochemical Impedance spectroscopy is conducted by using CHI604E electrochemical analyzer (CH Instruments Inc., USA) assembled with home-built electrode setup and furnace. A schematic representation of the electrode set up is represented in figure 2B.1, where the samples are analysed in the form of dense pellets, gold grid connected with gold wire acts as the current collector and gas atmosphere is provided from the top portion of the set up. Maximum contact of the sample pellet with gold grid is assured by spring tightening system. Pellets are made with 0.5g of the as synthesised powder and pressed in a die of 13mm diameter. The pellets are calcined at 900˚C and then polished on both sides to get a smooth surface. The polished pellet is gold coated and used for EIS measurements. The AC impedance spectroscopy is done over a frequency range of 100mHz to 1MHz with an amplitude of 50mV, on cooling in the temperature range of 500 – 800˚C. The dwell time at each temperature is 2h to attain the equilibrium and subsequently the spectra are recorded.

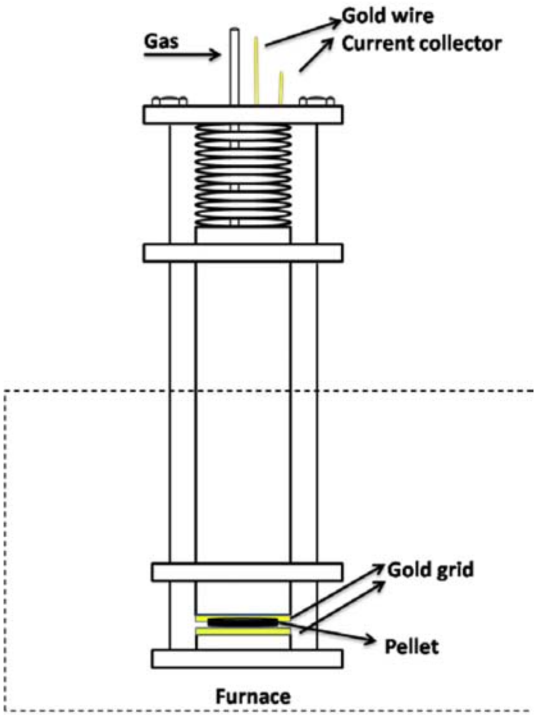

Figure 2B.1: Schematic representation of electrode set up for HT EIS analysis

2B.3. Results and Discussion

2B.3.1. Synthesis and Structural Characterisation

Phase formation and purity of the samples are analysed by PXRD. The recorded PXRD patterns of all the three samples are represented in figure 2B.2. A close analysis of the patterns indicates that the materials are formed in orthorhombic crystal system. The PXRD pattern of the un-doped compound $Ca_2Fe_2O_{5\pm\delta}$ matches with reported pattern with JCPDS reference number: 71-2108 crystallising in the Pcmn space group. $Ca_2Fe_{1.75}Co_{0.25}O_{5\pm\delta}$ is also matches with the parent pattern with the doped brownmillerite model $Ca_2Fe_{1.7}Si_{0.15}Zn_{0.15}O_5$ crystallising in the same space group with JCPDS reference code: 45-0569. In both the compounds, traces of impurity of CaO and Fe_3O_4 are also identified. The highest substitution without impurity formation and phase retention is attained with the composition $Ca_2FeCoO_{5\pm\delta}$, which formed as a pure phase matching with the pattern of Ca_2FeMnO_5 with JCPDS reference number: 88-0814 crystallising in the Pnma space group.

Detailed structural studies are conducted by the Rietveld refinement of the PXRD patterns using GSAS-EXPGUI software[1]. Resultant patterns are given in the figure 2B.3 and the data is represented in table 2B.1. The refinement of $Ca_2Fe_2O_{5\pm\delta}$ proceeded with an orthorhombic model with ICSD collection code: 14296, a better fit is obtained after inserting the impurity phases CaO (ICSD collection code: 75785) and Fe_3O_4 (ICSD collection code: 75785). All the parameters are refined and the impurity phases are refined quantitatively to determine the weight percentage. The structure consists of two Fe sites and three oxygen atoms. Fe1 forms tetrahedral units, $Fe1O_4$ with O2 and O3, and Fe2 forms octahedral units, $Fe2O_6$ with O1 and O3, where the O3 bridges the tetrahedral and octahedral chains. The unit cell representation is given in figure 2B.4a. $Ca_2Fe_{1.75}Co_{0.25}O_{5\pm\delta}$ is refined with same model; a good fit is obtained after adding the impurity phases Fe_3O_4 and $CaCO_3$. The refinement proceeded by equally substituting the tetrahedral and octahedral Fe site with Co in stoichiometric proportions. All the parameters including occupancy parameters are refined and a decrease in the occupancy of Co at the octahedral position from the nominal input concentration and a slight increase in the occupancy at the tetrahedral position are observed. The resultant occupancy at octahedral position is ~5.4% and tetrahedral position is ~6.35% than the

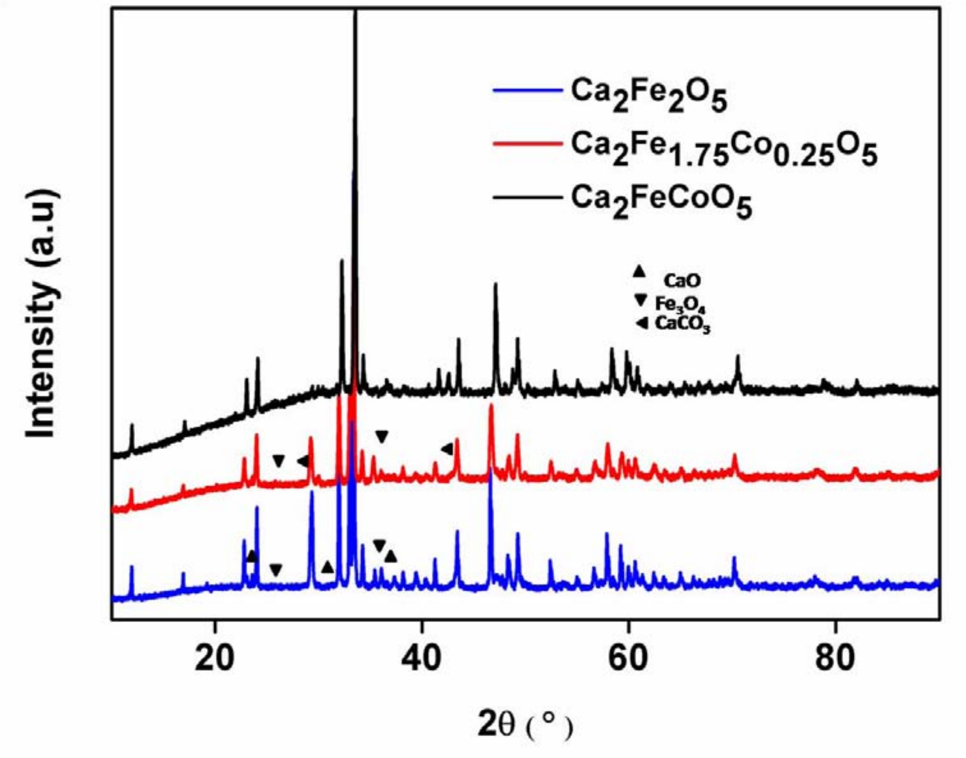

Figure 2B.2: Powder XRD patterns of the samples where the symbols represent the peak positions of impurity phases

nominal assignment of 6.25% resulting in the final stoichiometry of $Ca_2Fe_{1.74}Co_{0.24}O_5$. The polyhedral representation of unit cell is represented in figure 2B.4b.

On account of the similarity in PXRD patterns, attempt at refining the composition $Ca_2FeCoO_{5\pm\delta}$ also with the same model is done but resulted in an unacceptable fit. Matching JCPDS file suggested that the material crystallised in Pnma space group, and hence a model Ca_2FeMnO_5 in Pnma space group was selected and refinement was tried by changing the Mn position with the Co. This was also not fruitful, resulting in a sudden change in the unit cell parameters to unacceptable limits. Upon indexing, the unit cell parameters are found to be interchanged in comparison to the previous two systems, such that a' ~c, b'~ 2a, and c'~b. The reported structure for Ca_2FeCoO_5 crystallises in Pbcm space group and consists of two distinct octahedral and tetrahedral sites as suggested by the single crystal studies[2]. The material shows inter-layer and intra-layer ordering phenomenon. Inter-layer ordering occurs in such a way that, the Fe rich octahedra will coordinate to Co rich octahedra only and vice versa. Intra-layer ordering can be viewed as, within a layer the Fe rich octahedron/tetrahedron will coordinate to the Co rich octahedron/tetrahedron only. The interlayer ordering is observed in other calcium ferrates like Ca_2FeMnO_5 and $Ca_2Fe_{1.5}Cr_{0.5}O_5$, in that case Mn^{3+} and Cr^{3+} exhibits a strong site preference to the octahedral position[3], and hence intra-layer ordering will be absent[2]. In fact Ca_2FeCoO_5 is the only ferrate which shows both intra-layer and inter-layer ordering. The unit cell representation is given in figure 2B.4c.

Refinement of the structure proceeded smoothly with ICSD model: 169345, there are three different metal positions, viz., Co1(Fe1) in tetrahedral positions, Co2(Fe2) and Co3(Fe3) occupying the octahedral positions, and six different oxygen atoms in the structure. All the parameters including occupancy are refined to get a final composition of $Ca_2Fe_{1.05}Co_{0.95}O_{5\pm\delta}$. The ball stick model representing the structure of $Ca_2FeCoO_{5\pm\delta}$ is shown in figure 2B.5. The site 1d is occupied more by Fe (~80%) and less by Co, which forms the Fe rich octahedron represented as site A in the figure, whereas the 4a position occupied more by Co forming a Co rich octahedron, with Co3 and Fe3 ratio of 70%: 30%, which is denoted as site B in the figure. $Fe2(Co2)O_6$ octahedra are formed with O3, O4 and O6 oxygen atoms, where O6 bridges the octahedra with the Co rich tetrahedra. Co rich octahedra ($Co3(Fe3)O_6$) and Fe rich octahedra ($Fe2(Co2)O_6$) commonly shares O3 and O4. The Fe rich tetrahedra and Co rich octahedra are connected by means of O5 atoms as represented in the figure.

In addition to the difference in structure, a polyhedral distortion is also observed as the Co concentration is increased. The Oh-O-Td angle is more or less same in the first two varieties, viz. 139.98° and 140.61° in $Ca_2Fe_2O_{5\pm\delta}$ and $Ca_2Fe_{1.75}Co_{0.25}O_{5\pm\delta}$ respectively and increases in the $Ca_2FeCoO_{5\pm\delta}$ to 143.82°. A gradual decrease in the Oh-O-Oh angle is also observed along the series from 165.28° to 163.61°.

Surface states of the metals are analysed with XPS analysis. Figure 2B.6 represents the deconvoluted Fe2p XPS of the materials, the spectrum is fitted with five peaks confirming the presence of Fe in +3 oxidation state[4, 5]. The deconvoluted Co2p XP spectrum is given in figure 2B.7, the spectrum is fitted with two doublets for $2p_{1/2}$ and$2p_{3/2}$ region with a coupling constant of ~15eV. The peak at ~780eV and a broad satellite peak at ~788eV can be ascribed to the +3 oxidation state of Co and satellite peak present at 6eV higher than the $2p_{3/2}$ peak indicates the presence of Co(II) state[4-6]. From the area of the individual peaks, the percentage of Co(II) and Co(III) species are calculated. $Ca_2Fe_{1.75}Co_{0.25}O_{5\pm\delta}$ and $Ca_2FeCoO_{5\pm\delta}$ contains 68.86% and 74.75% surface Co in +3 oxidation state respectively.

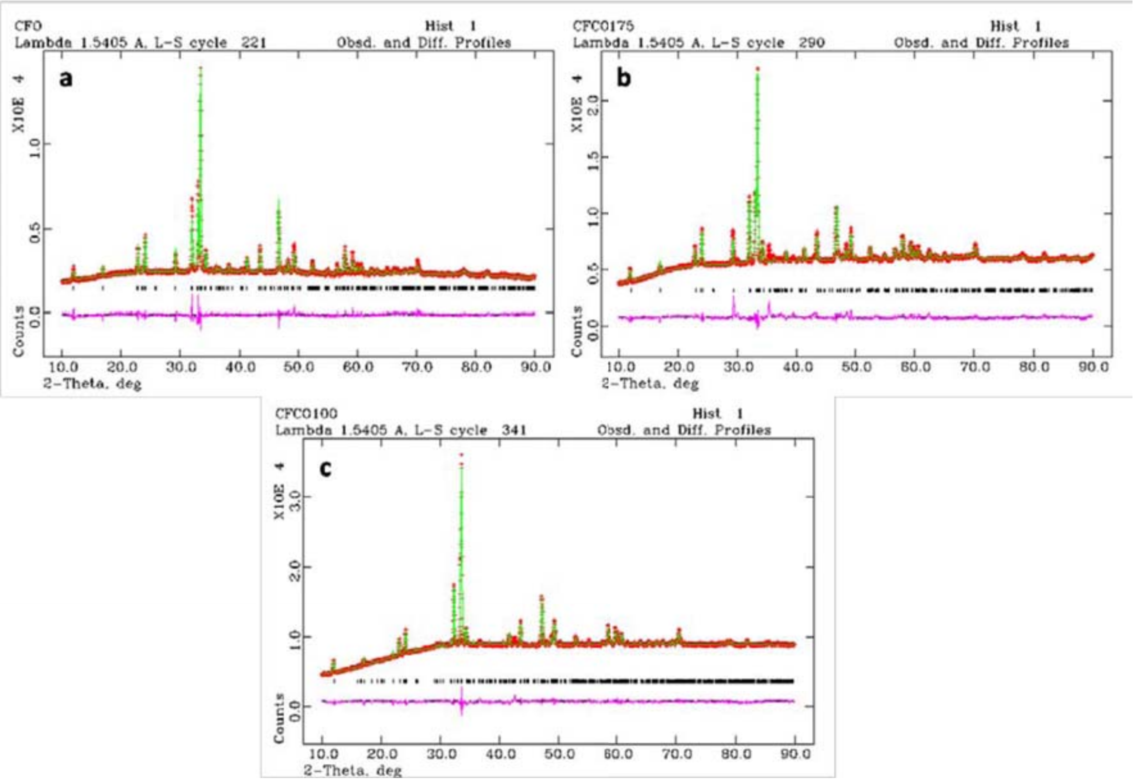

Figure 2B.3: Rietveld refined PXRD patterns of a) $Ca_2Fe_2O_{5\pm\delta}$ b) $Ca_2Fe_{1.75}Co_{0.25}O_{5\pm\delta}$ c) $Ca_2FeCoO_{5\pm\delta}$

Table 2B.1: Rietveld refinement data

Material		$Ca_2Fe_2O_{5\pm\delta}$	$Ca_2Fe_{1.75}Co_{0.25}O_{5\pm\delta}$	$Ca_2FeCoO_{5\pm\delta}$	
χ2		1.29	1.89	2.35	
wRp(%)		3.26	1.79	1.66	
Rp (%)		2.42	1.36	1.23	
Space group		Pcmn	Pcmn	Pbcm	
a		5.5953(1)	5.5745(2)	5.3596(1)	
b		14.7617(2)	14.7677(2)	11.0840(2)	
c		5.4237(1)	5.3999(1)	14.7893(2)	
Ca	x	0.023523	0.22960	Ca1	Ca2
				-0.007988	-0.488738

	y	0.108931	0.108883	0.758885	0.511944
	z	0.481264	0.476070	0.387727	0.607547
Fe1/Co1	x	0	0	Fe1	Co1
				-0.045956	0.429302
	y	0	0	0.531271	0.716078
	z	0	0	0.25000	0.25000
	Occupancy	0.9833	Fe: 0.8446 Co: 0.1082	1.0261	1.0181
Fe2/Co2	x	0.935084	0.935746	Fe2	Co2
				-0.499167	-0.511687
	y	0.250000	0.25000	0.75000	0.75000
	z	0.946397	0.94306	0.50000	0.50000
	Occupancy	1.0097	Fe: 0.8844 Co: 0.1271	0.8140	0.1240
O1	x	0.238170	0.240763	0.09148	
	y	0.983867	0.983685	0.69356	
	z	0.258984	0.266735	0.25	
	Occupancy	0.984480	0.987322	1.022	
O2	x	0.073149	0.067866	0.5928	
	y	0.142049	0.141957	0.56399	
	z	0.021618	0.028481	0.25	
	Occupancy	1.001453	1.026854	1.021	
O3	x	0.874449	0.882798	-0.258810	
	y	0.250000	0.250000	0.61815	
	z	0.601177	0.593653	0.48739	
	Occupancy	1.006836	1.026698	0.972	
Impurity Phases (wt%)		Fe_3O_4 – 1.3 CaO- 3.1	Fe_3O_4 - 4.8 $CaCO_3$- 6.5	--	

*$Ca_2FeCoO_{5\pm\delta}$: Fe3/Co3 (0,0,0), Occupancy : Fe3:0.2819; Co3: 0.6986; O4 (-0.758350,0.62830,0.48739), Occupancy: 0.992; O5(0.01902,0.46770,0.35745), Occupancy: 1.038; O6(0.50922,0.78219,0.35589) Occupancy: 1.024

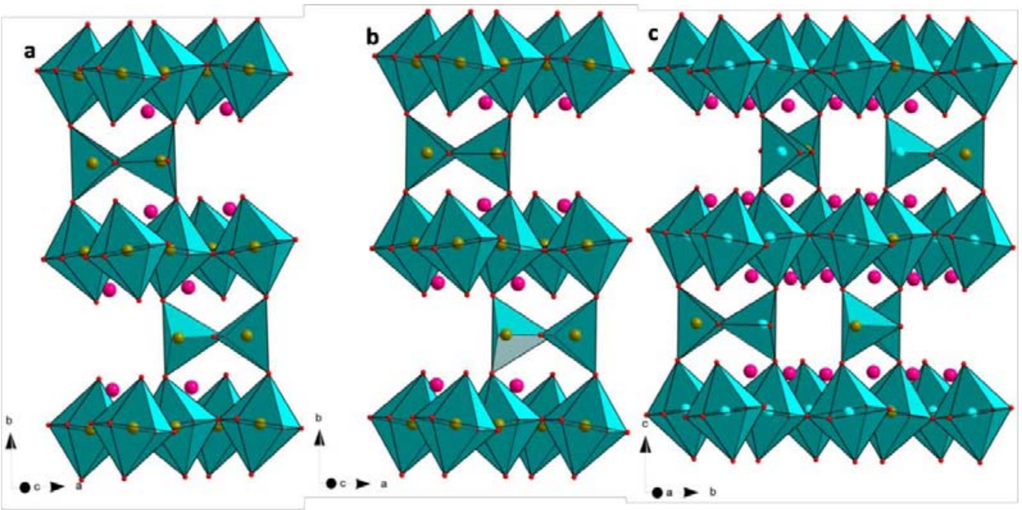

Figure 2B.4: Polyhedral representation of unit cells a) $Ca_2Fe_2O_{5\pm\delta}$ b) $Ca_2Fe_{1.75}Co_{0.25}O_{5\pm\delta}$ and c) $Ca_2FeCoO_{5\pm\delta}$

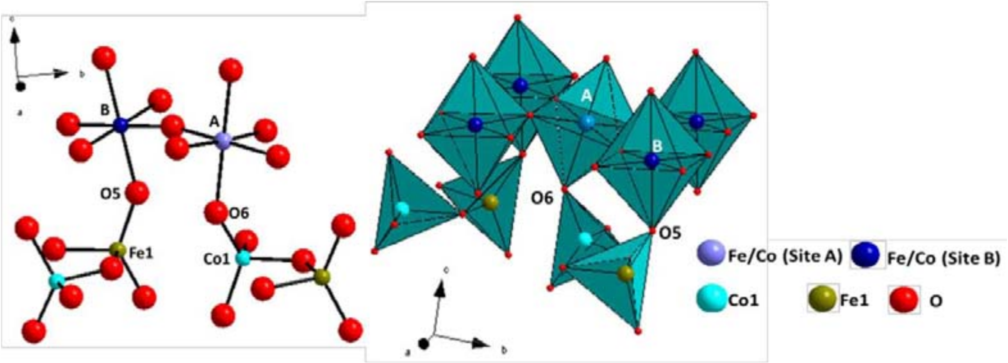

Figure 2B.5: Ball and stick and polyhedral representation of $Ca_2FeCoO_{5\pm\delta}$ showing inter and intra layer ordering phenomena, where site A represents Fe rich octahedra, B represents Co rich octahedra

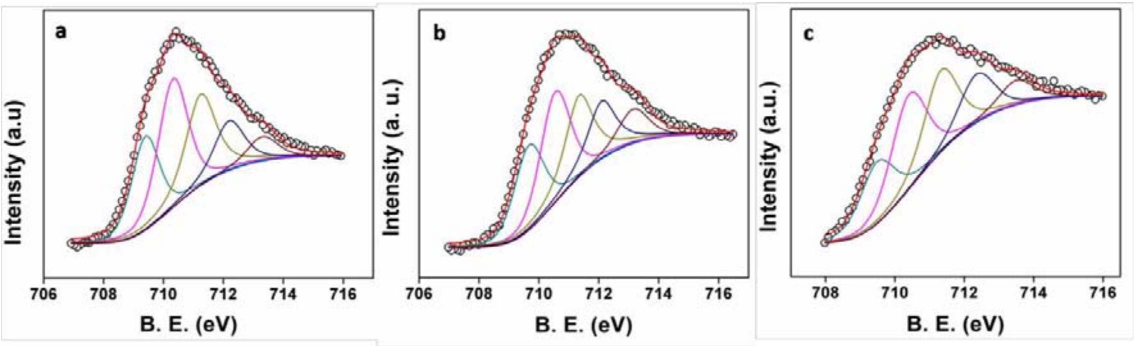

Figure 2B.6: Deconvoluted Fe2p XPS spectra of a) $Ca_2Fe_2O_{5\pm\delta}$ b) $Ca_2Fe_{1.75}Co_{0.25}O_{5\pm\delta}$ c) $Ca_2FeCoO_{5\pm\delta}$

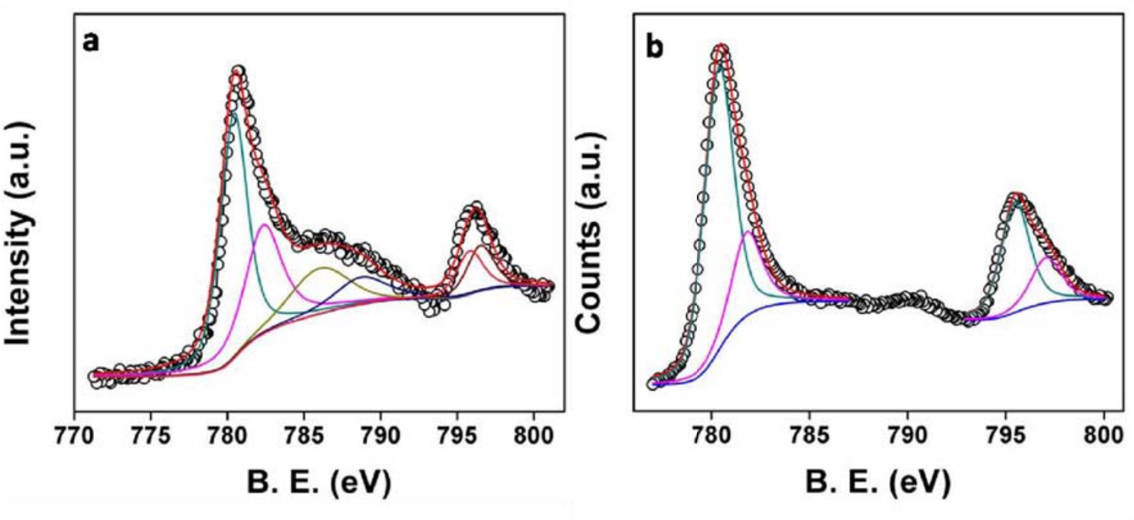

Figure 2B.7: Deconvoluted Co2p XPS spectra of a) $Ca_2Fe_{1.75}Co_{0.25}O_{5\pm\delta}$ and b) $Ca_2FeCoO_{5\pm\delta}$

The surface morphology is analysed by SEM analysis. The particles are found to be agglomerated as shown in figure 2B.8, owing to the high temperature synthesis route. The surface elemental composition has been analysed by EDS technique and the data is tabulated in table 2B.2. Surface composition is in agreement with the stoichiometry of the compound. Further analysis of the concentration of the metal species by MP-AES technique confirms that the bulk composition is also in accordance with the final stoichiometry. The data is tabulated in table 2B.2. Surface area analysis by the BET method suggests that the materials possess low surface area on account of the high temperature synthesis. The data is incorporated in table 2B.3

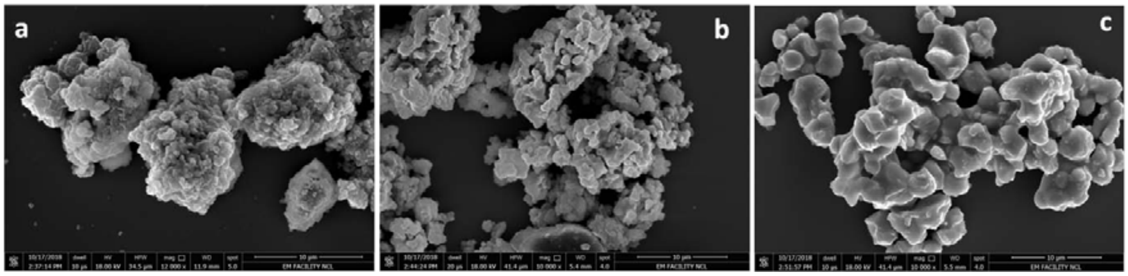

Figure 2B.8: SEM images of a) $Ca_2Fe_2O_{5\pm\delta}$ b) $Ca_2Fe_{1.75}Co_{0.25}O_{5\pm\delta}$ c) $Ca_2FeCoO_{5\pm\delta}$

Table 2B.2: Surface composition from EDS and Bulk composition from MP-AES analysis

Materials	$Ca_2Fe_2O_{5\pm\delta}$				$Ca_2Fe_{1.75}Co_{0.25}O_{5\pm\delta}$				$Ca_2FeCoO_{5\pm\delta}$			
Elements	Surface composition(Weight %)		Bulk Composition (%)		Surface composition(Weight %)		Bulk Composition (%)		Surface composition(Weight %)		Bulk Composition (%)	
	Calculated	Observed	Calculated	Observed	Calculated	Observed	Calculated	Observed	Calculated	Observed	Calculated	Observed
Ca	29.5	32.9	29.5	32.8	29	33.5	41.7	45.5	29	31.6	41.1	46.5
Fe	41	30.2	41.1	44.5	35.8	20.3	50.6	47.1	20.3	21.9	28.7	25.3
Co	--	--	--	--	5.4	6.59	7.7	7.4	21.6	13.8	30.2	28.2
O	29.4	36.9	--	--	29.4	39.5	--	--	29.1	32.7	--	--

Table 2B.3: Surface area data from BET analysis of $Ca_2Fe_{2-x}Co_xO_{5\pm\delta}$

Material	Surface area (m^2/g)
$Ca_2Fe_2O_{5\pm\delta}$	4.129
$Ca_2Fe_{1.75}Co_{0.25}O_{5\pm\delta}$	1.513
$Ca_2FeCoO_{5\pm\delta}$	5.092

2B.3.2. Room Temperature Electrochemical Characterisation

Detailed electrochemical studies of these compounds are carried out by CV and RDE and RRDE techniques in alkaline medium at room temperature

2B.3.2.1. ORR Activity in Alkaline Medium

The ORR activity of the materials are analysed by CV and LSV techniques. Figure 2B.9a represents cyclic voltammogram recorded at 900rpm, in N_2 and O_2 saturated 0.1M KOH, with a scan rate of 50mV/s. The dotted lines represent the scan in N_2 saturation and solid lines represent the scan in O_2 saturation. Analysis of the profile clearly indicates a reduction peak in the O_2 saturated solution. More detailed data on the activity is obtained by linear sweep voltammetry. Figure 2B.9b compares the LSVs of the three samples at 1600 rpm rotation speed and 10mV/s scan rate, clearly on Co doping there is an improvement in the activity. Figure 2B.10 shows individual LSVs of the samples at varying rotation speed with O_2 saturation and 10mV/s scan rate. The blank data is collected by saturating the solution with N_2 without rotating working electrode. The onset potential of the two compositions are 0.811V *vs* RHE, and for the $Ca_2FeCoO_{5\pm\delta}$, the

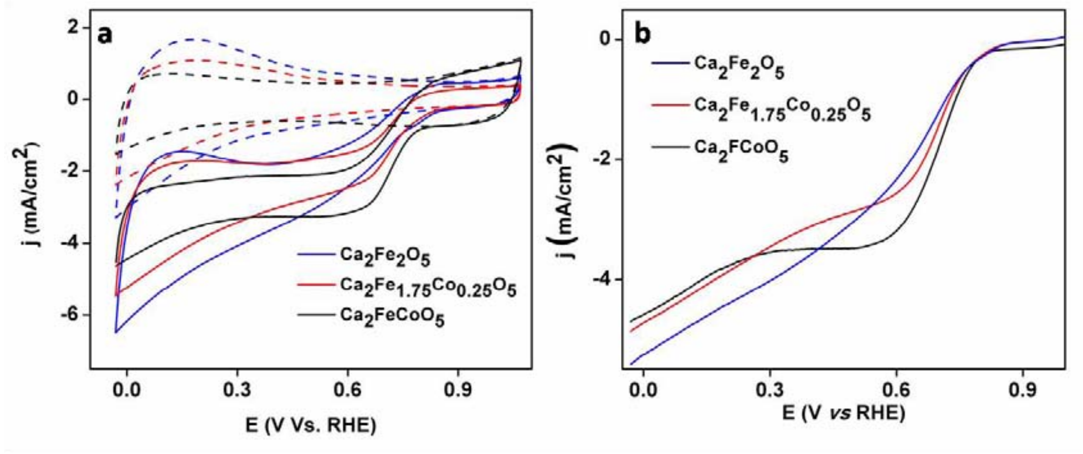

Figure 2B.9: a) Cyclic voltammograms of sample recorded at 50mV/s and 900rpm rotation speed of the working electrode, dotted line represents the pattern with N_2 saturation and solid line represents the scan in O_2 saturated 0.1M KOH solution b) Comparison of the linear sweep voltammogram with 10mV/s scan rate and 1600rpm rotation speed, in O_2 saturated 0.1M KOH solution

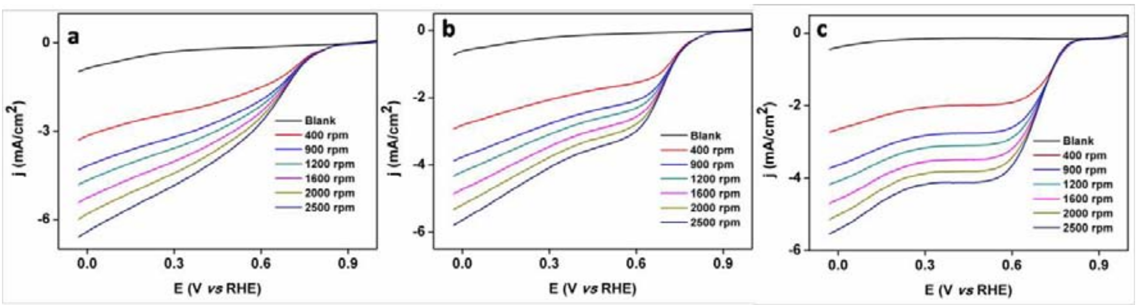

Figure 2B.10: Individual linear sweep voltammograms of the samples a) $Ca_2Fe_2O_{5\pm\delta}$ b) $Ca_2Fe_{1.75}Co_{0.25}O_{5\pm\delta}$ c) $Ca_2FeCoO_{5\pm\delta}$ with various rotation speeds, where the blank data is collected with N_2 saturation and 0rpm rotation speed of the working electrode onset is 10mV positive compared to the rest. The limiting current values are also found to improve with Co doping, indicating the increase in the available active sites with increase in Co concentration.

Detailed mechanistic study on the ORR has been conducted by K-L and Tafel analysis of LSV data. Figure 2B.11a represents the K-L plot calculated at 0.09V *vs* RHE from various rotation speeds. The compound $Ca_2Fe_2O_{5\pm\delta}$ distinctly shows two slopes indicating multiple electron transfer mechanism with an overall slope value of $0.555mAcm^{-2}S^{1/2}$. The next compound $Ca_2Fe_{1.75}Co_{0.25}O_{5\pm\delta}$ also behaved somehow similarly with an overall slope value of $0.5572\ mAcm^{-2}S^{1/2}$, however a straight line is obtained with $Ca_2FeCoO_{5\pm\delta}$ with a slope value of $0.5264\ mAcm^{-2}S^{1/2}$. Tafel calculations are done from LSV at 1600 rpm and plotted in figure 2B.11b. The compounds $Ca_2Fe_2O_{5\pm\delta}$ and $Ca_2Fe_{1.75}Co_{0.25}O_{5\pm\delta}$ exhibit a slope value of -142.1mV/d and -124.5mV/d indicating a similar rate determining step of first electron reduction in both the compounds. However, for the compound $Ca_2FeCoO_{5\pm\delta}$ the slope value is -59.2mV/d, indicating the surface migration of reduced species to be the *rds* in overall process as explained in annexure, which in turn points to the enhancement of catalytic activity of the material[7-9].

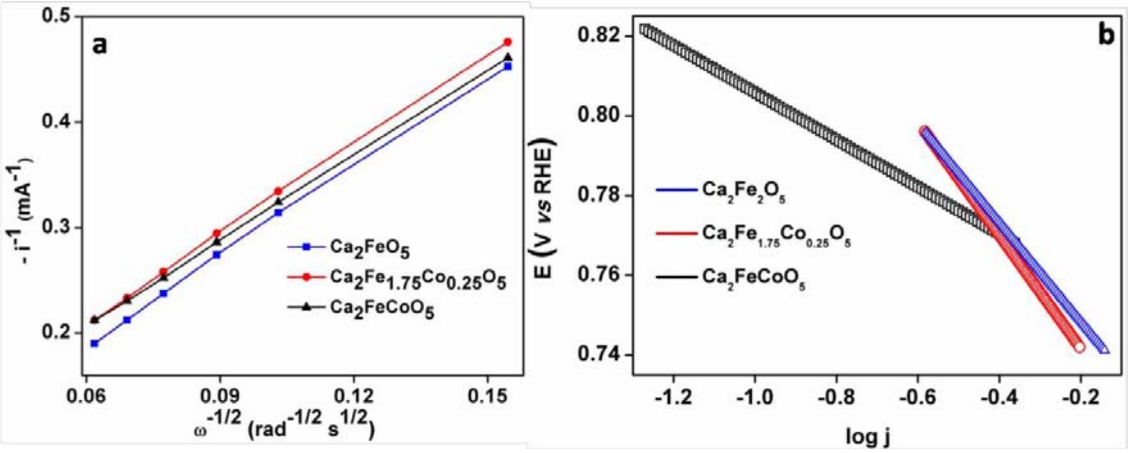

Figure 2B.11: a) K-L plot calculated from LSV data at various rotation speed and 0.09V *vs* RHE b) Tafel plot, calculated from LSV data at 1600rpm rotation speed of the working electrode

A more clear data on the electron transfer behaviour of the material is obtained by RRDE experiments[10]. The relation of applied potential on the electron transfer number and the peroxide yield is plotted in figure 2B.12. All the three compounds exhibit a near

4 electron transfer mechanism in the given potential window. $Ca_2FeCoO_{5\pm\delta}$ exhibits a stable transfer mechanism throughout the potential range; at higher potentials $Ca_2FeCoO_{5\pm\delta}$ exhibits close to four electron transfer and lowest peroxide yield. The peroxide yield is found to be maximum for $Ca_2Fe_2O_{5\pm\delta}$ and the effect of increased doping is clearly visible from the reduced peroxide yield at higher potentials. Also, there is an inflection potential point near 0.4V *vs* RHE, where $Ca_2FeCoO_{5\pm\delta}$ and $Ca_2Fe_{1.75}Co_{0.25}O_{5\pm\delta}$ shift to higher electron transfer and lower peroxide emission. In order to understand the change at this potential, the materials are subjected to the same potential and analysed by XRD and XPS. The crystal structure of the materials is found to remain same before and after the potential treatment, PXRD patterns before and after the treatment is represented in figure 2B.13. To understand more, the surface state of the materials are analysed by XPS after the potential treatment. The Fe state remained same at +3 state even after the treatment, whereas the Co state analysis suggests that there is an increase in the Co(II) in both the compounds at this potential. There is an increase from

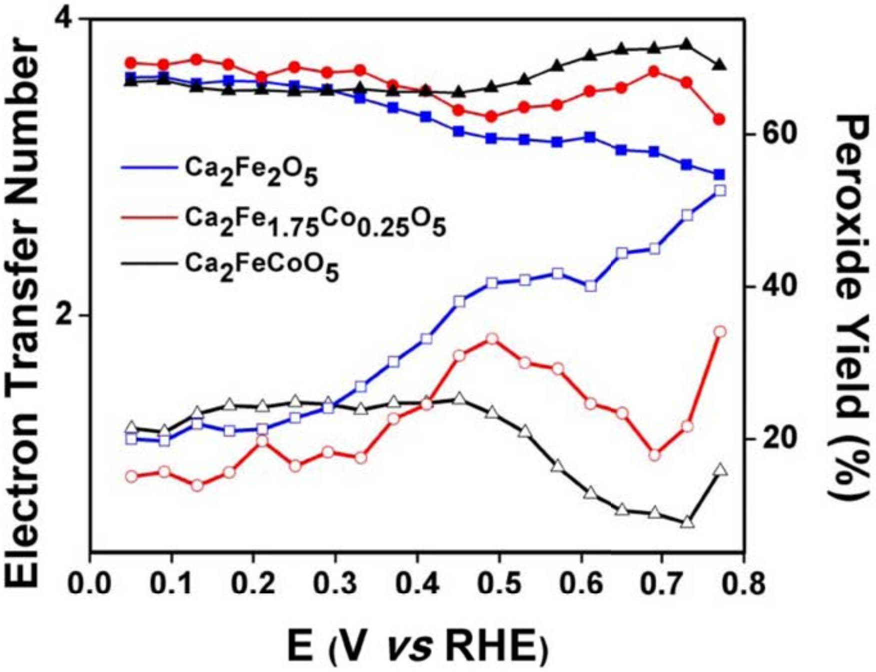

Figure 2B.12: Combined electron transfer number and peroxide yield response with varying the potential with respect to RHE calculated from RRDE, the solid symbol represents the electron count data (left y axis) and the empty symbols represents the peroxide yield (right y axis)

37% to 41% and from 25% to 39% in $Ca_2Fe_{1.75}Co_{0.25}O_{5\pm\delta}$ and $Ca_2FeCoO_{5\pm\delta}$ respectively. The XP spectra of the compounds after the treatment is represented in the figure 2B.14

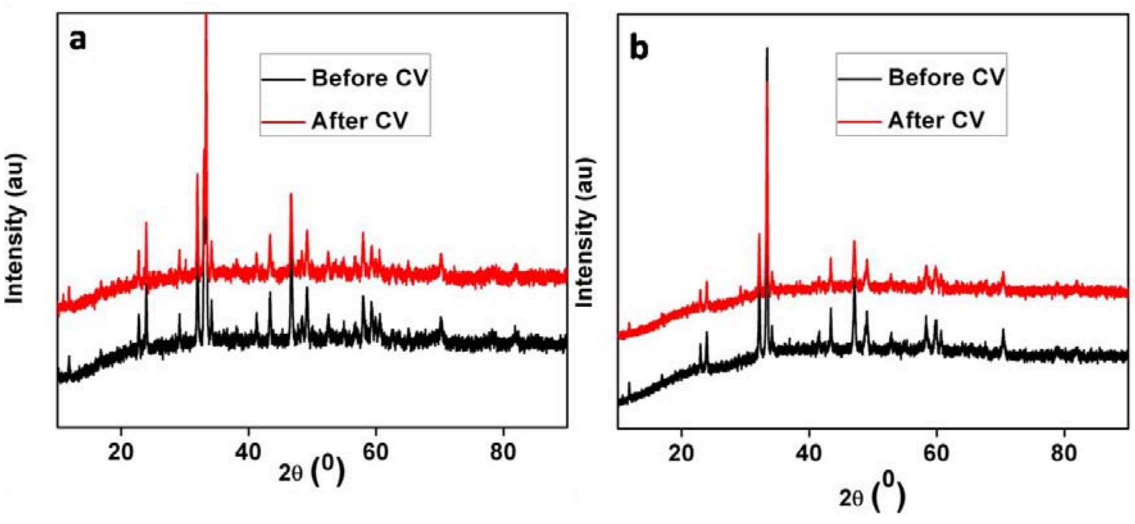

Figure 2B.13: PXRD patterns of the a) $Ca_2Fe_{1.75}Co_{0.25}O_{5\pm\delta}$ and b) $Ca_2FeCoO_{5\pm\delta}$ before and after the potential treatment

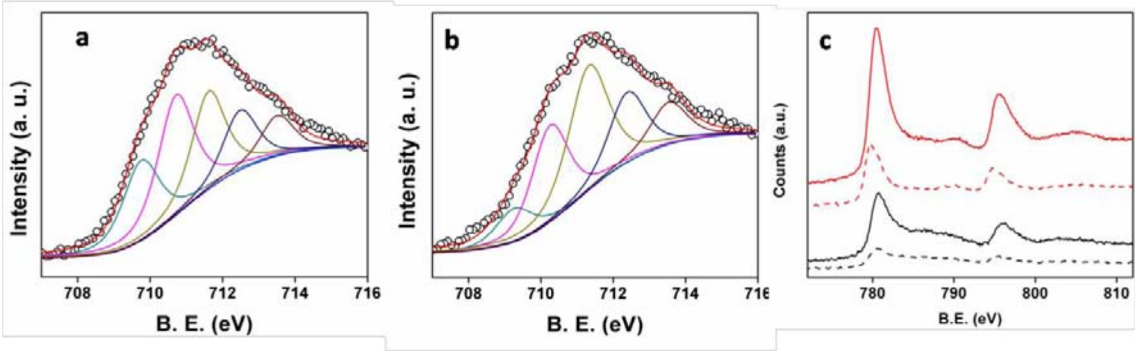

Figure 2B.14: Deconvoluted Fe2p XPS of the a) $Ca_2Fe_{1.75}Co_{0.25}O_{5\pm\delta}$ and b) $Ca_2FeCoO_{5\pm\delta}$ after the potential treatment b) Comparison of Co2p XPS of the $Ca_2Fe_{1.75}Co_{0.25}O_{5\pm\delta}$ (black) and $Ca_2FeCoO_{5\pm\delta}$ (red) before and after the potential treatment, solid line represents spectra recorded before the treatment and dotted line represent spectra after the treatment

2B.3.2.2. OER Activity in Alkaline Medium

OER activity is monitored in 0.1M KOH with N_2 saturation. Figure 2B.15a shows the cyclic voltammogram of the samples at 1600 rpm and 10mV/s scan rate in N_2 saturated solution. There is a clear improvement in onset value and the current response as the Co is introduced to the lattice. The onset potential of the material $Ca_2FeCoO_{5\pm\delta}$ is 1.53V *vs* RHE, $Ca_2Fe_{1.75}Co_{0.25}O_{5\pm\delta}$ and $Ca_2Fe_2O_{5\pm\delta}$ exhibited overpotential of 11mV and 29mV respectively with respect to the latter, the activity is also compared with Vulcan carbon, which exhibits an onset of 1.82V *vs* RHE. For comparison, the current density is plotted at 1.8V *vs* RHE represented in the inset of the figure, and it is clear that the compound $Ca_2FeCoO_{5\pm\delta}$ exhibited maximum current density value.

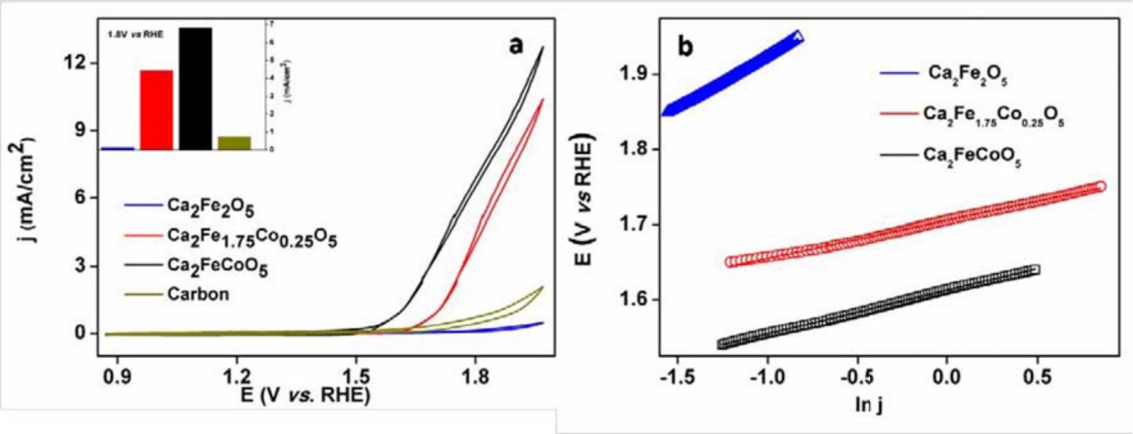

Figure 2B.15: a) OER Cyclic voltammograms of the samples, recorded at 10mV/s scan rate and 1600rpm rotation speed in N_2 saturated 0.1M KOH, inset image shows the comparison of the current density at 1.8V vs RHE and b) OER Tafel plots calculated from the CV data at 1600rpm

Mechanistic aspect of OER is studied by Tafel method and is represented in figure 2B.15b. The parent compound exhibits a slope value of 139mV/d and as Co concentration incorporated in the lattice increased, the slope value shifts to 50.32mV/d and 58.05mV/d respectively for $Ca_2Fe_{1.75}Co_{0.25}O_{5\pm\delta}$ and $Ca_2FeCoO_{5\pm\delta}$. This points to a clear shift of *rds* in the mechanism from first electron transfer to surface migration and further second electron transfer, as suggested by De Faria[11] explained in annexure and a clear improvement in the catalytic activity by Co incorporation.

2B.3.3.High Temperature Analysis

2B.3.3.1. High Temperature XRD

Based on the interesting properties, the composition $Ca_2FeCoO_{5\pm\delta}$ is selected for further high temperature analysis. The practical applicability of the material in various high temperature applications is limited by the phase stability in the operating condition. The material's phase stability at varying temperatures is analysed by non-ambient XRD in various gas atmospheres by Anton Paar XRK900 system. The material phase is analysed at the temperature varying from 500-800°C in O_2 and N_2 atmospheres and the resultant patterns are represented in figure 2B.16. The material exhibited excellent stability in O_2 rich and lean atmosphere, which is crucial OTM and SOFC applications.

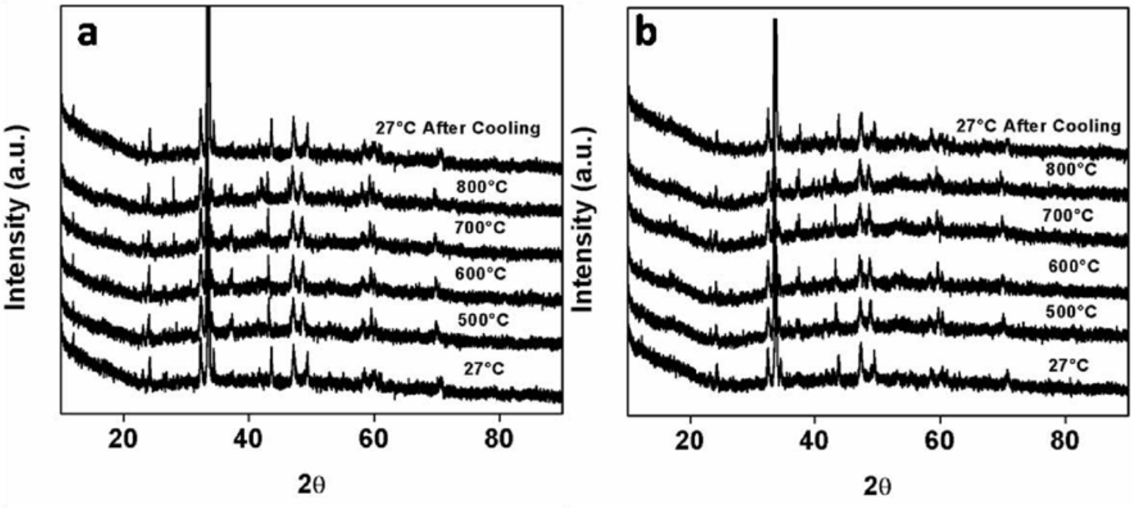

Figure 2B.16: HT-PXRD of $Ca_2FeCoO_{5\pm\delta}$ in a) N_2 atmosphere, and b) O_2atmosphere

2B.3.3.2. High Temperature Impedance Analysis

High temperature Impedance analysis is performed in O_2 and N_2 atmospheres with the temperature ranging from 500 to 800°C. The Nyquist plot representation of impedance data is shown in figure 2B.17. The representation shows no semi-circle, commonly observed for the metal oxide systems due to the contribution from the inductive effect, and the data could not be fitted with equivalent circuit having contribution from grain, grain boundary and electrode resistance. Hence the data is solved by considering the equivalent circuit with an inductor and a resistor as represented in figure 2B.18, which gives the value of overall cumulative contribution only. There is a considerable improvement of conductivity by around ten times on Co doping in the lattice. The data is tabulated in table 2B.4, the conductivities of both the materials improve with increasing in temperature and in the Co doped material, the conductivity is similar in O_2 rich and lean atmospheres, which is a direct implication of the pure oxide ion conductivity.

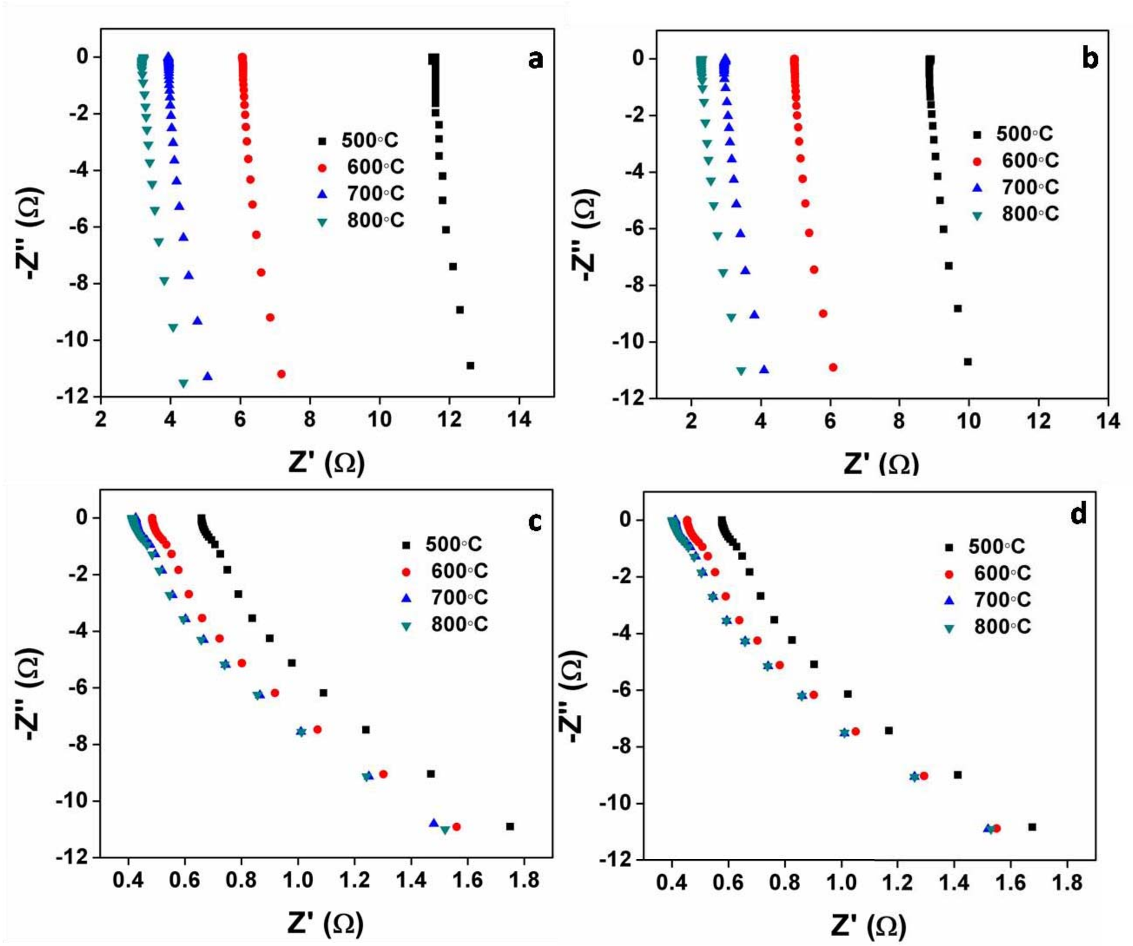

Figure 2B.17: Nyquist plot of $Ca_2Fe_2O_{5\pm\delta}$ and $Ca_2FeCoO_{5\pm\delta}$, where the data is collected a) and c) in N_2 atmosphere and b) and d) in O_2 atmosphere

Figure 2B.18: Equivalent circuit for fitting the Nyquist plot, R represents the resistor and L inductor

Table 2B.4: High resistivity calculated from EIS analysis

Temperature	Resistivity (Ωcm)			
	$Ca_2Fe_2O_{5\pm\delta}$		$Ca_2FeCoO_{5\pm\delta}$	
	N_2	O_2	N_2	O_2
500	89.5	68.7	5.9	5.1
600	46.3	37.8	4.3	4.0
700	30.1	22.4	3.7	3.6
800	24.7	17.7	3.6	3.5

2B.4. Summary and Conclusion

The goal of the chapter was to find out the role of increased Co doping in the structure and overall electrochemical properties of the material. The material $Ca_2FeCoO_{5\pm\delta}$ exhibited interesting inter and intra layer ordering phenomenon in the structure. The room temperature ORR is improved by Co doping. The electron transfer mechanism and the peroxide yield approach a desirable pathway with increasing Co concentration. An inflection point is observed in e-n plot where the transfer number increases rapidly. Analysis at the point revealed an increase in Co(II) concentration in the material. The OER activity in terms of current, onset and Tafel slope improves to a considerable magnitude on Co incorporation to the lattice. The high temperature phase analysis proves the stability of the material in O_2 rich and lean atmospheres. The high temperature conductivity is enhanced more than ten times by the incorporation of Co in the lattice and the behaviour in O_2 rich and lean atmospheres suggests pure oxide ion conductivity.

2B.5. References

1. Toby, B., EXPGUI, a graphical user interface for GSAS. *Journal of Applied Crystallography* **2001,** *34* (2), 210-213.

2. Ramezanipour, F.; Greedan, J. E.; Grosvenor, A. P.; Britten, J. F.; Cranswick, L. M. D.; Garlea, V. O., Intralayer Cation Ordering in a Brownmillerite Superstructure:

Synthesis, Crystal, and Magnetic Structures of Ca_2FeCoO_5. *Chemistry of Materials* **2010,** *22* (21), 6008-6020.

3. Ramezanipour, F.; Cowie, B.; Derakhshan, S.; Greedan, J. E.; Cranswick, L. M. D., Crystal and magnetic structures of the brownmillerite compound $Ca_2Fe_{1.039(8)}Mn_{0.962(8)}O_5$. *Journal of Solid State Chemistry* **2009,** *182* (1), 153-159.

4. Dhankhar, S.; Tiwari, P.; Baskar, K.; Basu, S.; Singh, S., Effect of low Cobalt doping on morphology and properties of calcium ferrite and its application as cathode in Solid Oxide Fuel Cell. *Current Applied Physics* **2017,** *17* (4), 467-473.

5. Biesinger, M. C.; Payne, B. P.; Grosvenor, A. P.; Lau, L. W. M.; Gerson, A. R.; Smart, R. S. C., Resolving surface chemical states in XPS analysis of first row transition metals, oxides and hydroxides: Cr, Mn, Fe, Co and Ni. *Applied Surface Science* **2011,** *257* (7), 2717-2730.

6. Oku, M.; Sato, Y., In-situ X-ray photoelectron spectroscopic study of the reversible phase transition between CoO and Co_3O_4 in oxygen of 10−3 Pa. *Applied Surface Science* **1992,** *55* (1), 37-41.

7. Taylor, R. J.; Humffray, A. A., Electrochemical studies on glassy carbon electrodes: II. Oxygen reduction in solutions of high pH (pH>10). *Journal of Electroanalytical Chemistry and Interfacial Electrochemistry* **1975,** *64* (1), 63-84.

8. Ge, X.; Sumboja, A.; Wuu, D.; An, T.; Li, B.; Goh, F. W. T.; Hor, T. S. A.; Zong, Y.; Liu, Z., Oxygen Reduction in Alkaline Media: From Mechanisms to Recent Advances of Catalysts. *ACS Catalysis* **2015,** *5* (8), 4643-4667.

9. Hu, P.; Song, Y.; Chen, L.; Chen, S., Electrocatalytic activity of alkyne-functionalized AgAu alloy nanoparticles for oxygen reduction in alkaline media. *Nanoscale* **2015,** *7* (21), 9627-9636.

10. Zhou, R.; Zheng, Y.; Jaroniec, M.; Qiao, S.-Z., Determination of the Electron Transfer Number for the Oxygen Reduction Reaction: From Theory to Experiment. *ACS Catalysis* **2016,** *6* (7), 4720-4728.

11. De Faria, L. A.; Boodts, J. F. C.; Trasatti, S., Electrocatalytic properties of ternary oxide mixtures of composition $Ru_{0.3}Ti_{(0.7-x)}Ce_xO_2$: oxygen evolution from acidic solution. *Journal of Applied Electrochemistry* **1996,** *26* (11), 1195-1199.

Chapter 3

$Ba_2In_2O_5$ System

Part A

Role of transition metal doping in the structure and room temperature bifunctional activity of $Ba_2In_2O_5$

3A.1. Introduction

$Ba_2In_2O_5$ is a well studied system in the brownmillerite family for its high oxide and protonic conductivity[1-4] and was first synthesised by Kwestroo et al. in 1977 by the reaction of $BaCO_3$ and In_2O_3 at 1300°C[5]. B site cation, In^{3+} in its stable oxidation state, does not undergo reduction too easily and does not possess strong octahedral or tetrahedral site preference. Due to the charge mismatch between A and B sites, all oxygen sites of perovskite cannot be occupied leading to the brownmillerite structure, consisting of alternate InO_6 octahedral and InO_4 tetrahedral layers with oxygen vacancies ordered in a two dimensional plane[3, 6, 7]. Conductivity study of the material showed a sudden transition leading to fast ion conduction at ~925°C observed by Goodenough et al[3] and was later interpreted as the order-disorder transition involving the oxygen vacancies in the lattice by Zhang and Smyth[6]. Above the transition temperature, the conductivity increased at least by one order of magnitude and below the temperature, electronic contribution is significant[6]. The material gained considerable attention since its conductivity at 1000°C is comparable to the yttria stabilised zirconia (YSZ), which is the most widely employed ion conducting electrolyte[3, 8, 9]. Predominant mode of intrinsic disorder in the material is Frenkel defect. Defect concentration will be significant at lower temperature as evidenced by the low Frenkel energy, and the conductivity by the ordered form at lower temperature is attributed to the Frenkel defects[10]. In the structure there are three crystallographically different oxygen sites, O1 in the equatorial plane of the octahedra through which octahedral groups are connected, O2, in apical site which bridges the tetrahedra and octahedra, and O3 connecting the tetrahedral groups and lies in the equatorial plane of the tetrehedra[7, 8]. Oxygen vacancies preferentially form at O1 site than the O2 site, whereas structural tolerance for vacancy in the O3 site is very poor. The displaced oxygen can be readily accommodated in the coordinatively unsaturated tetrahedral layer[10]. The orthorhombic phase changes to tetragonal and further completely disorders to defective cubic perovskite form at 1075°C. Mobile oxygen concentration increases continuously in the temperature range from 925°C and above 1075°C, full population of oxide ions becomes mobile[7, 8]. Ab-initio study suggests that orthorhombic to tetragonal phase transition is first order at around 925°C and to cubic at 1075°C is a second order phase transition[11].

Doping In position in $Ba_2In_2O_5$ is also well studied for conductivity, magnetic studies and catalysis[12-19]. Jijil et al reported the Ce doping in $Ba_2In_2O_5$ and consequent improvement in the room temperature oxygen reduction activity comparable to active non-platinum systems[20]. Progressive doping and structure property correlation was also studied elaborately[21]. With increasing Ce doping, activity was found to be enhanced; however with 100% Ce in the B site which forms a perfect cubic perovskite, activity became poor suggesting a strong correlation of structure and oxygen vacancy on the property. Overall disorder and B site symmetry increased on Ce doping and consequently improved the ORR activity upto 75% Ce doping. A transition from tetragonal to highly disordered cubic perovskite on doping with >25% Co in $Ba_2In_2O_5$ and associated improvement in the room temperature ORR activity was also observed by the same group[22].

Considering all these reports, in this chapter we have selected $Ba_2In_2O_5$ as the parent structure and doped transition metals (Mn/Fe/Co/Ni/Cu) at 12.5atom% in the In position. Aliovalent doping in the In^{3+} position can alter the oxygen vacancy concentration[23]. The main goal of the chapter is to understand the design principle of bifunctional oxygen catalyst by the choice of transition metals and the effect of metal dopant in the structure and overall bifunctional activity of the material.

3A.2. Experimental Section

3A.2.1. Synthesis of $Ba_2In_{1.75}M_{0.25}O_{5\pm\delta}$ (M = Mn/Fe/Co/Ni/Cu)

$Ba_2In_2O_{5\pm\delta}$ and cerium and transition metal doped varieties with stoichiometry $Ba_2InCe_{0.75}M_{0.5}O_{5\pm\delta}$ (M= Mn/Fe/Co/Ni/Cu) are synthesised by the solid state reaction at 1300°C, of precursors $BaCO_3$ (Min. 99.0%, Sigma Aldrich), In_2O_3 (99.99%, Aldrich), $MnCO_3$ (99.9%, Alfa Aeser), Fe_2O_3 (99.98%, Sigma Aldrich), $CoCO_3$ (Co- 43-47%, Sigma Aldrich), NiO (99%, Alfa Aeser) and CuO (99%, Thomas Baker). The precursors are weighed stoichiometrically and ground well in a mortar and pestle. Decarbonisation has been done at 900°C, ground again and made a pellet and fired at 1300°C for 12h.

3A.2.2. Characterisation

Phase purity and structure is analysed with powder x-ray diffraction (PXRD) as described in chapter 2A. Detailed structural studies are done by Rietveld refinement of

PXRD patterns by using GSAS-EXPGUI suit of programs. Morphology and surface composition are analysed by SEM-EDAX. Surface states of the cations are analysed by X-ray photoelectron spectroscopy (XPS) analysis as described in chapter 2A.

3A.2.3. Electrochemical Analysis

Electrochemical analysis is conducted in 0.1M KOH solution as described in chapter2A.

3A.3. Results and Discussion

3A.3.1. Synthesis and Structural Characterisation

Materials with composition $Ba_2In_{1.75}M_{0.25}O_{5\pm\delta}$ (M = Mn/Fe/Co/Ni/Cu) is successfully synthesised in the brownmillerite related phase at 1300°C. The phase purity is analysed by PXRD and the patterns are represented in figure 3A.1. The parent brownmillerite $Ba_2In_2O_{5\pm\delta}$ formed as $Ba_2In_2O_5.xH_2O$ crystallising in the tetragonal crystal system, slight impure phase of unreacted $BaCO_3$ could also be observed in the pattern. Transition metal doped materials formed in orthorhombic brownmillerite structure crystallising in Ibm2 space group matching with the reference pattern with JCPDS number: 01-081-2473.

Structural studies are conducted by Rietveld refinement of PXRD pattern with GSAS-EXPGUI suit of programs[24]. The parent structure is refined with hydrated form of $Ba_2In_2O_5$ with ICSD collection code: 89439.The structure consists of two separate sites for B site cation, octahedral and tetrahedral sites and three crystallographically different O sites, O1 connects the octahedral groups, O2 bridges the octahedral and tetrahedral layers, and O3 connects the tetrahedral groups. The refinement proceeded smoothly to get the final unit cell parameters. The impurity phase of $BaCO_3$ is also inserted and refined quantitatively. The final weight percentage of impurity phase obtained is 8.7% and the fitted profile is represented in figure 3A.2a. The final unit cell is obtained with parameters a=b=4.1605(6) and c=8.9285(1) and the representative unit cell polyhedral arrangement is given in figure 3A.3a. The material $Ba_2In_{1.75}Mn_{0.25}O_{5\pm\delta}$ is refined with orthorhombic model crystallising in Ibm2 space group on account of the matching JCPDS reference pattern, but it resulted in an unacceptable fit. Refinement of the structure has been carried out by interchanging the unit cell dimensions in the model, resulting in the space group Ima2. The refinement

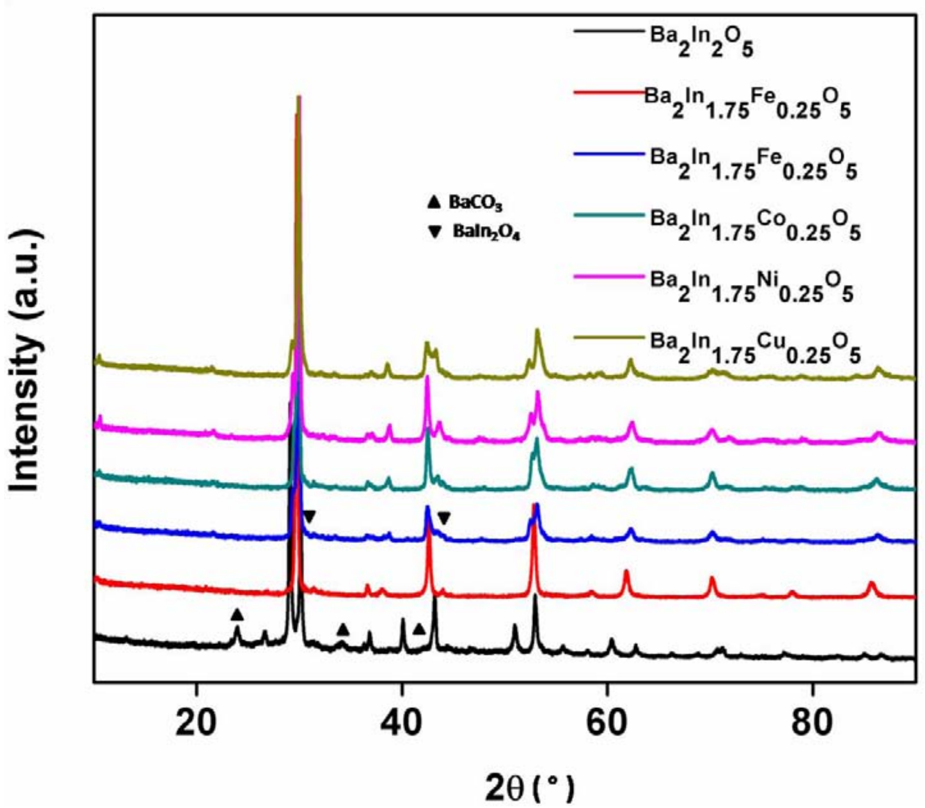

Figure 3A.1: Powder XRD patterns of the materials synthesised at 1300°C

proceeded smoothly with the $Ba_2In_2O_5$ model with ICSD collection code 89438. Structure consists of two In sites, one each in tetrahedral and octahedral coordination and the dopant element is equally substituted to tetrahedral and octahedral sites for refinement. All the parameters including occupancy parameters are refined. A better fit is observed by putting in the impurity phase of $BaCO_3$ and $BaIn_2O_4$. A quantitative phase analysis is carried out resulting in an estimation of 1.7% $BaCO_3$ and 10.6% $BaIn_2O_4$. The refined pattern is represented in figure 3A.2b, and the polyhedral representation of the unit cell is represented in figure 3A.3b. $Ba_2In_{1.75}Fe_{0.25}O_{5\pm\delta}$ refinement is carried out with the Ibm2 model, and is also not fruitful. Refinement proceeded smoothly with the same model as used with $Ba_2In_{1.75}Mn_{0.25}O_{5\pm\delta}$. The refinement resulted in a smooth difference curve and the refined pattern is given in figure 3A.2c. The materials $Ba_2In_{1.75}Co_{0.25}O_{5\pm\delta}$ and $Ba_2In_{1.75}Ni_{0.25}O_{5\pm\delta}$ are also refined with the same model with no impurity phase. The refined patterns are represented in figure 3A.2d and 3A.2e respectively. On account of the similarity in the XRD patterns, the material refinement of $Ba_2In_{1.75}Cu_{0.25}O_{5\pm\delta}$ was also tried with the same model, but resulted in unacceptable profile parameters. A model has been selected by interchanging a and b axes with those represented in ISCD collection code: 73937. A smooth profile is obtained after refinement as represented in the figure 3A.2f. The polyhedral representation of the unit cell obtained after refinement is shown in figure 3A.3c and detailed Rietveld refinement data is tabulated in Table 3A.1

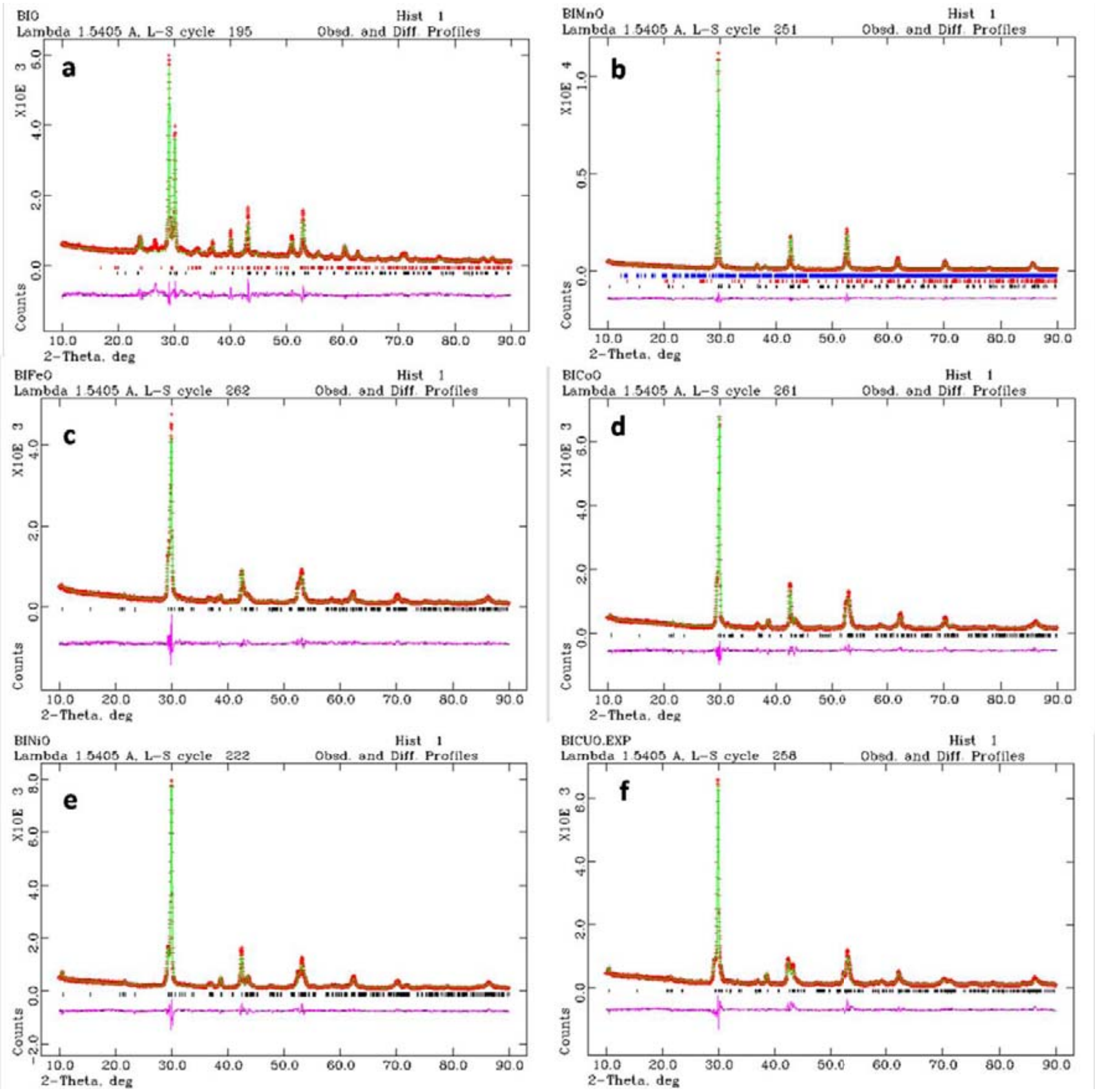

Figure 3A.2: Rietveld refined PXRD patterns of a) $Ba_2In_2O_{5\pm\delta}$ b) $Ba_2In_{1.75}Mn_{0.25}O_{5\pm\delta}$ c) $Ba_2In_{1.75}Fe_{0.25}O_{5\pm\delta}$ d) $Ba_2In_{1.75}Co_{0.25}O_{5\pm\delta}$ e) $Ba_2In_{1.75}Ni_{0.25}O_{5\pm\delta}$ f) $Ba_2In_{1.75}Cu_{0.25}O_{5\pm\delta}$

Detailed surface state analysis is conducted by XP spectroscopy. The data is calibrated by fitting the C1s spectrum to 248.8 eV. Figure 3A.4 a to e represent the deconvoluted XP spectra of respective metal dopants. Mn $2p_{3/2}$ spectra is fitted with two peaks at 641.2 eV and 643.5 eV corresponding to Mn(III) and Mn(II) states[25-27]. Fe$2p_{3/2}$ spectrum

Table 3A.1: Structural parameters obtained from Rietveld refinement

Material		$Ba_2In_{1.75}Mn_{0.25}O_{5\pm\delta}$	$Ba_2In_{1.75}Fe_{0.25}O_{5\pm\delta}$	$Ba_2In_{1.75}Co_{0.25}O_{5\pm\delta}$	$Ba_2In_{1.75}Ni_{0.25}O_{5\pm\delta}$	$Ba_2In_{1.75}Cu_{0.25}O_{5\pm\delta}$
Space group		Ima2	Ima2	Ima2	Ima2	Ibm2
Cell parameter	a	16.9975(9)	16.7569(1)	16.6267(7)	16.6145(3)	6.0588(4)
	b	5.9886(6)	6.0658(3)	6.0091(2)	6.0659(1)	16.6798(9)
	c	5.9894(6)	5.9672(4)	5.9462(2)	5.9681(1)	5.9333(3)
χ^2		3.37	2.38	2.61	3.35	3.38
R_p (%)		9.2	8.1	7.5	8.7	9.1
wR_p (%)		11.9	10.2	9.7	10.9	11.6
Ba	x	0.113767	0.111475	0.111346	0.110896	0.013087
	y	0.001771	0.014945	0.013000	0.016208	0.110247
	z	0.515471	0.503844	0.506073	0.511033	0.506535
In1 occupancy		0.8672	0.8771	0.8883	0.8730	0.8668
M1 Occupancy		0.1109	0.1287	0.1344	0.1217	0.1135
In2	x	0.2500	0.250000	0.250000	0.250000	0.936330
	y	0.952221	0.953945	0.955958	0.891547	0.250000
	z	0.011372	0.009362	0.009382	0.622483	0.009361
occupancy		0.8722	0.8828	0.8597	0.8749	0.8835
M2	x	0.250000	0.988478	0.250000	0.250000	0.935640
	y	0.957788	0.196776	0.984641	0.931117	0.250000
	z	0.009891	0.331929	0.030452	0.036963	-0.015765
occupancy		0.1176	0.1133	0.1073	0.1300	0.1313
O1	x	1.002261	0.992808	0.988129	0.991641	0.281529
	y	0.253891	0.241808	0.250063	0.250521	0.987876
	z	0.298174	0.311431	0.281222	0.297303	0.224240
occupancy		1.0144	0.9606	1.0131	0.9607	1.0165
O2	x	0.138975	0.139136	0.139703	0.14216	0.053420
	y	0.041741	0.047981	0.059981	0.050961	0.139024
	z	0.053868	0.070644	0.052446	0.048766	0.039030
occupancy		1.0140	1.0299	1.0643	1.0385	1.0643
O3	x	0.250000	0.250000	0.250000	0.250000	0.875836
	y	0.882973	0.897952	0.883703	0.891547	0.250000
	z	0.637664	0.635222	0.611107	0.622483	0.619134
Occupancy		1.0169	1.0774	1.1686	1.1396	1.1862

[a]$Ba_2In_2O_5$: spacgroup: P4/mmm; χ^2: 4.92; R_p: 8.7%; wR_p: 11.5%; Ba(0,0,0.282);In1(0.5,0.5,0.5); In2(0.5,0.5,0); O1(0.5,0.5,0.244197); O2(0,0.5,0.5); O3 (0.341814,0,0); [b]In1/M1(0,0,0)

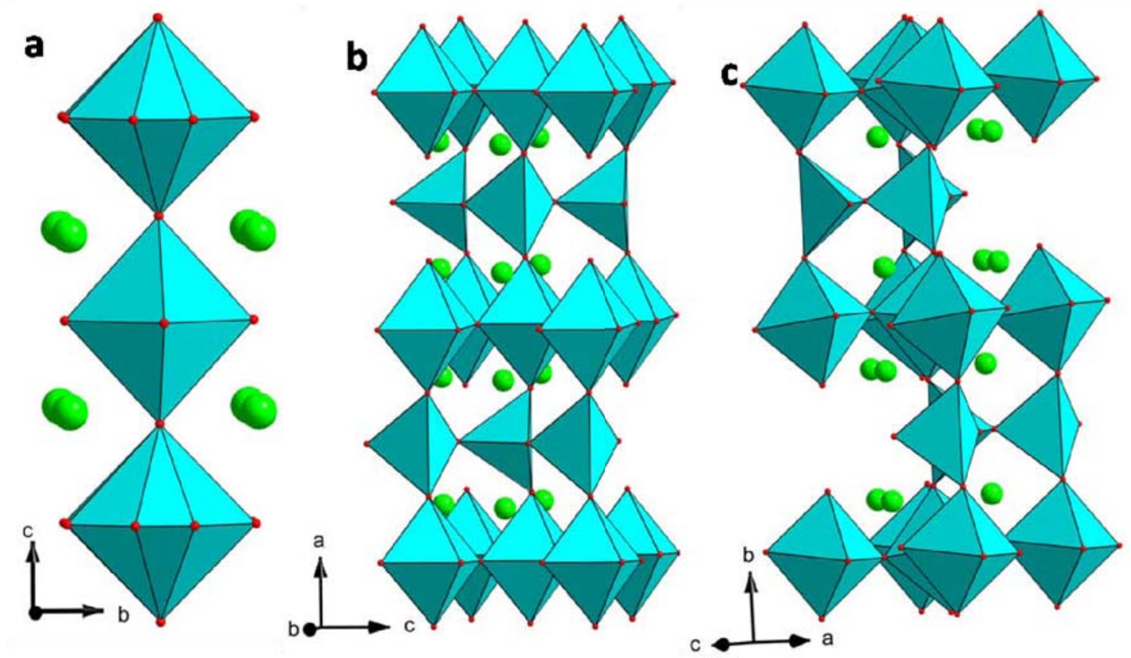

Figure 3A.3: polyhedral representation of unit cells of a) $Ba_2In_2O_{5\pm\delta}$ crystallising in the P4/mmm space group b) $Ba_2In_{1.75}Mn_{0.25}O_{5\pm\delta}$ in Ima2 space group c) $Ba_2In_{1.75}Cu_{0.25}O_{5\pm\delta}$ in Ibm2 space group

is fitted with five peaks suggesting the presence of Fe in +3 oxidation state[27, 28]. The Co2p spectra and Ba3d spectra overlap at same binding energy, however upon deconvolution, the individual peaks are separated[29]. Since the Ba3d peak is at slightly higher binding energy than the Co2p peak. Deconvolution of the spectra with peaks at 778.5eV and 793.8eV for $2p_{1/2}$ and $2p_{3/2}$ respectively with a coupling constant of ~15eV proves that the Co exists in +3 oxidation state, also the absence of satellite features rules out the existence of +2 state[27, 28, 30]. Analysis of the XP spectra of Ni and Cu indicate their existence in +2 oxidation state. Peak at 855.3eV and an intense shake up satellite peak at 860eV proves the presence of Ni(II) state[27, 31, 32]. $Cu2p_{1/2}$ region is fitted with a single peak at 933.2eV indicating the Cu(II) state[33, 34].

Morphology and surface composition is analysed by SEM-EDS technique. The SEM images are represented in figure 3A.5, the materials are found to agglomerate to form large particles of size extending to several micrometers, attributed to the high temperature synthesis at 1300°C. The surface composition analysed by EDS analysis is tabulated in table 3A.2. The observed surface composition is in agreement with the calculated weight percentage considering the stoichiometry of the materials.

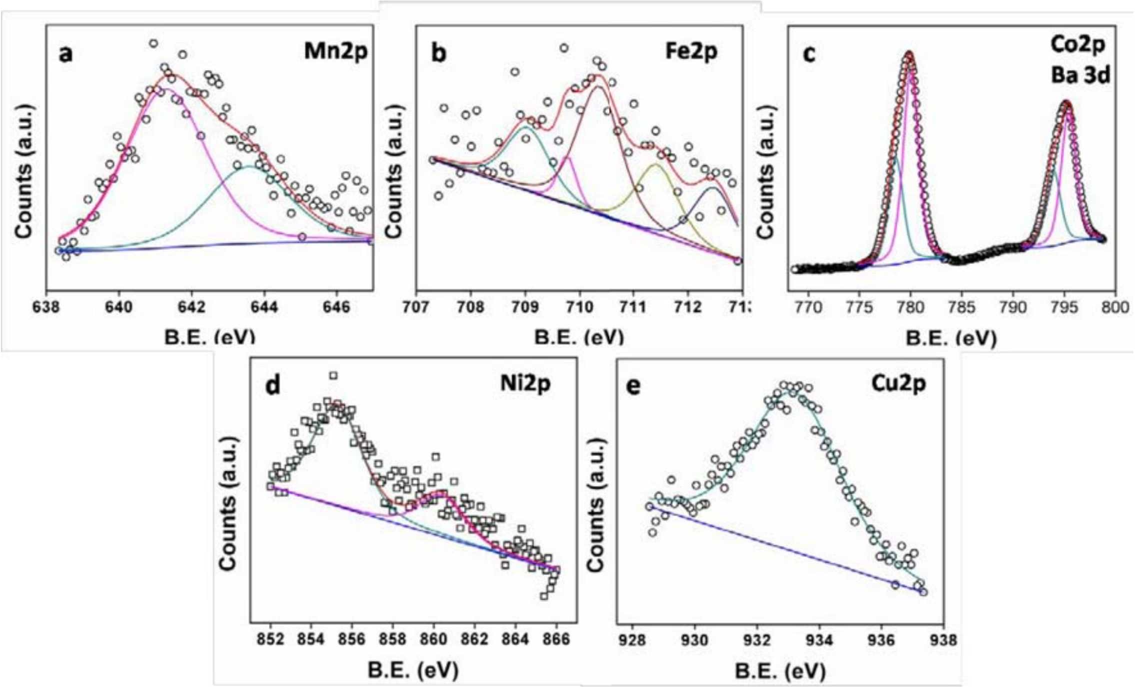

Figure 3A.4: Deconvoluted XPS of the materials a) Mn2p spectra of $Ba_2In_{1.75}Mn_{0.25}O_{5\pm\delta}$ b) Fe2p spectra of $Ba_2In_{1.75}Fe_{0.25}O_{5\pm\delta}$ c) Co2p and Ba3d spectra of $Ba_2In_{1.75}Co_{0.25}O_{5\pm\delta}$ d) Ni2p spectra of $Ba_2In_{1.75}Ni_{0.25}O_{5\pm\delta}$ e) Cu2p spectra of $Ba_2In_{1.75}Cu_{0.25}O_{5\pm\delta}$

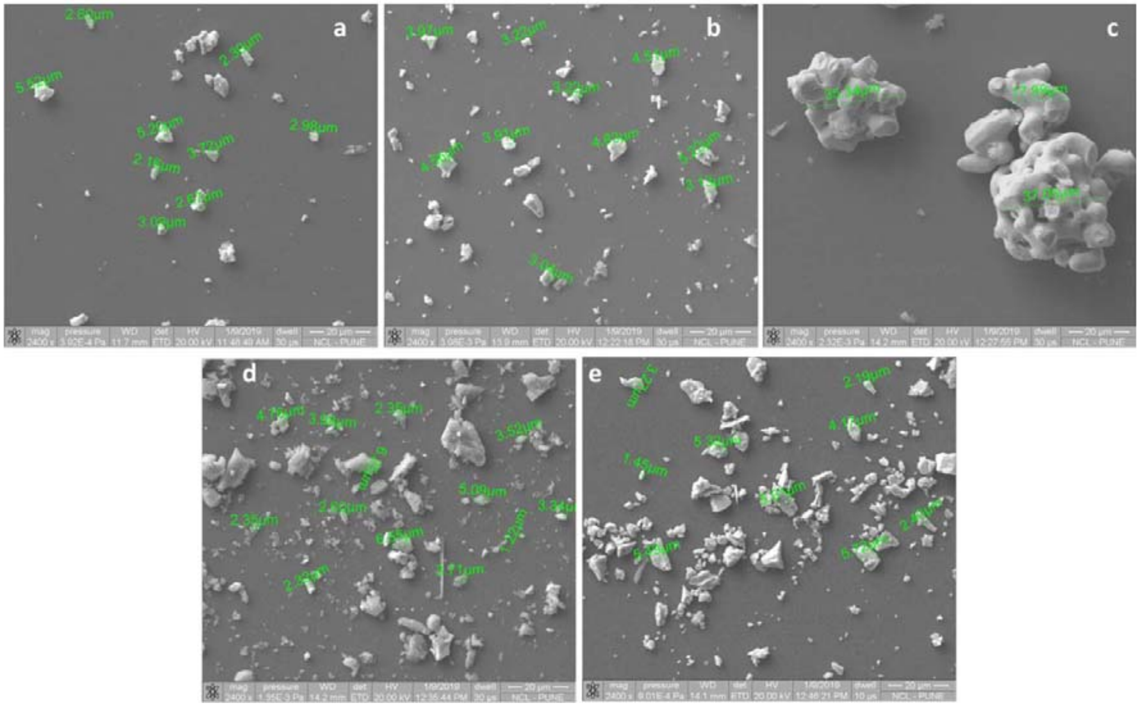

Figure 3A.5: SEM images of a) $Ba_2In_{1.75}Mn_{0.25}O_{5\pm\delta}$ b) $Ba_2In_{1.75}Fe_{0.25}O_{5\pm\delta}$ c) $Ba_2In_{1.75}Co_{0.25}O_{5\pm\delta}$ d) $Ba_2In_{1.75}Ni_{0.25}O_{5\pm\delta}$ e) $Ba_2In_{1.75}Cu_{0.25}O_{5\pm\delta}$

Table 3A.2: Calculated weight percentage and observed surface composition from EDS data

Element	Weight %									
	$Ba_2In_{1.75}Mn_{0.75}O_{5\pm\delta}$		$Ba_2In_{1.75}Fe_{0.75}O_{5\pm\delta}$		$Ba_2In_{1.75}Co_{0.75}O_{5\pm\delta}$		$Ba_2In_{1.75}Ni_{0.75}O_{5\pm\delta}$		$Ba_2In_{1.75}Cu_{0.75}O_{5\pm\delta}$	
	Calculated	Observed	Calculated	Observed	Calculated	Observed	Calculated	Observed	Calculated	Observed
Ba	48.2	43.7	48.2	52.9	48.2	45.7	48.2	51.3	48.1	54.2
In	35.3	26.3	35.3	28.5	35.2	24.3	35.2	27.6	35.1	26.5
Fe/Mn/Co/Ni/Cu	2.4	2.6	2.5	4.8	2.6	3.3	2.6	3.4	2.8	3.1
O	14.1	27.4	14.1	13.7	14	26.7	14	17.6	14	16.1

3A.3.2. Electrochemical Characterisation

Detailed electrochemical studies of these compounds are carried out by CV and RDE method under alkaline medium at room temperature

3A.3.2.1. ORR Activity in Alkaline Medium

ORR activity is monitored in 0.1M KOH with N_2 and O_2 saturation by CV and LSV techniques. The combined cyclic voltammogram is represented in the figure 3A.6a. The dotted pattern represents the scan in N_2 saturation with 900rpm and 50mV/s scan rate, upon oxygen saturation a clear reduction peak is observed in all the compounds, pattern in solid line represents the scan in O_2 saturated solution with 50mV/s scan rate and 900rpm rotation speed of the working electrode.

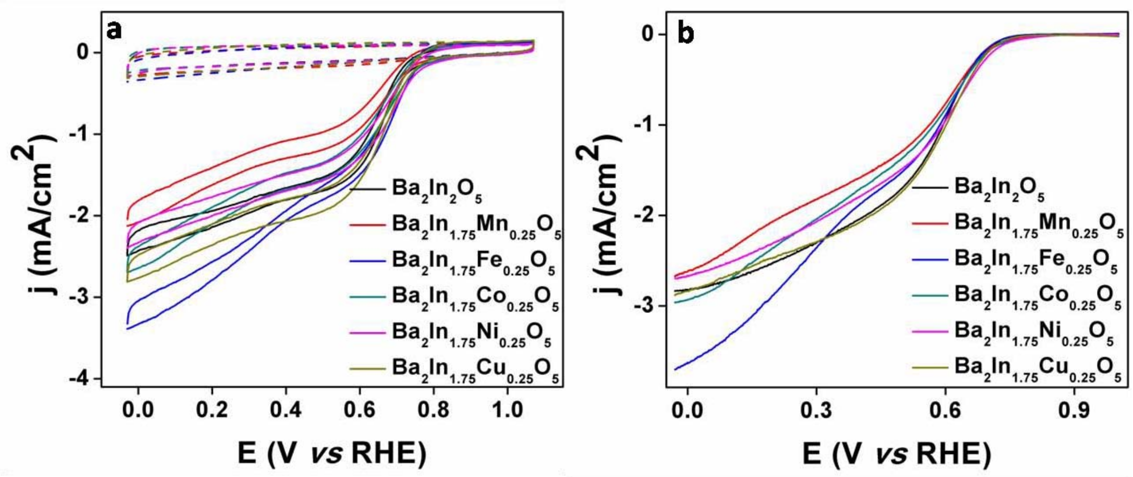

Figure 3A.6 a) Cyclic voltammogram of the samples, dashed line represents the scan in N_2 saturation and solid line represents the scan with O_2 saturation, with scan rate of 50mV/s and 900 rpm rotation speed b) comparison of linear sweep voltammograms of the sample recorded in O_2 saturation, 10mV/s scan rate and 1600 rpm rotation speed of the working electrode, the data is corrected by blank run in N_2saturation with 0rpm rotation speed.

Detailed analysis of the ORR behaviour is conducted by linear sweep voltammetry. Comparison of LSVs recorded at 1600rpm in O_2 saturation is represented in figure 3A.6b. The data is subtracted from the blank data with N_2 saturation to understand reduction behaviour in O_2 saturation. Analysing the parameters such as onset potential and current density suggested no clear trend in activity with metal doping. The onset potential is in the range of 0.77V to 0.73V which is a very small difference than expected on incorporation of transition metal centre. Better current response is exhibited by the parent compound and least by the Mn doped material. The better activity of the parent material can be attributed to the disordered tetragonal symmetry, which allows the oxygen vacancies to take part in the reaction, in comparison to the other doped materials which crystallises in the perfect orthorhombic structure. Individual LSVs of the materials with various rotation speeds are represented in figure 3A.7

Detailed study on the ORR kinetics is done by Koutechy-Levich and Tafel analysis. K-L calculation is done at 0.21V *vs* RHE from the LSV data at various rotation speeds as per the equation given in annexure[35, 36]. All the materials exhibited more or less similar slope values indicating similar type of electron transfer process in all the materials. Tafel plot is represented in figure 3A.8b, lowest Tafel slope value of -115mV/d is obtained for $Ba_2In_2O_{5\pm\delta}$ indicating the first electron transfer step as the rate determining step as explained in the annexure[35, 37]. The trend of the doped materials are in the order $Ba_2In_{1.75}Fe_{0.25}O_{5\pm\delta}$ (-123 mV/d) > $Ba_2In_{1.75}Cu_{0.25}CoO_{5\pm\delta}$ (-133 mV/d) > $Ba_2In_{1.75}Mn_{0.25}O_{5\pm\delta}$ (-138 mV/d) > $Ba_2In_{1.75}Co_{0.25}O_{5\pm\delta}$ (-143 mV/d) > $Ba_2In_{1.75}Ni_{0.25}O_{5\pm\delta}$ (-123 mV/d).

More reliable data on the electron transfer mechanism and the peroxide yield is obtained by RRDE analysis[38]. Dependence of electron transfer number and the peroxide yield with applied potential calculated from the RRDE experiments is represented in figure 3A.9. The highest electron transfer behaviour is exhibited by $Ba_2In_{1.75}Fe_{0.25}O_{5\pm\delta}$ and $Ba_2In_{1.75}Mn_{0.25}O_{5\pm\delta}$ and lowest by the parent and the Cu doped variety. $Ba_2In_{1.75}Ni_{0.25}O_{5\pm\delta}$ and $Ba_2In_{1.75}Co_{0.25}O_{5\pm\delta}$ exhibited intermediate electron transfer behaviour. The electron transfer number in all the compounds is between 2-4, indicating intermediate electron transfer process generally observed in the oxide materials. $Ba_2In_2O_{5\pm\delta}$ and $Ba_2In_{1.75}Cu_{0.25}O_{5\pm\delta}$ at lower potentials yielded a maximum of ~80% peroxide, indicating a near 2 electron transfer mechanism in the compounds. The lowest value for the peroxide yield at 38% is obtained for the material $Ba_2In_{1.75}Fe_{0.25}$-$O_{5\pm\delta}$ at higher potentials.

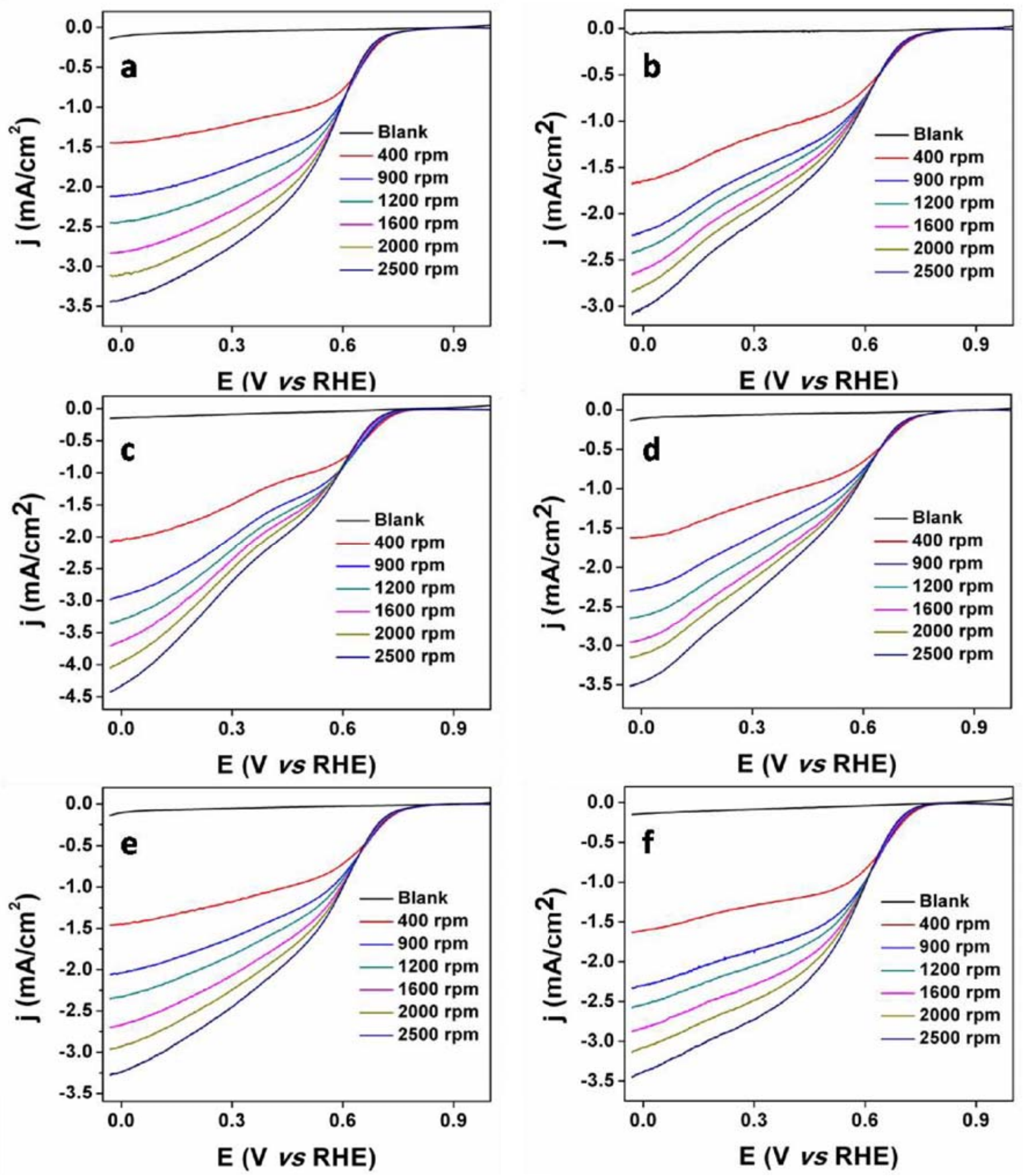

Figure 3A.7 : LSVs at various rotation speeds in oxygen saturation and 10mV/s scan rate of a) $Ba_2In_2O_{5\pm\delta}$ b) $Ba_2In_{1.75}Mn_{0.25}O_{5\pm\delta}$ c) $Ba_2In_{1.75}Fe_{0.25}O_{5\pm\delta}$ d) $Ba_2In_{1.75}Co_{0.25}O_{5\pm\delta}$ e) $Ba_2In_{1.75}Ni_{0.25}O_{5\pm\delta}$ and f) $Ba_2In_{1.75}Cu_{0.25}O_{5\pm\delta}$; blank data is collected in N_2saturation and 0rpm rotation speed

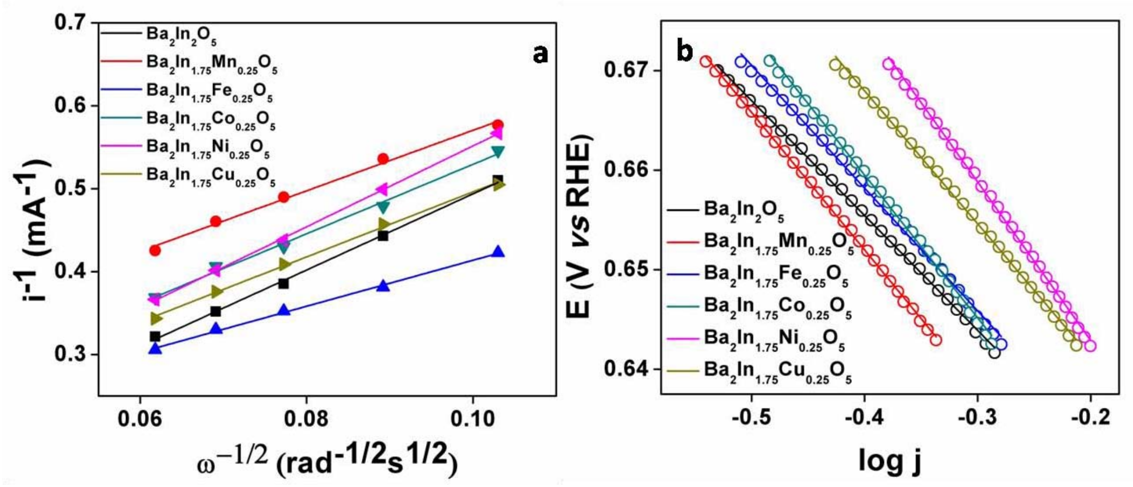

Figure 3A.8: a) K-L plot at 0.21V *vs* RHE calculated from LSV data at various rotation speeds, the symbols represent the original data and the line represents the linear fit of the data. b) Tafel plot of the samples calculated from the LSV data at 1600rpm rotation speed, the empty circles represents the original data and the solid line represents the linear fit of the data

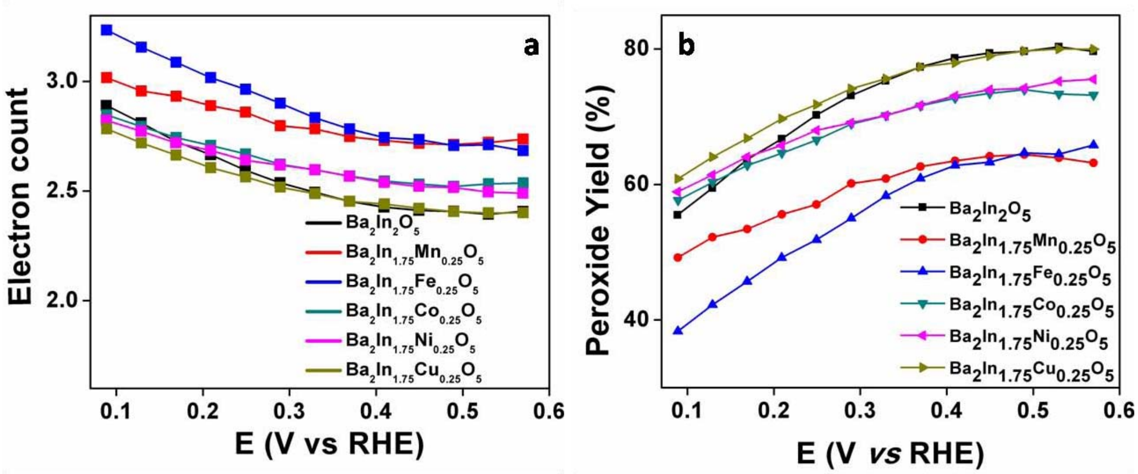

Figure 3A.9: Dependence of a) electron transfer number and b) peroxide yield on the applied potential, calculated from the RRDE data at 1600 rpm in O_2 saturated 0.1M KOH solution

3A.3.2.2. OER Activity in Alkaline Medium

OER activity is monitored with N_2 saturated 0.1M KOH. Figure 3A.10a represents the OER LSV recorded with 10mV/s scan rate and 1600rpm rotation speed of the working electrode. Better onset potentials and current response is obtained for

$Ba_2In_{1.75}Co_{0.25}O_{5\pm\delta}$ followed by the $Ba_2In_2O_{5\pm\delta}$. Comparison of the current response is plotted at 1.6V *vs* RHE represented in the inset of the figure. The compound $Ba_2In_{1.75}Co_{0.25}O_5$ exhibited predominantly higher current response in comparison with the other materials. The order of the response is $Ba_2In_{1.75}Co_{0.25}O_{5\pm\delta}$ > $Ba_2In_2O_{5\pm\delta}$ > $Ba_2In_{1.75}Cu_{0.25}O_{5\pm\delta}$ > $Ba_2In_{1.75}Fe_{0.25}O_{5\pm\delta}$ ~$Ba_2In_{1.75}Mn_{0.25}O_{5\pm\delta}$ ~$Ba_2In_{1.75}Ni_{0.25}O_{5\pm\delta}$.

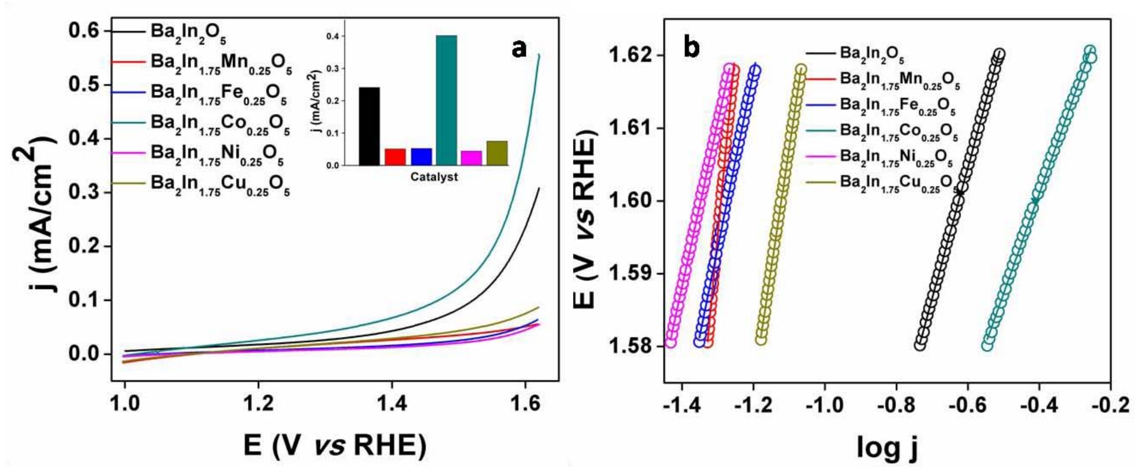

Figure 3A.10: a) OER linear sweep voltammogram recorded at 1600 rpm rotation speed, with 10mV/s scan rate in N_2 saturated 0.1M KOH, the inset image compares the current response at V *vs* RHE b) OER Tafel plots calculated from LSV data at 1600rpm rotation speed

OER Tafel calculations are also performed to understand about the kinetics of the reaction. Slope values obtained range from 399mV/d for $Ba_2In_{1.75}Mn_{0.25}O_{5\pm\delta}$ to 41mV/d for $Ba_2In_2O_{5\pm\delta}$ indicating the different rate determining steps in the reaction. High Tafel slopes of the range ~300mV/d are already reported for some perovskite related oxides at high pH[39]. The trend in slope values are in the order $Ba_2In_2O_{5\pm\delta}$ (41mV/d) < $Ba_2In_{1.75}Ni_{0.25}O_{5\pm\delta}$ (74mV/d) < $Ba_2In_{1.75}Co_{0.25}O_{5\pm\delta}$ (79mV/d) < $Ba_2In_{1.75}Cu_{0.25}O_{5\pm\delta}$ (130mV/d) < $Ba_2In_{1.75}Fe_{0.25}O_{5\pm\delta}$ (148mV/d) < $Ba_2In_{1.75}Mn_{0.25}O_{5\pm\delta}$ (399mV/d). The rate determining step in the parent compound is the surface migration after the second electron transfer reaction as suggested by De Faria et al explained in the annexure[40]. There observed a transition of *rds* from the first electron transfer to surface migration with Ni and Co dopants indicating better catalytic performance by the materials. In Cu and Fe doped materials, the *rds* is the first electron transfer.

Considering ORR and OER activities, on introducing the transition metal into the lattice there is no considerable improvement in the bifunctional activity, except Co which showed a marginal improvement in OER activity. Co doping resulted in better performance, however the parent material supersedes in performance in terms of better ORR and OER Tafel slope. The electron transfer number is lower for $Ba_2In_2O_{5\pm\delta}$ and better for Fe doped variety. OER current response is comparable in $Ba_2In_2O_{5\pm\delta}$ and $Ba_2In_{1.75}Co_{0.25}O_{5\pm\delta}$. The better activity of the parent compound can be attributed to the more disordered tetragonal crystal structure making the oxygen vacancies available for the electron transfer process; in contradiction the doped materials formed a perfect orthorhombic brownmillerite structure with ordered oxygen vacant layer.

3A.4. Summary and Conclusion

The brownmillerite compound $Ba_2In_2O_{5\pm\delta}$ and its transition metal doped analogues with stoichiometry $Ba_2In_{1.75}M_{0.25}O_{5\pm\delta}$ are synthesised by solid state reaction at 1300°C. The detailed structural studies by Rietveld refinement suggested that the parent compound crystallised in the highly disordered tetragonal structure and on doping, perfect brownmillerite structure with orthorhombic symmetry is formed. ORR and OER activity monitoring in the alkaline medium showed no clear trend of transition metal doping in the activity. ORR onset potential is comparable in all the compounds, relatively better current response is exhibited by parent material and Cu doped material. The electron transfer number is lowest for the parent material, however it exhibited better mechanism and catalytic activity as evidenced from the ORR and OER Tafel slope values. The probable reason for the better performance of the parent compound can be the highly disordered tetragonal structure with disordered oxygen vacancies. The properties of the transition metal dopants, do not seem to have an overwhelming effect in the catalytic activity.

3A.5. References

1. Jankovic, J.; Wilkinson, D. P.; Hui, R., Proton Conductivity and Stability of $Ba_2In_2O_5$ in Hydrogen Containing Atmospheres. *Journal of The Electrochemical Society* **2011,***158* (1), B61-B68.

2. Shin, J. F.; Hussey, L.; Orera, A.; Slater, P. R., Enhancement of the conductivity of $Ba_2In_2O_5$ through phosphate doping. *Chemical Communications* **2010,***46* (25), 4613-4615.

3. Goodenough, J. B.; Ruiz-Diaz, J. E.; Zhen, Y. S., Oxide-ion conduction in $Ba_2In_2O_5$ and $Ba_3In_2MO_8$ (M=Ce, Hf, or Zr). *Solid State Ionics* **1990,***44* (1), 21-31.

4. Fluri, A.; Gilardi, E.; Karlsson, M.; Roddatis, V.; Bettinelli, M.; Castelli, I. E.; Lippert, T.; Pergolesi, D., Anisotropic Proton and Oxygen Ion Conductivity in Epitaxial $Ba_2In_2O_5$ Thin Films. *The Journal of Physical Chemistry C* **2017,***121* (40), 21797-21805.

5. Kwestroo, W.; van Gerven, H. C. A.; Langereis, C., Compounds in the system BaO - In_2O_3. *Materials Research Bulletin* **1977,***12* (2), 157-160.

6. Zhang, G. B.; Smyth, D. M., Defects and transport of the brownmillerite oxides with high oxygen ion conductivity — $Ba_2In_2O_5$. *Solid State Ionics* **1995,***82* (3), 161-172.

7. Speakman, S. A.; Richardson, J. W.; Mitchell, B. J.; Misture, S. T., In-situ diffraction study of $Ba_2In_2O_5$. *Solid State Ionics* **2002,***149* (3), 247-259.

8. Adler, S. B.; Reimer, J. A.; Baltisberger, J.; Werner, U., Chemical structure and oxygen dynamics in $Ba_2In_2O_5$. *Journal of the American Chemical Society* **1994,***116* (2), 675-681.

9. Prasanna, T. R. S.; Navrotsky, A., Energetics of the oxygen vacancy order-disorder transition in $Ba_2In_2O_5$. *Journal of Materials Research* **1993,***8* (7), 1484-1486.

10. Fisher, C. A. J.; Islam, M. S.; Brook, R. J., A Computer Simulation Investigation of Brownmillerite-Structured $Ba_2In_2O_5$. *Journal of Solid State Chemistry* **1997,***128* (1), 137-141.

11. Lee, Y.-L.; Morgan, D., Ab initio Study of Oxygen-Vacancy Ordering in Oxygen Conducting $Ba_2In_2O_5$. *Meeting Abstracts* **2007,***MA2007-01* (22), 948.

12. Animitsa, I. E.; Kochetova, N. A.; Shaikhlislamova, A. R., Electric and thermogravimetric properties of brownmillerites based on barium oxides. *Russian Journal of Electrochemistry* **2007,***43* (6), 708-713.

13. Niwa, J.; Suehiro, T.; Kishi, K.; Ikeda, S.; Maeda, M., Structure and electrical characteristics of Ce^{4+}-doped $Ba_2In_2O_5$. *Journal of Materials Science* **2003,***38* (18), 3791-3795.

14. Shin, J. F.; Apperley, D. C.; Slater, P. R., Silicon Doping in $Ba_2In_2O_5$: Example of a Beneficial Effect of Silicon Incorporation on Oxide Ion/Proton Conductivity. *Chemistry of Materials* **2010,***22* (21), 5945-5948.

15. Jarry, A.; Joubert, O.; Suard, E.; Zanotti, J. M.; Quarez, E., Location of deuterium sites at operating temperature from neutron diffraction of $BaIn_{0.6}Ti_{0.2}Yb_{0.2}O_{2.6-n}(OH)_{2n}$, an electrolyte for proton-solid oxide fuel cells. *Physical Chemistry Chemical Physics* **2016,** *18* (23), 15751-15759.

16. Yang, C.; Shu, T.; Zhang, H.; Ji, D.; Shou, Z.; Xiong, C.; Yang, S.; Li, G.; Liao, F.; Lin, J., Synthesis, structure and conductivity of $BaIn_{0.8}Mn_{0.2}O_{3-\delta}$. *Solid State Ionics* **2014,** *257*, 42-52.

17. Berastegui, P.; Hull, S.; García-García, F. J.; Eriksson, S. G., The Crystal Structures, Microstructure and Ionic Conductivity of $Ba_2In_2O_5$ and $Ba(In_xZr_{1-x})O_{3-x/2}$. *Journal of Solid State Chemistry* **2002,** *164* (1), 119-130.

18. Rolle, A.; Roussel, P.; Giridharan, N. V.; Suard, E.; Vannier, R.-N., A neutron diffraction study of the oxygen diffusion in molybdenum doped $Ba_2In_2O_5$. *Solid State Ionics* **2008,** *179* (35), 1986-1995.

19. Wang, D.; Zou, Z.; Ye, J., Photocatalytic Water Splitting with the Cr-Doped $Ba_2In_2O_5/In_2O_3$ Composite Oxide Semiconductors. *Chemistry of Materials* **2005,** *17* (12), 3255-3261.

20. Jijil, C. P.; Unni, S. M.; Sreekumar, K.; Devi, R. N., Disordered Brownmillerite $Ba_2InCeO_{5+\delta}$ with Enhanced Oxygen Reduction Activity. *Chemistry of Materials* **2012,** *24* (14), 2823-2828.

21. Jijil, C. P.; Bhange, S. N.; Kurungot, S.; Devi, R. N., Effect of B Site Coordination Environment in the ORR Activity in Disordered Brownmillerites $Ba_2In_{2-x}Ce_xO_{5+\delta}$. *ACS Applied Materials & Interfaces* **2015,** *7* (5), 3041-3049.

22. Jijil, C. P.; Patil, I. M.; Kakade, B.; Devi, R. N., Cobalt-Doped $Ba_2In_2O_5$ Brownmillerites: An Efficient Electrocatalyst for Oxygen Reduction in Alkaline Medium. *ACS Omega* **2018,** *3* (2), 1710-1717.

23. Cuesta, A.; Aranda, M. A. G.; Sanz, J.; de la Torre, Á. G.; Losilla, E. R., Mechanism of stabilization of dicalcium silicate solid solution with aluminium. *Dalton Transactions* **2014,** *43* (5), 2176-2182.

24. Toby, B., EXPGUI, a graphical user interface for GSAS. *Journal of Applied Crystallography* **2001,** *34* (2), 210-213.

25. Guo, D.; Wu, Z.; An, Y.; Li, X.; Guo, X.; Chu, X.; Sun, C.; Lei, M.; Li, L.; Cao, L.; Li, P.; Tang, W., Room temperature ferromagnetism in $(Ga_{1-x}Mn_x)_2O_3$ epitaxial thin films. *Journal of Materials Chemistry C* **2015,** *3* (8), 1830-1834.

26. Si, C.; Zhang, J.; Wang, Y.; Ma, W.; Gao, H.; Lv, L.; Zhang, Z., Nanoporous Platinum/$(Mn,Al)_3O_4$ Nanosheet Nanocomposites with Synergistically Enhanced Ultrahigh Oxygen Reduction Activity and Excellent Methanol Tolerance. *ACS Applied Materials & Interfaces* **2017,***9* (3), 2485-2494.

27. Biesinger, M. C.; Payne, B. P.; Grosvenor, A. P.; Lau, L. W. M.; Gerson, A. R.; Smart, R. S. C., Resolving surface chemical states in XPS analysis of first row transition metals, oxides and hydroxides: Cr, Mn, Fe, Co and Ni. *Applied Surface Science* **2011,***257* (7), 2717-2730.

28. Thundiyil, S.; Kurungot, S.; Devi, R. N., Bifunctional Oxygen Reduction and Evolution Activity in Brownmillerites $Ca_2Fe_{(1-x)}Co_xO_5$. *ACS Omega* **2019,***4* (1), 31-38.

29. Norman, C.; Leach, C., In situ high temperature X-ray photoelectron spectroscopy study of barium strontium iron cobalt oxide. *Journal of Membrane Science* **2011,***382* (1), 158-165.

30. Baird, T.; Campbell, K. C.; Holliman, P. J.; W. Hoyle, R.; Stirling, D.; Williams, B. P.; Morris, M., Characterisation of cobalt–zinc hydroxycarbonates and their products of decomposition. *Journal of Materials Chemistry* **1997,***7* (2), 319-330.

31. Zhou, T.; Cao, Z.; Zhang, P.; Ma, H.; Gao, Z.; Wang, H.; Lu, Y.; He, J.; Zhao, Y., Transition metal ions regulated oxygen evolution reaction performance of Ni-based hydroxides hierarchical nanoarrays. *Scientific Reports* **2017,***7* (1), 46154.

32. Sun, T.; Xu, L.; Yan, Y.; Zakhidov, A. A.; Baughman, R. H.; Chen, J., Ordered Mesoporous Nickel Sphere Arrays for Highly Efficient Electrocatalytic Water Oxidation. *ACS Catalysis* **2016,***6* (3), 1446-1450.

33. Wu, C.-K.; Yin, M.; O'Brien, S.; Koberstein, J. T., Quantitative Analysis of Copper Oxide Nanoparticle Composition and Structure by X-ray Photoelectron Spectroscopy. *Chemistry of Materials* **2006,***18* (25), 6054-6058.

34. Shuai, M.; Liao, L.; Lu, H. B.; Zhang, L.; Li, J. C.; Fu, D. J., Room-temperature ferromagnetism in Cu+implanted ZnO nanowires. *Journal of Physics D: Applied Physics* **2008,***41* (13), 135010.

35. Ge, X.; Sumboja, A.; Wuu, D.; An, T.; Li, B.; Goh, F. W. T.; Hor, T. S. A.; Zong, Y.; Liu, Z., Oxygen Reduction in Alkaline Media: From Mechanisms to Recent Advances of Catalysts. *ACS Catalysis* **2015,***5* (8), 4643-4667.

36. Hu, P.; Song, Y.; Chen, L.; Chen, S., Electrocatalytic activity of alkyne-functionalized AgAu alloy nanoparticles for oxygen reduction in alkaline media. *Nanoscale* **2015,** *7* (21), 9627-9636.

37. Taylor, R. J.; Humffray, A. A., Electrochemical studies on glassy carbon electrodes: II. Oxygen reduction in solutions of high pH (pH>10). *Journal of Electroanalytical Chemistry and Interfacial Electrochemistry* **1975,** *64* (1), 63-84.

38. Zhou, R.; Zheng, Y.; Jaroniec, M.; Qiao, S.-Z., Determination of the Electron Transfer Number for the Oxygen Reduction Reaction: From Theory to Experiment. *ACS Catalysis* **2016,** *6* (7), 4720-4728.

39. Han, B.; Risch, M.; Lee, Y.-L.; Ling, C.; Jia, H.; Shao-Horn, Y., Activity and stability trends of perovskite oxides for oxygen evolution catalysis at neutral pH. *Physical Chemistry Chemical Physics* **2015,** *17* (35), 22576-22580.

40. De Faria, L. A.; Boodts, J. F. C.; Trasatti, S., Electrocatalytic properties of ternary oxide mixtures of composition $Ru_{0.3}Ti_{(0.7-x)}Ce_xO_2$: oxygen evolution from acidic solution. *Journal of Applied Electrochemistry* **1996,** *26* (11), 1195-1199.

Part B

Role of Ce and transition metal co-doping in structure , room temperature bifunctional activity and high temperature conductivity of $Ba_2In_2O_5$

3B.1. Introduction

Cerium doping in $Ba_2In_2O_5$ is reported to enhance high temperature and room temperature electrochemistry of the material[1-4]. Ce(IV) is a well known redox centre and it can withstand local changes in the oxygen concentration, also doping in the In(III) position can disorder the oxygen vacancies in the structure[5, 6]. The change of structure from orthorhombic to tetragonal and finally to perfect cubic structure at increasing concentration of Ce is already reported[1, 2]. The ORR activity is found to improve up to 75% of Ce doping where the tetragonal brownmillerite structure is preserved and with complete B site occupancy led to a cubic perovskite structure with full occupancy of oxygen sites[1].

Since we could not find a clear trend on the bifunctional activity by first row transition metal doping, as detailed in chapter 3A, we have proceeded to dope Ce in B site to incorporate a redox center in the lattice. The metal dopants in chapter 3A is in stable +3 or +2 oxidation states and the aliovalent doping with a redox centre can further alter the oxygen vacancy concentration in the material and in turn improve their catalytic property[7]. In this chapter, Ce and transition metals are co-doped in the lattice at 37.5atom% and 12.5atom% respectively and analysed for any structural changes and consequent effects on bifunctional activity by the materials.

3B.2. Experimental Section

3B.2.1. Synthesis of $Ba_2InCe_{0.75}M_{0.25}O_{5\pm\delta}$ (M = Mn/Fe/Co/Ni/Cu)

$Ba_2In_2O_{5\pm\delta}$ and cerium and transition metal doped varieties with stoichiometry $Ba_2InCe_{0.75}M_{0.5}O_{5\pm\delta}$ (M= Mn/Fe/Co/Ni/Cu) are synthesised by the solid state reaction at 1300°C, of precursors $BaCO_3$ (min. 99%, Sigma Aldrich), $Ce(OH)_4$ (Aldrich), In_2O_3 (99.99%, Aldrich), $MnCO_3$ (99.9%, Alfa Aerser), Fe_2O_3 (99.98%, Sigma Aldrich), $CoCO_3$ (Co-43-47%, Sigma Aldrich), NiO (99%, Alfa Aeser) and CuO (99%, Thomas Baker). The precursors are weighed stoichiometrically and ground well in a mortar and pestle. Decarbonisation is done at 900°C, ground again and made a pellet and fired at 1300°C for 12h.

3B.2.2. Characterisation

Phase purity of the sample is analysed by Philips PXRD as mentioned in chapter 2A. The surface composition and morphology is analysed by SEM-EDS. Surface states of the metals are analysed by XPS, deconvolution of the spectra are done as mentioned in chapter 2A.

3B.2.3. Electrochemical Analysis

Electrochemical analysis is done in 0.1M KOH. The electrode preparation and the scan is done as mentioned in the chapter 2A

3B.3. Results and Discussion

3B.3.1. Synthesis and Structural Characterisation

Phase purity of the synthesised brownmillerite oxides are analysed by PXRD. The material $Ba_2InCe_{0.75}Mn_{0.25}O_{5\pm\delta}$ forms a cubic structure with small concentrations of impurity phases, $BaCeO_3$ and $BaMnO_3$. $Ba_2InCe_{0.75}Fe_{0.25}O_{5\pm\delta}$ matches with tetragonal form of brownmillerite. The materials $Ba_2InCe_{0.75}Co_{0.25}O_{5\pm\delta}$, $Ba_2InCe_{0.75}Ni_{0.25}O_{5\pm\delta}$, and $Ba_2InCe_{0.75}Cu_{0.25}O_{5\pm\delta}$ form cubic perovskite related structure. In the case of Ni and Cu doping, impurity phase of NiO and $Ba_{0.98}Cu_{1.06}O_{2.14}$ (JCPDS file number: 01-082-0726) could be identified.

Detailed structural studies are conducted by Rietveld refinement of XRD patterns. $Ba_2InCe_{0.75}Mn_{0.25}O_{5\pm\delta}$ pattern is refined with cubic form of $Ba_2In_2O_5$ with ICSD collection code: 51682. The cubic form of $Ba_2In_2O_{5\pm\delta}$ exists only at high temperatures[8] with completely disordered oxygen vacancy. Refinement proceeded smoothly to get a good fit after inserting the impurity phases of $BaCeO_3$ and $BaMnO_3$. The structure is a perfect cubic perovskite crystallising in space group Pm-3m, with single crystallographic sites for oxygen and In. In site is stoichiometrically substituted with Ce^{+4} and Mn^{+3}, all the parameters including occupancy are refined and the impurity phases $BaCeO_3$ and $BaMnO_3$ are quantitatively refined to get the individual weight percentage of 0.73% and 0.67% respectively. The refined profile is represented in figure 3B.2. XRD pattern of $Ba_2InCe_{0.75}Fe_{0.25}O_{5\pm\delta}$ is refined with a tetragonal model of $Ba_2In_2O_5$, with collection code 89439 ($Ba_2In_2O_5.xH_2O$). The tetragonal structure is explained in chapter 3A, and the

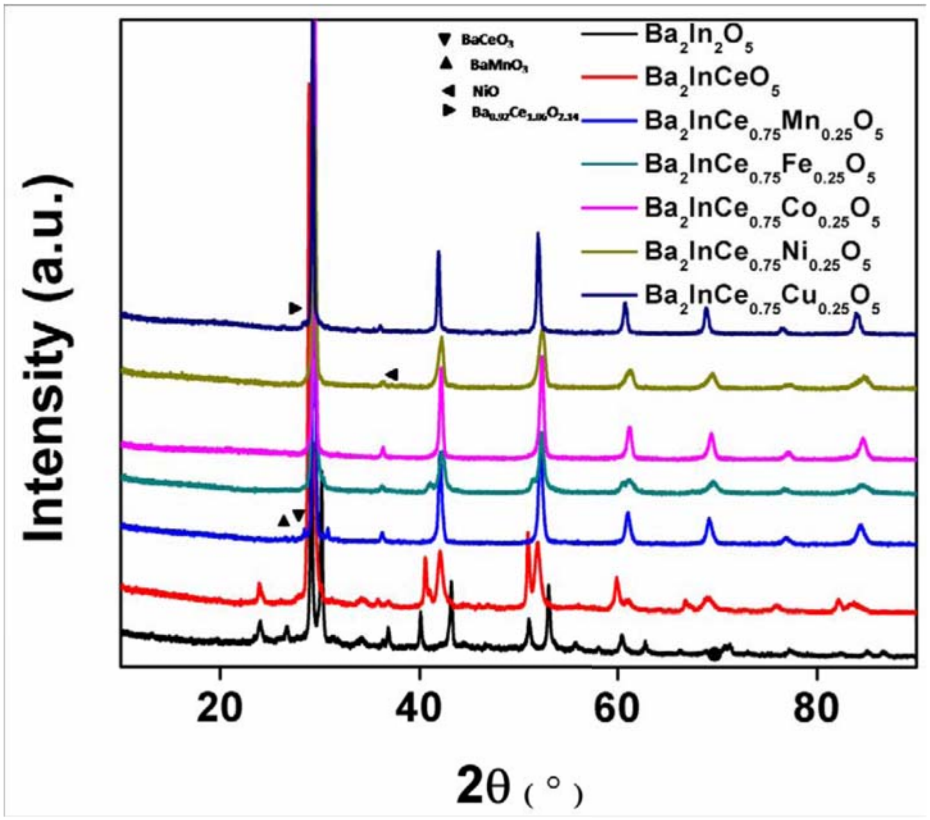

Figure 3B.1: PXRD patterns of the samples with marked impurity phases

refinement proceeded smoothly with the same model to get a good fit. $Ba_2InCe_{0.75}Co_{0.25}O_{5\pm\delta}$, $Ba_2InCe_{0.75}Ni_{0.25}O_{5\pm\delta}$ and $Ba_2InCe_{0.75}Cu_{0.25}O_{5\pm\delta}$ are also refined with the high temperature cubic model mentioned earlier. Impurity phases of NiO and $Ba_{0.92}Cu_{1.06}O_{2.14}$ are inserted for Ni and Cu doped compounds respectively and the impurity phases are quantitatively estimated to be 4% and 8% respectively. Detailed result of Rietveld refinement is tabulated in table 3B.1 and the representative polyhedral representation of unit cell is given in figure 3B.3

Surface composition and morphology is analysed by SEM-EDS technique. The materials are found to be sintered due to synthesis at high temperatures. The SEM images of the materials are represented in figure 3B.3. Surface compositions of all the compounds are tabulated in the table 3B.2, observed surface compositions are in agreement with the calculated weight percentage considering the stoichiometry.

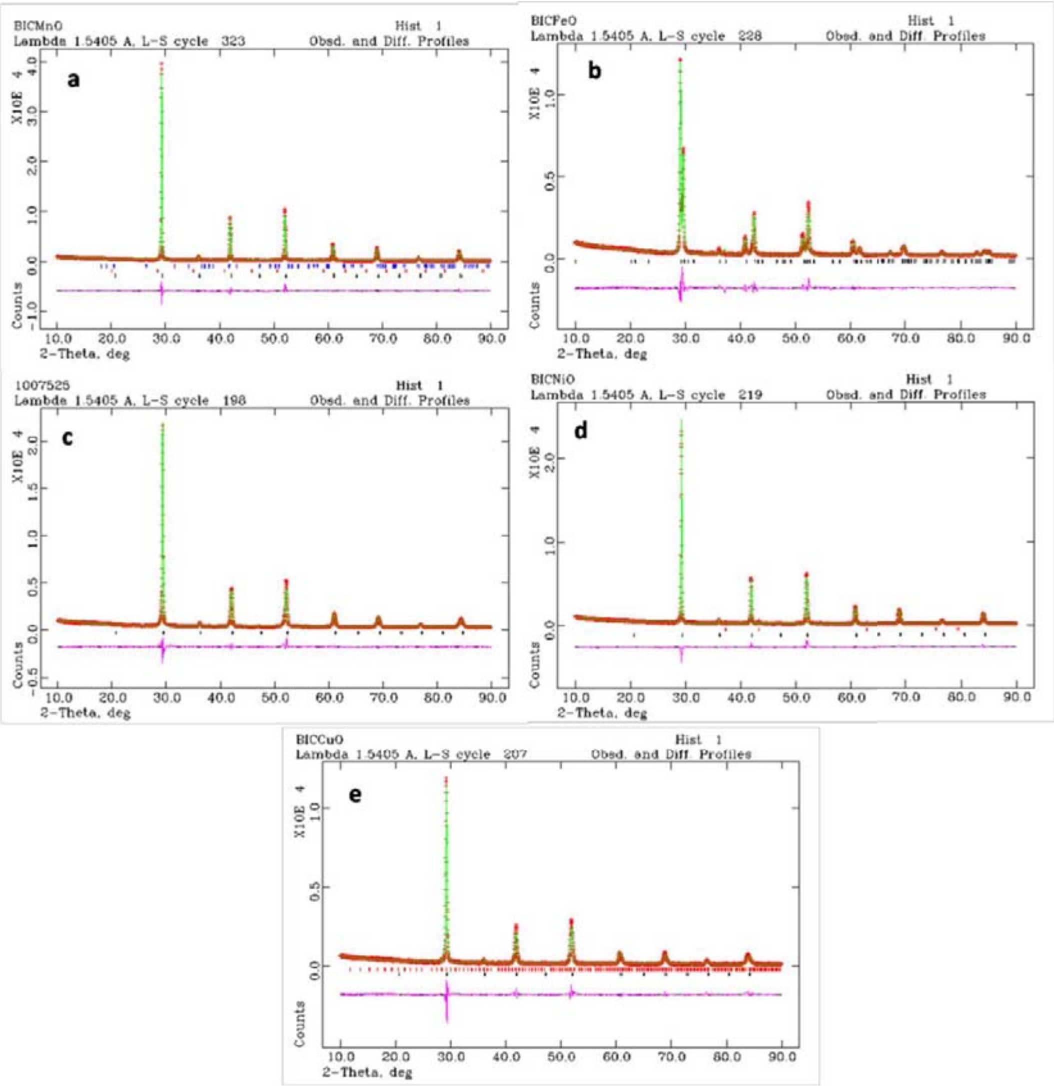

Figure 3B.2: Rietveld refined XRD patterns of a) Ba$_2$InCe$_{0.75}$Mn$_{0.25}$O$_{5\pm\delta}$ b) Ba$_2$InCe$_{0.75}$Fe$_{0.25}$O$_{5\pm\delta}$ c) Ba$_2$InCe$_{0.75}$Co$_{0.25}$O$_{5\pm\delta}$ d) Ba$_2$InCe$_{0.75}$Ni$_{0.25}$O$_{5\pm\delta}$ and e) Ba$_2$InCe$_{0.75}$Mn$_{0.25}$O$_{5\pm\delta}$

Table 3B.1: Rietveld refinement data

Material	Ba$_2$InCe$_{0.75}$Fe$_{0.25}$O$_{5\pm\delta}$	Ba$_2$InCe$_{0.75}$Mn$_{0.25}$O$_{5\pm\delta}$	Ba$_2$InCe$_{0.75}$Co$_{0.25}$O$_{5\pm\delta}$	Ba$_2$InCe$_{0.75}$Ni$_{0.25}$O$_{5\pm\delta}$	Ba$_2$InCe$_{0.75}$Cu$_{0.25}$O$_{5\pm\delta}$
Space group	P4/mmm	Pm-3m	Pm-3m	Pm-3m	Pm-3m
Unitcell parameters	4.2851(3) 8.6783(3)	4.2906(1)	4.2818(6)	4.2987(2)	4.3038(5)

χ^2		4.8	5.6	4.6	3.5	4.0
Rp		11.6	8.3	6.6	6.5	8.9
wRp		14.5	10.5	8.8	8.3	11.2
occupancy	In1	0.4872	0.4954	0.5008	0.4965	0.5043
	Ce1	0.3732	0.3691	0.3776	0.3716	0.3785
	M1	0.1298	0.1171	0.1230	0.1063	0.1227
	O1	1.0000	0.8505	0.8407	0.8741	0.8333

*$Ba_2InCe_{0.75}Fe_{0.25}O_{5\pm\delta}$:Ba1(0,0,0.278733) In1/Ce1/Fe1(0.5,0.5,0.5) In2/Ce2/Fe2(0.5,0.5,0); occupancy In2:0.5261; Ce2:0.3910; Fe2:0.1511; O1(0.5,0.5,0.260995); O2(0,0,0.5) occupancy: 0.9519; O3(0.373814,0,0) Occupancy: 0.5[b] Ba(0.5,0.5.0.5); In1/Ce1/M1(0,0,0); O1(0.5.0.0)

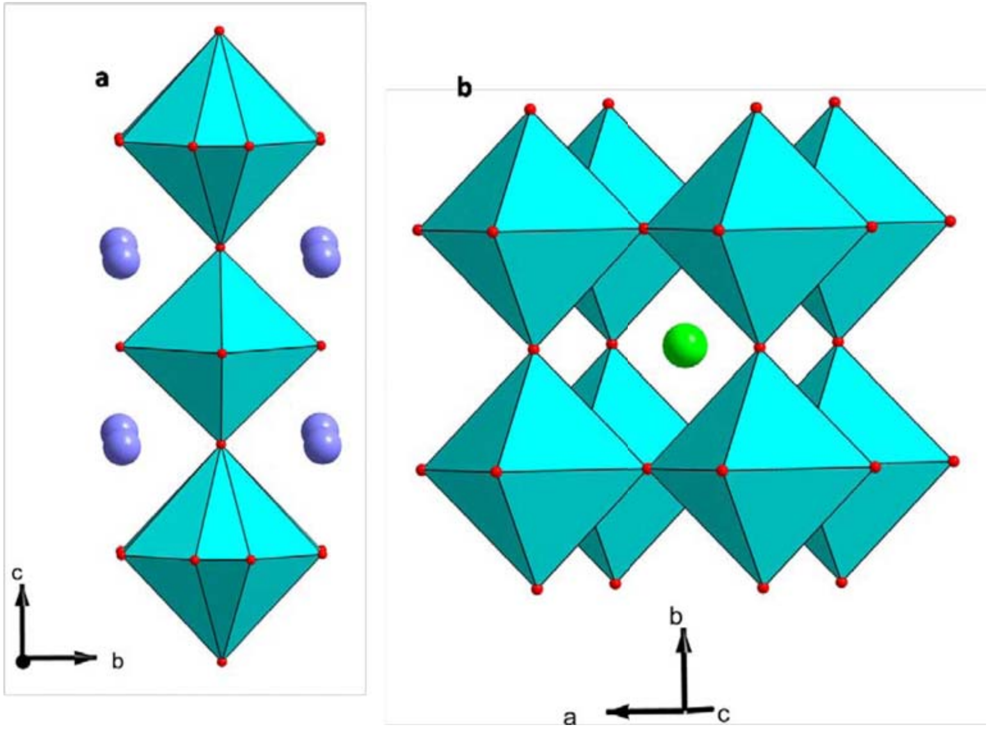

Figure 3B.3: Polyhedral representation of unit cell of a) $Ba_2InCe_{0.75}Fe_{0.25}O_{5\pm\delta}$ crystallised in P4/mmm space group and b) $Ba_2InCe_{0.75}Mn_{0.25}O_{5\pm\delta}$ in Pm-3m space group

Table 3B.2 Surface composition data from EDS analysis

Element	Weight (%)									
	$Ba_2InCe_{0.75}Mn_{0.25}O_{5\pm\delta}$		$Ba_2InCe_{0.75}Fe_{0.25}O_{5\pm\delta}$		$Ba_2InCe_{0.75}Co_{0.25}O_{5\pm\delta}$		$Ba_2InCe_{0.75}Ni_{0.25}O_{5\pm\delta}$		$Ba_2InCe_{0.75}Cu_{0.25}O_{5\pm\delta}$	
	Calculated	Observed	Calculated	Observed	Calculated	Observed	Calculated	Observed	Calculated	Observed
Ba	46.7	49.1	46.7	50.25	46.6	46.2	46.6	49.2	46.5	48.1
In	19.5	15.6	19.5	15.81	19.5	13	19.5	15.7	19.4	16.3
Ce	17.9	18.6	17.9	16.47	17.8	20.2	17.8	18.5	17.8	18.4
M	2.3	2.1	2.4	2.0	2.5	2.3	2.5	2.6	2.7	1.8
O	13.6	14.5	13.6	15.5	13.6	18.3	13.6	14.0	13.6	15.4

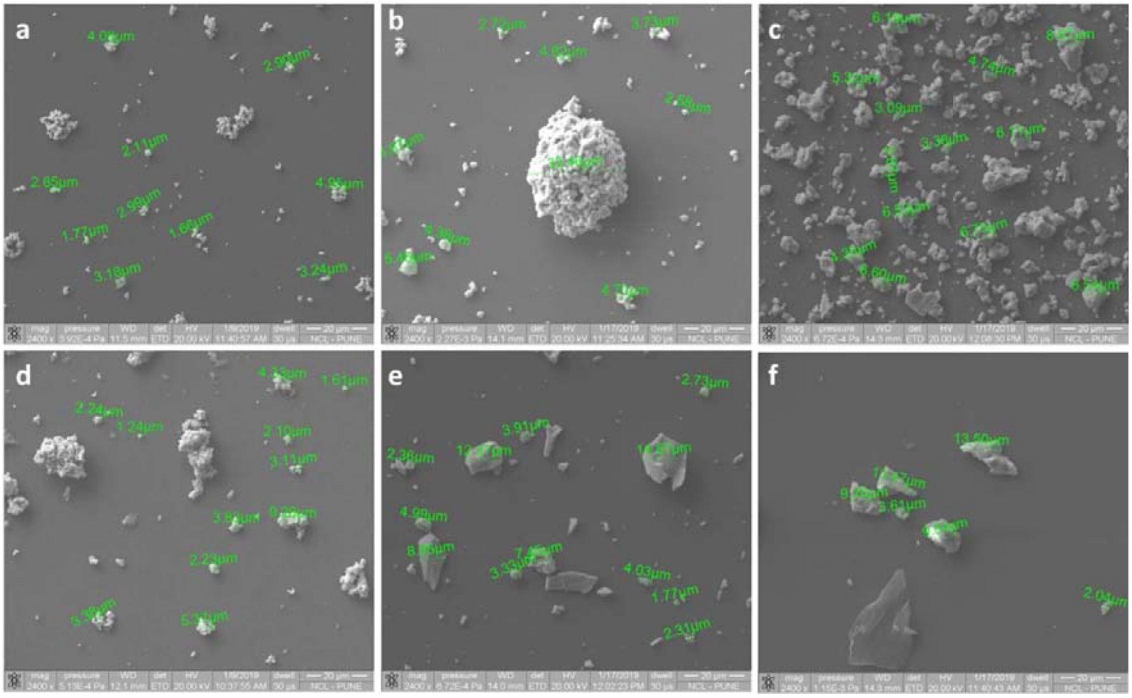

Figure 3B.4: SEM images of a) $Ba_2InCeO_{5\pm\delta}$ b) $Ba_2InCe_{0.75}Mn_{0.25}O_{5\pm\delta}$ c) $Ba_2InCe_{0.75}Fe_{0.25}O_{5\pm\delta}$ d) $Ba_2InCe_{0.75}Co_{0.25}O_{5\pm\delta}$ e) $Ba_2InCe_{0.75}Ni_{0.25}O_{5\pm\delta}$ f) $Ba_2InCe_{0.75}Cu_{0.25}O_{5\pm\delta}$

Surface composition is analysed by XPS analysis. The Ce 3d spectra are deconvoluted with eight peaks namely u, u’, u’’, u’’’, v, v’, v’’, v’’’, among which u’ and v’ are the characteristics of +3 state and u, u’’, u’’’, v, v’’ and v’’’ that of +4 state of Ce[9, 10]. The deconvoluted XP spectra are given in figure 3B.6 and the peak position data is represented in the table 3B.3. We have also calculated the percentage of Ce^{3+} by the equation represented below[11]. The composition data is also incorporated in the table 3B.3. Ce^{3+} concentration is maximum in Ni and Fe doped compound and minimum in the Co containing compound.

$$[Ce^{3+}] = \frac{A_{u'} + A_{v'}}{A_u + A_{u'} + A_{u'}, + A_{u'''} + A_v + A_{v'} + A_{v''} + A_{v'''}}$$

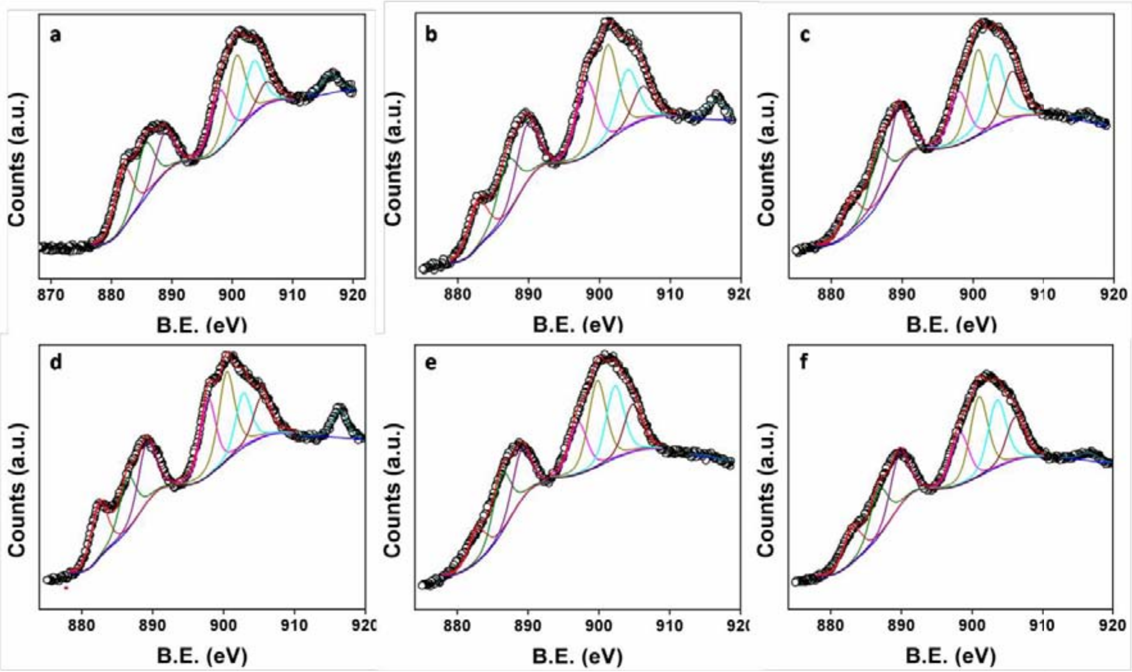

Figure 3B.5: Deconvoluted Ce3d XPS spectra of a) $Ba_2InCeO_{5\pm\delta}$ b) $Ba_2InCe_{0.75}Mn_{0.25}O_{5\pm\delta}$ c) $Ba_2InCe_{0.75}Fe_{0.25}O_{5\pm\delta}$ d) $Ba_2InCe_{0.75}Co_{0.25}O_{5\pm\delta}$ e) $Ba_2InCe_{0.75}Ni_{0.25}O_{5\pm\delta}$ f) $Ba_2InCe_{0.75}Cu_{0.25}O_{5\pm\delta}$

Dopant metal states are analysed by XPS analysis. Figure 3B.7 represents the deconvoluted 2p XPS of the dopant metals. Mn2p spectrum is fitted with a single peak at 642.2eV for $2p_{1/2}$ and at 653.5eV for $2p_{3/2}$ confirming the presence of Mn in +3 state only[12]. The coupling constant between $2p_{3/2}$ and $2p_{1/2}$ is ~12eV[13-15]. Fe2p XP spectrum is deconvoluted as explained in the previous chapters[13, 16]. Peaks corresponding to Co2p

Table 3B.3: Ce3d deconvoluted peak details and Ce^{3+} concentration calculated from the data

Material	Peak positions (eV)								$[Ce^{3+}]$
	v	v'	v''	v'''	u	u'	u''	u'''	
$Ba_2InCeO_{5\pm\delta}$	882	885.6	888.8	897.9	900.7	903.6	905.6	916.2	28
$Ba_2InCe_{0.75}Mn_{0.25}O_{5\pm\delta}$	882.8	887	889.7	898	901	903.9	906	916.5	25.8
$Ba_2InCe_{0.75}Fe_{0.25}O_{5\pm\delta}$	882.8	886.7	889.5	897.9	900.7	903	905.5	916.3	31.5
$Ba_2InCe_{0.75}Co_{0.25}O_{5\pm\delta}$	882.5	886	889	897.8	900.4	902.8	905.3	916.3	23.3
$Ba_2InCe_{0.75}Ni_{0.25}O_{5\pm\delta}$	882.8	886.3	889	897	899.8	902.3	904.8	915	32.3
$Ba_2InCe_{0.75}Cu_{0.25}O_{5\pm\delta}$	883	886.8	889.7	898.3	900.9	903.5	906	916.6	29.7

and Ba3d states overlaps in the same binding energy region, yet individual peaks are identified by deconvolution. Analysis of the spectrum reveals the presence of Co in +3 oxidation state only.[13, 16-19]. Ni2p spectrum is deconvoluted with a peak at 854 eV and an intense satellite peak at 6eV higher, confirming the Ni(II) surface state[20, 21]. $Cu2p_{3/2}$ region is fitted with peak at 933.8eV and a strong satellite peak at 942eV, characteristics of d^9 system confirming the Cu(II) state[22, 23].

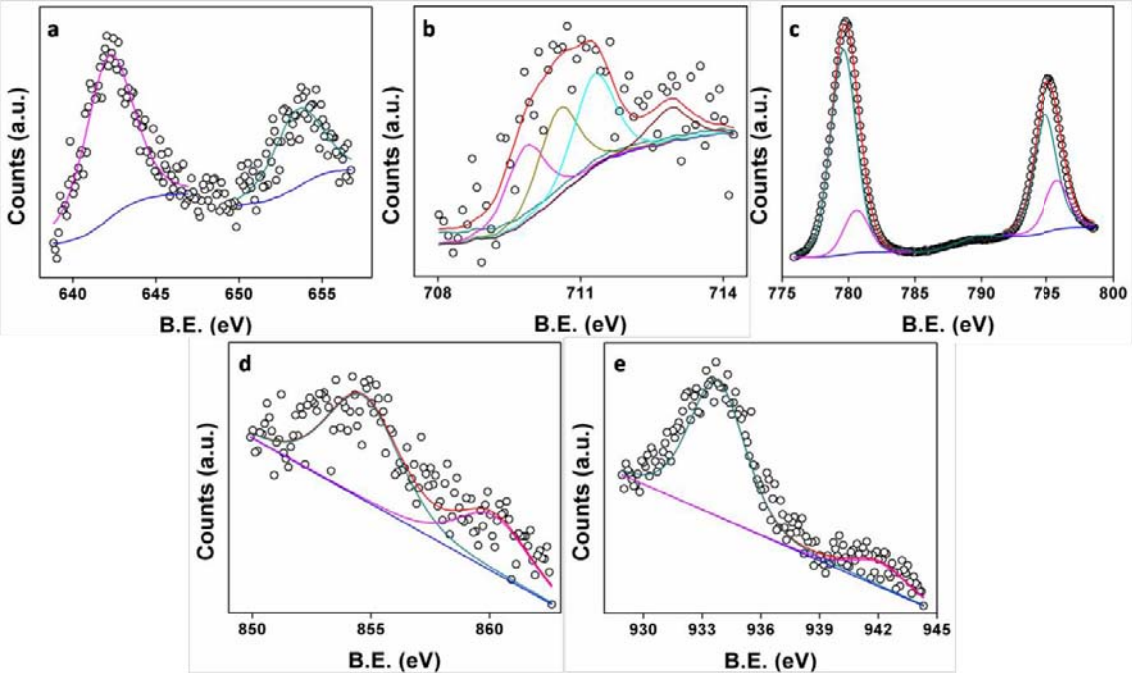

Figure 3B.6: Deconvoluted a) Mn2p XPS of Ba$_2$InCe$_{0.75}$Mn$_{0.25}$O$_{5\pm\delta}$ b) Fe2p XPS Ba$_2$InCe$_{0.75}$Fe$_{0.25}$O$_{5\pm\delta}$ c) Co2p XPS of Ba$_2$InCe$_{0.75}$Co$_{0.25}$O$_{5\pm\delta}$ d) Ni2p XPS of Ba$_2$InCe$_{0.75}$Ni$_{0.25}$O$_{5\pm\delta}$ e) Co2p XPS of Ba$_2$InCe$_{0.75}$Cu$_{0.25}$O$_{5\pm\delta}$

3B.3.2. Electrochemical Characterisation

Detailed electrochemical studies of these compounds are carried out by CV and RDE method under alkaline medium at room temperature

3B.3.2.1. ORR activity in Alkaline Medium

Room temperature ORR analysis is conducted by CV and LSV analysis. Combined cyclic voltammogram of the materials, recorded at 900rpm rotation speed and 50mV/s scan rate is represented in figure 3B.8a. The dotted pattern represents the scan in N_2 saturation and the solid pattern at O_2 saturation. A clear reduction peak is exhibited by all the materials in the O_2 saturation. Detailed monitoring of the reduction region is carried out by LSV analysis. Comparison of linear sweep voltammograms of the samples at 1600rpm and 10mV/s scan rate in O_2 saturated solution is represented in the figure 3B.8b. The data represented is corrected with blank run in N_2 saturation with 0rpm before plotting. The materials exhibited only slight variations in onset potential. The inset represents the onset region to get a clear idea on the trend of onset values.

$Ba_2InCe_{0.75}Co_{0.25}O_{5\pm\delta}$ exhibited a better onset value in comparison with the rest of the materials (~0.78V *vs* RHE) followed by $Ba_2InCe_{0.75}Mn_{0.25}O_{5\pm\delta}$ (0.76V *vs* RHE), and $Ba_2InCe_{0.75}Fe_{0.25}O_{5\pm\delta}$ (~0.74 V *vs* RHE), the compounds $Ba_2InCe_{0.75}Ni_{0.25}O_{5\pm\delta}$, $Ba_2InCe_{0.75}Co_{0.25}O_{5\pm\delta}$, and $Ba_2In_2O_{5\pm\delta}$ exhibited almost same value for onset (0.73V *vs* RHE). The current response is also found to be better for $Ba_2InCe_{0.75}Co_{0.25}O_{5\pm\delta}$ followed by $Ba_2InCe_{0.75}Ni_{0.25}O_{5\pm\delta}$ and $Ba_2InCe_{0.75}Cu_{0.25}O_{5\pm\delta}$. Individual LSVs of the samples are represented in figure 3B.9.

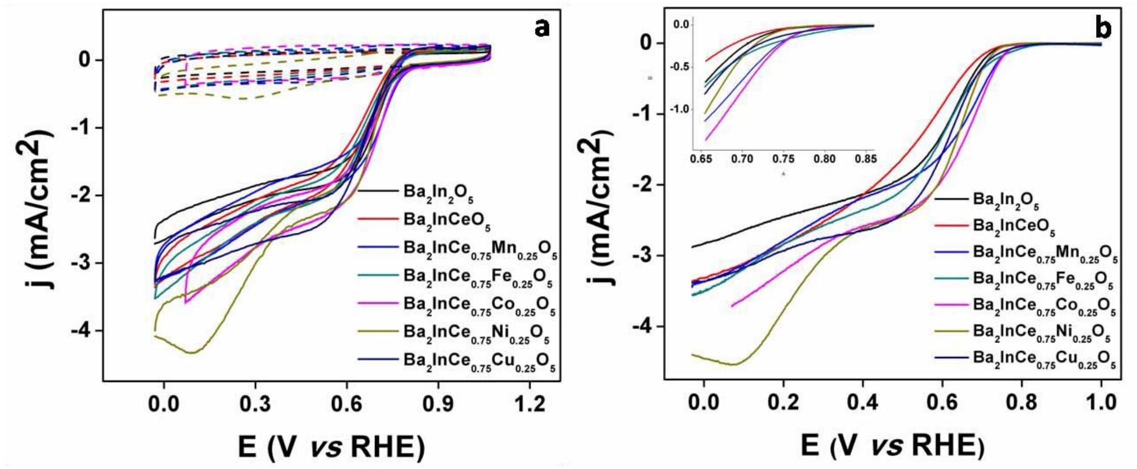

Figure 3B.7: a)Cyclic voltammogram of the samples recorded with 900rpm rotation speed and 50mV/s scan rate, the dotted line represents the scan in N_2 saturation and the solid line is one in the O_2 saturation b) Comparison of linear sweep voltammogram of the samples at 1600 rpm and 10mV/s scan rate in O_2 saturation

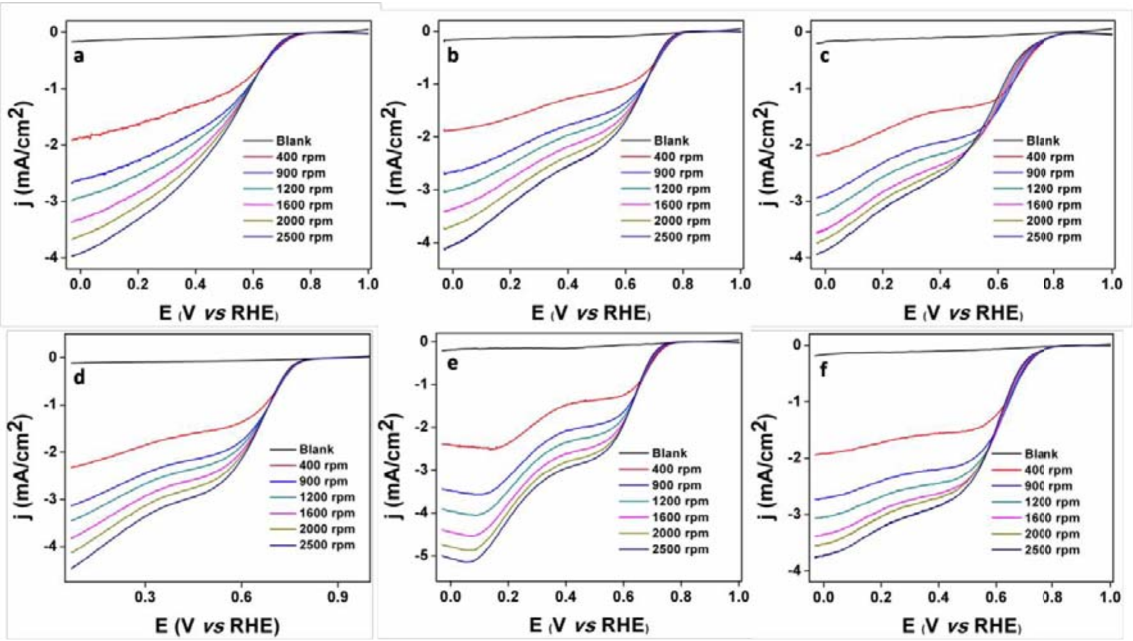

Figure 3B.8: Linear sweep voltammograms at various rotation speeds of a) $Ba_2InCeO_{5\pm\delta}$ b) $Ba_2InCe_{0.75}Mn_{0.25}O_{5\pm\delta}$ c) $Ba_2InCe_{0.75}Fe_{0.25}O_{5\pm\delta}$ d) $Ba_2InCe_{0.75}Co_{0.25}O_{5\pm\delta}$ e) $Ba_2InCe_{0.75}Ni_{0.25}O_{5\pm\delta}$ f) $Ba_2InCe_{0.75}Co_{0.25}O_{5\pm\delta}$ blank run is performed with N_2 saturation and 0rpm rotation speed.

Detailed analysis of ORR Kinetics is conducted by K-L and Tafel analysis. K-L calculations have been carried out using the equation[24] given in annexure. Calculation of electron transfer number from slope values indicates that these materials follow multiple electron transfer steps. Figure 3b represents the Tafel plot; the parent brownmillerite exhibited a slope value of -131 mV/d, indicating the first electron transfer as the rate determining step. $Ba_2InCe_{0.75}Mn_{0.25}O_{5\pm\delta}$ (-143 mV/d) and $Ba_2InCe_{0.75}Co_{0.25}O_{5\pm\delta}$ (-140 mV/d) exhibited similar slope behavior indicating the same *rds* as with the parent material. The slope values obtained for $Ba_2InCeO_{5\pm\delta}$ (-233 mV/d), $Ba_2InCe_{0.75}Cu_{0.25}O_{5\pm\delta}$ (-193 mV/d) and $Ba_2InCe_{0.75}Fe_{0.25}O_{5\pm\delta}$ (-212 mV/d) are relatively higher than the usual slope values observed for active metal oxides. Lowest slope value is shown by $Ba_2InCe_{0.75}Ni_{0.25}O_{5\pm\delta}$ (-100 mV/d) suggesting a transition of *rds* from first electron transfer to the surface migration of the reduced species[25]. The detailed mechanism is explained in annexure.

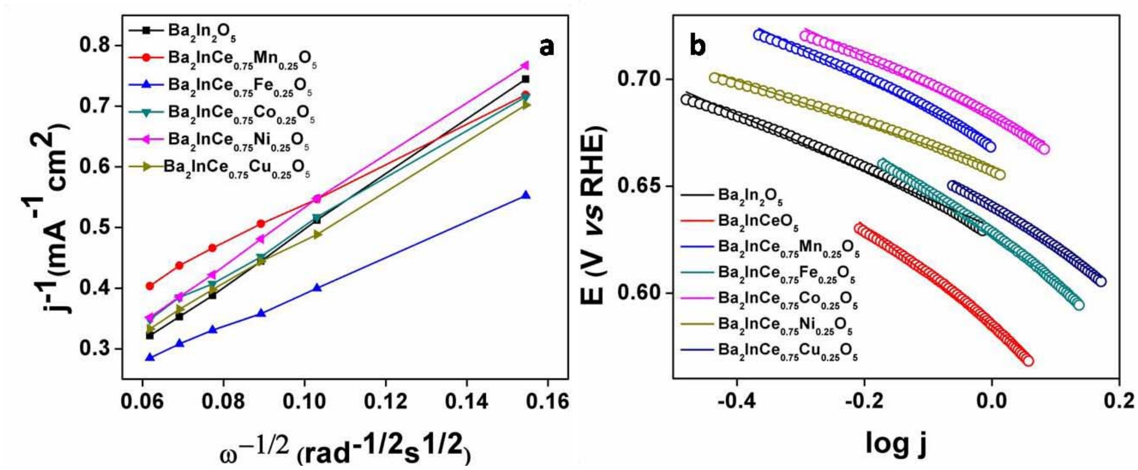

Figure 3B.9: a) Koutechy-Levich plot, calculated from LSV data in various rotation speeds at 0.13V *vs* RHE, solid symbols represents calculated data and the line represent the linear fit of the data b) Tafel plot calculated from LSV data at 1600rpm, empty circles represents the data and the solid line is the linear fit of the data.

Experimental data on the electron transfer behaviour and peroxide yield is obtained from RRDE experiments. Figure 3B.11a shows the electron transfer number dependence on applied potential. Analysis of the data confirms that the materials follow an intermediate electron transfer process and the mechanism can be indirect 2+2 pathway. Ni doped material showed a relatively better electron transfer process and the electron transfer number reaches 3.2 at higher potentials. All the transition metal doped materials exhibited better electron transfer performance than the parent brownmillerite, while with Co doping, the mechanism is found to be similar to that of parent brownmillerite. The peroxide yield with potential is represented in figure 3B.11b, as the potential increased, the peroxide yield is reduced, and the lowest value is obtained for Ni doped material (~39%).

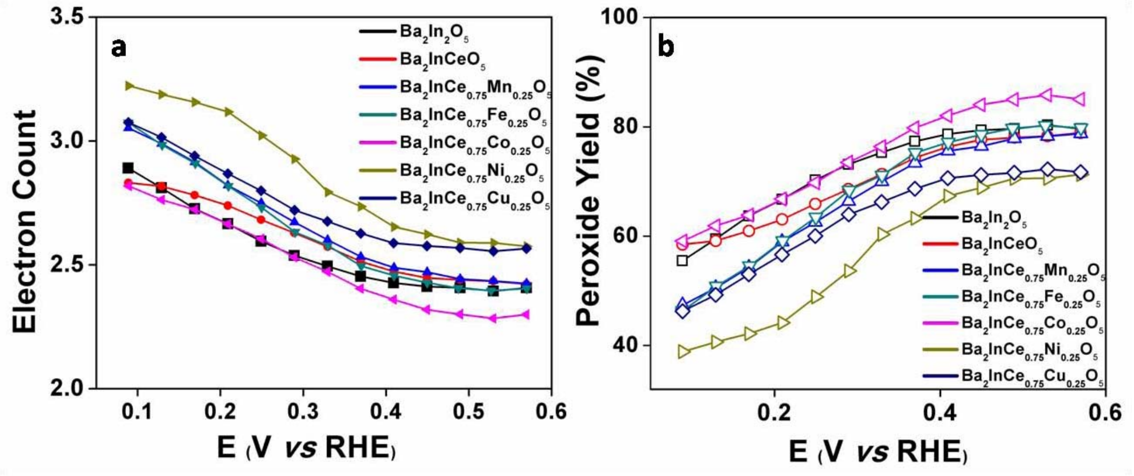

Figure 3B.10: Dependence of a) electron transfer number and b) peroxide yield to the applied potential calculated from RRDE data at 1600rpm in O_2 saturation.

3B.3.2.2. OER Activity in Alkaline Medium

OER activity is monitored in 0.1M KOH with N_2 saturation. Figure 3B.12a represents the LSV data at 1600 rpm and 10mV/s scan rate. Materials exhibit poor OER performance in the applied potential range and onset value of all the materials are almost same. Comparison of current density at 1.6V *vs* RHE gives a clear idea on the trend as $Ba_2InCe_{0.75}Fe_{0.25}O_{5\pm\delta}$ > $Ba_2InCe_{0.75}Ni_{0.25}O_{5\pm\delta}$ > $Ba_2InCeO_{5\pm\delta}$ > $Ba_2In_2O_{5\pm\delta}$ > $Ba_2InCe_{0.75}Cu_{0.25}O_{5\pm\delta}$ > $Ba_2InCe_{0.75}Co_{0.25}O_{5\pm\delta}$ > $Ba_2InCe_{0.75}Mn_{0.25}O_{5\pm\delta}$. Rate determining step in the electron transfer process is analysed by Tafel analysis. Figure 3B.12B shows the Tafel plot calculated from the LSV data, the trend observed is $Ba_2InCe_{0.75}Co_{0.25}O_{5\pm\delta}$ (114mV/d) < $Ba_2InCe_{0.75}Mn_{0.25}O_{5\pm\delta}$ (160mV/d) < $Ba_2InCe_{0.75}Fe_{0.25}O_{5\pm\delta}$ (168mV/d) < $Ba_2InCe_{0.75}Ni_{0.25}O_{5\pm\delta}$ (180mV/d) < $Ba_2InCe_{0.75}Cu_{0.25}O_{5\pm\delta}$ (185mV/d) < $Ba_2In_2O_{5\pm\delta}$ (190mV/d) < $Ba_2InCeO_{5\pm\delta}$ (192mV/d) indicating that transition metal incorporation plays an important role in the electron transfer process[26].

Transition metal and Cerium co-doping in $Ba_2In_2O_{5\pm\delta}$ improved ORR and OER activity to a small extent. Ce and transition metal co-doping improved the onset and current response in room temperature ORR and OER. ORR current response and onset values are better for Co and Mn doped material, they also exhibit better Tafel slope values in comparison to the other materials, however electron transfer pathway is observed to be near 2 electron mechanism in Co based material and Ni showed near 4 electron mechanism. OER current response is better for Fe doped material, however the mechanism analysed by OER Tafel slopes, indicate Mn and Co based materials are superior in the electron transfer process.

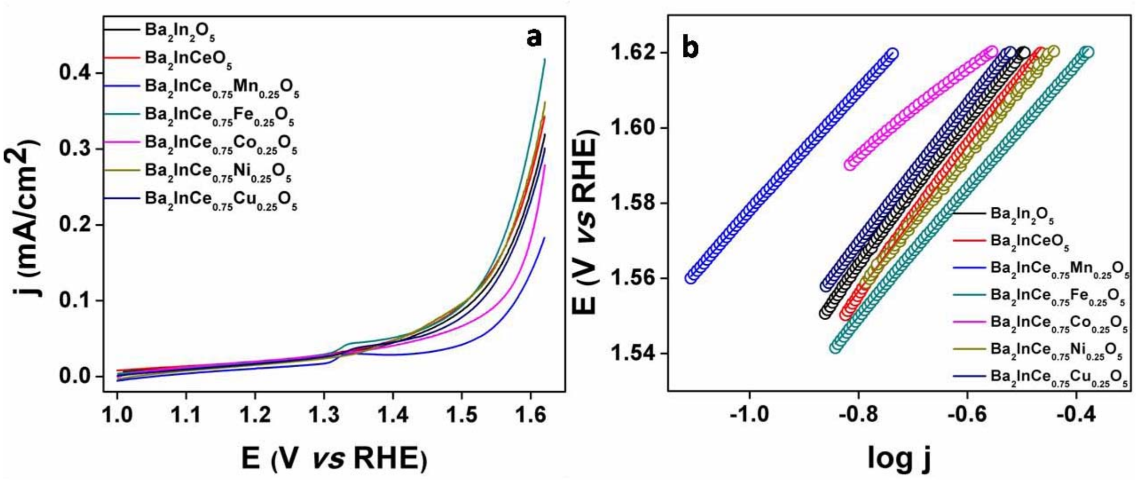

Figure 3B.11: a) OER LSV collected with 1600 rpm rotation speed and scan rate 10mV/s in N_2 saturation b) OER Tafel plot calculated from the LSV data, the empty circles represents the calculated data and the line represents the linear fit of the data

3B.5. Summary and Conclusion

Transition metal and Cerium co-doped brownmillerite oxides are synthesised at 1300°C. Detailed structural studies show that with Fe doping a disordered tetragonal structure and with rest of the elements, a perfect cubic perovskite structure is formed. Cubic structure results from the complete disorder in the oxygen vacancies, which is otherwise observed only in the high temperature phase of $Ba_2In_2O_5$. ORR and OER activity is improved nominally on 12.5% doping of transition metal along with 37.5% Ce, however the bifunctional activity is not comparable to the active transition metal based oxides. Tuning the dopant concentration may further improve the catalytic activity of the materials.

3B.5. References

1. Jijil, C. P.; Bhange, S. N.; Kurungot, S.; Devi, R. N., Effect of B Site Coordination Environment in the ORR Activity in Disordered Brownmillerites $Ba_2In_{2-x}Ce_xO_{5+\delta}$. *ACS Applied Materials & Interfaces* **2015,** *7* (5), 3041-3049.

2. Jijil, C. P.; Unni, S. M.; Sreekumar, K.; Devi, R. N., Disordered Brownmillerite $Ba_2InCeO_{5+\delta}$ with Enhanced Oxygen Reduction Activity. *Chemistry of Materials* **2012,** *24* (14), 2823-2828.

3. Goodenough, J. B.; Ruiz-Diaz, J. E.; Zhen, Y. S., Oxide-ion conduction in $Ba_2In_2O_5$ and $Ba_3In_2MO_8$ (M=Ce, Hf, or Zr). *Solid State Ionics* **1990,** *44* (1), 21-31.

4. Niwa, J.; Suehiro, T.; Kishi, K.; Ikeda, S.; Maeda, M., Structure and electrical characteristics of Ce^{4+}-doped $Ba_2In_2O_5$. *Journal of Materials Science* **2003,** *38* (18), 3791-3795.

5. Mogensen, M.; Sammes, N. M.; Tompsett, G. A., Physical, chemical and electrochemical properties of pure and doped ceria. *Solid State Ionics* **2000,** *129* (1), 63-94.

6. Mueller, D. N.; Machala, M. L.; Bluhm, H.; Chueh, W. C., Redox activity of surface oxygen anions in oxygen-deficient perovskite oxides during electrochemical reactions. *Nature Communications* **2015,** *6* (1), 6097.

7. Cuesta, A.; Aranda, M. A. G.; Sanz, J.; de la Torre, Á. G.; Losilla, E. R., Mechanism of stabilization of dicalcium silicate solid solution with aluminium. *Dalton Transactions* **2014,** *43* (5), 2176-2182.

8. Berastegui, P.; Hull, S.; Eriksson, S. G., Oxygen Disorder and Conductivity in Pyrochlore and Perovskite-Based Compounds. *Materials Science Forum* **2001,** *378-381*, 487-492.

9. Mullins, D. R.; Overbury, S. H.; Huntley, D. R., Electron spectroscopy of single crystal and polycrystalline cerium oxide surfaces. *Surface Science* **1998,** *409* (2), 307-319.

10. Ansari, S. A.; Khan, M. M.; Ansari, M. O.; Kalathil, S.; Lee, J.; Cho, M. H., Band gap engineering of CeO2 nanostructure using an electrochemically active biofilm for visible light applications. *RSC Advances* **2014,** *4* (32), 16782-16791.

11. Meng, F.; Wang, L.; Cui, J., Controllable synthesis and optical properties of nano-CeO_2 via a facile hydrothermal route. *Journal of Alloys and Compounds* **2013,** *556*, 102-108.

12. Biesinger, M. C.; Lau, L. W. M.; Gerson, A. R.; Smart, R. S. C., Resolving surface chemical states in XPS analysis of first row transition metals, oxides and hydroxides: Sc, Ti, V, Cu and Zn. *Applied Surface Science* **2010,** *257* (3), 887-898.

13. Biesinger, M. C.; Payne, B. P.; Grosvenor, A. P.; Lau, L. W. M.; Gerson, A. R.; Smart, R. S. C., Resolving surface chemical states in XPS analysis of first row transition metals, oxides and hydroxides: Cr, Mn, Fe, Co and Ni. *Applied Surface Science* **2011,** *257* (7), 2717-2730.

14. Guo, D.; Wu, Z.; An, Y.; Li, X.; Guo, X.; Chu, X.; Sun, C.; Lei, M.; Li, L.; Cao, L.; Li, P.; Tang, W., Room temperature ferromagnetism in $(Ga_{1-x}Mn_x)_2O_3$ epitaxial thin films. *Journal of Materials Chemistry C* **2015,** *3* (8), 1830-1834.

15. Si, C.; Zhang, J.; Wang, Y.; Ma, W.; Gao, H.; Lv, L.; Zhang, Z., Nanoporous Platinum/$(Mn,Al)_3O_4$ Nanosheet Nanocomposites with Synergistically Enhanced Ultrahigh Oxygen Reduction Activity and Excellent Methanol Tolerance. *ACS Applied Materials & Interfaces* **2017,** *9* (3), 2485-2494.

16. Thundiyil, S.; Kurungot, S.; Devi, R. N., Bifunctional Oxygen Reduction and Evolution Activity in Brownmillerites $Ca_2Fe_{(1-x)}Co_xO_5$. *ACS Omega* **2019,** *4* (1), 31-38.

17. Baird, T.; Campbell, K. C.; Holliman, P. J.; W. Hoyle, R.; Stirling, D.; Williams, B. P.; Morris, M., Characterisation of cobalt–zinc hydroxycarbonates and their products of decomposition. *Journal of Materials Chemistry* **1997,** *7* (2), 319-330.

18. Norman, C.; Leach, C., In situ high temperature X-ray photoelectron spectroscopy study of barium strontium iron cobalt oxide. *Journal of Membrane Science* **2011,** *382* (1), 158-165.

19. Jijil, C. P.; Patil, I. M.; Kakade, B.; Devi, R. N., Cobalt-Doped Ba2In2O5 Brownmillerites: An Efficient Electrocatalyst for Oxygen Reduction in Alkaline Medium. *ACS Omega* **2018,** *3* (2), 1710-1717.

20. Sun, T.; Xu, L.; Yan, Y.; Zakhidov, A. A.; Baughman, R. H.; Chen, J., Ordered Mesoporous Nickel Sphere Arrays for Highly Efficient Electrocatalytic Water Oxidation. *ACS Catalysis* **2016,** *6* (3), 1446-1450.

21. Zhou, T.; Cao, Z.; Zhang, P.; Ma, H.; Gao, Z.; Wang, H.; Lu, Y.; He, J.; Zhao, Y., Transition metal ions regulated oxygen evolution reaction performance of Ni-based hydroxides hierarchical nanoarrays. *Scientific Reports* **2017,** *7* (1), 46154.

22. Shuai, M.; Liao, L.; Lu, H. B.; Zhang, L.; Li, J. C.; Fu, D. J., Room-temperature ferromagnetism in Cu+implanted ZnO nanowires. *Journal of Physics D: Applied Physics* **2008,** *41* (13), 135010.

23. Wu, C.-K.; Yin, M.; O'Brien, S.; Koberstein, J. T., Quantitative Analysis of Copper Oxide Nanoparticle Composition and Structure by X-ray Photoelectron Spectroscopy. *Chemistry of Materials* **2006,** *18* (25), 6054-6058.

24. Taylor, R. J.; Humffray, A. A., Electrochemical studies on glassy carbon electrodes: II. Oxygen reduction in solutions of high pH (pH>10). *Journal of Electroanalytical Chemistry and Interfacial Electrochemistry* **1975,** *64* (1), 63-84.

25. Ge, X.; Sumboja, A.; Wuu, D.; An, T.; Li, B.; Goh, F. W. T.; Hor, T. S. A.; Zong, Y.; Liu, Z., Oxygen Reduction in Alkaline Media: From Mechanisms to Recent Advances of Catalysts. *ACS Catalysis* **2015,** *5* (8), 4643-4667.

26. De Faria, L. A.; Boodts, J. F. C.; Trasatti, S., Electrocatalytic properties of ternary oxide mixtures of composition $Ru_{0.3}Ti_{(0.7-x)}Ce_xO_2$: oxygen evolution from acidic solution. *Journal of Applied Electrochemistry* **1996,** *26* (11), 1195-1199.

Part C

Role of Co and Ce co-doping in the structure and electrochemical properties of $Ba_2In_2O_5$

3C.1. Introduction

Improved activity by co-doping of Ce and first row transition metal is demonstrated in chapter 3B. The activity can be further improved by increasing the doping concentrations in the B site with Ce or transition metal. The role of increased Ce doping in the In site is already well studied for room temperature and high temperature conductivity[1-3].

Ce and Co co-doped $Ba_2In_2O_5$ system exhibited a reasonably better bifunctional activity as observed in chapter 3B. In this chapter we have selected cobalt doping to study the effect of varying doping in the structure and bifunctional property. Role of varying Ce and Co doping separately in the electrochemical ORR activity is already reported[2-4]. Role of Co in improving the B site activity in ORR and OER are also well known[5-7]. The goal of the chapter, hence is to understand the structural changes associated with the varying co-doping concentrations of the metals and synergistic effect of the metals in the overall bifunctional activity.

3C.2. Experimental Section

3C.2.1. Synthesis of $Ba_2In_{2-x+y}Ce_xCo_yO_{5\pm\delta}$

Cerium and cobalt co-doped varieties with stoichiometry $Ba_2In_{2-x+y}Ce_xCo_yO_{5\pm\delta}$ (x = 0.5, 0.75 and y = 0.25, 0.5, 0.75) are synthesised by solid state reaction at 1300°C, from precursors $BaCO_3$ (min. 99.0%, Sigma Aldrich), $Ce(OH)_4$ (Aldrich), In_2O_3 (99.99%, Aldrich) and $CoCO_3$ (Co-43-47%, Sigma Aldrich). The precursors are weighed stoichiometrically and ground well in a mortar and pestle. Decarbonisation is done at 900°C, ground again and made a pellet and fired at 1300°C for 12h.

3C.2.2. Characterisation

Phase purity is analysed with PXRD and the structural studies are conducted by Rietveld refinement of the PXRD patterns as explained in the previous chapters. Surface state is analysed by XPS, morphology and surface composition is analysed by SEM-EDS studies. High temperature phase stability is analysed by PXRD in N_2, O_2, and 5%H_2/Ar atmosphere.

3C.2.3. Electrochemical Analysis

Room temperature ORR and OER monitored in alkaline solution with O_2 and N_2 saturation. The sample preparation method and procedure is explained in the chapter 2A.

High temperature conductivity study of the pellet is performed in CHI400 series instrument in N_2 and O_2 atmospheres. The pellet making procedure and data collection methodology is explained in chapter 2B.

3C.3. Results and Discussion

3C.3.1. Synthesis and Structural Characterisation

Five compositions with stoichiometry $Ba_2In_{(2-x+y)}Ce_xCo_yO_{5\pm\delta,}$ where x =0.25, 0.5, 0.75 and 1 and y =0.25, 0.5, 0.75 is synthesized by solid state reaction of the precursors. Phase purity is analysed by PXRD analysis. Figure 3C.1a displays the PXRD patterns of the sample. Effect of doping is clearly observable from the PXRD patterns. Figure 3C.1b indicates the zoomed image of the PXRD pattern in the 2θ range from 28° to 31°. A clear trend of doping in the lattice is observed from the figure. As Co concentration increased, there is a clear shift of peak towards higher angles and in case of increasing Ce concentration, there is a shift towards lower wavelength. The effect is systematically analysed with compositions by fixing any of the metal dopant concentration. By fixing Ce concentration as in $Ba_2In_{0.75}CeCo_{0.25}O_{5\pm\delta}$ and $Ba_2In_{0.5}CeCo_{0.5}O_{5\pm\delta}$, the peak shifts to higher 2θ as the Co concentration increased. And with fixed Co concentration as in $Ba_2InCe_{0.75}Co_{0.25}O_{5\pm\delta}$ and $Ba_2In_{0.75}CeCo_{0.25}O_{5\pm\delta,}$ as well as $Ba_2InCe_{0.5}Co_{0.5}O_{5\pm\delta}$ and $Ba_2In_{0.5}CeCo_{0.25}O_5$, the peak shifts to lower 2θ value as the Ce concentration increased. The reason of the change in position can be attributed to the lowering of unit cell volume when Co^{+3} increased, on account of the smaller size and increase in the unit cell volume with increasing Ce, due to the larger size of Ce^{+4} in comparison with In^{3+}.

Rietveld refinement of PXRD pattern has been employed to get a detailed structural data. Earlier Rietveld refinement study on the Ce doping in $Ba_2In_2O_5$ suggests that the structure consists of highly disordered oxygen vacancy and the system changes from brownmillerite to perfect cubic perovskite structure with complete disordered oxygen vacancy on increasing Ce[2, 3]. In a separate study on Co doping, the cubic phase is

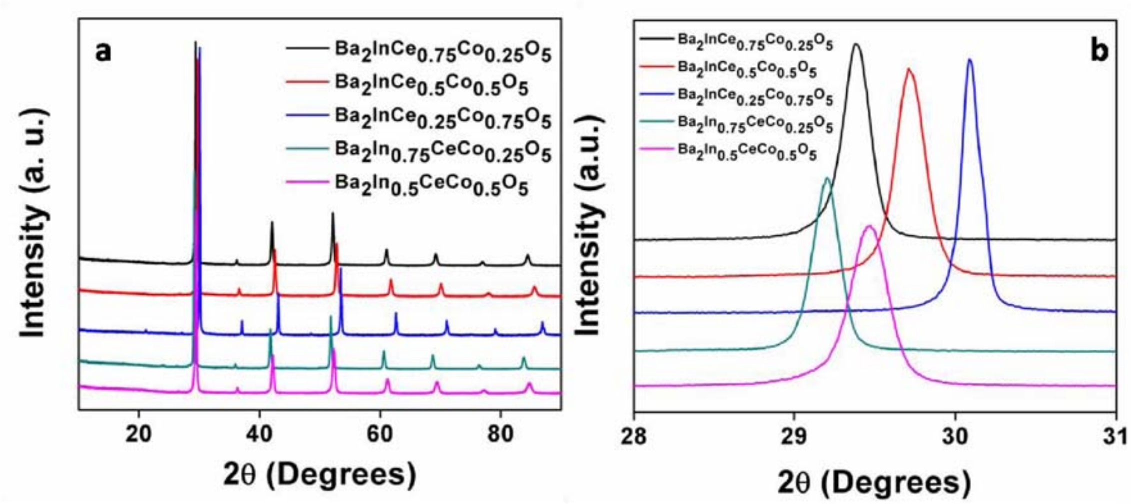

Figure 3C.1: a) PXRD pattern of the samples b) zoomed image of the PXRD pattern to showing the shift in peak position with varying doping.

observed with more than 50% doping in the In position only[4]. Co doped $Ba_2In_{(2-x+y)}Ce_xCo_yO_5$ with x =0.25, 0.5, 0.75 and 1 and y =0.25, 0.5, 0.75 crystallised in cubic Pm-3m space group and refinement proceeded smoothly with a high temperature cubic phase of $Ba_2In_2O_5$ with ICSD collection code 51682[8]. Refinement proceeded smoothly with stoichiometrically substituting In position with Ce and Co. However refinement of the composition $Ba_2InCe_{0.25}Co_{0.75}O_{5\pm\delta}$ was not successful with the same model. Another model with doubling the unit cell parameters are considered for refining the structure. Cubic double perovskite model Ba_2SbTbO_6 crystallising in the Fm3m space group (ICSD collection code 38332) is selected for refining the structure. The structure has two crystallographically different sites for Sb and Tb and refinement proceeded with stoichiometrically changing both the site occupancies with In, Ce and Co equally. The refined profiles are represented in figure 3C.2 and the data is tabulated in table 3C.1.

Polyhedral representation of cubic unit cell is shown in the figure 3C.3. From the structural data, variation of unit cell parameter and volume with dopant concentration is also anlaysed. Figure 3C.4a indicates the relation of unit cell parameter with Ce concentration, the black symbol represents the psuedocubic parameter and red symbols represents cell volume; as the Ce concentration increases, unit cell length and volume also increases on account of the higher size of Ce^{4+} compared to In^{3+}. There is a large difference in the unit cell parameters with the same Ce content (x = 1) and lower or higher Co content. Figure 3C.4b indicates the variation of unit cell parameter with Co

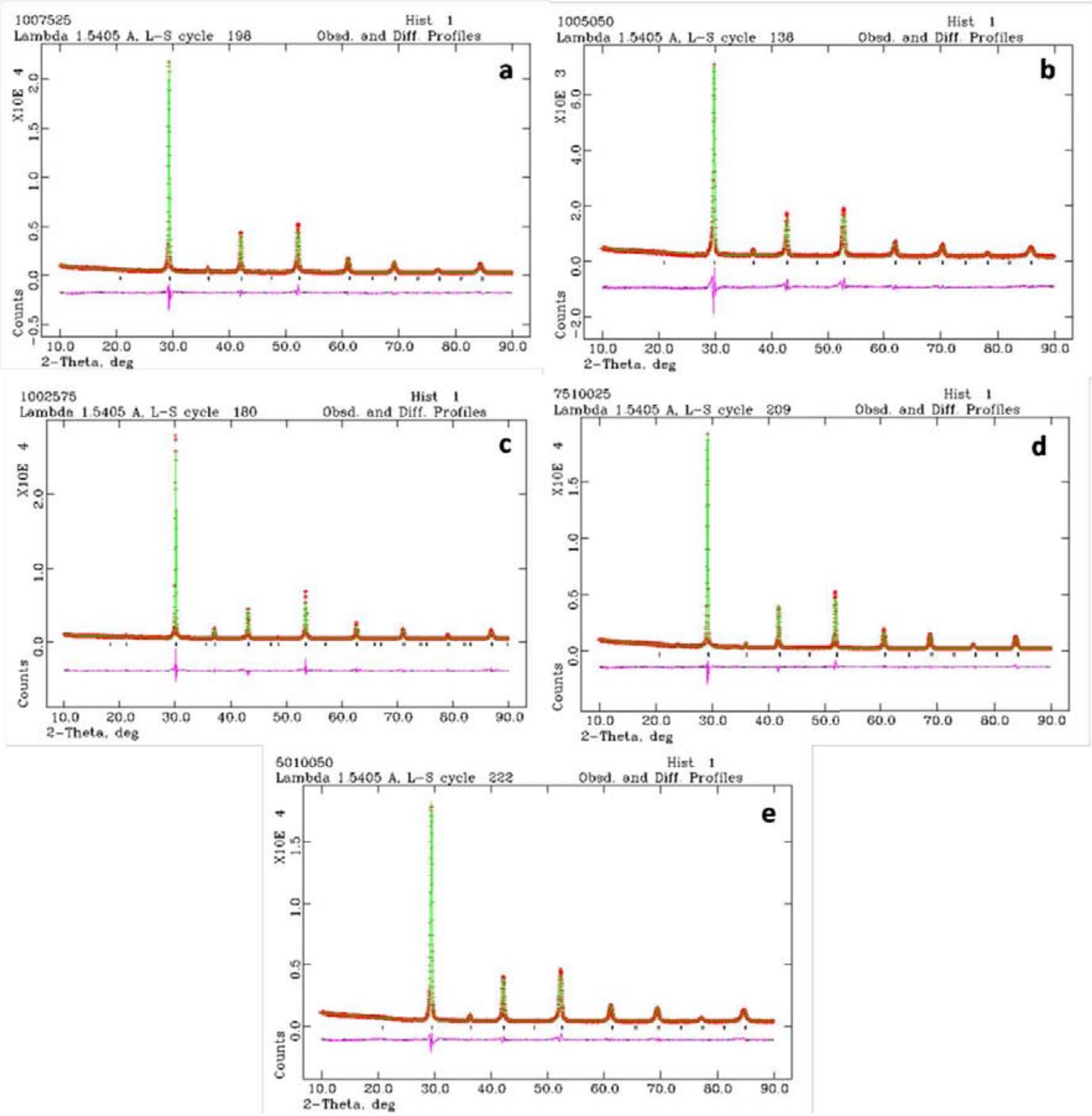

Figure 3C.2: Rietveld refined PXRD patterns of a) Ba$_2$InCe$_{0.75}$Co$_{0.25}$O$_{5\pm\delta}$ b) Ba$_2$InCe$_{0.5}$Co$_{0.5}$O$_{5\pm\delta}$ c) Ba$_2$InCe$_{0.25}$Co$_{0.75}$O$_{5\pm\delta}$ d) Ba$_2$In$_{0.75}$CeCo$_{0.25}$O$_{5\pm\delta}$ e) Ba$_2$In$_{0.5}$CeCo$_{0.25}$O$_{5\pm\delta}$

Table 3C.1: Rietveld refinement data

Material		$Ba_2InCe_{0.75}Co_{0.25}O_{5\pm\delta}$	$Ba_2InCe_{0.5}Co_{0.5}O_{5\pm\delta}$	$Ba_2InCe_{0.25}Co_{0.75}O_{5\pm\delta}$	$Ba_2In_{0.75}CeCo_{0.25}O_{5\pm\delta}$	$Ba_2In_{0.5}CeCo_{0.5}O_{5\pm\delta}$
Space group		Pm-3m	Pm-3m	Fd3m	Pm-3m	Pm-3m
a		4.28181(6)	4.23308(6)	8.38336(4)	4.30494(2)	4.27040(3)
χ^2		4.5	4.4	4.7	4.1	3.2
Rp		6.6	8.8	5.8	6.8	5.3
wRp		8.8	11.8	8	8.8	6.9
Occ.	In	0.5008	0.4962	0.5193 0.5092	0.3741	0.2472
	Ce	0.3776	0.2501	0.1294 0.1240	0.5006	0.4977
	Co	0.1230	0.2443	0.3811 0.3706	0.1158	0.2390
	O	0.8407	0.8617	0.5092	0.8471	0.84200

*Ba(0.5,0.5,0.5) In/Ce/Co(0,0,0) O(0.5,0,0) **$Ba_2InCe_{0.25}Co_{0.75}O_5$: Ba(0.25,0.25,0.25) In1/Ce1/Co1 (0.5,0.5,0.5) In2/Ce2/Co2 (0,0,0) O (0.227943,0,0)

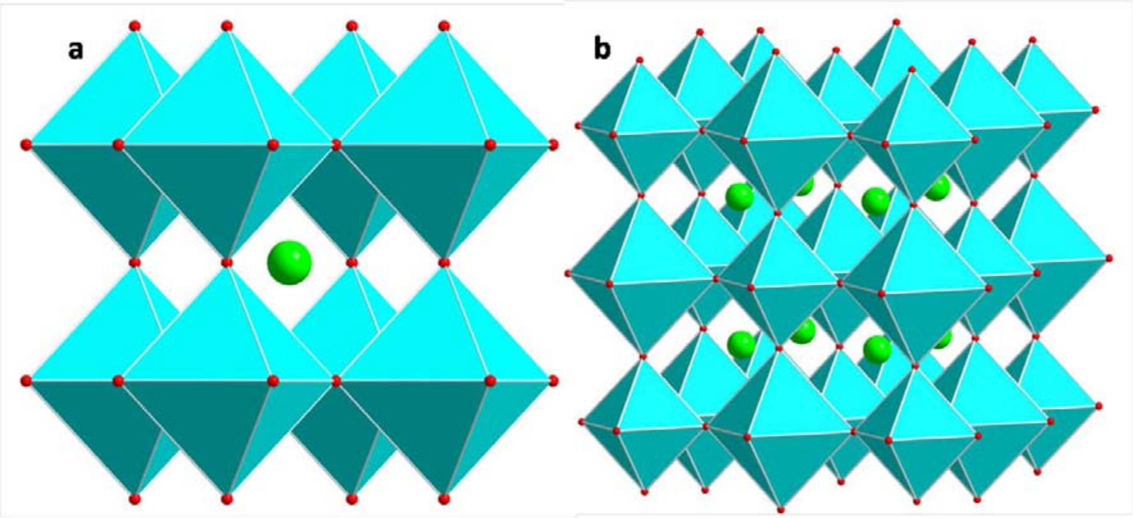

Figure 3C.3: Polyhedral representation of cubic unit cell of a) $Ba_2InCe_{0.75}Co_{0.25}O_{5\pm\delta}$ formed in Pm-3m space group and b) $Ba_2InCe_{0.25}Co_{0.75}O_{5\pm\delta}$ in Fd3m space group

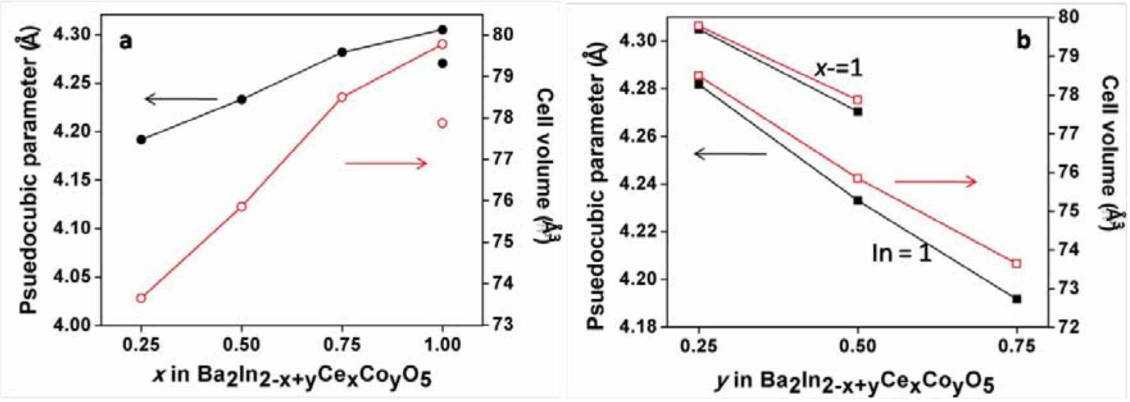

Figure 3C.4: Dependence of pseudo cubic unit cell parameter and cell volume on a) Ce concentration and b) Co concentration

concentration, with fixed In and Ce content separately. As expected unit cell parameters are reduced with increased Co doping due to the small size of Co^{+3}. When In is fixed to be 1, unit cell length and consequently volume is much smaller than when Ce is fixed to be 1. Close analysis of the structure also reveals the effect of doping in the bond lengths, as given in Table 3C.2. The bond lengths are reduced with increasing Co content and increased with increase in Ce content. There are two different O1-O1 distances due to the difference in size of InO_6 octahedra, $In1O_6$ octahedron is larger than the $In2O_6$ octahedron. There is a very small deviation from the ideal bond angle in some of the materials, it is found that the angle reaches the ideal value as the Co concentration increased, and the case is true when the Co is fixed and Ce increased. The structure $Ba_2InCe_{0.25}Co_{0.75}O_{5\pm\delta}$ remains as an exception on account of the crystallization in another space group with different structure.

Table 3C.2: Bond length and angle data from Rietveld refinement

Material	O1-O1 length (Å)	In-O length (Å)	O-In-O angle (°)
$Ba_2InCe_{0.75}Co_{0.25}O_{5\pm\delta}$	4.282	2.141	179.98
$Ba_2InCe_{0.5}Co_{0.5}O_{5\pm\delta}$	4.233	2.117	179.98
$Ba_2In_{0.75}CeCo_{0.25}O_{5\pm\delta}$	4.305	2.152	179.99
$Ba_2In_{0.5}Ce_{0.25}Co_{0.5}O_{5\pm\delta}$	4.27	2.135	180
$Ba_2InCe_{0.25}Co_{0.75}O_{5\pm\delta}$	4.562 (In1) 3.822 (In2)	2.281 (In1-O) 1.911 (In2-O)	179.99

Detailed surface state analysis is performed by XPS analysis. Ce3d XPS is deconvoluted as explained in chapter 3B. Deconvoluted XP spectra are represented in figure 3C.5. The deconvoluted peaks suggest the existence of Ce in both +3 and +4 states[9, 10]. Ce^{3+} concentration is also calculated by the equation given in chapter 3B[11]. For a fixed In concentration, as the Co increased, the Ce^{3+} concentration increases, but with the fixed concentration of Ce and increasing Co or fixed concentration of Co and increasing Ce, the concentration of Ce(III) does not follow any regular trend.

Peaks corresponding to Co2p XPS and Ba3d XPS overlap at the same binding energy. Upon deconvolution, the peaks corresponding to Ba3d and Co2p are separated. The deconvoluted XP spectra are represented in figure 3C.6. Analysis of the same indicates the presence of Co in +3 states only. Absence of satellite peak further confirms the absence of Co^{2+} state[12, 13].

Surface composition is analysed by EDS technique. The data is tabulated in table 3C.4 and is in agreement with the expected stoichiometry. The morphology of the samples are analysed by SEM, indicating sintered micrometer size particles on account of the high temperature synthesis as represented in figure 3C.7.

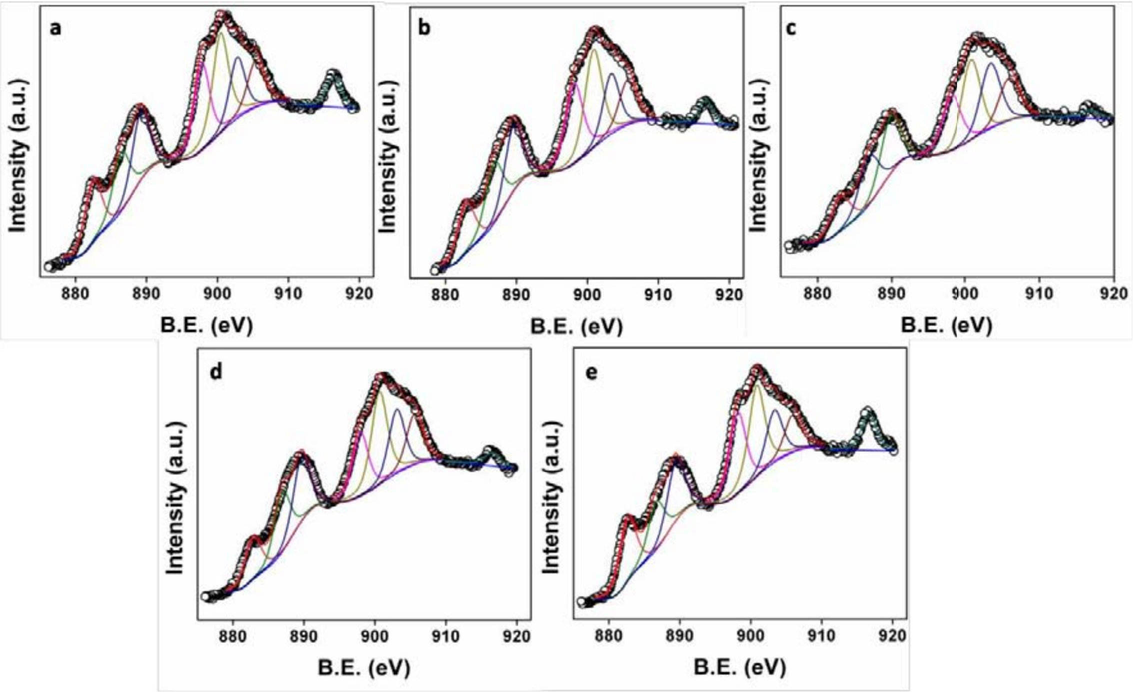

Figure 3C.5: Deconvoluted Ce3d XPS of a) $Ba_2InCe_{0.75}Co_{0.25}O_{5\pm\delta}$ b) $Ba_2InCe_{0.5}Co_{0.5}O_{5\pm\delta}$ c) $Ba_2InCe_{0.25}Co_{0.75}O_{5\pm\delta}$ d) $Ba_2In_{0.75}CeCo_{0.25}O_{5\pm\delta}$ e) $Ba_2In_{0.5}CeCo_{0.5}O_{5\pm\delta}$

Table 3C.3: Ce3d peak data and Ce^{3+} concentration from XPS data

Material	v	v'	v''	v'''	u	u'	u''	u'''	$[Ce^{3+}]$ (%)
$Ba_2InCe_{0.75}Co_{0.25}O_{5\pm\delta}$	882.5	886.4	889.2	897.8	900.4	902.8	905.3	916.3	23.27
$Ba_2InCe_{0.5}Co_{0.5}O_{5\pm\delta}$	882.8	886.8	889.6	898	900.9	903.4	905.6	916.6	24.10
$Ba_2InCe_{0.25}Co_{0.75}O_{5\pm\delta}$	883	886.8	889.8	898	900.8	903.4	905.9	916.8	29.35
$Ba_2In_{0.75}CeCo_{0.25}O_{5\pm\delta}$	882.8	887	889.6	897.9	900.6	903	905.6	916.5	28.48
$Ba_2In_{0.5}CeCo_{0.5}O_{5\pm\delta}$	882.6	886.6	889.3	898	900.8	903.3	905.9	916.7	21.94

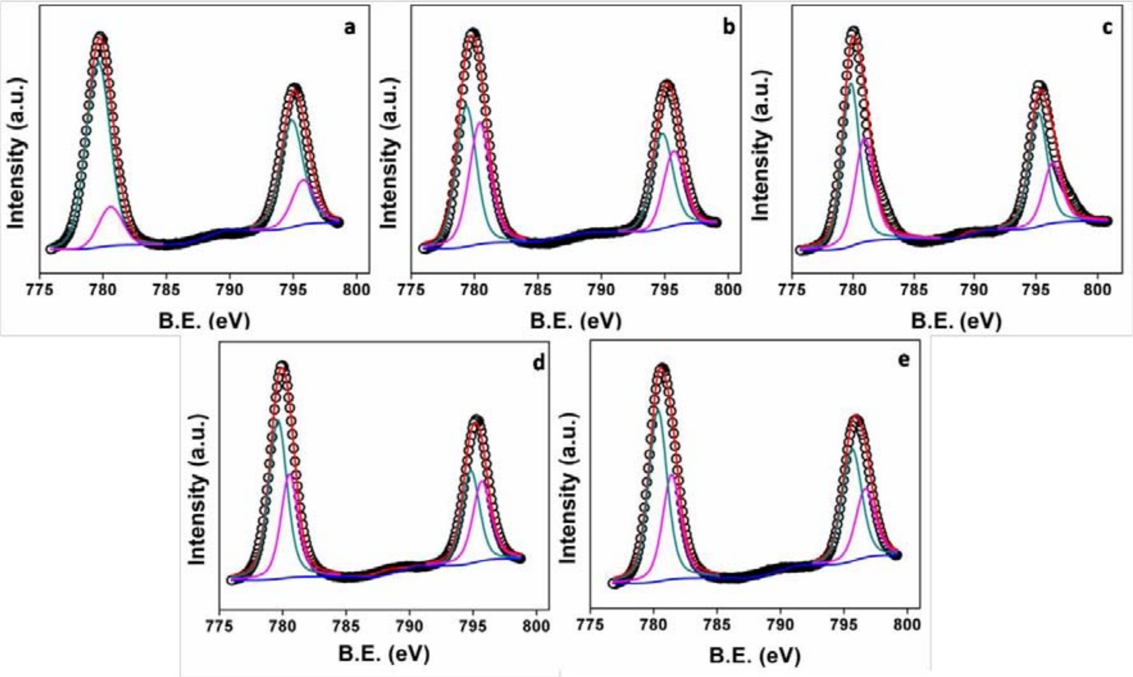

Figure 3C.6: Deconvoluted Co2p (Ba3d) XPS of a) $Ba_2InCe_{0.75}Co_{0.25}O_{5\pm\delta}$ b) $Ba_2InCe_{0.5}Co_{0.5}O_{5\pm\delta}$ c) $Ba_2InCe_{0.25}Co_{0.75}O_{5\pm\delta}$ d) $Ba_2In_{0.75}CeCo_{0.25}O_{5\pm\delta}$ e) $Ba_2In_{0.5}CeCo_{0.5}O_{5\pm\delta}$

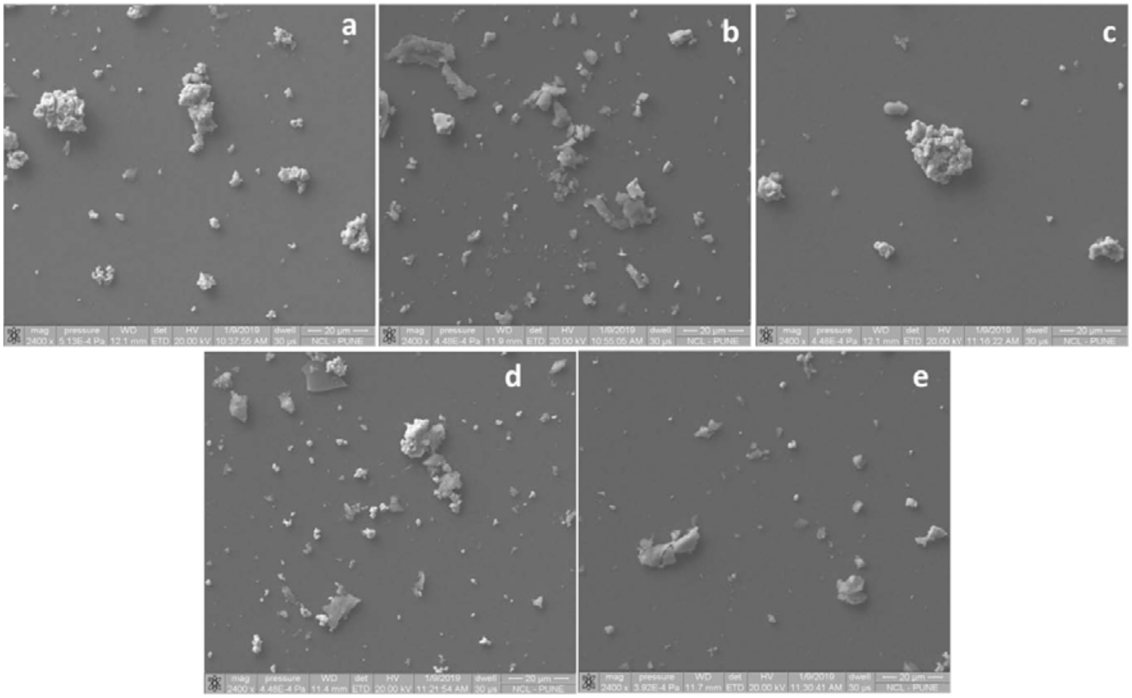

Figure 3C.7: SEM images of a) $Ba_2InCe_{0.75}Co_{0.25}O_{5\pm\delta}$ b) $Ba_2InCe_{0.5}Co_{0.5}O_{5\pm\delta}$ c) $Ba_2InCe_{0.25}Co_{0.75}O_{5\pm\delta}$ d) $Ba_2In_{0.75}CeCo_{0.25}O_{5\pm\delta}$ e) $Ba_2In_{0.5}CeCo_{0.5}O_{5\pm\delta}$

Table 3C.4: Surface composition of metals from EDS analysis

Material	Weight (%)									
	$Ba_2InCe_{0.75}Co_{0.25}O_{5\pm\delta}$		$Ba_2InCe_{0.5}Co_{0.5}O_{5\pm\delta}$		$Ba_2InCe_{0.25}Co_{0.75}O_{5\pm\delta}$		$Ba_2In_{0.75}CeCo_{0.25}O_{5\pm\delta}$		$Ba_2In_{0.5}CeCo_{0.5}O_{5\pm\delta}$	
Element	Observed	Calculated	Observed	Calculated	Observed	Calculated	Observed	Calculated	Observed	Calculated
Ba	46.2	46.6	48.3	48	48.1	50	48.5	46.1	46.4	47.2
In	12.9	19.4	11.7	20.2	13.7	21	9.5	14.5	7.1	9.9
Ce	20.2	17.8	14.9	12.3	8.7	6.3	24.5	23.5	21.5	24.1
Co	2.3	2.5	6.7	5.2	8.3	8.1	2.4	2.5	6.1	5.1
O	18.3	13.5	18.3	14.1	21.2	14.6	15.1	13.4	18.9	13.8

3C.3.2. Electrochemical Characterisation

Detailed electrochemical studies of these compounds are carried out by CV and LSV method under alkaline medium at room temperature.

3C.3.2.1. ORR Activity in Alkaline Medium

Figure 3C.8a represents cyclic voltammogram comparison of the samples with 900rpm rotation speed of the electrode and 50mV/s. The dotted pattern represents the scan in N_2 saturated 0.1M KOH and solid line represents the scan in O_2 saturation. A clear reduction peak is observed in O_2 saturation indicating ORR activity by the compound. Figure 3C.8b represents the linear sweep voltammogram in O_2 saturation at 1600 rpm. A blank data is recorded with 0rpm and N_2 saturation and is subtracted from the data for understanding the intrinsic behaviour of the sample. The inset image gives a clear view of onset region. There is a clear improvement in onset value as the Co concentration increased. The composition with maximum Co concentration exhibits better onset value of 0.823V *vs* RHE, which is ~100mV positive than the compound with lowest Co concentration, viz., $Ba_2In_{0.75}CeCo_{0.25}O_{5\pm\delta}$. The analysis is done by fixing one metal concentration and varying the other to understand the effect of doping. Close analysis of the profile suggests that there is a considerable improvement in the activity with fixed Ce and increased Co in $Ba_2In_{0.75}CeCo_{0.25}O_{5\pm\delta}$ and $Ba_2In_{0.5}CeCo_{0.5}O_{5\pm\delta}$, ie., onset value increases by 68mV with increase in Co by 12.5atom%. A similar improvement of onset value of 20mV also occurs with increase in Ce content by fixing the Co at *y* = 0.5, in $Ba_2InCe_{0.5}Co_{0.5}O_{5\pm\delta}$ and $Ba_2In_{0.5}CeCo_{0.5}O_{5\pm\delta}$. The current response also follows the same trend indicating the creation of more and more active sites with increased doping. Individual LSVs of the sample with various rotation speeds in O_2 saturated solution is represented in figure 3C.9.

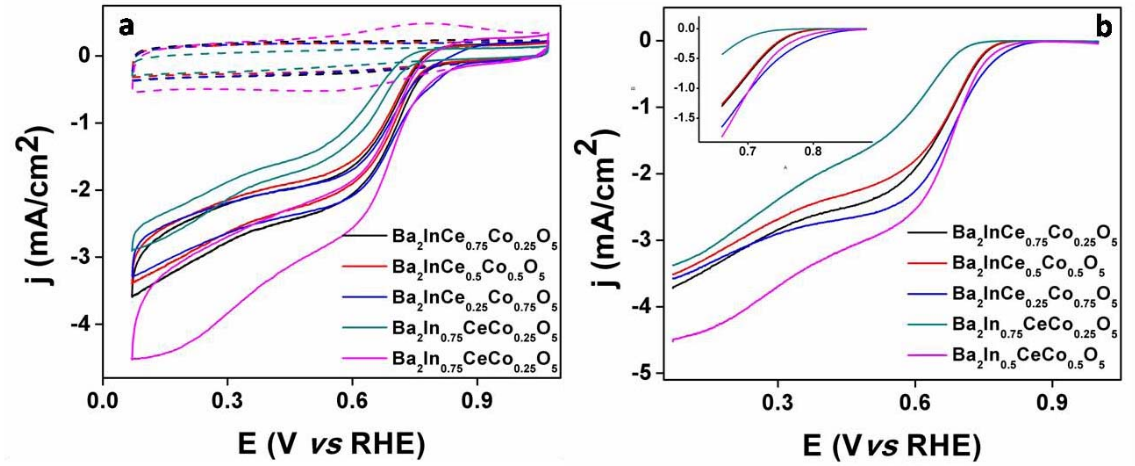

Figure 3C.8: a) Cyclic voltammograms of the samples recorded with 900rpm rotation speed of the working electrode and 50mV/s scan rate. The dotted line represents the scan in N_2 saturation and the solid line represents the scan in O_2 saturation. b) Comparison of blank data subtracted LSV at 1600rpm in O_2 saturation recorded with 10mV/s scan rate; inset image represents the onset region.

Kinetics of the ORR is analysed by Koutechy-Levich and Tafel method. The principle of these methods is explained in annexure[14, 15]. K-L plot at 0.37V *vs* RHE is represented in figure 3C.10a. K-L slope values obtained are $0.303 mAcm^{-2}s^{1/2}$ for $Ba_2InCe_{0.75}Co_{0.25}O_{5\pm\delta}$, $0.292\ mAcm^{-2}s^{1/2}$ for $Ba_2InCe_{0.5}Co_{0.5}O_{5\pm\delta}$, $0.312 mAcm^{-2}s^{1/2}$ for $Ba_2InCe_{0.25}Co_{0.75}O_{5\pm\delta}$, $0.383\ mAcm^{-2}s^{1/2}$ for $Ba_2In_{0.75}CeCo_{0.25}O_{5\pm\delta}$ and $0.233 mAcm^{-2}s^{1/2}$ for $Ba_2In_{0.5}CeCo_{0.25}O_{5\pm\delta}$, the values indicate intermediate electron transfer mechanism in all the compounds[15]. Figure 3C.10b represents Tafel plot, the values of the slopes obtained are -98.8, -94.3, -138, -140.6 and -110mV/d for $Ba_2InCe_{0.75}Co_{0.25}O_{5\pm\delta}$, $Ba_2InCe_{0.5}Co_{0.5}O_{5\pm\delta}$, $Ba_2InCe_{0.25}Co_{0.75}O_{5\pm\delta}$, $Ba_2In_{0.75}CeCo_{0.25}O_{5\pm\delta}$ and $Ba_2In_{0.5}CeCo_{0.5}O_{5\pm\delta}$ respectively. From these slope values, it is clear that the co-doped brownmillerites possess more electron donating catalytic sites. With fixed Ce concentration and increase in Co concentration, the slope values decrease, indicating a clear shift of *rds* in the mechanism from first

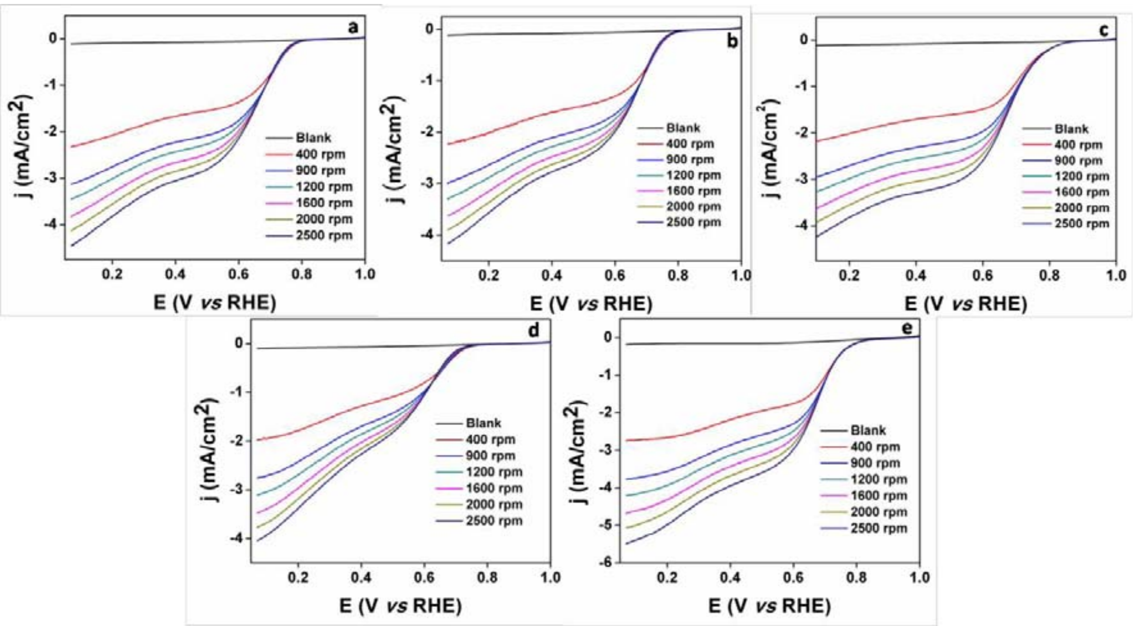

Figure 3C.9: Linear sweep voltammograms at various rotation speeds of a) $Ba_2InCe_{0.75}Co_{0.25}O_{5\pm\delta}$ b) $Ba_2InCe_{0.5}Co_{0.5}O_{5\pm\delta}$ c) $Ba_2InCe_{0.25}Co_{0.75}O_{5\pm\delta}$ d) $Ba_2In_{0.75}CeCo_{0.25}O_{5\pm\delta}$ e) $Ba_2In_{0.5}CeCo_{0.5}O_{5\pm\delta}$

electron reduction to surface migration[14]. However the reverse trend is observed by fixing the Co content and increasing Ce content. Lowest value of Tafel slope is obtained for the sample with optimum concentration of Co and Ce, viz., $Ba_2InCe_{0.5}Co_{0.5}O_{5\pm\delta}$.

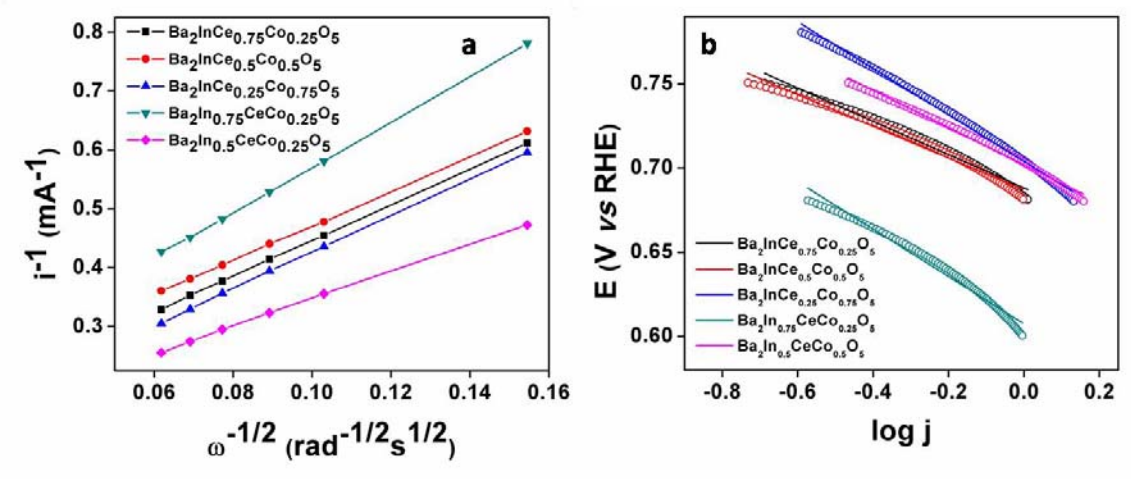

Figure 3C.10: a) Koutechy Levich plot, calculated from LSV data at 0.37V vs RHE b) Tafel plot, calculated from LSV data at 1600 rpm.

Clear idea on the electron transfer behaviour and peroxide yield is obtained from RRDE experiments. The calculations are explained in annexure[16]. Figure 3C.11 represents the electron transfer number at varying potentials. The trend of doping concentration is clearly observed from the figure. With fixed In concentration, with increasing the Co concentration, electron transfer number increases. But the trend is not observed with fixing the Ce concentration and increasing the Co concentration as in $Ba_2In_{0.75}CeCo_{0.25}O_{5\pm\delta}$ and $Ba_2In_{0.5}CeCo_{0.5}O_{5\pm\delta}$, instead there is a decrease in the electron transfer number with increasing Co. There is a considerable increase in the electron transfer number with fixed Co concentration and increasing the Ce concentration, as in $Ba_2InCe_{0.75}Co_{0.25}O_{5\pm\delta}$ and $Ba_2In_{0.75}CeCo_{0.25}O_{5\pm\delta}$, as well as $Ba_2InCe_{0.5}Co_{0.5}O_{5\pm\delta}$ and $Ba_2In_{0.5}CeCo_{0.5}O_{5\pm\delta}$. Figure 3C.11b represents peroxide yield with applied potential, peroxide yield is too high for the materials proving the intermediate 2+2 electron mechanism in the compounds. But there is a clear improvement in the behaviour on increased Co doping by fixing the In and with increased Ce content by fixing the Co content.

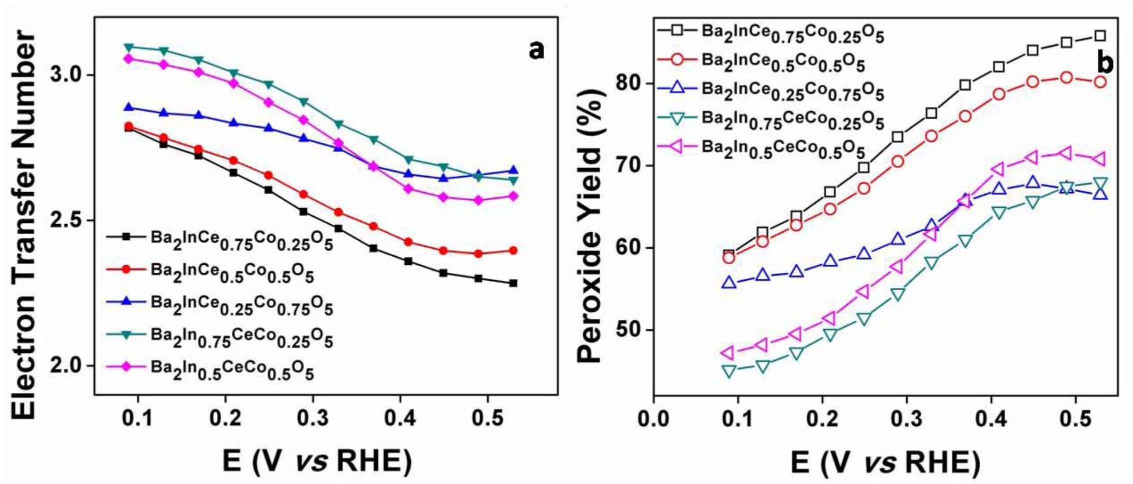

Figure 3C.11: Dependence of a) electron transfer number and b) Peroxide yield on applied potential calculated from RRDE data at 1600 rpm with 10mV/s scan rate and O_2 saturation

3C.3.2.2. OER Activity in Alkaline Medium

OER activity is monitored in 1M KOH and better activity is exhibited by the material with optimum Ce and Co concentration ie, $Ba_2InCe_{0.75}Co_{0.25}O_{5\pm\delta}$. Current response is analysed at 1.8V *vs* RHE as represented in the inset of figure 3C.12a, current response is found to improve with the Ce concentration with fixing the In concentration ie, from $Ba_2InCe_{0.25}Co_{0.75}O_{5\pm\delta}$ to $Ba_2InCe_{0.75}Co_{0.25}O_{5\pm\delta}$. The kinetics of the reaction is studied with Tafel analysis; figure 3C.12b represents the Tafel plot. The trend of slope values are found to be in the order $Ba_2In_{0.5}CeCo_{0.5}O_{5\pm\delta}$ (40.4mV/d) < $Ba_2In_{0.5}CeCo_{0.5}O_{5\pm\delta}$ (41.6mV/d) < $Ba_2InCe_{0.25}Co_{0.75}O_{5\pm\delta}$ (44.1mV/d) < $Ba_2InCe_{0.75}Co_{0.25}O_{5\pm\delta}$ (44.9mV/d) < $Ba_2InCe_{0.5}Co_{0.5}O_{5\pm\delta}$ (46.7mV/d). The slope values of all the materials are almost same (~40mV/d) indicating a similar *rds* of migration after the second electron transfer in the mechanism for all the materials[17].

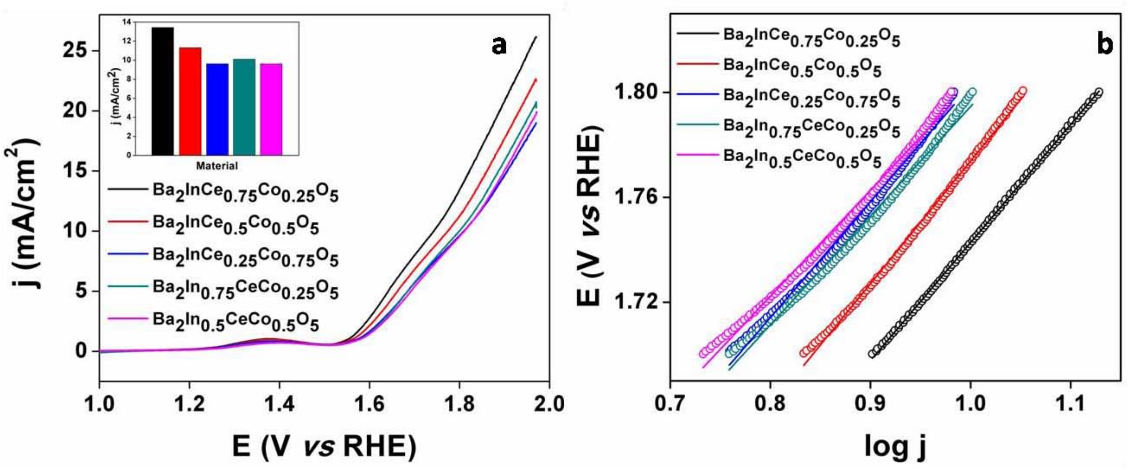

Figure 3C.12: a) OER Linear sweep voltammogram recorded at 1600rpm rotation speed with 10mV/s scan rate in N_2 saturated electrolyte, inset image represents the current density comparison at 1.8V *vs* RHE b) OER Tafel plots calculated from LSV data at 1600 rpm, empty circles represents the data and the solid line represents the linear fit of the data

3C.3.3. High Temperature Analysis

The material $Ba_2InCe_{0.5}Co_{0.5}O_{5\pm\delta}$ is selected for the high temperature analysis, which has optimum Co and Ce concentration and reasonably high room temperature activity. High temperature phase stability followed by Impedance analysis is conducted in various gas atmospheres.

3C.3.3.1. High Temperature Phase Stability Analysis

High temperature phase analysis is conducted with non-ambient XRD in N_2, O_2 and 5% H_2/Ar atmosphere. Figure 3C.13 shows PXRD patterns at various temperatures and in different gas atmospheres. Close analysis reveals that the material is extremely stable in all the atmosphere and temperatures. The material retains the phase even after cooling down to room temperature. The stability in oxygen rich and lean atmosphere is the required property for applications in fuel cells or oxide ion conducting membranes.

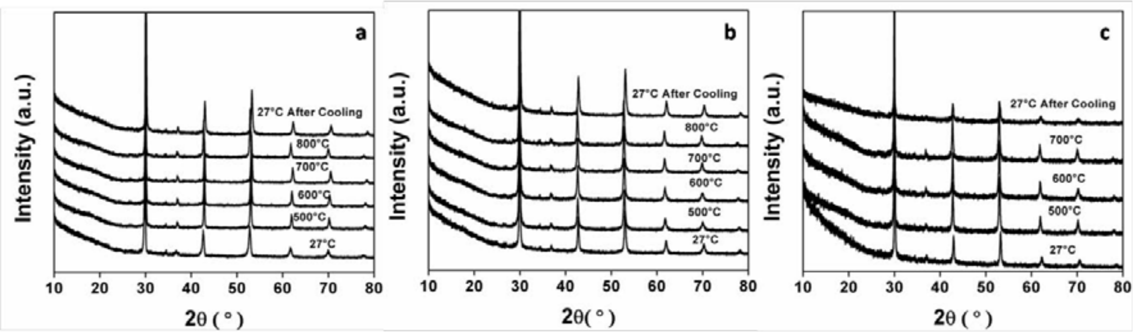

Figure 3C.13: HT-PXRD pattern of the sample in a) N_2 atmosphere b) O_2 atmosphere and c) 5% H_2/Ar atmosphere

3C.3.3.2 High Temperature Impedance Analysis

High temperature conductivity is analysed by impedance spectroscopy at each temperature, on cooling from 800°C to 500°C as explained in the chapter 2B. The data obtained is more of inductive part as in case of materials reported in chapter 2B and the same equivalent circuit is used for solving the data. Figure 3C.13 represents the Nyquist plot in N_2 and O_2 atmospheres at various gas temperatures. The conductivity data is represented in table 3C.6 indicating an improvement in conductivity with temperature and at 800°C resistivity value reaches values as low as 60.3Ωcm in O_2 atmosphere.

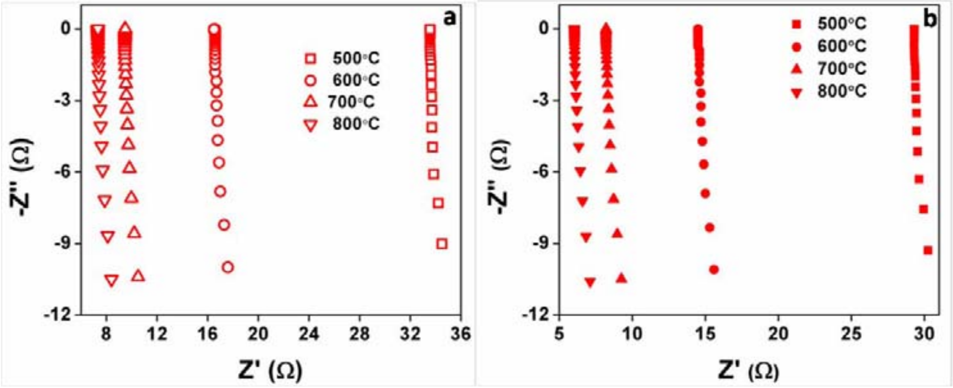

Figure 3C.14: Nyquist plot at various temperatures in a) N_2 atmosphere and b) O_2 atmosphere

Table 3C.5: High temperature resistivity calculated from EIS data

Temperature (°C)	Resistivity (Ωcm)	
	N_2	O_2
800	73.4	60.3
700	95.9	82.5
600	166.9	145.8
500	337.9	294.6

3C.4. Summary and Conclusion

The materials with stoichiometry $Ba_2In_{2-x+y}Ce_xCo_yO_{5\pm\delta}$ crystallise in the cubic system of brownmillerite even with a 12.5% doping with Co. The $Ba_2In_2O_5$ usually forms a non-stoichiometric cubic perovskite structure with complete disordering of oxygen vacancy only at high temperature, however, in this work, the lower temperature cubic phase could be stabilised with Co and Ce co-doping. As the Co concentration increased, there is a shift in XRD peak to higher angles and with increase in Ce, the peak shifts to lower angle due to the mismatch of size of Ce^{4+} and Co^{3+} with In^{3+}. Room temperature electrochemistry is studied, indicating that there is an improvement in activity with Co and Ce doping. Better current response and onset value is obtained for the material with maximum Co concentration. OER data suggests that, better activity in terms of onset and current values is obtained for the material with optimum Co and Ce concentration. The OER Tafel slope indicates that the materials are highly catalytic active with migration of oxidised species after the second electron transfer as the rate determining step in overall mechanism. The phase is stable in high temperature with oxidising and reducing atmospheres and the analysis of high temperature conductivity by Impedance analysis indicates an improvement in conductivity with temperature in both O_2 rich and lean atmospheres.

3C.5. References

1. Goodenough, J. B.; Ruiz-Diaz, J. E.; Zhen, Y. S., Oxide-ion conduction in Ba2In2O5 and Ba3In2MO8 (M=Ce, Hf, or Zr). *Solid State Ionics* **1990,***44* (1), 21-31.

2. Jijil, C. P.; Bhange, S. N.; Kurungot, S.; Devi, R. N., Effect of B Site Coordination Environment in the ORR Activity in Disordered Brownmillerites Ba2In2−xCexO5+δ. *ACS Applied Materials & Interfaces* **2015,***7* (5), 3041-3049.

3. Jijil, C. P.; Unni, S. M.; Sreekumar, K.; Devi, R. N., Disordered Brownmillerite Ba2InCeO5+δ with Enhanced Oxygen Reduction Activity. *Chemistry of Materials* **2012,***24* (14), 2823-2828.

4. Jijil, C. P.; Patil, I. M.; Kakade, B.; Devi, R. N., Cobalt-Doped Ba2In2O5 Brownmillerites: An Efficient Electrocatalyst for Oxygen Reduction in Alkaline Medium. *ACS Omega* **2018,***3* (2), 1710-1717.

5. Thundiyil, S.; Kurungot, S.; Devi, R. N., Bifunctional Oxygen Reduction and Evolution Activity in Brownmillerites Ca2Fe(1−x)CoxO5. *ACS Omega* **2019,***4* (1), 31-38.

6. Kowalski, D.; Kiuchi, H.; Motohashi, T.; Aoki, Y.; Habazaki, H., Activation of Catalytically Active Edge-Sharing Domains in Ca2FeCoO5 for Oxygen Evolution Reaction in Highly Alkaline Media. *ACS Applied Materials & Interfaces* **2019,***11* (32), 28823-28829.

7. Tsuji, E.; Motohashi, T.; Noda, H.; Kowalski, D.; Aoki, Y.; Tanida, H.; Niikura, J.; Koyama, Y.; Mori, M.; Arai, H.; Ioroi, T.; Fujiwara, N.; Uchimoto, Y.; Ogumi, Z.; Habazaki, H., Brownmillerite-type Ca2FeCoO5 as a Practicable Oxygen Evolution Reaction Catalyst. *ChemSusChem* **2017,***10* (14), 2864-2868.

8. Berastegui, P.; Hull, S.; Eriksson, S. G., Oxygen Disorder and Conductivity in Pyrochlore and Perovskite-Based Compounds. *Materials Science Forum* **2001,***378-381*, 487-492.

9. Ansari, S. A.; Khan, M. M.; Ansari, M. O.; Kalathil, S.; Lee, J.; Cho, M. H., Band gap engineering of CeO2 nanostructure using an electrochemically active biofilm for visible light applications. *RSC Advances* **2014,***4* (32), 16782-16791.

10. Mullins, D. R.; Overbury, S. H.; Huntley, D. R., Electron spectroscopy of single crystal and polycrystalline cerium oxide surfaces. *Surface Science* **1998,***409* (2), 307-319.

11. Meng, F.; Wang, L.; Cui, J., Controllable synthesis and optical properties of nano-CeO2 via a facile hydrothermal route. *Journal of Alloys and Compounds* **2013,***556*, 102-108.

12. Biesinger, M. C.; Payne, B. P.; Grosvenor, A. P.; Lau, L. W. M.; Gerson, A. R.; Smart, R. S. C., Resolving surface chemical states in XPS analysis of first row transition metals, oxides and hydroxides: Cr, Mn, Fe, Co and Ni. *Applied Surface Science* **2011,***257* (7), 2717-2730.

13. Baird, T.; Campbell, K. C.; Holliman, P. J.; W. Hoyle, R.; Stirling, D.; Williams, B. P.; Morris, M., Characterisation of cobalt–zinc hydroxycarbonates and their products of decomposition. *Journal of Materials Chemistry* **1997,***7* (2), 319-330.

14. Taylor, R. J.; Humffray, A. A., Electrochemical studies on glassy carbon electrodes: II. Oxygen reduction in solutions of high pH (pH>10). *Journal of Electroanalytical Chemistry and Interfacial Electrochemistry* **1975,***64* (1), 63-84.

15. Ge, X.; Sumboja, A.; Wuu, D.; An, T.; Li, B.; Goh, F. W. T.; Hor, T. S. A.; Zong, Y.; Liu, Z., Oxygen Reduction in Alkaline Media: From Mechanisms to Recent Advances of Catalysts. *ACS Catalysis* **2015,***5* (8), 4643-4667.

16. Zhou, R.; Zheng, Y.; Jaroniec, M.; Qiao, S.-Z., Determination of the Electron Transfer Number for the Oxygen Reduction Reaction: From Theory to Experiment. *ACS Catalysis* **2016,***6* (7), 4720-4728.

17. De Faria, L. A.; Boodts, J. F. C.; Trasatti, S., Electrocatalytic properties of ternary oxide mixtures of composition Ru0.3Ti(0.7-x)CexO2: oxygen evolution from acidic solution. *Journal of Applied Electrochemistry* **1996,***26* (11), 1195-1199.

Chapter 4

Role of transitional metal doping in electrochemical properties of $Sr_{0.7}Na_{0.3}SiO_{3-\delta}$

4.1. Introduction

$SrSiO_3$ falls in the family of compounds with general formula ABO_3, but with very different structure of that of perovksites, mainly arising due to the strong tetrahedral site preference of Si^{4+}. The material crystallises in monoclinic system and consists of interconnected SiO_4 tetrahedral units. Each SiO_4 tetrahedron shares a corner to form ordered Si_3O_9 units and edge shared SrO_8 units formed above and below the planes of Si_3O_9 units are coordinated by three terminal oxygens of three different Si_3O_9 units[1-3]. $SrSiO_3$ is also reported to crystallise in trigonal crystal system, where the silicate groups are disordered statistically over three equivalent positions[4].

In such a tetrahedral anion complex, introduction of oxygen vacancy is quite difficult since it corner shares to overcome the oxygen vacancy formation. Doping the structure with bulkier cations is a strategy to spatially separate the tetrahedral units and oxygen vacancy. Hence doping with alkali metal has been employed to introduce steric hindrance to corner sharing of neighbouring Si_3O_9 units[5, 6].

Na doping and K doping in the A site as well as the resulting superior conductivity was reported by Prof. J. B. Goodenough during 2012-2014[1, 2, 5]. K doping resulted in a hygroscopic material and the pellet was found to break after a period of time due to swelling[2, 7, 8], whereas Na doping resulted in a stable product. An anomalous conduction behaviour was observed with 30% Na doping in the A site and is suggested to be due to the transition from vacancy conduction to interstitial conduction mechanism. The possibility of proton conduction mechanism by water absorption was ruled out by TGA analysis, which failed to observe any weight loss by water elimination[5]. The reason for the higher conductivity was confirmed to be oxide ion conductivity, since non-oxygen deficient sample with stoichiometry $Sr_{0.6}La_{0.2}Na_{0.1}SiO_3$ exhibited lower conductivity than the Na doped compound[5]. Independence of conductivity to the partial pressure of oxygen further confirmed that the material is pure oxide ion conductor. Detailed NMR studies by Xu et al., also support the oxide ion conduction by vacancy creation. They have observed breakage of Si_3O_9 to Si_3O_8 unit by detailed ^{29}Si NMR studies[9]. Because of higher conductivity, matching thermal expansion with components and better dispersion, these materials are projected as good candidates for SOFC application[10].

Immediately after the above studies, another significant research on the same material with a counter point of view emerged from the group of Prof. S. J. Skinner[8, 11], suggesting the reason of the conductivity to be Na ion conductivity by the impurity phase and not O ion conductivity as reported earlier. The impurity phase was identified as a glassy amorphous phase and could not be discovered by XRD analysis. In addition, better fit of neutron diffraction data was obtained by low or zero Na occupancy than the proposed stoichiometry[4, 8, 11-14].

Interestingly, later studies could not obtain as much conductivity as in the early reports. And only the amorphous phase of the impurity was found to contribute to the conductivity and not the crystalline phase, which was proved by separately synthesising and analysing both phases. Recrystallisation and HT-XRD analysis proved the formation and crystallisation of an amorphous impurity phase in the material, supported by independent thermal analysis[14]. A clear phase separation of Na rich and lean phases was observed from ToF-SIMS[11]. More about the impurity concentration was explored by solid state NMR technique, where a varied temperature analysis resulted in the understanding of Na^+ exchange phenomenon in the material[15-17]. Detailed NMR studies by Chien et al proved that Na can be incorporated in the lattice only up to 10 mol%, and more than that leads to the formation of impure phase[18].

The objective of the chapter is to study the effect of transition metal doping on the structure and electrochemical properties of the material. 30% doping in the A site with Na is selected for the study considering the reports on vacancy concentration and anomalously high conductivity. 5% of Si in the B site is substituted with transition metal to introduce catalytic centre and improved conductivity to have a final composition of $Sr_{0.7}Na_{0.3}Si_{0.95}M_{0.05}O_{3-\delta}$ where, M = Mn/Fe/Co/Ni/Cu.

4.2. Experimental Section

4.2.1. Synthesis of $Sr_{0.7}Na_{0.3}Si_{0.95}M_{0.05}O_{3-\delta}$

$SrSiO_3$, A site doping with Na and B site doping with transition metals to get a final composition $Sr_{0.7}Na_{0.3}Si_{0.95}M_{0.05}O_{3-\delta}$ (M= Mn/Fe/Co/Ni/Cu) proceeded through solid state reaction of precursors $SrCO_3$ (99%, Loba Chemie), Na_2CO_3 (99.5%, Loba Chemie), SiO_2 (99%, Thomas Baker), $MnCO_3$ (99.9% Alfa Aeser), Fe_2O_3 (99.98%, Sigma Aldrich), $CoCO_3$ (Co- 43-47%, Sigma Aldrich), NiO (99%, Alfa Aeser) and CuO (99%, Thomas Baker). The precursors are weighed stoichiometrically and ground well in a mortar and pestle. Decarbonisation is done at 700°C, ground again and made a pellet and fired at 1050°C for 12h.

4.2.2. Characterisation

Phase purity and structure is analysed by PXRD. Surface states of dopant metal is analysed by XPS analysis, mapping of the samples for the distribution of the elements is also performed by XPS elemental mapping. Morphology of the samples is analysed by SEM and FE-SEM. Detailed point analysis of metal concentration is performed by EDS. High temperature phase stability in various gas atmospheres are conducted by non-ambient XRD in different temperatures and in N_2, O_2 and 5%H_2/Ar gas atmospheres.

^{17}O enrichment in the sample is carried out by treating the finely ball milled powder in H_2 flow for 2h at 800°C, followed by flushing out the H_2 gas by N_2 gas for 30min then passing ^{17}O gas mixture (70%, Cambridge Isotope Laboratories Inc.) is passed for 2min and the sample is allowed it to cool in the same atmosphere by blocking the outlet. The enriched sample is analysed by solid state NMR.

^{29}Si MAS-NMR experiments are performed in Bruker Avance Neo WB 500 MHz 4mm double resonance H/F X probe head with a silicon resonance frequency of 99.42 MHz. Powdered specimens are packed into a 4mm Zirconia rotor. Spectra are acquired at a spinning rate of 10kHz with peak positions referenced to an external standard of Sodium trimethylsilylpropanesulfonate (DSS) at 0ppm. Spectra are recorded using a pulse width of 2.82μs at 600W. ^{23}Na MAS-NMR experiments are carried out in the same instrument with ^{23}Na frequency of 132.38MHz. The 4mm Zirconia rotor is spun at a rate of 14kHz for acquiring the spectra. The peak positions are referenced to an external standard of 1M NaCl solution at 0ppm. All spectra are recorded using a pulse width of 0.3μs at 346W. ^{17}O MAS solid state NMR experiments are carried out in a Bruker Avance 300 MHz spectrometer equipped with 7.05T wide bore super conducting magnet and a 4mm magic angle spinning probe head. The samples are spun at 14 KHz and spectra are recorded with pulse width of 0.25μs.

4.2.3. Electrochemical Analysis

Room temperature electrochemical analysis is carried out in 0.1M KOH using a three electrode system and sample for the analysis is prepared as explained in chapter 2A

High temperature electrochemical impedance spectroscopy is analysed by CH Instrument in varying concentrations of oxygen and nitrogen. Experimental procedure explained in detail in chapter 2B.

4.3. Results and Discussion

4.3.1. Synthesis and Structural Characterization

Phase purity is analysed by PXRD analysis. Parent structure, $SrSiO_3$ crystallised with impurity phases as reported earlier. The major phase matches with $SrSiO_3$, JCPDS file number: 01-087-0474 and the impurity phase of Sr_2SiO_4 matches with JCPDS file number: 039-1256. 30% substitution of Sr with Na resulted in a single phase compound matching with the $SrSiO_3$ pattern (JCPDS file number: 01-087-0474). In $Sr_{0.7}Na_{0.3}Si_{0.95}M_{0.05}O_{3-\delta}$ compounds also, major phase matches with the same reference pattern. Impurity profile analysis of the patterns show minor quantities of silica or transition metal oxide based phases except in case of Fe doping which formed as a pure phase. Small concentrations of unreacted SiO_2 is identified in Mn and Cu doped compounds, whereas, Co doped material contains a mixed oxide $Sr_2CoSi_2O_7$ (JCPDS file number: 016-0857) phase. In the case of Ni doped material, NiO (JCPDS file number: 01-078-0423) and $Na_2SrSi_2O_6$ (JCPDS file number: 032-1159) impurity phases are identified.

Detailed structural analysis is performed with Rietveld refinement of PXRD pattern using GSAS-EXPGUI suit of software[19]. All the compounds crystallised in monoclinic C21/c space group and reference model $SrSiO_3$ with ISCD collection code 59308 is selected for refinement. Rietveld refinement proceeded smoothly with all the compounds after inserting the impurity phases in the model. Crystal data of the Co based impurity was not available in the database and we could arrive on a model with similar cell parameters containing Mn instead of Co. The model $Sr_2MnSi_2O_5$ (ICSD collection code: 261227) with exchanging the Mn with Co is selected and the pattern of

$Sr_{0.7}Na_{0.3}Si_{0.95}Co_{0.05}O_{3-\delta}$ is refined quantitatively. Figure 4.2 shows the Rietveld refined patterns of the samples and the data is tabulated in table 4.1.

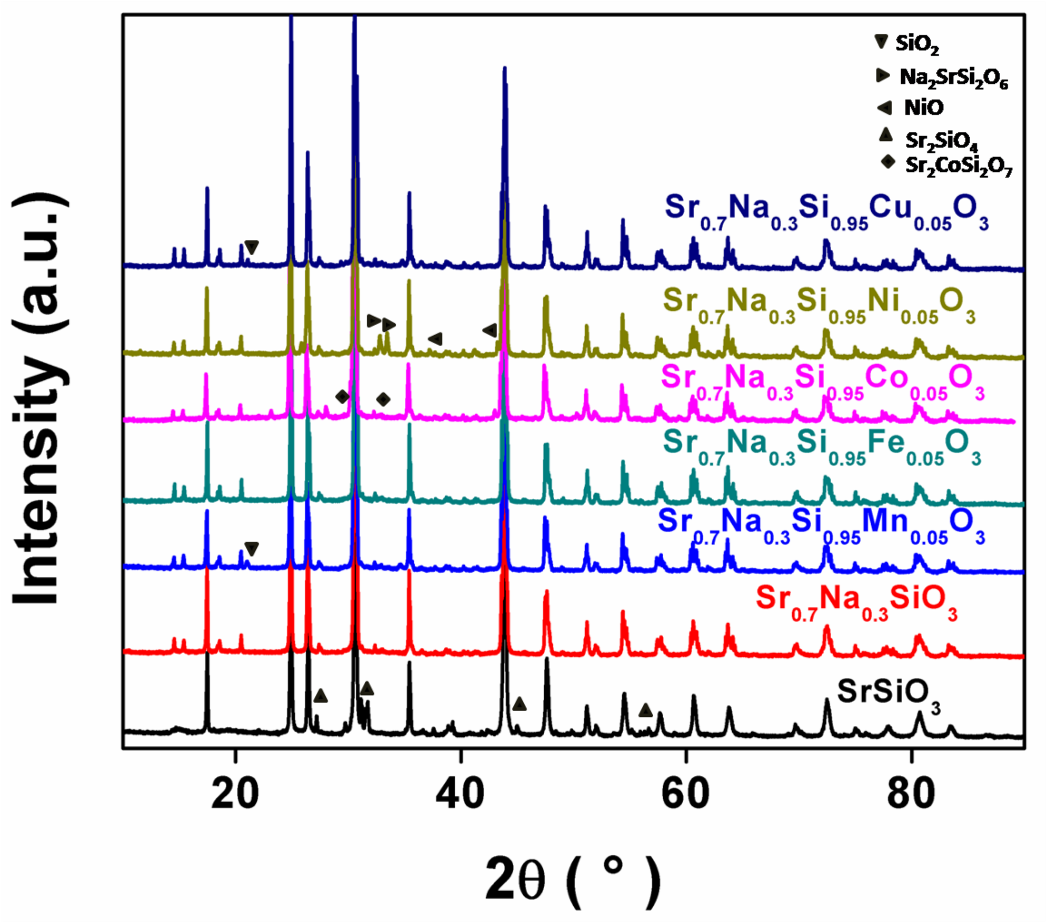

Figure 4.1: PXRD patterns of the materials collected at room temperature. Impurity peaks are indicated by symbols

A close analysis of the patterns shows an unusual negative difference curve in the low angle region. A probable reason is wrong or extra occupancy of dopants in the metal sites giving extra weightage to peaks. This is further investigated by refining the patterns with different possibilities of zero occupation in A and B sites, In all the cases the fit obtained is un-acceptable, indicating an inherent problem of the structure model or space group selected. The impurity of metal based silicate in Co has also led to the ambiguity of complete Co occupation in the impurity phase or in the main phase. This is clarified by calculating the impurity weight percentage considering the below equation, which indicates the scenario where no cobalt is incorporated in the lattice of the main $SrSiO_3$ phase. Rietveld refinement resulted in a bad fit without Na and Co, and resulted in an impurity weight percentage of 44%, instead of 19% anticipated if all the Co is present in the impurity phase. Here also the refined pattern was not acceptable in terms of the fit confirming the possibility of incorporation of doped metal in to the lattice position. The details are given in table 4.2.

$$0.5SrCO_3 + 0.7Na_2CO_3 + SiO_2 + 0.05CoCO_3$$
$$\rightarrow Sr_{0.7}Na_{0.3}Si_{0.95}Co_{0.05}O_{3-\delta} \ or\ 0.85Sr_{0.7}Na_{0.3}SiO_{3-\delta} + 0.05Sr_2CoSi_2O_7$$

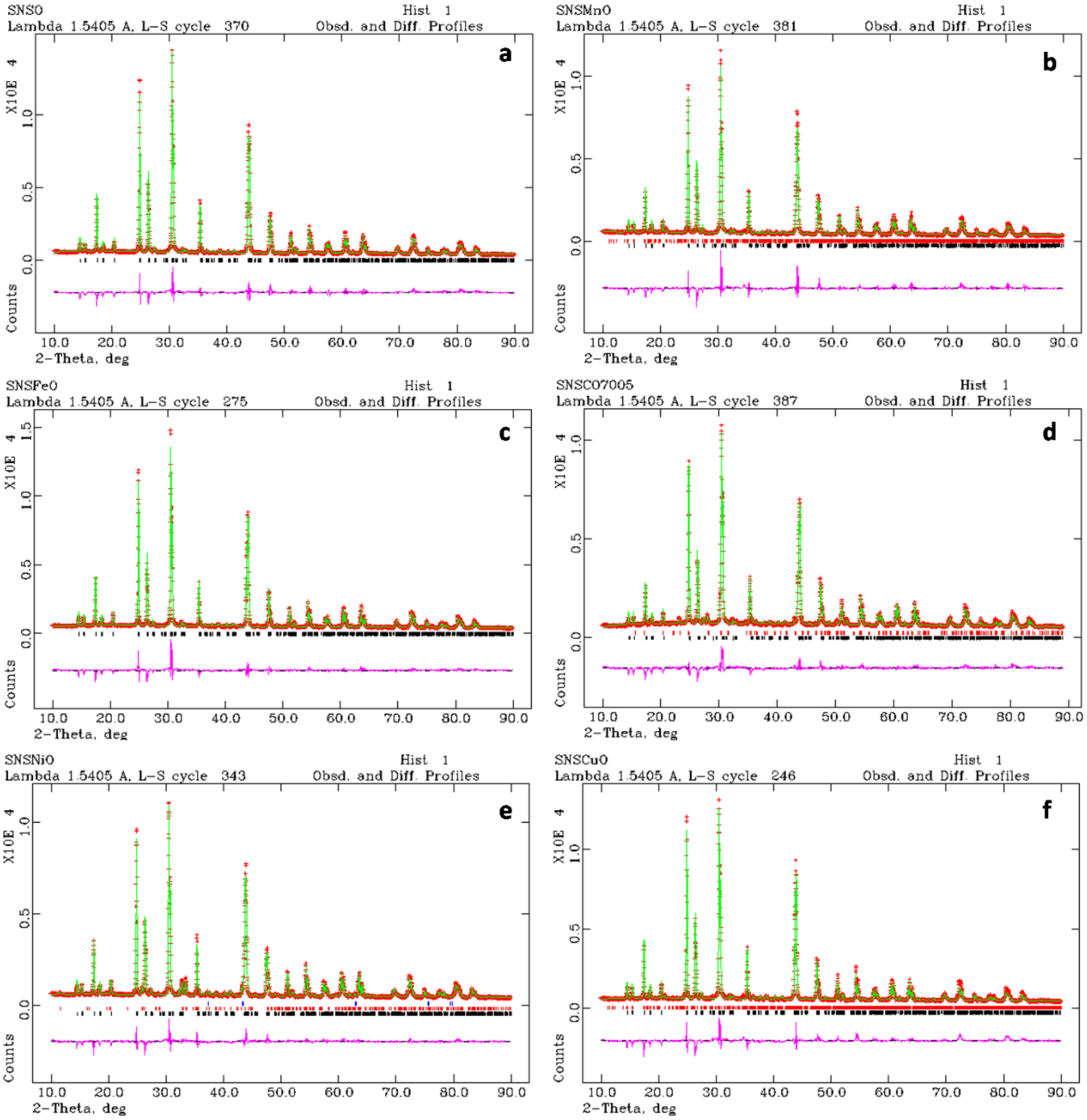

Figure 4.2: Rietveld refined patterns of a) $Sr_{0.7}Na_{0.3}SiO_{3-\delta}$ b) $Sr_{0.7}Na_{0.3}Si_{0.95}Mn_{0.05}O_{3-\delta}$ c) $Sr_{0.7}Na_{0.3}Si_{0.95}Fe_{0.05}O_{3-\delta}$ d) $Sr_{0.7}Na_{0.3}Si_{0.95}Co_{0.05}O_{3-\delta}$ e) $Sr_{0.7}Na_{0.3}Si_{0.95}Ni_{0.05}O_{3-\delta}$ and f) $Sr_{0.7}Na_{0.3}Si_{0.95}Cu_{0.05}O_{3-\delta}$

Polyhedral representation of the structure is represented in figure 4.3. A site cations are arranged in a layer above and below the isolated B_3O_9 units. There are two crystallographically different sites for B site cations, five sites for O atoms and a single site for A cations. Si/M1 B site is coordinated with four different O atoms, O1, O2, O3 and O5, among which O1 and O2 are terminal oxygens and O5 and O3 are the bridging oxygens. In the second tetrahedron, Si/M2 coordinates to two different oxygens, viz., two O4 and two O3 atoms to form a tetrahedron. The tetrahedra share two O3 and an O5 in common to form isolated M_3O_9 units.

Surface states of dopant metals are confirmed by XPS analysis and the deconvoluted spectra are given in figure 4.4. Mn2$p_{1/2}$ XPS is fitted with two peaks at 641.2eV and 642.8eV and 2$p_{3/2}$ at ~12eV higher binding energy corresponding to the +2 and +3 states[20, 21]. Signal to noise ratio of Fe2p XP spectra obtained is very poor, and is fitted with five peaks corresponding to Fe^{+3} oxidation state only. Co2p XP spectrum is deconvoluted with two peaks at 779.7eV and 781.3eV corresponding to +2 and +3 states, a broad satellite peak is observed at 787.8eV corresponding to +2 oxidation state and the coupling constant between 2$p_{1/2}$ and 2$p_{3/2}$ is ~15eV[20, 22]. Ni2p XPS resolved with peak at 855eV corresponding to +2 state[23, 24]. In the Cu 2p XP spectrum, a strong satellite is observed at 940eV along with the peaks corresponding to 2$p_{1/2}$ and 2$p_{3/2}$ at 933eV and 943eV respectively[25, 26].

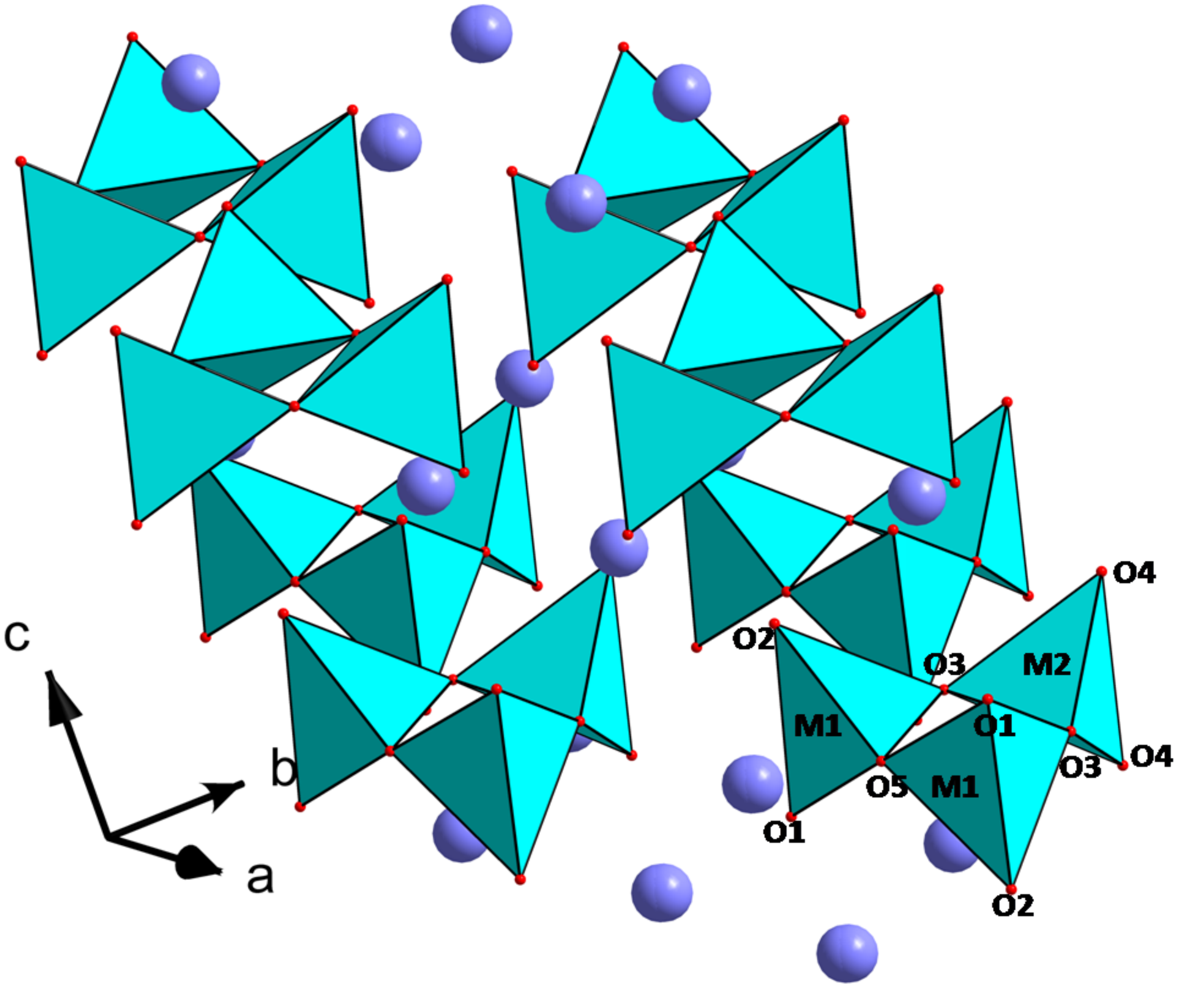

Figure 4.3: Representative image of polyhedral representation of unit cell obtained after Rietveld refinement. Blue balls represent Sr and red balls represent O. Five different oxygen sites are represented as O1 to O5, two sites for B site metal represented as M1 and M2

Table 4.1: Rietveld refinement data

Material		$Sr_{0.7}Na_{0.3}SiO_{3-\delta}$	$Sr_{0.7}Na_{0.3}Si_{0.95}Mn_{0.05}O_{3-\delta}$	$Sr_{0.7}Na_{0.3}Si_{0.95}Fe_{0.05}O_{3-\delta}$	$Sr_{0.7}Na_{0.3}Si_{0.95}Co_{0.05}O_{3-\delta}$	$Sr_{0.7}Na_{0.3}Si_{0.95}Ni_{0.05}O_{3-\delta}$	$Sr_{0.7}Na_{0.3}Si_{0.95}Cu_{0.05}O_{3-\delta}$
χ^2		5.9	6.1	4.9	4.04	3.3	6.5
Rp		6.8	7.1	6.1	5.1	5.1	6.7
wRp		9.0	9.7	8.1	7.0	6.8	9.3
a		12.3300(2)	12.3054(2)	12.334(1)	12.3285(2)	12.3361(4)	12.3341(2)
b		7.1387(1)	7.1279(1)	7.1451(7)	7.1420(9)	7.1467(1)	7.4116(9)
c		10.8774(1)	10.8575(1)	10.8832(1)	10.8785(1)	10.8838(1)	10.8829(1)
Sr 1	x	0.086466	0.087920	0.087018	0.087072	0.086927	0.087024
	y	0.240327	0.239381	0.239494	0.239416	0.239250	0.239710
	z	0.498973	0.498878	0.499254	0.499355	0.499410	0.499261

Occ.	Sr1 Sr2	0.7434 0.7510	0.7549	0.7422 0.7471	0.7789 0.7472	0.7360 0.7433	0.7443 0.7508
Na1		0.084431 0.241816 0.498538	0.087179 0.210941 0.490910	0.083884 0.243925 0.498866	0.084181 0.243236 0.499156	0.083763 0.245368 0.499105	0.083922 0.244967 0.499244
Occ.	Na1 Na2	0.3781 0.3860	0.2211 0.3509	0.3598 0.3648	0.3311 0.3674	0.3488 0.3582	0.3625 0.3706
Si1		0.124744 0.458008 0.244827	0.123249 0.455684 0.244943	0.124727 0.459024 0.244737	0.124016 0.459079 0.244876	0.125281 0.460463 0.247071	0.124092 0.457253 0.244681
Occ.		0.9517	0.9095	0.9032	0.9260	0.9054	0.8962
Si2		0.000 0.833291 0.25000	0.00000 0.831000 0.250000	0.000 0.831853 0.25000	0.0000 0.830346 0.250000	0.0000 0.831549 0.25000	0.0000 0.831854 0.25000
Occ.		0.9535	0.9084	0.9032	0.9295	0.9111	0.9049
M1			0.185842 0.561021 0.134166	0.123073 0.474105 0.232461	0.117135 0.470347 0.231229	0.133971 0.490612 0.250275	0.117539 0.457967 0.231843
Occ.			0.0641	0.0426	0.0486	0.0421	0.0419
M2			0.0000 0.816610 0.25000	0.0000 0.820046 0.25000	0.0000 0.814171 0.25000	0.0000 0.821548 0.250000	0.0000 0.822834 0.250000
Occ			0.0184	0.0437	0.0511	0.0438	0.0432
O1		0.132967 0.402312 0.104615	0.131841 0.405096 0.107032	0.132097 0.402139 0.104467	0.135238 0.400098 0.105224	0.132513 0.394560 0.385482	0.132844 0.402120 0.103907
Occu.		0.9894	0.9470	0.9797	0.9823	0.9913	0.978
O2		0.226577 0.394149 0.384271	0.227384 0.387801 0.383762	0.227495 0.394916 0.384572	0.229206 0.391471 0.383033	0.228154 0.394560 0.385482	0.227601 0.394765 0.384957
Occu.		0.9688	0.9727	0.9683	0.9742	0.9779	0.9704
O3		0.109083 0.69061 0.249383	0.110272 0.683342 0.250350	0.108609 0.690479 0.249118	0.107028 0.688708 0.247841	0.108609 0.690513 0.248906	0.108620 0.690704 0.249642
Occu.		0.9764	0.9737	0.9642	0.9681	0.9678	0.9644

O 4		0.048639 0.945938 0.391143	0.049213 0.948482 0.392189	0.047696 0.947008 0.391293	0.046840 0.953378 0.390340	0.046226 0.949277 0.391796	0.048537 0.947523 0.392020
Occu.		0.9791	0.9764	0.9737	0.9681	0.9786	0.9786
O 5		0.000 0.364372 0.2500	0.0000 0.369890 0.25000	0.0000 0.365425 0.25000	0.0000 0.371278 0.25000	0.000 0.367188 0.25000	0.0000 0.365339 0.25000
Occu.		0.9616	0.9684	0.9456	0.9535	0.9568	0.9442
Impurity			SiO_2: 2.8%		$Sr_2CoSi_2O_5$: 9.1%	$Na_2SrSi_2O_6$:10% NiO: 2%	SiO_2:1.8%

*Sr2/Na2(0.25,0.25,0)

Table 4.2: Impurity percentage in different scenario

Scenario	$Sr_2CoSi_2O_7$ weigh (%)
Refinement without Na and Co	44%
Refinement without Co	4%
Refinement with Na and Co	9%

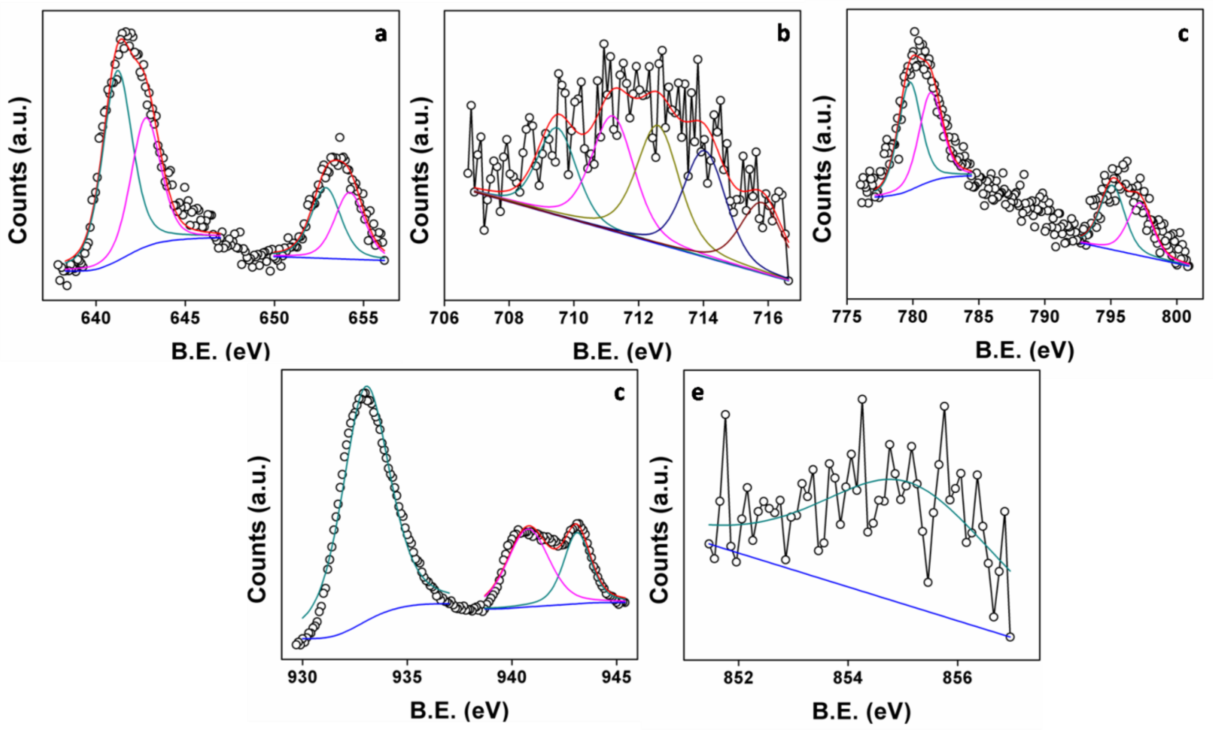

Figure 4.4: Deconvoluted 2p XP spectra of a) Mn in $Sr_{0.7}Na_{0.3}Si_{0.95}Mn_{0.05}O_{3-\delta}$ b) Fe in $Sr_{0.7}Na_{0.3}Si_{0.95}Fe_{0.05}O_{3-\delta}$ c) Co in $Sr_{0.7}Na_{0.3}Si_{0.95}Co_{0.05}O_{3-\delta}$ d) Cu in $Sr_{0.7}Na_{0.3}Si_{0.95}Cu_{0.05}O_{3-\delta}$ e) Ni in $Sr_{0.7}Na_{0.3}Si_{0.95}Ni_{0.05}O_{3-\delta}$

Morphology of the sample is analysed by SEM imaging, particles are found to be agglomerated to have size of several micrometers as noted in figure 4.5. The material is made into pellet and sintered at 1050°C, the pellet surface is observed to be uneven after sintering. Analysis of the surface with FE-SEM imaging showed different morphology in the pellet suggesting crystallisation of some phase with some smooth background. Images are represented in figure 4.6. More clear images of crystallisation on $Sr_{0.7}Na_{0.3}SiO_{3-\delta}$, with different magnification is represented in figure 4.7.

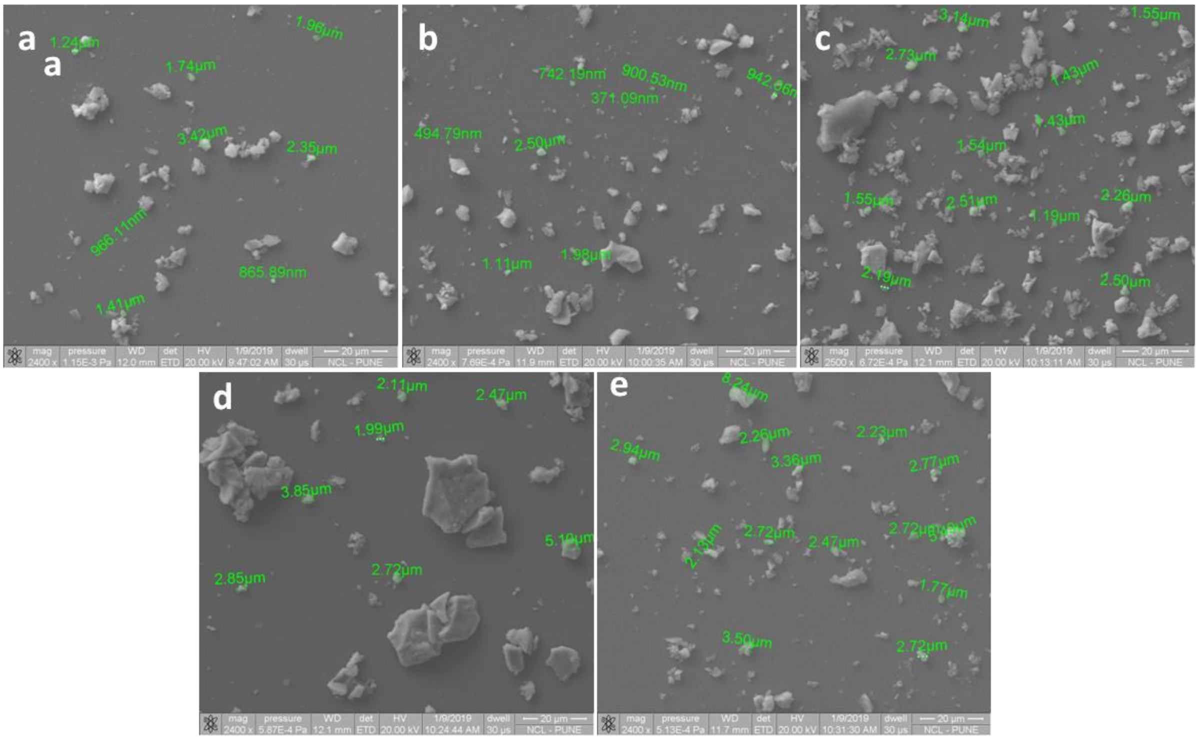

Figure 4.5: SEM images of a) $Sr_{0.7}Na_{0.3}Si_{0.95}Mn_{0.05}O_{3-\delta}$ b) $Sr_{0.7}Na_{0.3}Si_{0.95}Fe_{0.05}O_{3-\delta}$ c) $Sr_{0.7}Na_{0.3}Si_{0.95}Co_{0.05}O_{3-\delta}$ d) $Sr_{0.7}Na_{0.3}Si_{0.95}Ni_{0.05}O_{3-\delta}$ e) $Sr_{0.7}Na_{0.3}Si_{0.95}Cu_{0.05}O_{3-\delta}$

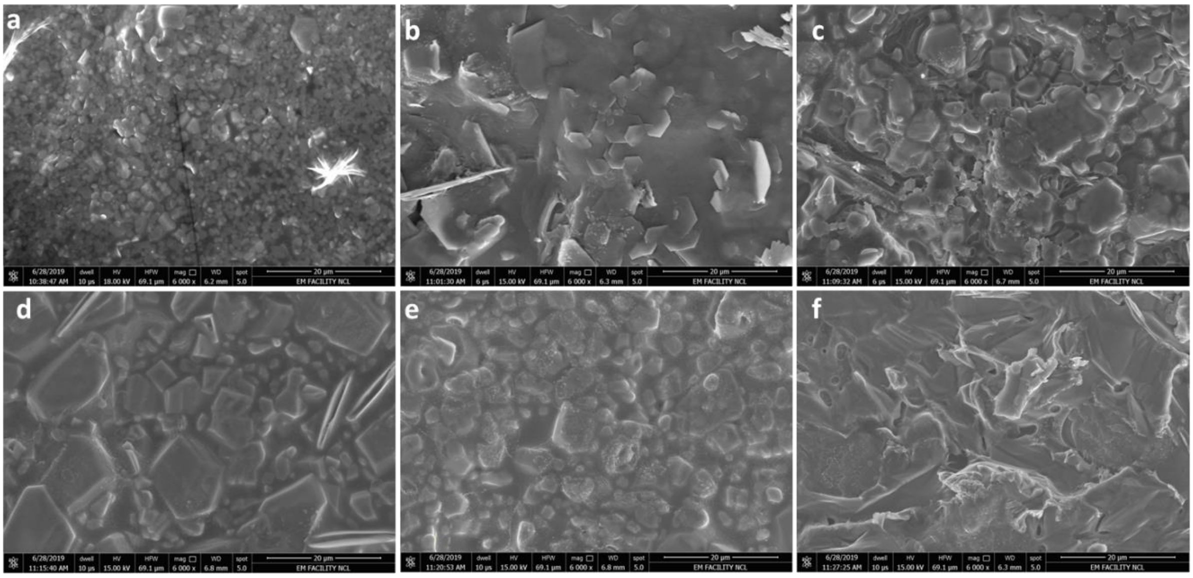

Figure 4.6: FE-SEM images of recrystallised pellets of a) $Sr_{0.7}Na_{0.3}SiO_{3-\delta}$ b) $Sr_{0.7}Na_{0.3}Si_{0.95}Mn_{0.05}O_{3-\delta}$ c) $Sr_{0.7}Na_{0.3}Si_{0.95}Fe_{0.05}O_{3-\delta}$ d) $Sr_{0.7}Na_{0.3}Si_{0.95}Co_{0.05}O_{3-\delta}$ e) $Sr_{0.7}Na_{0.3}Si_{0.95}Ni_{0.05}O_{3-\delta}$ f) $Sr_{0.7}Na_{0.3}Si_{0.95}Cu_{0.05}O_{3-\delta}$

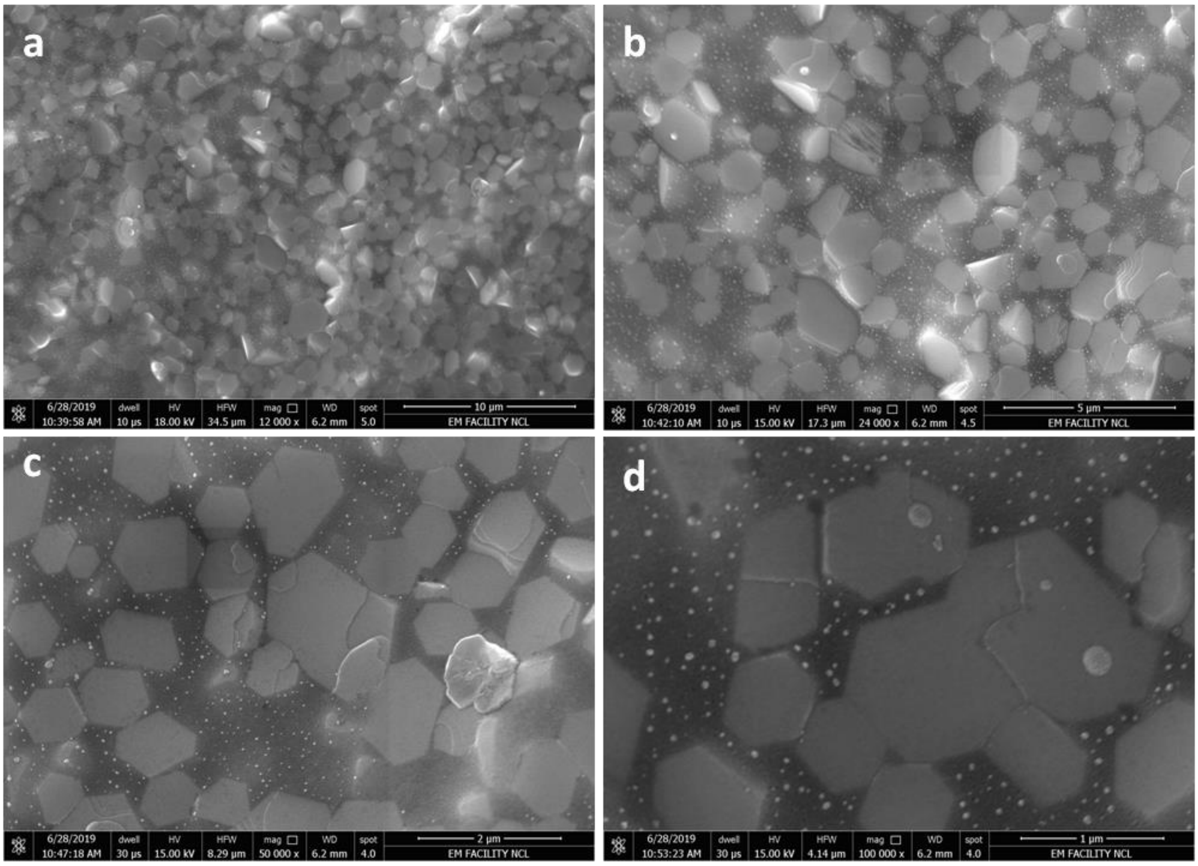

Figure 4.7: Clear image showing the crystallisation in $Sr_{0.7}Na_{0.3}SiO_{3-\delta}$ with different magnification

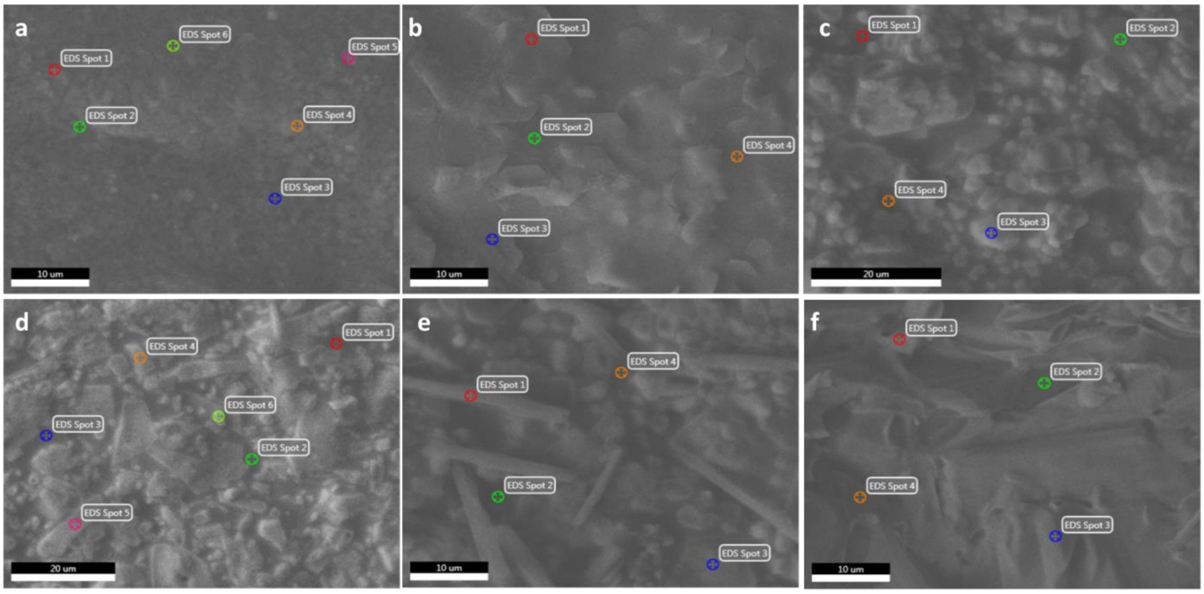

Figure 4.8: Different spots in recrystallised pellet selected for point analysis a) $Sr_{0.7}Na_{0.3}SiO_{3-\delta}$ b) $Sr_{0.7}Na_{0.3}Si_{0.95}Mn_{0.05}O_{3-\delta}$ c) $Sr_{0.7}Na_{0.3}Si_{0.95}Fe_{0.05}O_{3-\delta}$ d) $Sr_{0.7}Na_{0.3}Si_{0.95}Co_{0.05}O_{3-\delta}$ e) $Sr_{0.7}Na_{0.3}Si_{0.95}Ni_{0.05}O_{3-\delta}$ f) $Sr_{0.7}Na_{0.3}Si_{0.95}Cu_{0.05}O_{3-\delta}$

Elemental concentration in different points in the recrystallised pellets are analysed by EDS point analysis. The selected spots are given in figure 4.8 and the table 4.3 represents the surface elemental composition in different points. The visible needle shaped crystals are selected as point 1 and 3 (shape 1) and the plane background is selected as point 2 and 4 (shape 2). The elemental compositions in point 1 and 3 are almost in the range and same is the case with point 2 and 3 and the data tabulated is an average of two points. The data gives a clear idea on the phase separation of the materials. The elements are found to be distributed preferentially in certain areas. To cross check whether this type of separation is there in the green pellets also, as synthesised material is homogenised by ballmilling and pressed into pellet and further analysed by SEM and EDS. The points on the pellet for analysis are selected arbitrarily since there is no observable difference in the morphology before recrystallisation. The EDS profile of green pellet is represented in figure 4.9. Table 4.4 contains the data corresponding to the points. The same pellet is analysed after recrystallisation at 1050°C, denoted in the figure 4.8 and data incorporated in the table 4.3 making clear that the phase separation is visible only after recrystallistaion. Here, a clear phase separation with Na rich phase and Na lean phase as reported earlier is observed and the Na containing phase is rich in the dopant material.

Table 4.3: Surface composition of elements from EDS analysis

Materials	Weight (%)					
	Elements	Sr	Na	Si	M	O
$Sr_{0.7}Na_{0.3}SiO_{3-\delta}$	shape1	64.9	0.42	13.9	--	20.8
	shape2	35.3	7.9	23.3	--	33.5
$Sr_{0.7}Na_{0.3}Si_{0.95}Mn_{0.05}O_{3-\delta}$	Shape1	26.3	10.5	6.9	12.03	44.3
	Shape2	14.8	15.1	7.7	19.8	42.6
$Sr_{0.7}Na_{0.3}Si_{0.95}Fe_{0.05}O_{3-\delta}$	Shape1	20.4	10.9	18.4	13.1	37.2
	Shape2	59.3	0.69	11.5	0.23	28.26
$Sr_{0.7}Na_{0.3}Si_{0.95}Co_{0.05}O_{3-\delta}$	Shape1	66.45	0.36	13.6	0.7	18.9
	Shape2	30.5	7.12	20.5	10.6	31.3
$Sr_{0.7}Na_{0.3}Si_{0.95}Ni_{0.05}O_{3-\delta}$	Shape1	52.1	2.12	10.6	0.6	34.61
	Shape2	34.1	11.1	14.4	4.7	35.6
$Sr_{0.7}Na_{0.3}Si_{0.95}Cu_{0.05}O_{3-\delta}$	Shape1	14.5	26.5	9.4	7.9	41.6
	Shape2	15.5	19.2	15.8	5.95	43.5

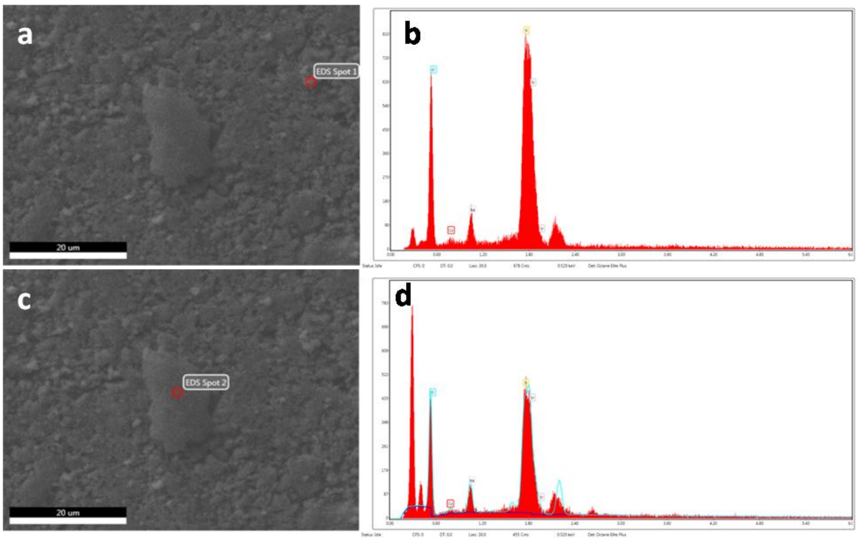

Figure 4.9: SEM-EDS point analysis spot and corresponding EDS profile of the green pellet made by ball milling the as synthesised material

Table 4.4: EDS point analysis data of the green pellet

Element	Sr	Na	Si	Co	O
Point1	41.4	4.7	17.7	2.6	33.5
Point2	40.8	6.9	15.8	1.6	34.8
Overall area	43.3	5.4	17.6	2.7	30.9

Surface mapping of the recrystallised materials are conducted by XPS mapping also. The data is represented in figure 4.10 and a close analysis of the map clearly indicates the differential concentration of elements on the surface. In the 30micron area, higher metal concentration is distributed in specific areas as observed by the colour difference in the map supporting the phase segregation in the material.

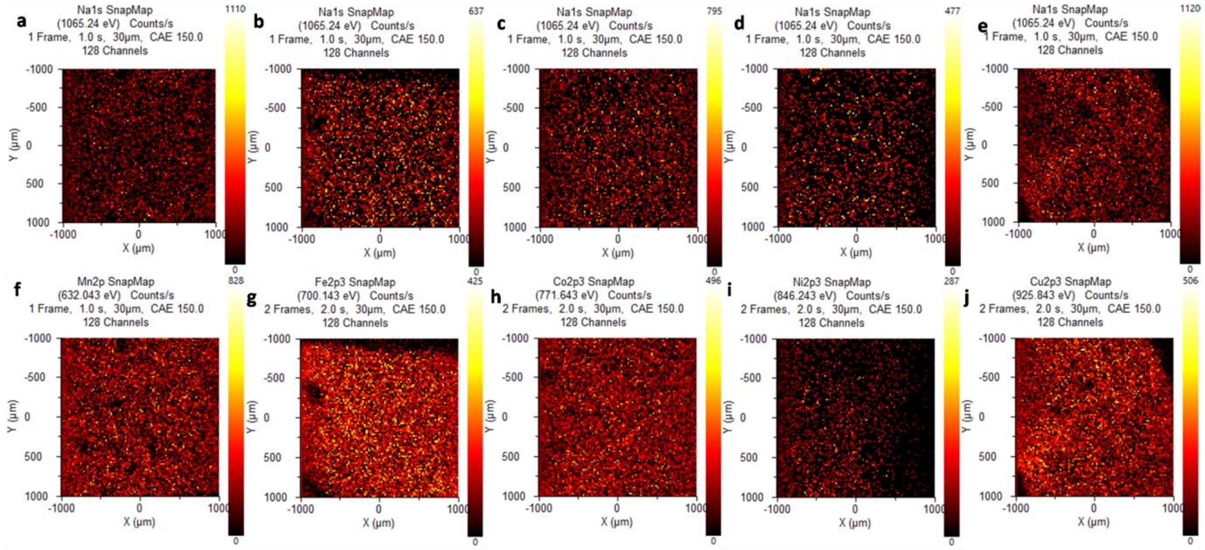

Figure 4.10: XPS map of surface elements where a) and f) Na and Mn in $Sr_{0.7}Na_{0.3}Si_{0.95}Mn_{0.05}O_{3-\delta}$ b) and g) Na and Fe in $Sr_{0.7}Na_{0.3}Si_{0.95}Fe_{0.05}O_{3-\delta}$ c) and h) Na and Co in $Sr_{0.7}Na_{0.3}Si_{0.95}Co_{0.05}O_{3-\delta}$ d) and i) Na and Ni in $Sr_{0.7}Na_{0.3}Si_{0.95}Ni_{0.05}O_{3-\delta}$ e) and j) Na and Cu in $Sr_{0.7}Na_{0.3}Si_{0.95}Cu_{0.05}O_{3-\delta}$

Interesting behavior of amorphisation and recrystallisation is observed with material on ballmilling and reheating. The material turned in to amorphous type of phase with broad peaks on ballmilling at 400rpm for 2h, where the impurity peak completely disappeared and it regains its original phase on recrystallisation at 1050°C. The behavior is represented with XRD pattern in figure 4.11

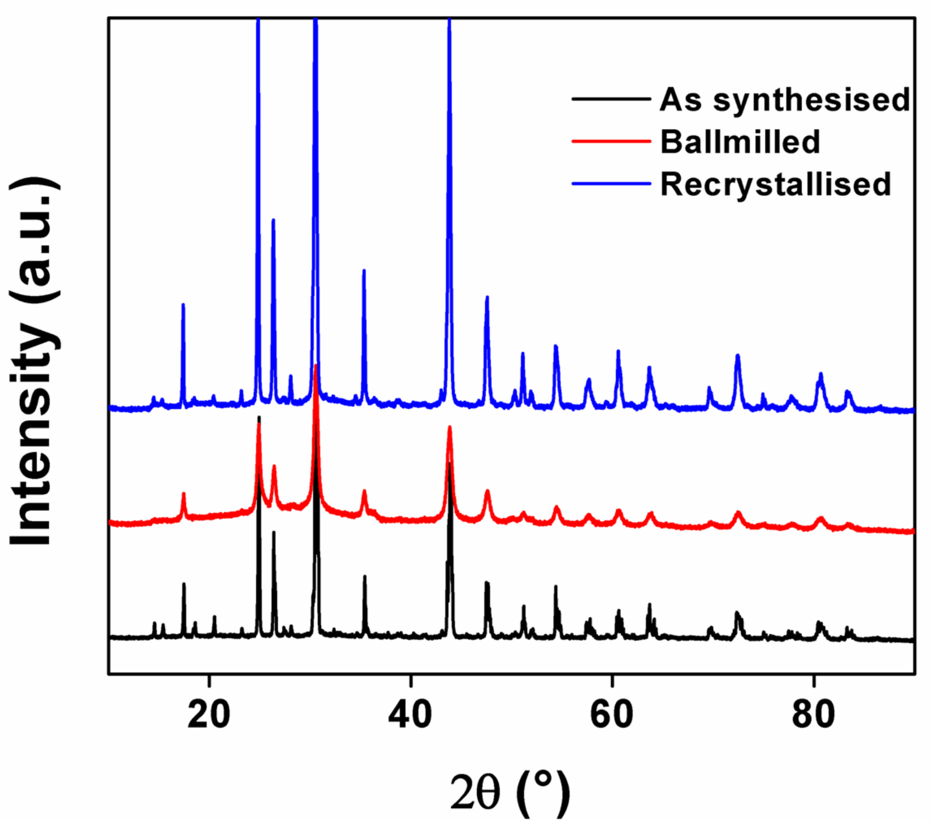

Figure 4.11: XRD pattern showing amorphisation on ballmilling and regaining the original phase on recrystallisation

Materials are studied by NMR spectroscopy to understand more about the local structure and phase. Figure 4.12 represents the ^{29}Si MAS NMR spectra of the samples. ^{29}Si NMR of $SrSiO_3$ has three peaks, the peak at -86.5ppm corresponds to Si_3O_9 sites of α-$SrSiO_3$ phase, additional peaks at -96.5ppm and -111.67ppm correspond to Q3 and Q4 sites probably from the impurity Sr_2SiO_4 or unreacted SiO_2. With Na doping in addition to the above peaks, three more peaks emerged in the spectrum. The peak at -86.47ppm corresponds to the α-$SrSiO_3$ phase, broad peaks at -82.66ppm, -89.47ppm and -98.81ppm correspond to glassy amorphous phase. Other two peaks at -94.75ppm and -105.82ppm can be assigned to the impurity SiO_2 phase. The glassy phase and SiO_2 phase observed in the NMR is not observable from the PXRD. Further, Co doped material as synthesised and ball milled are also analysed by NMR. Both these materials exhibited similar NMR spectra. The peak at -85 to -86ppm can be assigned to Si_3O_9 sites of α-

$SrSiO_3$. As observed for Na doped material, peak corresponding to the amorphous glassy phase is observed at -82ppm and -89ppm in Co doped material also. Peaks at -92 and -102ppm corresponding to SiO_2 are also present in the NMR spectra of both varieties. Interestingly, on Co incorporation, two additional different environments are observed around -72ppm and a sharp peak around -108ppm compared to the rest of the materials[4, 12, 15, 17, 18].

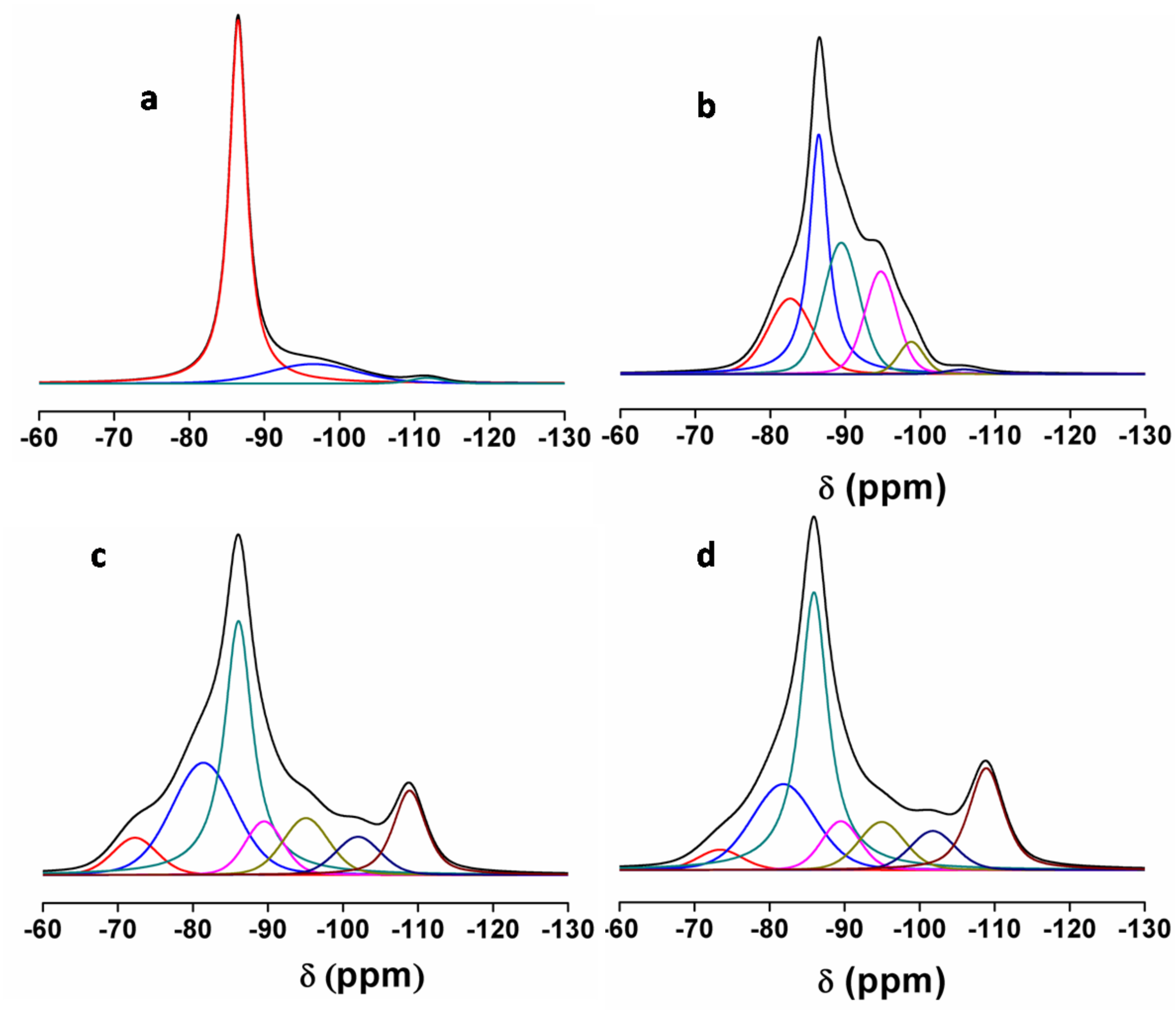

Figure 4.12: ^{29}Si MAS NMR spectra of a) $SrSiO_3$ b) $Sr_{0.7}Na_{0.3}SiO_{3-\delta}$ c) as synhesised$Sr_{0.7}Na_{0.3}Si_{0.95}Co_{0.05}O_{3-\delta}$ and d) ball milled $Sr_{0.7}Na_{0.3}Si_{0.95}Co_{0.05}O_{3-\delta}$

^{23}Na NMR spectra of the samples are represented in figure 4.13. The peaks at 8.95 and 2.8ppm in $Sr_{0.7}Na_{0.3}SiO_{3-\delta}$ correspond to a glassy type phase. These peaks are present in NMR spectra of as synthesized and ball milled $Sr_{0.7}Na_{0.3}Si_{0.95}Co_{0.05}O_{3-\delta}$. In addition a broad and a sharp peak is also observed in the spectrum indicating the formation of multiple phases[4, 12, 15, 17, 18].

^{17}O NMR spectrum after ^{17}O enrichment in ball milled $Sr_{0.3}Na_{0.7}Si_{0.95}Co_{0.05}O_{3-\delta}$ as mentioned in the experimental section is given in figure 4.14. The detection of ^{17}O in the spectrum proves an uptake of O in this material and indicates the probability of O vacancies. Three sharp peaks at chemical shift 48ppm, 99.1ppm and, 377.8ppm are observed clearly indicating three different oxygen environments in the lattice[18, 27]. Combining the results of NMR with SEM and EDS data, a possibility of phase separation can be proposed. The phases which are not observed with XRD are visible in the NMR results. Clear phase segregation is observed in SEM only after recrystallistaion, whereas NMR results suggest that the phase segregation exists even with the as synthesised form and ball milled form of the material

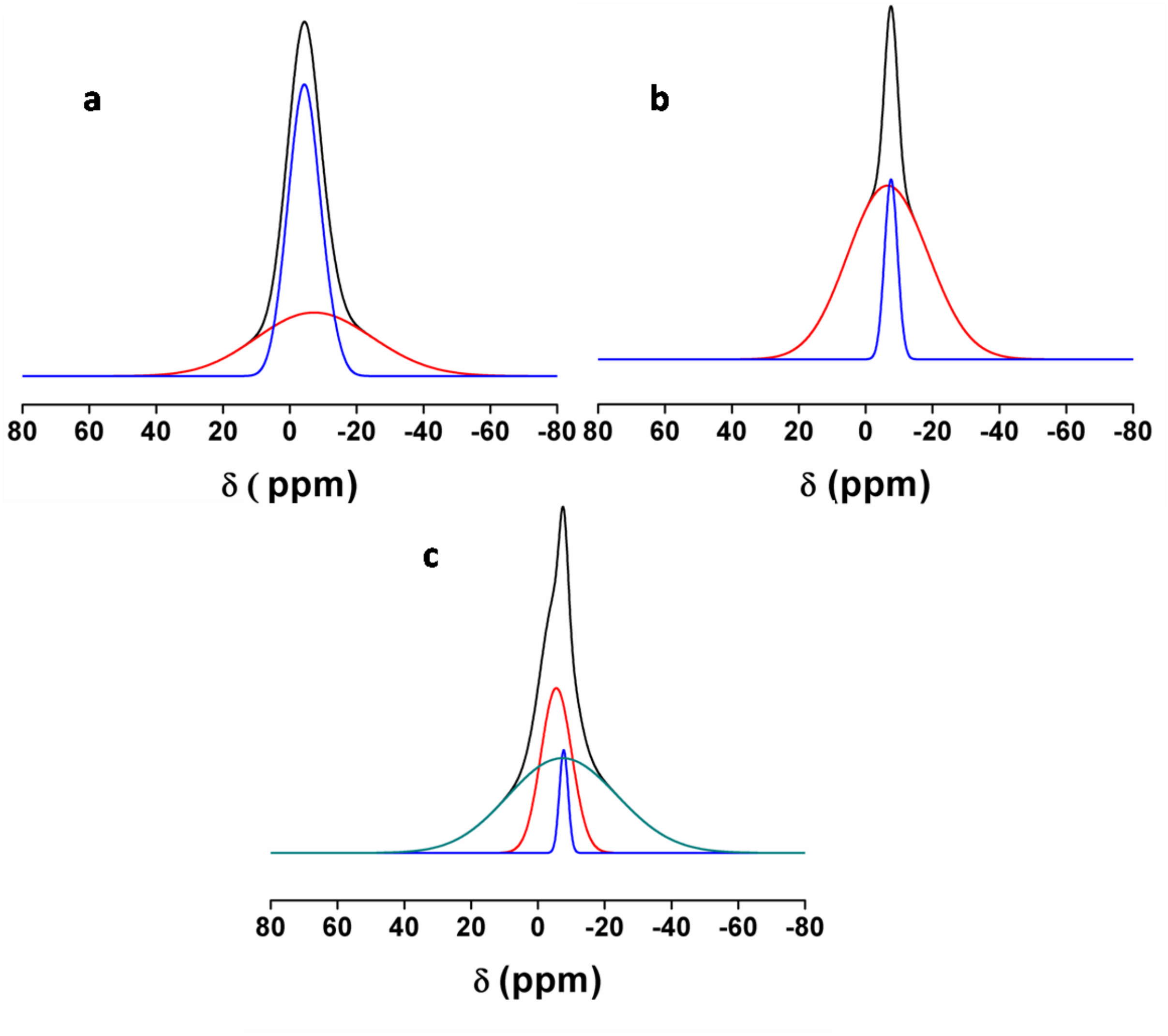

Figure 4.13: ^{23}Na NMR spectra of a) $Sr_{0.7}Na_{0.3}SiO_{3-\delta}$ b) as synthesised $Sr_{0.7}Na_{0.3}Si_{0.95}Co_{0.05}O_{3-\delta}$ and c) ball milled $Sr_{0.7}Na_{0.3}Si_{0.95}Co_{0.05}O_{3-\delta}$

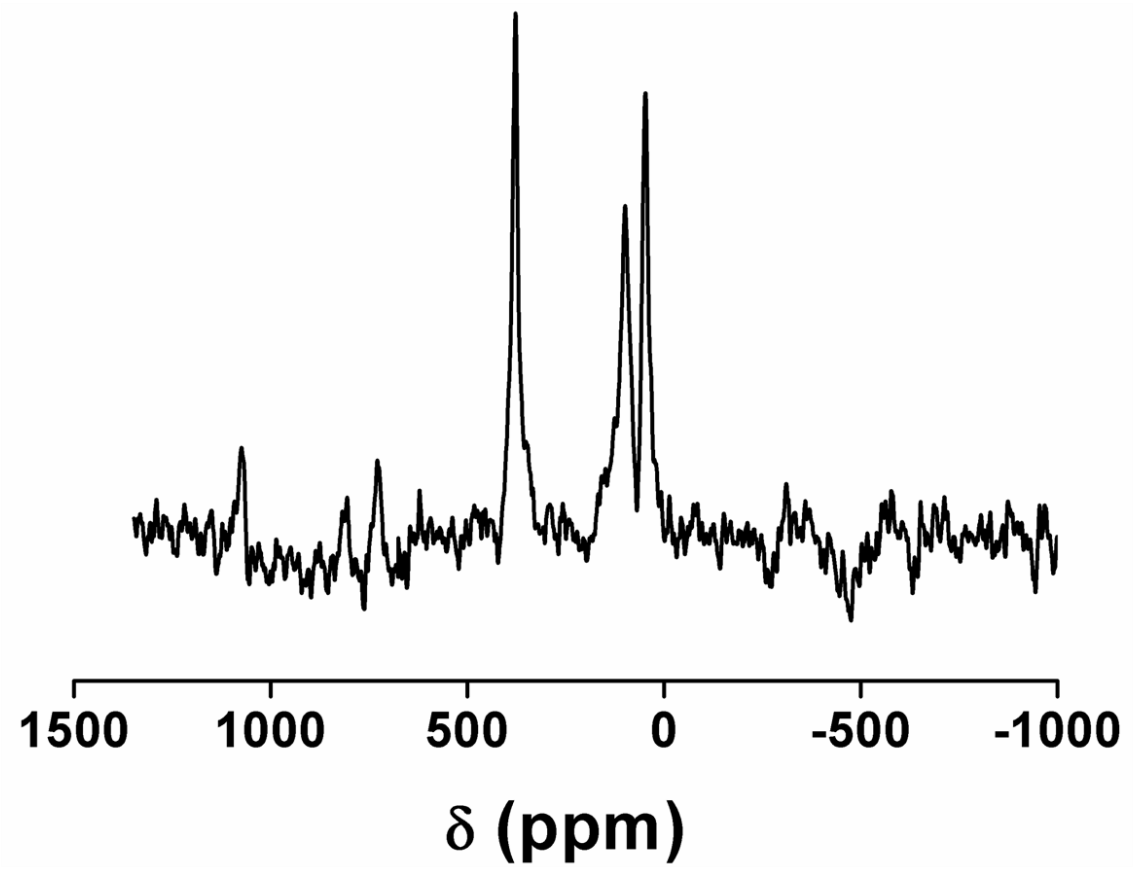

Figure 4.14: ^{17}O NMR spectrum after ^{17}O enrichment in ball milled $Sr_{0.7}Na_{0.3}Si_{0.95}Co_{0.05}O_{3-\delta}$

4.3.2. Electrochemical Characterization

Detailed electrochemical studies of these compounds are carried out by CV and RDE method under alkaline medium at room temperature

4.3.2.1. ORR Activity in Alkaline Medium

ORR activity is monitored in 0.1M KOH with N_2 and O_2 saturation. Figure 4.15a shows the cyclic voltammogram recorded with 50mV/s scan rate and 900 rpm rotation. The dotted lines represent the scan in N_2 saturation and in O_2 saturation, a clear reduction peak is observed, indicating the reduction activity of the material. For a clear insight on the activity trend with the metal doping, linear sweep voltammogram has been recorded with a scan rate of 10mV/s, a blank run is conducted by each of the sample in N_2 saturation and 0rpm rotation. Figure 4.15b shows the blank subtracted data collected at 1600 rpm. Fe doped material showed a better onset of 0.893V *vs* RHE with multiple steps in the profile, similarly for Co also there are two step onset potential, first at 0.893 V and second at 0.735V *vs* RHE, Mn doping also resulted in a good onset value of 0.783V *vs* RHE and rest of the compounds exhibit somewhat similar onset of ~0.72V *vs* RHE. Analysing the profile quality and current response, Co doped material exhibited a better current response followed by Ni doped material. Individual LSVs of the material represented in figure 4.16.

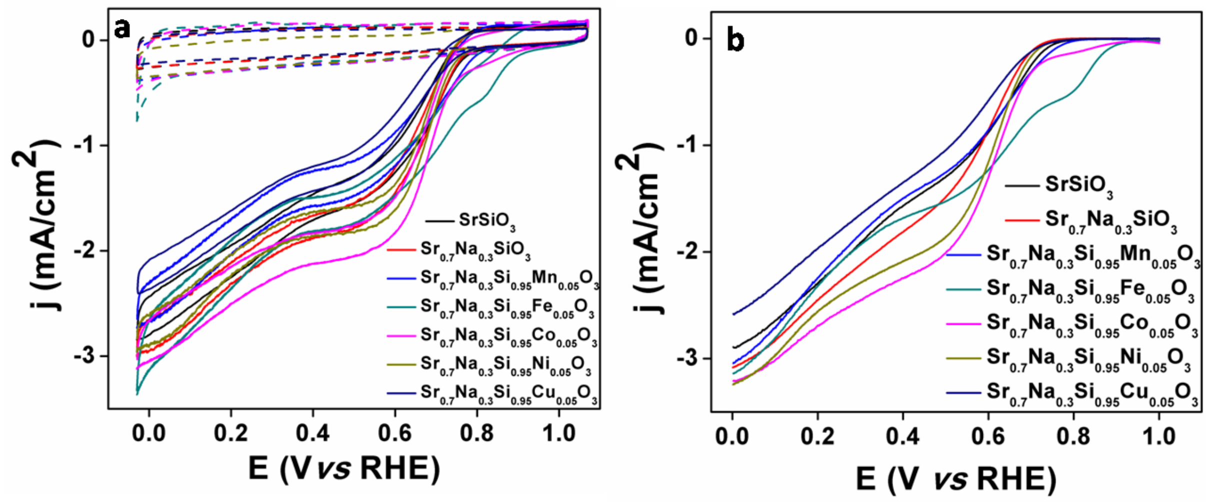

Figure 4.15: a) Cyclic voltammogram recorded at 900 rpm and 50 mV/s scan rate, dotted line represents the scan in N_2 saturation and solid line represents that in O_2 saturation. b) Linear sweep voltammogram in O_2 saturation withscan rate 10mV/s and 1600 rpm rotation speed

Detailed analysis of oxygen reduction behaviour is done by Tafel and K-L calculations as explained in annexure[28, 29]. Figure 4.14a represents the Tafel plot and the slope values are in the order $SrSiO_3$ (-320mV/d) > $Sr_{0.7}Na_{0.3}SiO_{3-\delta}$ (-222 mV/d) > $Sr_{0.7}Na_{0.3}Si_{0.95}Co_{0.05}O_{3-\delta}$ (-153 mV/d) > $Sr_{0.7}Na_{0.3}Si_{0.95}Ni_{0.05}O_{3-\delta}$ (-129 mV/d) > $Sr_{0.7}Na_{0.3}Si_{0.95}Mn_{0.05}O_{3-\delta}$ (-119 mV/d) > $Sr_{0.7}Na_{0.3}Si_{0.95}Cu_{0.05}O_{3-\delta}$ (-111 mV/d) > $Sr_{0.7}Na_{0.3}Si_{0.95}Fe_{0.05}O_{3-\delta}$ (-98 mV/d), indicating a clear improvement of values on transition metal doping. In the transition metal doped variety, the first electron transfer is the rate determining step and in Fe doped material a shift of *rds* in the mechanism to surface migration after the first electron reduction is observed[29]. K-L slope values are almost similar ranging from 2.9 to 3.8 for the materials indicating an intermediate electron transfer process.

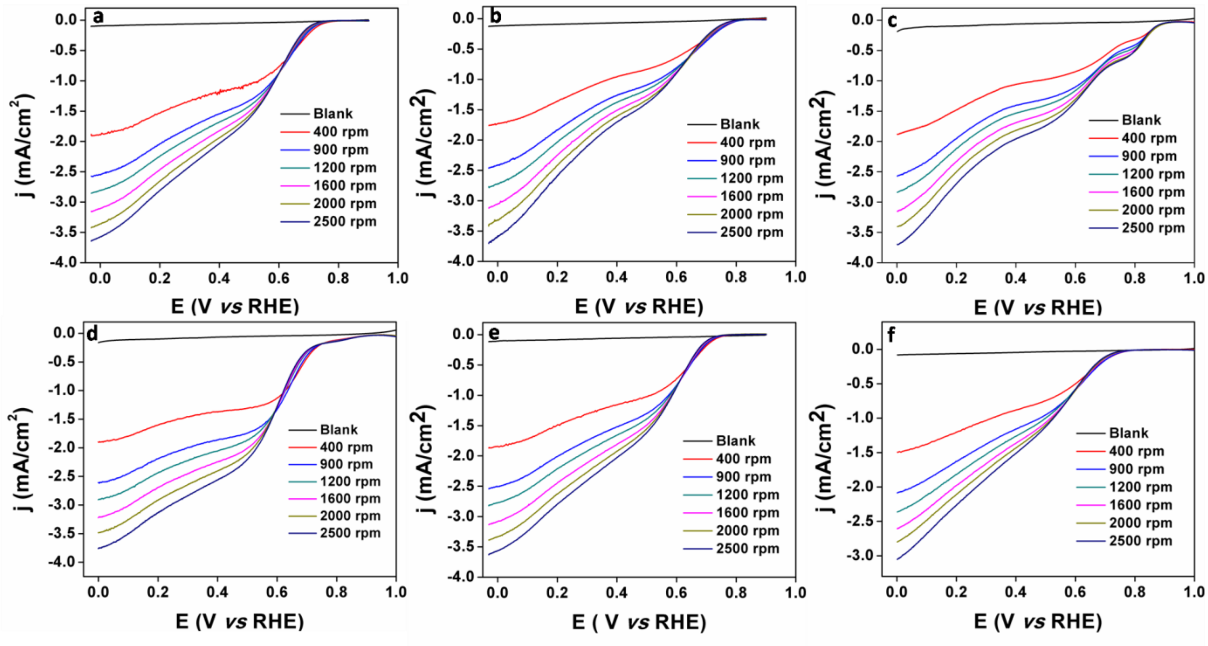

Figure 4.16: Linear sweep voltammograms at various rotation speeds recorded with 10mV/s scan rate in O_2 saturation, of a) $Sr_{0.7}Na_{0.3}SiO_{3-\delta}$ b) $Sr_{0.7}Na_{0.3}Si_{0.95}Mn_{0.05}O_{3-\delta}$ c) $Sr_{0.7}Na_{0.3}Si_{0.95}Fe_{0.05}O_{3-\delta}$ d) $Sr_{0.7}Na_{0.3}Si_{0.95}Co_{0.05}O_{3-\delta}$ e) $Sr_{0.7}Na_{0.3}Si_{0.95}Ni_{0.05}O_{3-\delta}$ f) $Sr_{0.7}Na_{0.3}Si_{0.95}Cu_{0.05}O_{3-\delta}$

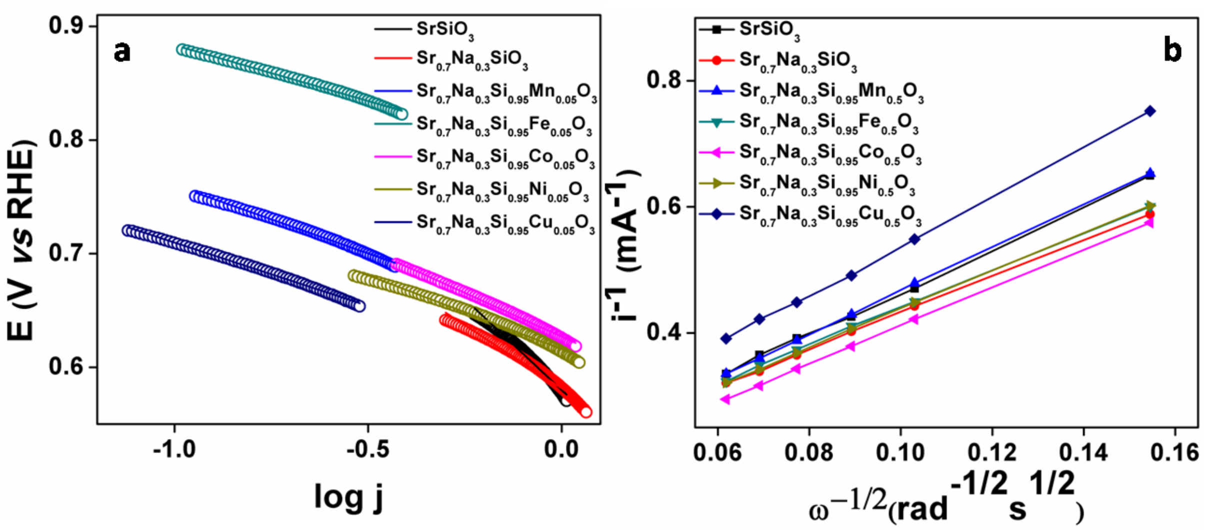

Figure 4.17: a) Tafel plot calculated from LSV data at 1600rpm, circles represent the data and lines represent the linear fit of the data. b) K-L plot calculated at 0.13V *vs* RHE from LSV data with various rotation speeds

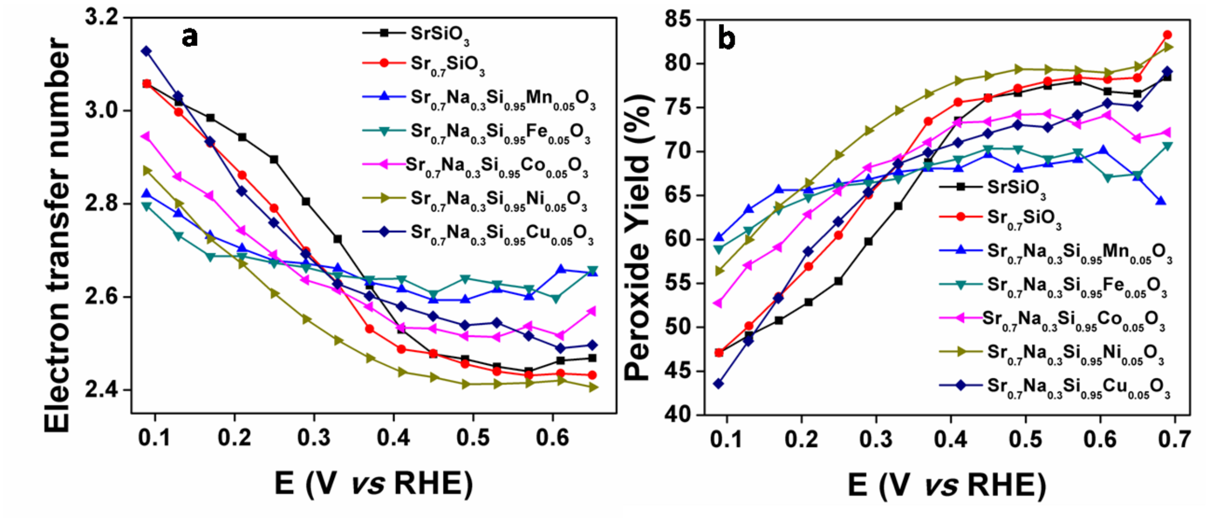

Figure 4.18: Dependence of a) electron transfer number and b) peroxide yield on applied potential, calculated from RRDE experiments with O_2 saturation, 10mV/s scanrate and 1600 rpm rotation speed of working electrode

Direct calculation of electron transfer number and peroxide yield is done by using RRDE experiments[30]. Figure 4.18a represents the electron transfer number plot calculated from RRDE experiments. All the materials exhibited intermediate mechanism as observed from the K-L slope values, the electron transfer number approaches to ~3 at higher potential only. Figure 4.18b represents the peroxide formation as a function of applied potential, at lower potential the peroxide yield is very high suggesting a 2 electron path way and at higher potential the yield reduced, approaching a direct reduction of oxygen to hydroxide.

4.3.2.2. OER Activity in Alkaline Medium

OER analysis is conducted in 0.1M KOH with N_2 saturation. Figure 4.19a represents the LSV at 1600rpm, with 10mV/s scan rate. Analysis clearly indicates that the Ni doped material exhibits a better onset and current response compared to the rest of the materials (inset image represents the current response plotted at 1.6V *vs* RHE). Fe doping and Co doping also improves the current and onset in comparison to the rest of the materials. Figure 4.19b represents the Tafel slope for oxygen evolution reaction, calculated from LSV at 1600rpm. Slope values of the materials are almost same indicating a similar rate determining step in the mechanism for all of the materials.

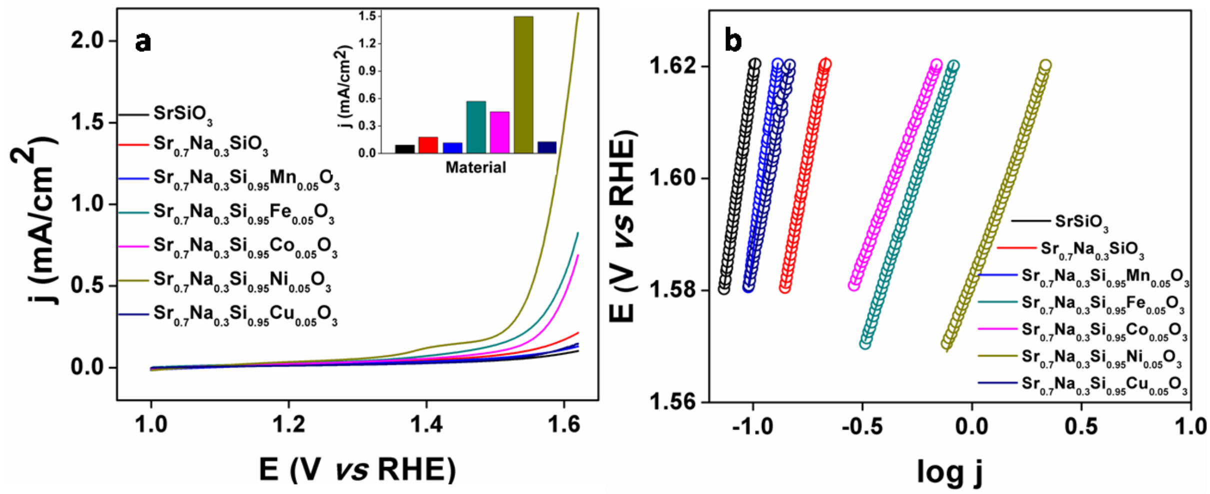

Figure 4.19: a) OER LSV with scan rate 10mV/s collected in N_2 saturation. Inset image compares the current density at 1.6V *vs* RHE. b) OER Tafel plots calculated from LSV data, circles represent data points and lines represent linear fit of the data

4.3.3. High Temperature Analysis

4.3.3.1. Non Ambient XRD

Materials are analysed for their phase stability at high temperatures and different gas atmosphere by non-ambient XRD. Figure 4.20 represents the non-ambient PXRD patterns collected from room temperature to 800°C in O_2 and N_2 gas atmosphere separately. The diffraction pattern is collected after cooling down the system also, to ensure the phase stability. The materials are found to exhibit excellent phase stability in both the atmospheres even at 800°C. The material retains its phase even after cooling down from the high temperature. Also we could not observe any crystallisation of glassy $Na_2Si_2O_5$ phase reported earlier by many groups[7, 18]. The glassy impurity phase, which was found to be the reason of high conductivity is reported to crystallise after 550°C and is stable as a crystalline phase at higher temperatures[14].

Figure 4.18 shows the non-ambient PXRD recorded in 5%H_2/Ar atmosphere at different temperatures. The material retains the original phase even in the reducing atmosphere, evidenced by the absence of any extra peaks emerging in the non-ambient conditions.

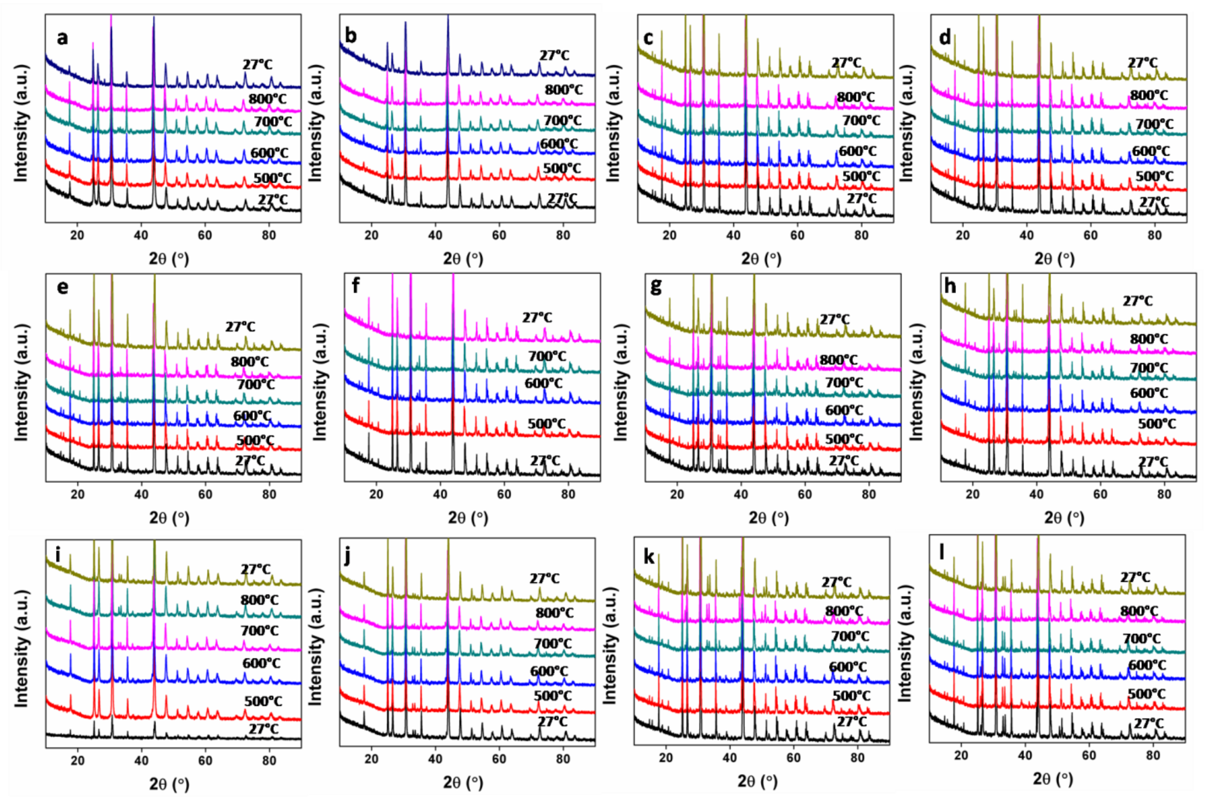

Figure 4.20: Non ambient XRD pattern of a) and b) $Sr_{0.7}Na_{0.3}SiO_{3-\delta}$ c) and d) $Sr_{0.7}Na_{0.3}Si_{0.95}Mn_{0.05}O_{3-\delta}$ e) and f) $Sr_{0.7}Na_{0.3}Si_{0.95}Fe_{0.05}O_{3-\delta}$ g) and h) $Sr_{0.7}Na_{0.3}Si_{0.95}Co_{0.05}O_{3-\delta}$ i) and j) $Sr_{0.7}Na_{0.3}Si_{0.95}Ni_{0.05}O_{3-\delta}$ k) and l) $Sr_{0.7}Na_{0.3}Si_{0.95}Cu_{0.05}O_{3-\delta}$ in N_2 and O_2 atmosphere respectively

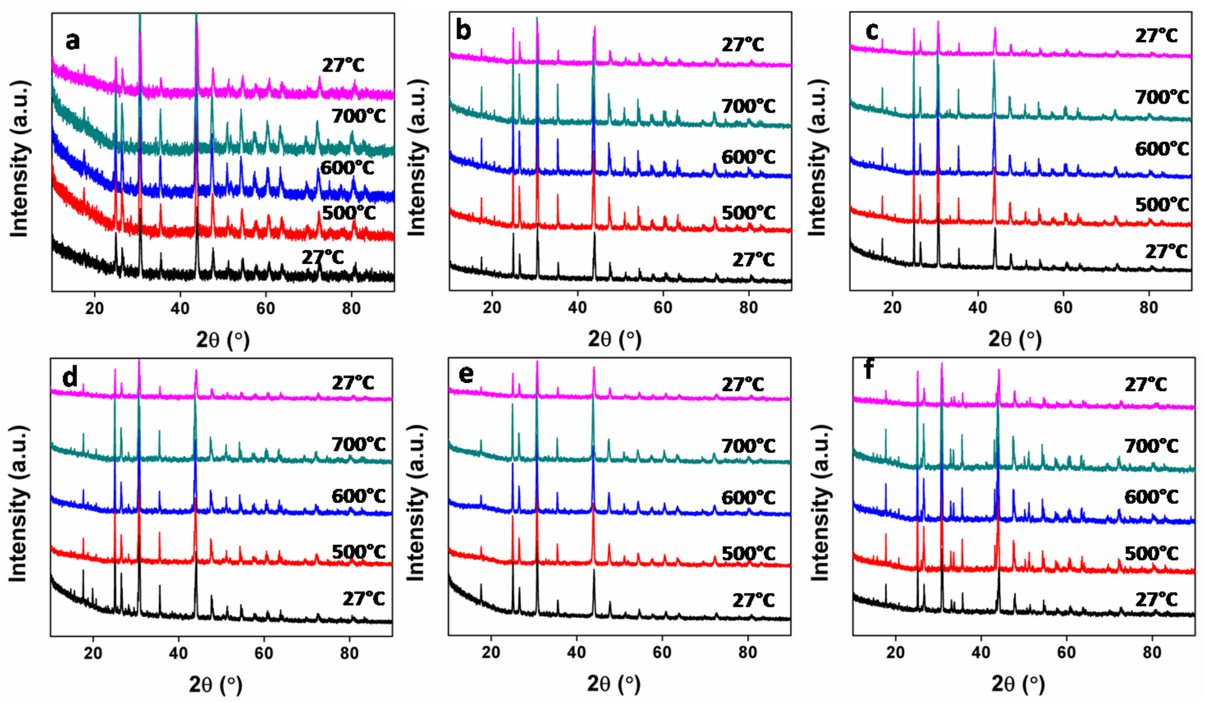

Figure 4.21: Non ambient XRD pattern of a) $Sr_{0.7}Na_{0.3}SiO_{3-\delta}$ b) $Sr_{0.7}Na_{0.3}Si_{0.95}Mn_{0.05}O_{3-\delta}$ c) $Sr_{0.7}Na_{0.3}Si_{0.95}Fe_{0.05}O_{3-\delta}$ d) $Sr_{0.7}Na_{0.3}Si_{0.95}Co_{0.05}O_{3-\delta}$ e) $Sr_{0.7}Na_{0.3}Si_{0.95}Ni_{0.05}O_{3-\delta}$ f) $Sr_{0.7}Na_{0.3}Si_{0.95}Cu_{0.05}O_{3-\delta}$ in H_2 atmosphere

4.3.3.2. High temperature Conductivity

Conductivity of the materials at varying temperatures is analysed by EIS technique using CH instrument. The sample pellet is sintered at 1100°C for densification and gold coated after polishing both the sides for better contact with the electrode before analysis. The electrode set up used is explained in chapter 2B. Polycrystalline material will have contribution from grain, grain boundary and electrode surface to the overall conductivity and can be separated by the Bauerle type model[31, 32]. The schematic of the grain-grain boundary model and corresponding Bauerle equivalent circuit is represented below in figure 4.22.

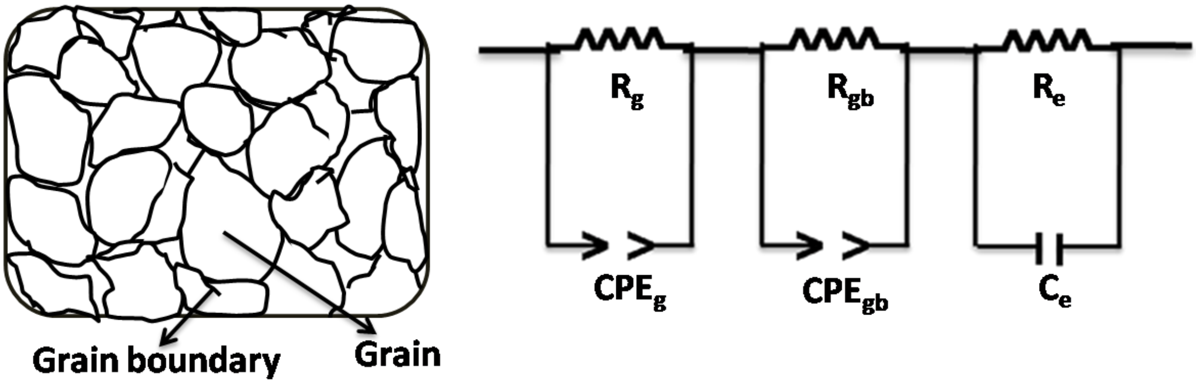

Figure 4.22: Polycrystalline ceramic sample with contribution from grain and grain boundary and equivalent circuit used to represent the bulk contribution from grain, boundary and electrode surface

According to the above mentioned equivalent circuit, Nyquist plot should reflect three consecutive semicircles. However we could not observe three semicircles probably due to the merging of semicircles in the frequency range applied. In perfectly dense samples separate contribution from grain and grain boundary may not be visible as separate semicircles and only an overall resistance value could be obtained[33]. The contribution from each component can be identified from the value of capacitance in parallel to the resistor after fitting with the above mentioned equivalent circuit.

Table 4.5: High temperature resistivity calculated from EIS analysis

	Material	Atmosphere	Temperature (°C)				E_a ($Jmol^{-1}$)
			500	600	700	800	
Resistivity (kΩ cm)	$SrSiO_3$	N_2	2534.7	1923.5	500.5	425.2	21.97
		O_2	1452.5	264.8	126.5	44.1	38.17
		1:1 N_2:O_2	1517.7	600.3	43.6	15.2-2	53.19
	$Sr_{0.7}Na_{0.3}SiO_{3-\delta}$	N_2	203.3	132.7	33.1	11.5	32.1
		O_2	736.1	171.9	42.1	15.4	43
		1:1 N_2:O_2	914.2	266.9	79.3	21.9	40.6
	$Sr_{0.7}Si_{0.3}Mn_{0.05}Si_{0.95}O_{3-\delta}$	N_2	9.96	2.41	1.4	1.3	22.62
		O_2	652.5	147.8	47.13	5.7	49.84
		1:1 N_2:O_2	15.3	11.5	2.41	1.52	27.52
	$Sr_{0.7}Si_{0.3}Fe_{0.05}Si_{0.95}O_3$	N_2	80.8	15.3	3.9	1.5	34.78
		O_2	217.7	130.2	29.1	5.7	58.31
		1:1 N_2:O_2	418.6	18.4	3.7	2.5	44.58
	$Sr_{0.7}Si_{0.3}Co_{0.05}Si_{0.95}O_{3-\delta}$	N_2	916.6	284.5	47.9	15.3	46.02
		O_2	457.3	177.9	48.1	1.2	23.8
		1:1 N_2:O_2	1831	677	84.8	21.2	50.18
	$Sr_{0.7}Si_{0.3}Ni_{0.05}Si_{0.95}O_{3-\delta}$	N_2	405.5	318.3	59.1	18.2	34.98
		O_2	370.5	107.5	26.7	10.7	39.68
		1:1 N_2:O_2	1047	324.6	61.3	16.4	46.14
	$Sr_{0.7}Si_{0.3}Cu_{0.05}Si_{0.95}O_{3-\delta}$	N_2	1238	652.4	87.7	55.6	31.76
		O_2	1952	256.1	43.3	17.2	53.46
		1:1 N_2:O_2	1704	343.4	83.3	16.5	50.22

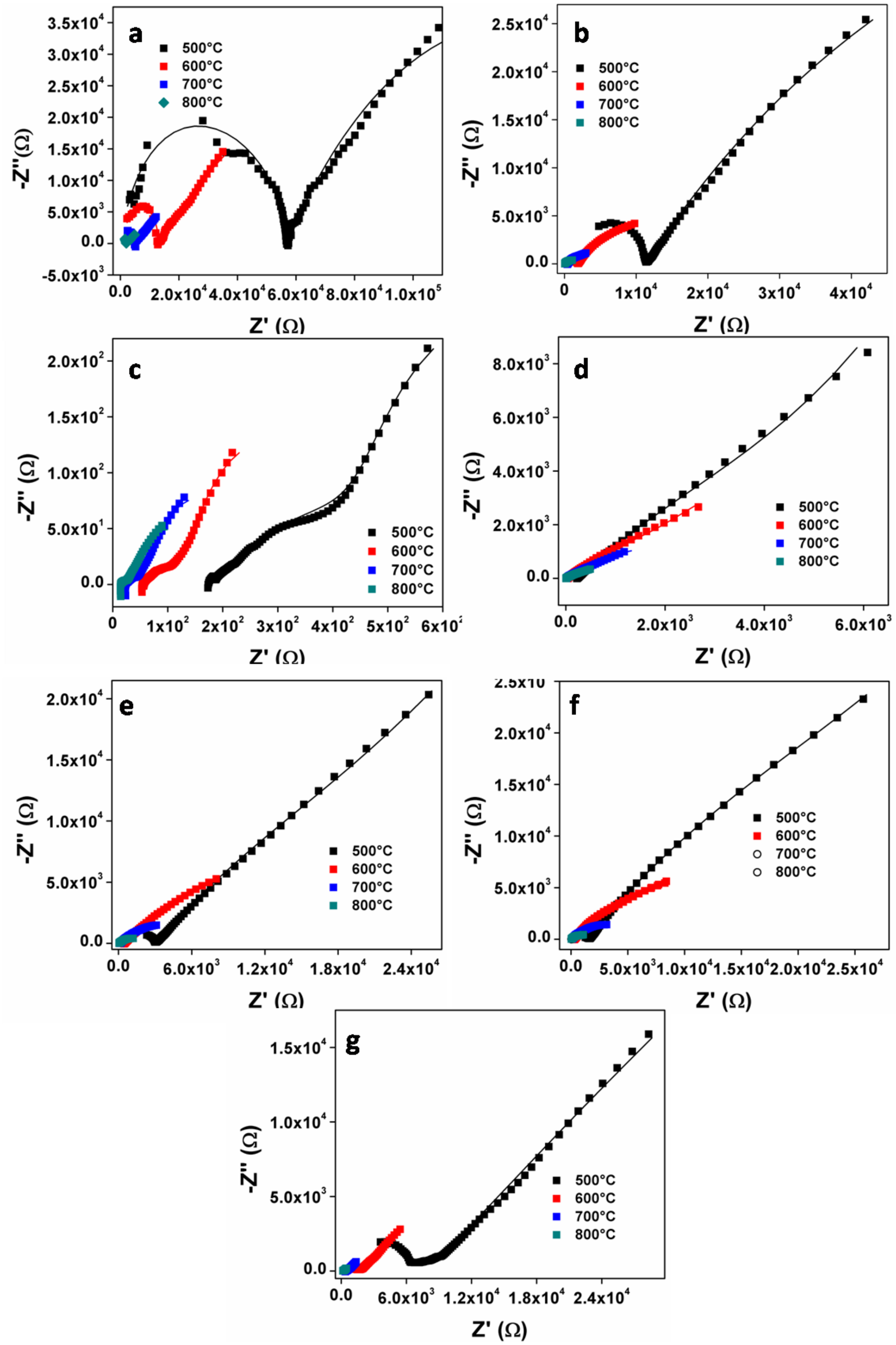

Figure 4.23: Nyquist plot representation of impedance data with varying temperature in N_2 atmosphere of a) $SrSiO_3$ b) $Sr_{0.7}Na_{0.3}SiO_3$ c) $Sr_{0.7}Na_{0.3}Si_{0.95}Mn_{0.05}O_{3-\delta}$ d) $Sr_{0.7}Na_{0.3}Si_{0.95}Fe_{0.05}O_{3-\delta}$ e) $Sr_{0.7}Na_{0.3}Si_{0.95}Co_{0.05}O_{3-\delta}$ f) $Sr_{0.7}Na_{0.3}Si_{0.95}Ni_{0.05}O_{3-\delta}$ g) $Sr_{0.7}Na_{0.3}Si_{0.95}Cu_{0.05}O_{3-\delta}$ where the symbols and lines represents the original data and the fit respectively

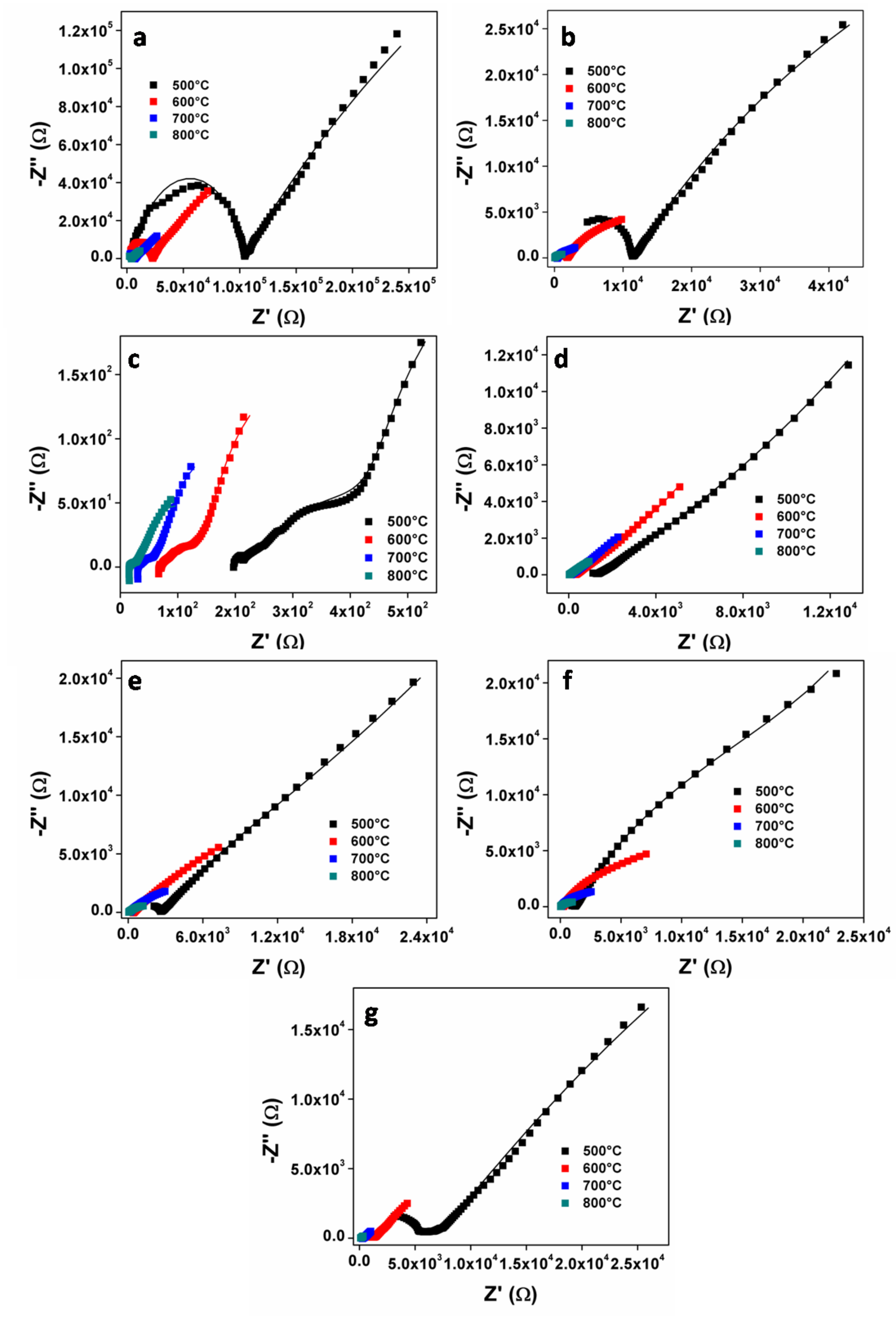

Figure 4.24: Nyquist plot representation of impedance data with varying temperature in O_2 atmosphere of a) $SrSiO_3$ b) $Sr_{0.7}Na_{0.3}SiO_3$ c) $Sr_{0.7}Na_{0.3}Si_{0.95}Mn_{0.05}O_{3-\delta}$ d) $Sr_{0.7}Na_{0.3}Si_{0.95}Fe_{0.05}O_{3-\delta}$ e) $Sr_{0.7}Na_{0.3}Si_{0.95}Co_{0.05}O_{3-\delta}$ f) $Sr_{0.7}Na_{0.3}Si_{0.95}Ni_{0.05}O_{3-\delta}$ g) $Sr_{0.7}Na_{0.3}Si_{0.95}Cu_{0.05}O_{3-\delta}$ where the symbols and lines represents the original data and the fit respectively

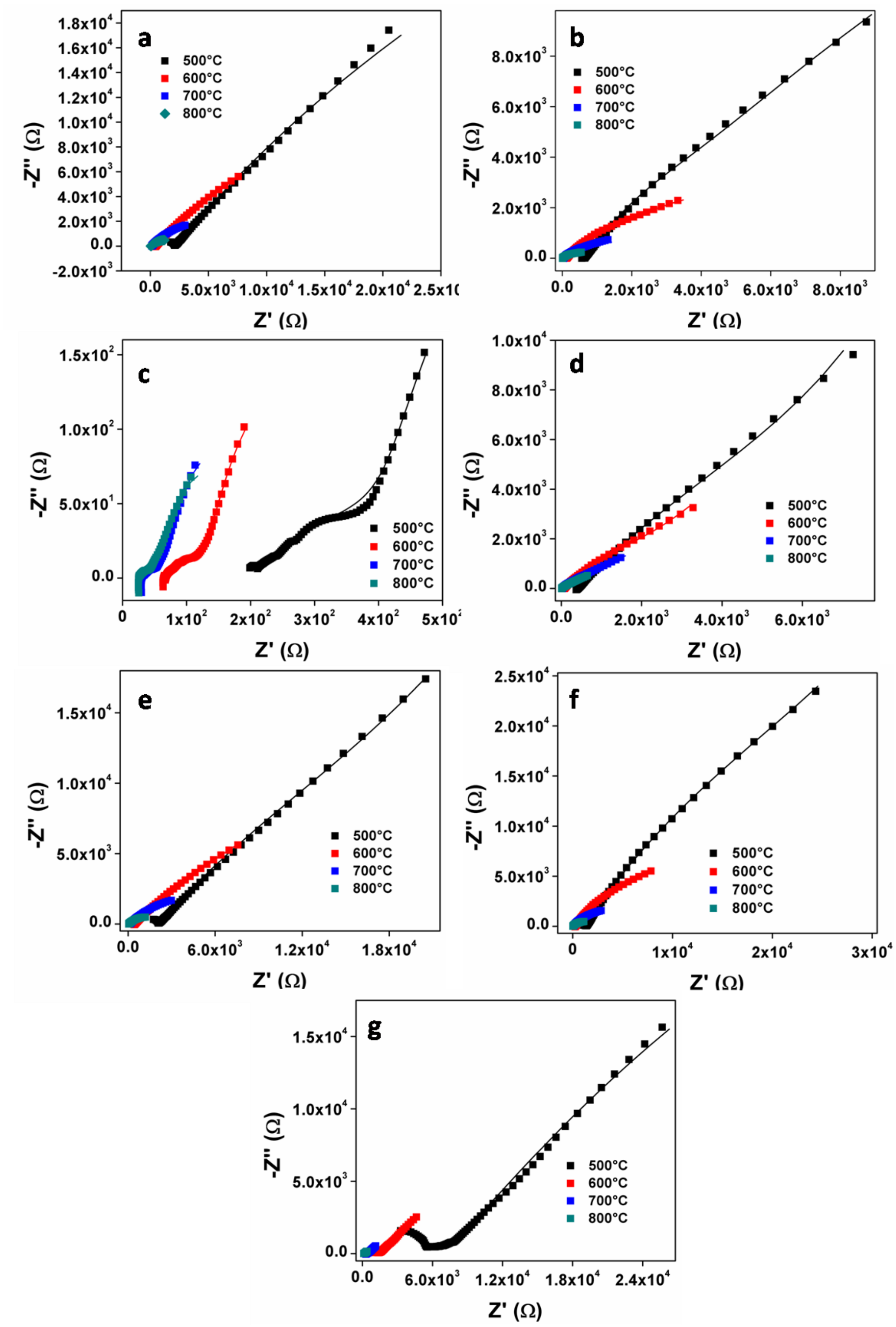

Figure 4.25: Nyquist plot representation of impedance data with varying temperature in 1:1 N_2:O_2 atmosphere of a) $SrSiO_3$ b) $Sr_{0.7}Na_{0.3}SiO_{3-\delta}$ c) $Sr_{0.7}Na_{0.3}Si_{0.95}Mn_{0.05}O_{3-\delta}$ d) $Sr_{0.7}Na_{0.3}Si_{0.95}Fe_{0.05}O_{3-\delta}$ e) $Sr_{0.7}Na_{0.3}Si_{0.95}Co_{0.05}O_{3-\delta}$ f) $Sr_{0.7}Na_{0.3}Si_{0.95}Ni_{0.05}O_{3-\delta}$ g) $Sr_{0.7}Na_{0.3}Si_{0.95}Cu_{0.05}O_{3-\delta}$, where the symbols and lines represents the original data and the fit respectively

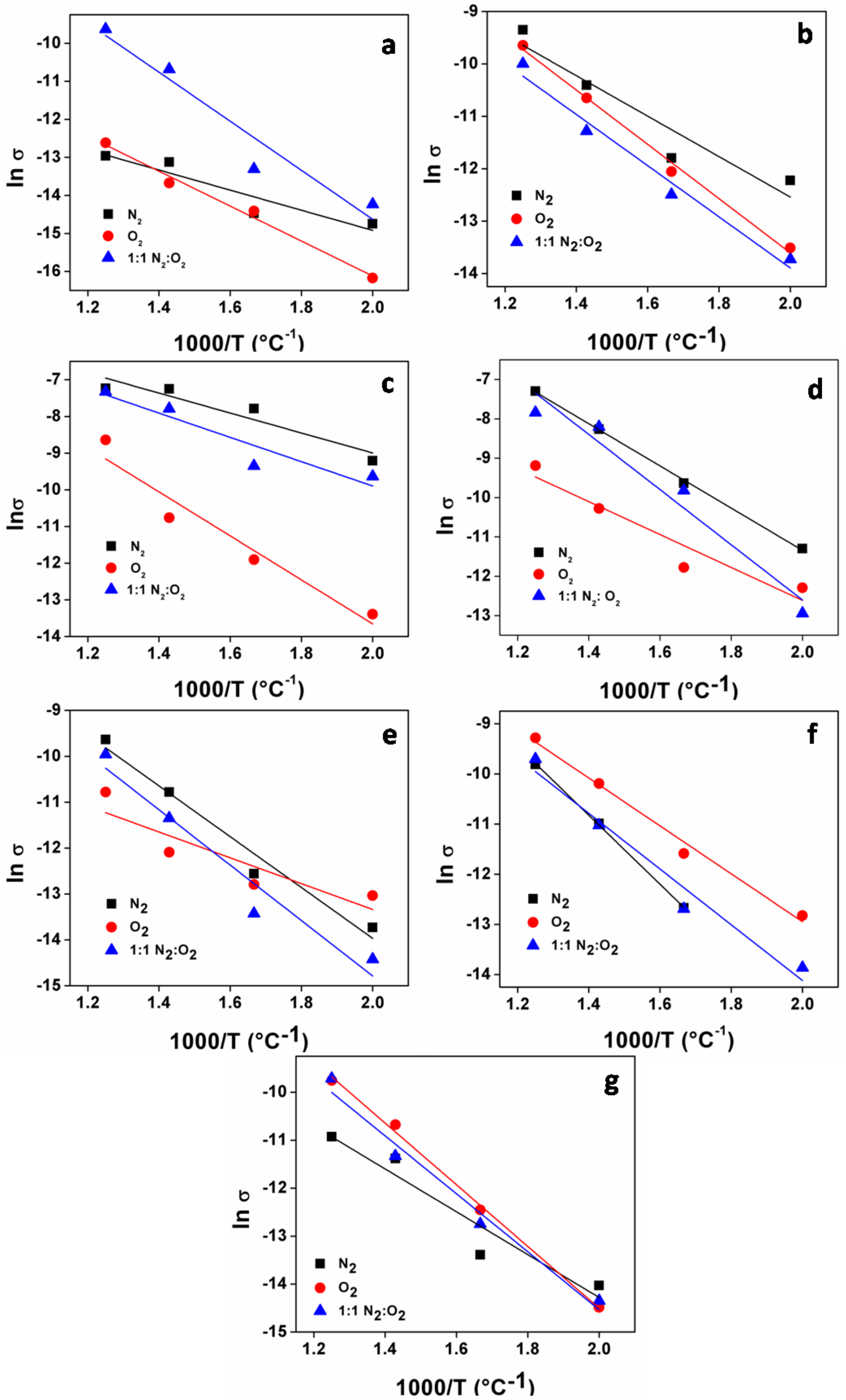

Figure 4.26: Arrhenius plot in different gas atmospheres of a) $SrSiO_3$ b) $Sr_{0.7}Na_{0.3}SiO_{3-\delta}$ c) $Sr_{0.7}Na_{0.3}Si_{0.95}Mn_{0.05}O_{3-\delta}$ d) $Sr_{0.7}Na_{0.3}Si_{0.95}Fe_{0.05}O_{3-\delta}$ e) $Sr_{0.7}Na_{0.3}Si_{0.95}Co_{0.05}O_{3-\delta}$ f) $Sr_{0.7}Na_{0.3}Si_{0.95}Ni_{0.05}O_{3-\delta}$ g) $Sr_{0.7}Na_{0.3}Si_{0.95}Cu_{0.05}O_{3-\delta}$ where the symbols and lines represents the original data and the linear fit respectively

Figure 4.23 represents the Nyquist plot representation of impedance data for the series of compounds in N_2 atmosphere. The samples are analysed in O_2 atmosphere and also in 1:1 N_2:O_2 mixture with varying temperature on cooling from 800°C to 500°C. Figure 4.24 and 4.25 represents the Nyquist plot representation of the data in O_2 atmosphere and N_2:O_2 1:1 mixture respectively. The solid squares in the plot represent the original data and the line represents the Z-fit of the data carried out in EC lab software. The contribution from grain and grain boundary is obtained and the total resistivity is calculated considering the dimensions of the sample. Detailed result in different gas atmospheres are represented in the table 4.5. It is noted that as the temperature increased, conductivity of the samples improved and all the doped products exhibited far better conductivity than the parent compound. Conductivity is further improved by the addition of transition metal in the B site, though we could not predict any trend in the role of transition metal in the lattice towards overall conductivity.

Activation energy calculation is also performed with conductivity data obtained by solving the impedance data. Arrhenius plot is represented in figure 4.23 and the detailed calculation is given in annexure. The activation energy in various gas atmospheres is also incorporated in table 4.5.

4.4. Summary and Conclusions

Sample with stoichiometry $Sr_{0.7}Na_{0.3}Si_{0.95}M_{0.05}O_3$ are synthesised by solid state method. Detailed structural study by Rietveld refinement of PXRD is carried out, the materials crystallise in monoclinic C 2 1/c space group with corner shared Si_3O_9 units. The detailed control analysis by quantitative Rietveld refinement confirms the incorporation of the doped metal in the lattice. SEM analysis suggests that on recrystallisation, the materials undergo phase separation, which is further analysed by point EDS analysis suggesting a clear segregation of metal concentration in certain spots.

Detailed ^{23}Na NMR, ^{29}SiNMR is also carried out to have an idea on the secondary phase. ^{17}O NMR study with the ^{17}O enriched sample proves the creation of oxygen vacancy in the lattice.

The room temperature activity is clearly improved with transition metal incorporation in the lattice, Co and Fe doped material exhibited better onset values and current response in ORR conditions. All the materials undergo an intermediate electron transfer with high peroxide formation. The Ni doped material shows predominantly higher activity for the OER in terms of onset and current response. The detailed Tafel analysis indicates a clear enhancement in slope value with transition metal doping in the lattice. Materials exhibit excellent phase stability in O_2 rich/lean and reducing atmospheres at higher temperatures. High temperature conductivity analysis suggests that there is considerable improvement in conductivity on doping, however the conductivity values obtained are lower than expected on the basis of literature, probably due to the phase segregation.

4.5. References

1. Singh, P.; Goodenough, J. B., $Sr_{1-x}K_xSi_{1-y}Ge_yO_{3-0.5x}$: a new family of superior oxide-ion conductors. *Energy & Environmental Science* **2012,** *5* (11), 9626-9631.

2. Martinez-Coronado, R.; Singh, P.; Alonso-Alonso, J.; Goodenough, J. B., Structural investigation of the oxide-ion electrolyte with $SrMO_3$ (M = Si/Ge) structure. *Journal of Materials Chemistry A* **2014,** *2* (12), 4355-4360.

3. Nishi, F., Strontium Metasilicate, $SrSiO_3$. *Acta Crystallographica Section C* **1997,** *53* (5), 534-536.

4. Evans, I. R.; Evans, J. S. O.; Davies, H. G.; Haworth, A. R.; Tate, M. L., On $Sr_{1-x}Na_xSiO_{3-0.5x}$ New Superior Fast Ion Conductors. *Chemistry of Materials* **2014,** *26* (18), 5187-5189.

5. Singh, P.; Goodenough, J. B., Monoclinic $Sr_{1-x}Na_xSiO_{3-0.5x}$: New Superior Oxide Ion Electrolytes. *Journal of the American Chemical Society* **2013,** *135* (27), 10149-10154.

6. Tolchard, J. R.; Islam, M. S.; Slater, P. R., Defect chemistry and oxygen ion migration in the apatite-type materials $La_{9.33}Si_6O_{26}$ and $La_8Sr_2Si_6O_{26}$. *Journal of Materials Chemistry* **2003,** *13* (8), 1956-1961.

7. Xu, J.; Liu, S.; Wang, Q.; Xiaofeng, J.; Li, X.; Kuang, X., Phase formation and conductivity degradation of $Sr_{1-x}K_xSiO_{3-0.5x}$ ionic conductors. *Journal of Materials Chemistry A* **2016,** *4* (17), 6313-6318.

8. Bayliss, R. D.; Cook, S. N.; Fearn, S.; Kilner, J. A.; Greaves, C.; Skinner, S. J., On the oxide ion conductivity of potassium doped strontium silicates. *Energy & Environmental Science* **2014,** *7* (9), 2999-3005.

9. Xu, J.; Wang, X.; Fu, H.; Brown, C. M.; Jing, X.; Liao, F.; Lu, F.; Li, X.; Kuang, X.; Wu, M., Solid-State 29Si NMR and Neutron-Diffraction Studies of $Sr_{0.7}K_{0.3}SiO_{2.85}$ Oxide Ion Conductors. *Inorganic Chemistry* **2014,** *53* (13), 6962-6968.

10. Wei, T.; Singh, P.; Gong, Y.; Goodenough, J. B.; Huang, Y.; Huang, K., $Sr_{3-3x}Na_{3x}Si_3O_{9-1.5x}$ (x = 0.45) as a superior solid oxide-ion electrolyte for intermediate temperature-solid oxide fuel cells. *Energy & Environmental Science* **2014,** *7* (5), 1680-1684.

11. Bayliss, R. D.; Cook, S. N.; Scanlon, D. O.; Fearn, S.; Cabana, J.; Greaves, C.; Kilner, J. A.; Skinner, S. J., Understanding the defect chemistry of alkali metal strontium silicate solid solutions: insights from experiment and theory. *Journal of Materials Chemistry A* **2014,** *2* (42), 17919-17924.

12. Tealdi, C.; Malavasi, L.; Uda, I.; Ferrara, C.; Berbenni, V.; Mustarelli, P., Nature of conductivity in $SrSiO_3$-based fast ion conductors. *Chemical Communications* **2014,** *50* (94), 14732-14735.

13. Fernández-Palacios, S.; Santos-Gómez, L. d.; Compana, J. M.; Porras-Vázquez, J. M.; Cabeza, A.; Marrero-López, D.; Losilla, E. R., Influence of the synthesis method on the structure and electrical properties of $Sr_{1-x}K_xGeO_{3-x/2}$. *Ceramics International* **2015,** *41* (5, Part A), 6542-6551.

14. Jee, Y.; Zhao, X.; Huang, K., On the cause of conductivity degradation in sodium strontium silicate ionic conductor. *Chemical Communications* **2015,** *51* (47), 9640-9642.

15. Inglis, K. K.; Corley, J. P.; Florian, P.; Cabana, J.; Bayliss, R. D.; Blanc, F., Structure and Sodium Ion Dynamics in Sodium Strontium Silicate Investigated by Multinuclear Solid-State NMR. *Chemistry of Materials* **2016,** *28* (11), 3850-3861.

16. Lei, X.; Jee, Y.; Huang, K., Amorphous Na2Si2O5 as a fast Na+ conductor: an ab initio molecular dynamics simulation. *Journal of Materials Chemistry A* **2015,** *3* (39), 19920-19927.

17. Peet, J. R.; Widdifield, C. M.; Apperley, D. C.; Hodgkinson, P.; Johnson, M. R.; Evans, I. R., Na+ mobility in sodium strontium silicate fast ion conductors. *Chemical Communications* **2015,** *51* (96), 17163-17165.

18. Chien, P.-H.; Jee, Y.; Huang, C.; Dervişoğlu, R.; Hung, I.; Gan, Z.; Huang, K.; Hu, Y.-Y., On the origin of high ionic conductivity in Na-doped $SrSiO_3$. *Chemical Science* **2016,** *7* (6), 3667-3675.

19. Toby, B., EXPGUI, a graphical user interface for GSAS. *Journal of Applied Crystallography* **2001,** *34* (2), 210-213.

20. Biesinger, M. C.; Payne, B. P.; Grosvenor, A. P.; Lau, L. W. M.; Gerson, A. R.; Smart, R. S. C., Resolving surface chemical states in XPS analysis of first row transition metals, oxides and hydroxides: Cr, Mn, Fe, Co and Ni. *Applied Surface Science* **2011,** *257* (7), 2717-2730.

21. Guo, D.; Wu, Z.; An, Y.; Li, X.; Guo, X.; Chu, X.; Sun, C.; Lei, M.; Li, L.; Cao, L.; Li, P.; Tang, W., Room temperature ferromagnetism in $(Ga_{1-x}Mn_x)_2O_3$ epitaxial thin films. *Journal of Materials Chemistry C* **2015,** *3* (8), 1830-1834.

22. Thundiyil, S.; Kurungot, S.; Devi, R. N., Bifunctional Oxygen Reduction and Evolution Activity in Brownmillerites $Ca_2Fe_{(1-x)}Co_xO_5$. *ACS Omega* **2019,** *4* (1), 31-38.

23. Zhou, T.; Cao, Z.; Zhang, P.; Ma, H.; Gao, Z.; Wang, H.; Lu, Y.; He, J.; Zhao, Y., Transition metal ions regulated oxygen evolution reaction performance of Ni-based hydroxides hierarchical nanoarrays. *Scientific Reports* **2017,** *7* (1), 46154.

24. Sun, T.; Xu, L.; Yan, Y.; Zakhidov, A. A.; Baughman, R. H.; Chen, J., Ordered Mesoporous Nickel Sphere Arrays for Highly Efficient Electrocatalytic Water Oxidation. *ACS Catalysis* **2016,** *6* (3), 1446-1450.

25. Biesinger, M. C.; Lau, L. W. M.; Gerson, A. R.; Smart, R. S. C., Resolving surface chemical states in XPS analysis of first row transition metals, oxides and hydroxides: Sc, Ti, V, Cu and Zn. *Applied Surface Science* **2010,** *257* (3), 887-898.

26. Wu, C.-K.; Yin, M.; O'Brien, S.; Koberstein, J. T., Quantitative Analysis of Copper Oxide Nanoparticle Composition and Structure by X-ray Photoelectron Spectroscopy. *Chemistry of Materials* **2006,** *18* (25), 6054-6058.

27. Kim, N.; Grey, C. P., Probing Oxygen Motion in Disordered Anionic Conductors with ^{17}O and ^{51}V MAS NMR Spectroscopy. *Science* **2002,** *297* (5585), 1317.

28. Taylor, R. J.; Humffray, A. A., Electrochemical studies on glassy carbon electrodes: II. Oxygen reduction in solutions of high pH (pH>10). *Journal of Electroanalytical Chemistry and Interfacial Electrochemistry* **1975,** *64* (1), 63-84.

29. Ge, X.; Sumboja, A.; Wuu, D.; An, T.; Li, B.; Goh, F. W. T.; Hor, T. S. A.; Zong, Y.; Liu, Z., Oxygen Reduction in Alkaline Media: From Mechanisms to Recent Advances of Catalysts. *ACS Catalysis* **2015,** *5* (8), 4643-4667.

30. Zhou, R.; Zheng, Y.; Jaroniec, M.; Qiao, S.-Z., Determination of the Electron Transfer Number for the Oxygen Reduction Reaction: From Theory to Experiment. *ACS Catalysis* **2016,** *6* (7), 4720-4728.

31. Hwang, J.-H.; McLachlan, D. S.; Mason, T. O., Brick Layer Model Analysis of Nanoscale-to-Microscale Cerium Dioxide. *Journal of Electroceramics* **1999,** *3* (1), 7-16.

32. Bauerle, J. E., Study of solid electrolyte polarization by a complex admittance method. *Journal of Physics and Chemistry of Solids* **1969,** *30* (12), 2657-2670.

33. Pérez-Coll, D.; Núñez, P.; Abrantes, J. C. C.; Fagg, D. P.; Kharton, V. V.; Frade, J. R., Effects of firing conditions and addition of Co on bulk and grain boundary properties of CGO. *Solid State Ionics* **2005,** *176* (37), 2799-2805.

Chapter 5

Towards Applications

5A.1. Introduction

Dense ceramic oxygen and mixed ionic conducting membranes have gained considerable attention in the near past on account of the high thermal, mechanical and chemical stabilities[1] and applications in various fields such as oxygen separation, partial oxidation of methane[2-4], syn gas conversion[5, 6] etc. Dense membranes work based on the chemical or electrical potential gradient in comparison to the conventional porous membrane, where the separation takes place through the pores. The pore size in the porous membranes are adjusted to achieve selectivity, whereas the material's intrinsic chemical property is made use in dense membranes for separation. The dense membranes are characterised by high permselectivity of the species in comparison with the porous membranes. Dense ceramic membranes can be of different geometries[3]. Disks, tubes, monoliths, capillaries and hollow fibers are the most common type of geometries of dense ceramic membranes. Disk geometries can be made by pressing the constituent material and sintering at high temperatures. The main difficulties associated with the geometry are the low surface to volume ratio and also the difficulty with the high temperature sealing[7, 8]. In order to overcome the engineering difficulties, tube membranes are fabricated by extrusion method. The hurdles with low surface area to volume ratio was partly accounted for by the flat sheet membranes proposed by Air Products and Chemicals Inc[9]. Hollow fiber membrane geometry is the advanced type of membranes with high surface area to volume ratio and least handling difficulties. Pioneering work on the membranes suggests that the hollow fiber membranes are associated with high permeation flux, easy assembly and module fabrication adding to the advantage to the use in industrial scale[9-14].

In this chapter, dense hollow fiber membranes are fabricated from the selected materials synthesised in previous chapters. The main goal of the chapter is to project the material as an OTM candidate, based on the feasibility of forming a dense membrane.

5A.2. Experimental Section

5A.2.1. Membrane Fabrication

$Ca_2FeCoO_{5\pm\delta}$ and $Sr_{0.7}Na_{0.3}Si_{0.95}Co_{0.05}O_{3-\delta}$ are selected for spinning into fibers. The materials are made in bulk by solid state method as mentioned in the chapters 2B and 4 respectively. The raw materials are ballmilled before pretreatment and during synthesis ballmilling is carried out intermittently at 400rpm for uniform phase formation. The phase formation is confirmed by XRD.

The synthesised materials are homogenised again by ballmilling for 2h at 400rpm. Phase inversion technique is used to fabricate the membrane out of the material[12, 15]. An optimised amount of polymer PSf is added to the weighed NMP solvent. After the complete dissolution of the polymer in solvent, weighed amount of homogenised material is added part by part with constant stirring with the help of overhead stirrer. The dope solution is kept overnight under stirring for homogeneity. The dope solution is transferred in to a stainless steel reservoir with N_2 pressure and spun through spinneret with 1.1mm inner diameter and 2.5mm outer diameter to coagulation bath containing deionised water maintained at room temperature. Schematic representation of spinning set up is represented in figure 5A.1. The green fiber collected is sintered at its optimised densification temperature to get final dense hollow fiber.

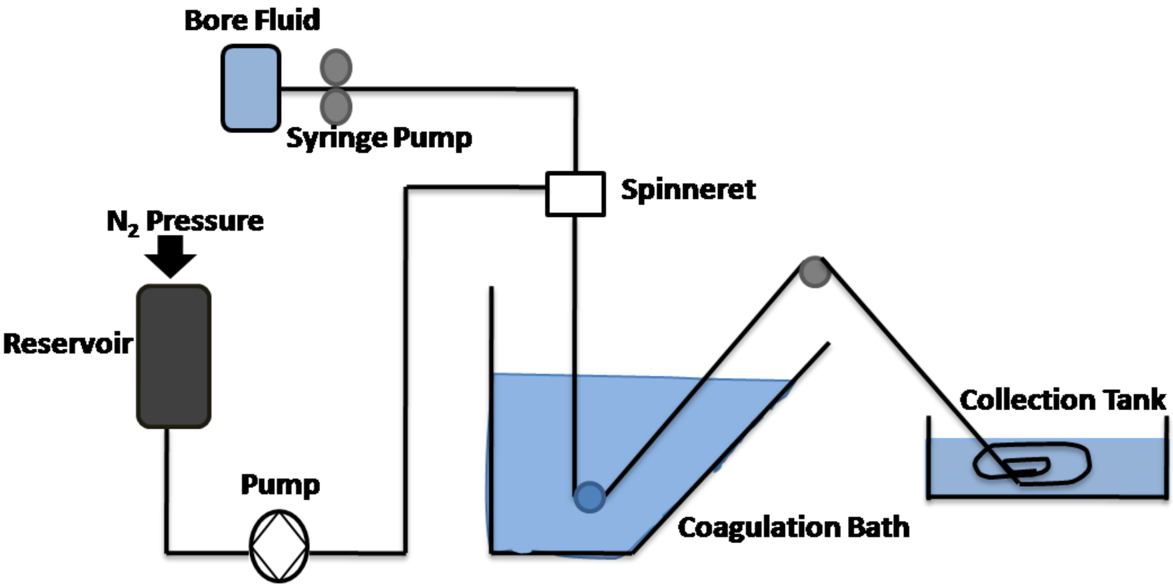

Figure 5A.1: Schematic representation of fiber spinning set up

We have also developed a method for one step fabrication technique for the ceramic oxide, where the precursor mixture is directly added in to the polymer solvent mixture. The phase formation and sintering takes place at the same temperature, so that elaborative process of multiple calcinations and processing could be minimised. Optimised parameters for each material is given in table 5A.1.

Table 5A.1: optimised parameters for phase inversion of hollow fiber

Material	Weight (%)			Air gap (cm)	Dope pressure (psi)	Water flow (ml/m)
	Material	PSf	NMP			
$Ca_2FeCoO_{5\pm\delta}$	51	10	39	4	25.5	1.5
$Sr_{0.7}Na_{0.3}Si_{0.95}Co_{0.05}O_{3-\delta}$	58	10	32	5	42.3	2.5
$Ca_2FeCoO_{5\pm\delta}$ one step process	51.3	9.5	39.2	4	46	2.5

5A.2.2. Characterisation

The morphology of the sintered fibers are analysed by SEM analysis. The fiber formed by one step method is ground and analysed for the phase formation after sintering by PXRD analysis. The retention of phase after sintering of the fibers fabricated from already calcined powders is also anlaysed by PXRD technique. The surface composition analysis is performed by EDS analysis.

5A.3. Results and Discussions

5A.3.1. $Sr_{0.7}Na_{0.3}Si_{0.95}Co_{0.05}O_{3-\delta}$ Fibers

The green fibers are sintered at 1100°C for 4h to get strong, dense self standing fibers. The initial material is formed with impure phase of unreacted SiO_2 and $Sr_2CoSi_2O_7$ and is used as such for fiber fabrication. The crushed fiber is analysed by PXRD. The impurity phases disappeared after sintering and a pure phase of the material is obtained. Figure 5A.2 represents the PXRD collected before fiber spinning and after sintering the fiber.

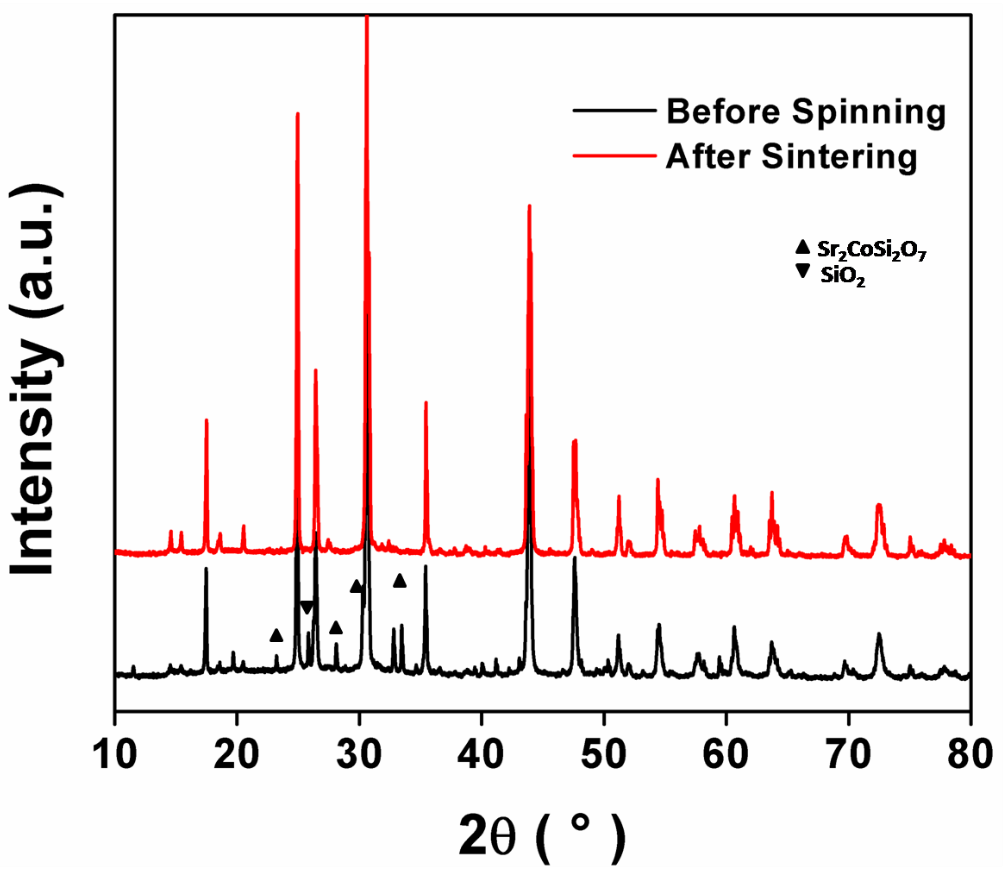

Figure 5A.2: PXRD pattern of material before and after fiber spinning

Figure 5A.3 represents the SEM image of the fiber after sintering at 1100°C. The surface is observed to be perfectly densified at 1100°C. It is quite lower temperature sintering compared with other state of the art hollow fiber membranes. The reduction in sintering temperature can save the cost of the overall process to a considerable extent.

The composition of the membrane surface is analysed by EDS analysis. Table 5A.2 represents the EDS data and the surface compositions are in good agreement with the calculated data on the basis of stoichiometry

Table 5A.2: EDS data of the sintered $Sr_{0.7}Na_{0.3}Si_{0.95}Co_{0.05}O_{3-\delta}$ fiber surface

			Weight (%)		
Element	Sr	Na	Si	Co	O
Calculated	42.1	4.7	18.3	2.0	32.9
Observed	42.1	6.0	11.9	1.88	38

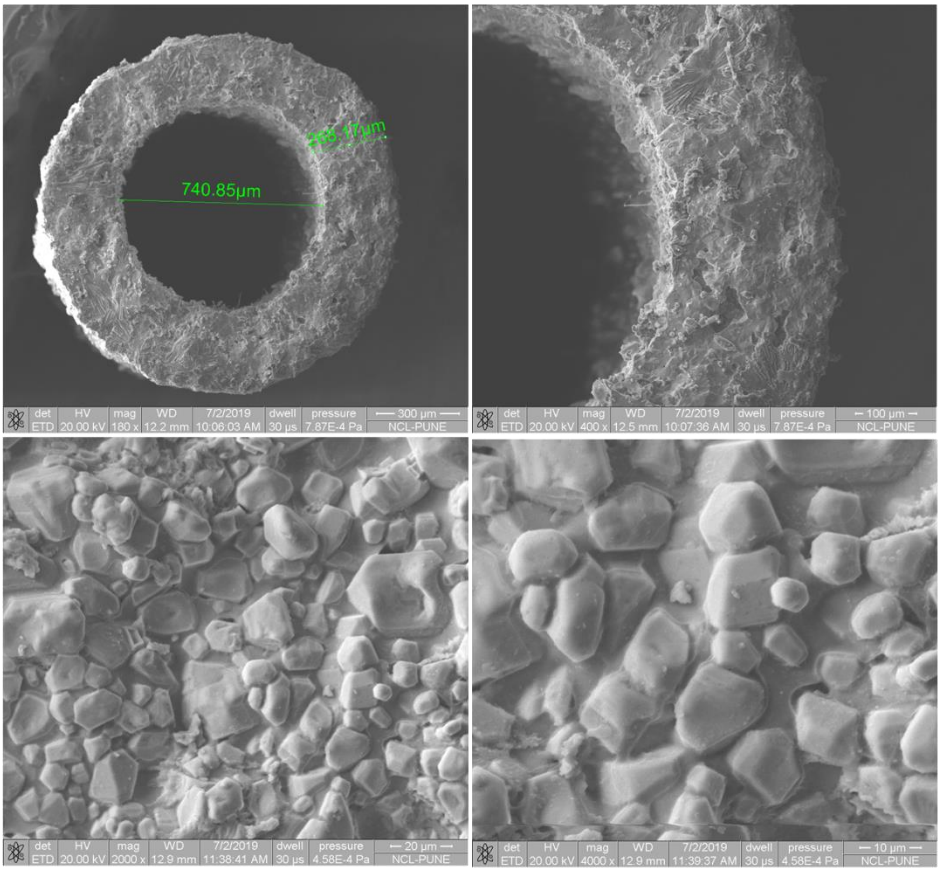

Figure 5A.3: SEM image of the $Sr_{0.7}Na_{0.3}Si_{0.95}Co_{0.05}O_{3-\delta}$ hollow fiber membrane sintered at 1100°C

5A.3.2. $Ca_2FeCoO_{5\pm\delta}$ Fibers

The sintering temperature is optimised to be 1250°C, at which the fiber densified thoroughly. The phase after sintering is confirmed by PXRD. A small extra phase formation of $CaSO_4$ (JCPDS file number: 01-072-0916), probably due to the reaction with the sulphates of the polymer solution, is observed along with the major brownmillerite phase of $Ca_2FeCoO_{5\pm\delta}$. The material synthesised in bulk had some unreacted CaO phase, which disappeared after sintering the fiber. The PXRD pattern of material before spinning and after sintering is represented in figure 5A.4

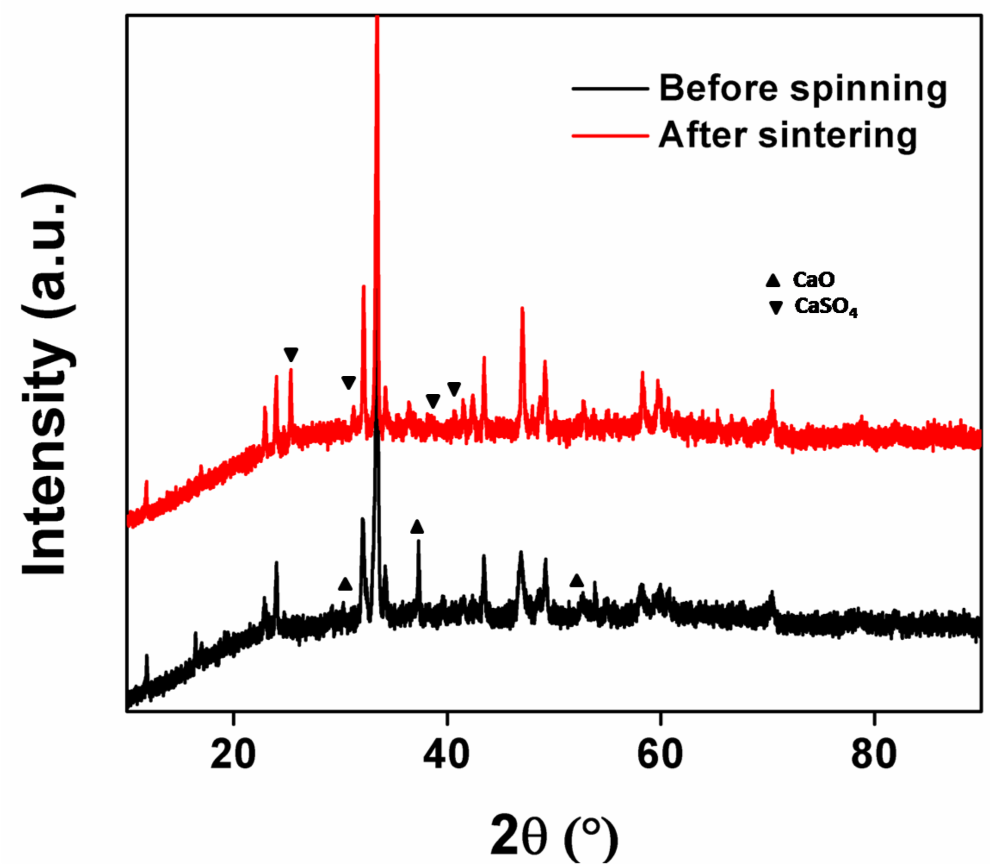

Figure 5A.4: PXRD patterns of the material before spinning and after sintering the fiber

Figure 5A.5 represents the SEM image of the fiber cross section calcined at 1200°C and 1250°C respectively for optimisation of sintering condition. A close anlaysis of the morphology shows a perfect grain formation and sintering at 1250°C only. Surface SEM image represented in figure 5A.6 shows a clear image of the grains formed at 1250°C.

Elemental composition of the surface is also analysed after sintering at 1250°C and is tabulated in table 5A.3. The data is in good agreement with the calculated value considering the stoichiometry of the compound.

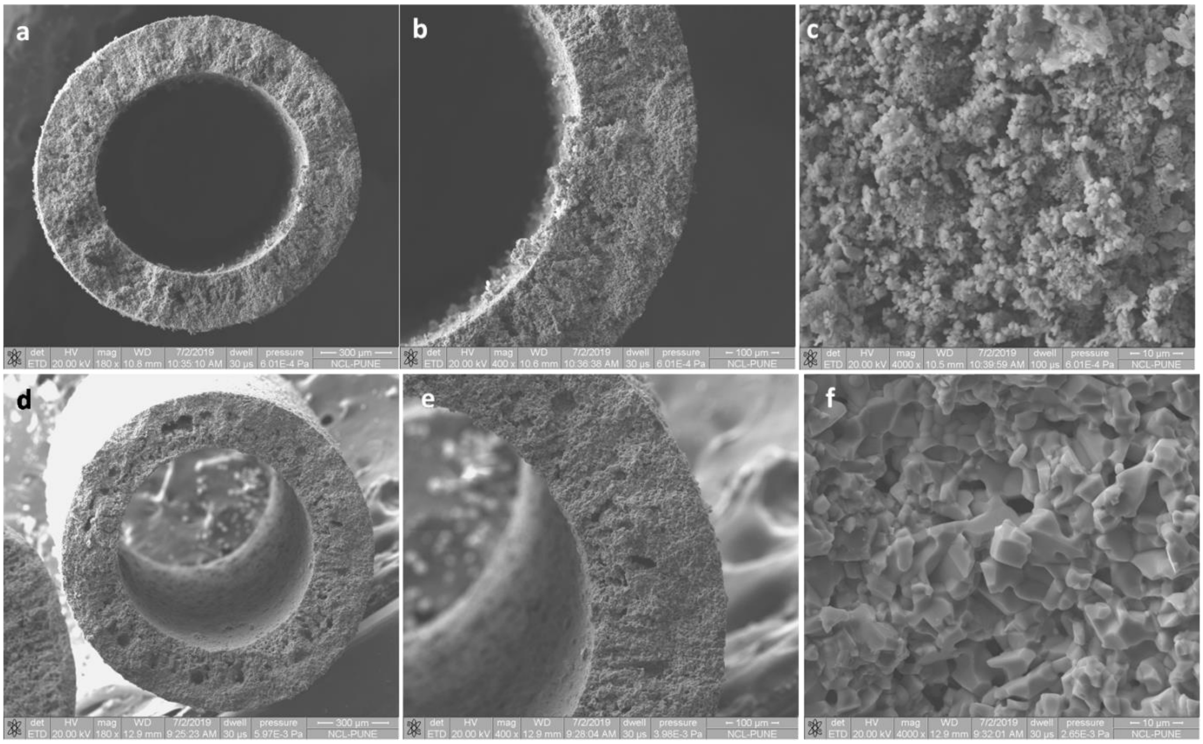

Figure 5A.5: SEM image of $Ca_2FeCoO_{5\pm\delta}$ hollow fiber cross section a), b) and c) sintered at 1200°C and d), e) and f) sintered at 1250°C

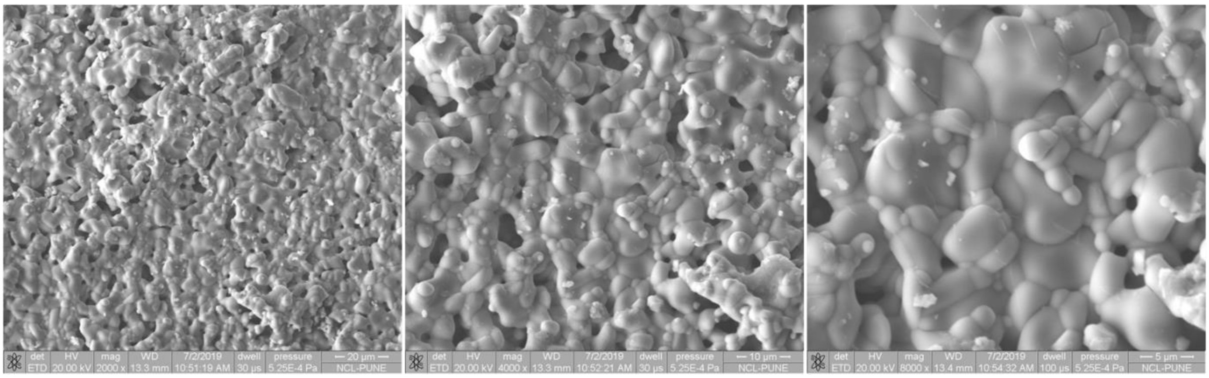

Figure 5A.6: SEM image of $Ca_2FeCoO_{5\pm\delta}$ hollow fiber surface sintered at 1250°C

Table 5A.3: EDS data of the sintered $Ca_2FeCoO_{5\pm\delta}$ fiber surface

	Weight (%)			
Elements	Ca	Fe	Co	O
Calculated	29.1	20.3	21.4	29.1
Observed	26.9	21.4	17.7	33.9

In both of the above cases, we could achieve perfect dense ceramic membranes in a one step fabrication process. The dense ceramic membranes are often made by multiple steps. For providing mechanical strength, a support layer is prepared first, followed by coating with intermediate layer multiple times and final separation layer. Each step includes several temperature processing steps and which in turn makes the ceramic fabrication much more expensive[16, 17]. We have eliminated all the above mentioned steps to get a dense sintered fiber at low temperature as 1100°C, which can save the overall cost of making the dense ceramic fibers.

5A.3.3. $Ca_2FeCoO_{5\pm\delta}$ Fibers: Single Step Process from Precursor Mixture

The cost of the process can be further saved if the calcination steps involved for the material synthesis can also be removed. We have proposed a novel concept of spinning the fiber directly from the precursor mixture. The precursor carbonate mixture as mentioned in chapter 2B, mixed stoichiometrically and homogenised by ball milling is used directly as the solid content for the dope solution. The green fiber obtained is optimised for its sintering temperature. Single step calcinations and sintering at 1250°C for 4h yield well sintered strong fibers. The phase formation in a single step calcination-sintering is confirmed by analysing the crushed powder by PXRD. We could obtain same phase as with the already calcined powder on sintering. A major brownmillerite phase of $Ca_2FeCoO_{5\pm\delta}$ (JCPDS file number: 0051-1883) is formed with a small impurity phase of $CaSO_4$ as with already calcined material. Figure 5A.7 compares the phase formation of fiber with raw mixture and already calcined material, the phase formation is complete by 1150°C, but the fiber gets sintered only at 1250°C.

The densification is optimised at different temperatures by the help of SEM images, figure 5A.8 shows the cross section image of the fiber at different temperatures and figure 5A.9 represents the SEM image of fiber surface at different temperatures. The sintering of the fiber starts at 1200°C and a strong completely sintered fiber is obtained at 1250°C.

Surface elemental composition is also analysed by EDS analysis at each temperature of optimisation and is tabulated in table 5A.4. The surface composition is in good agreement with the calculated value based on the stoichiometry.

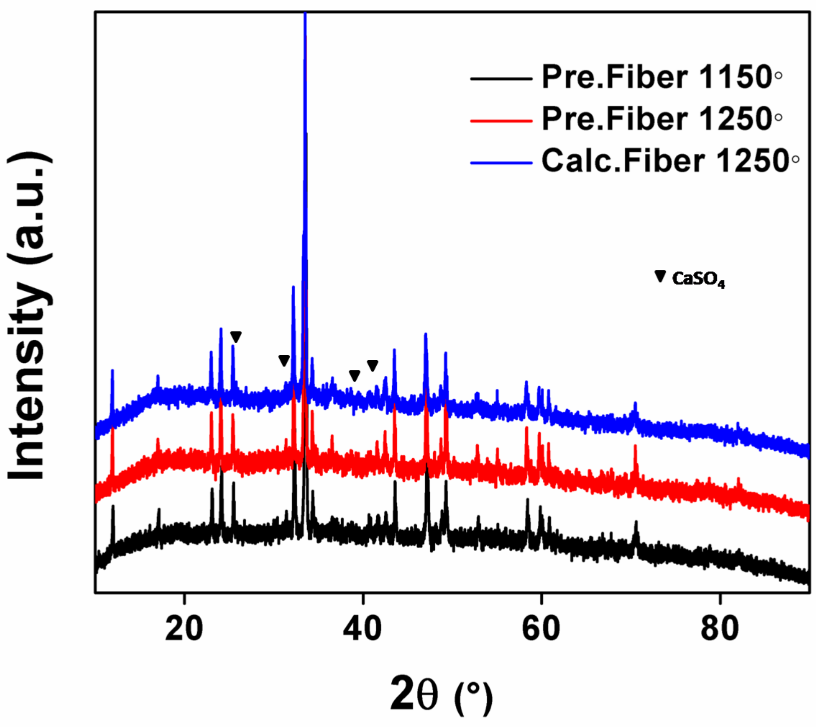

Figure 5A.7: PXRD pattern of the crushed fiber made from raw precursor and calcined material

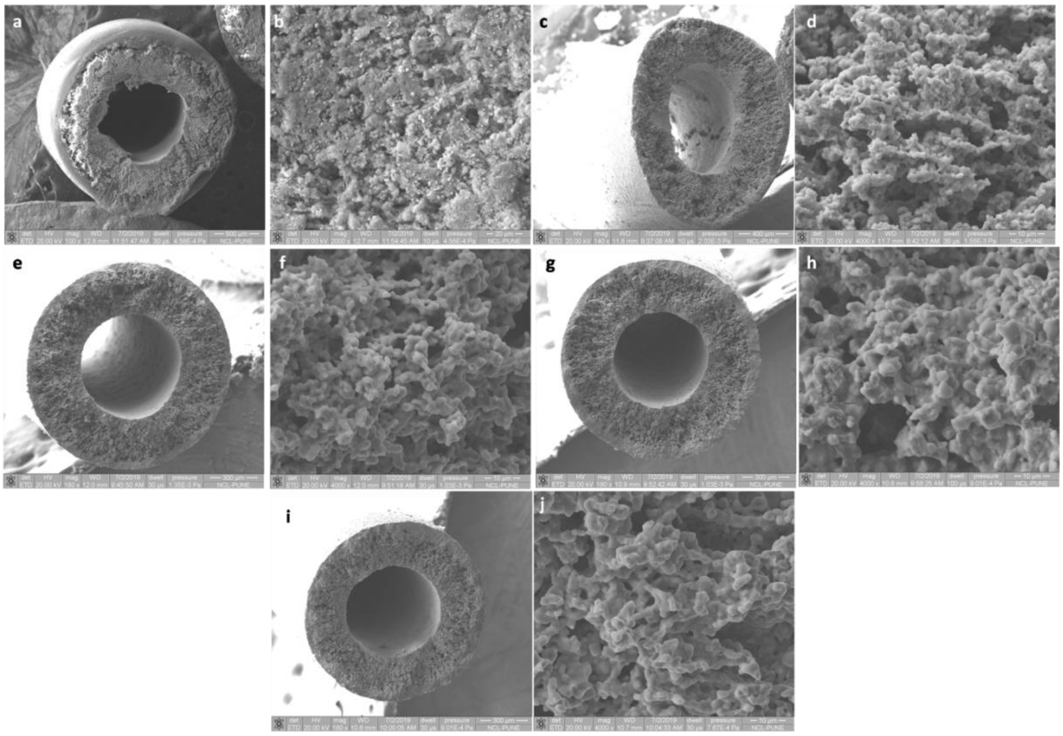

Figure 5A.8: SEM image of the fiber cross section calcined at different temperatures a) and b) green fiber c) and d) at 1100°C e) and f) at 1150°C g) and h) at 1200°C and i) and j) at 1250°C

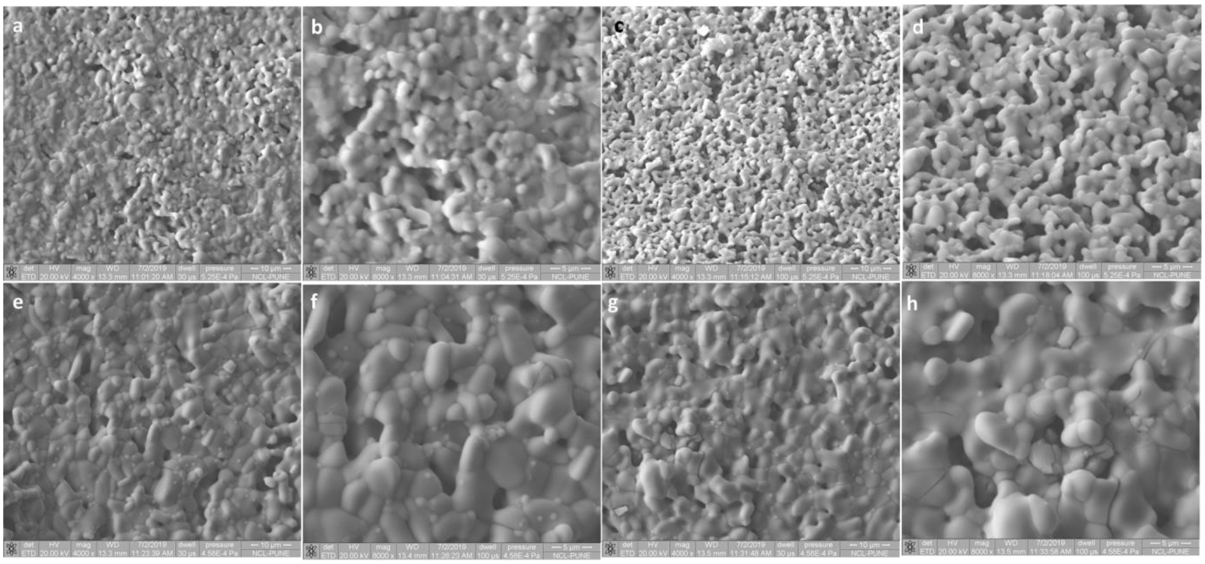

Figure 5A.9: SEM image of the fiber surface calcined at different temperatures a) and b) at 1100°C c) and d) at 1150°C e) and f) at 1200°C and g) and h) at 1250°C

Table 5A.4: Elemental composition of fiber surface at different temperatures

	Weight (%)			
Element	Ca	Fe	Co	O
1100°C	27.9	14.1	14.4	43.9
1150°C	25.2	18.1	16.2	40.3
1200°C	25.9	18.1	17.5	38.5
1250°C	27.6	19.2	17.8	35.4

The fiber fabrication directly from the precursor mixture of a perovskite related structure is a novel method developed to avoid multiple steps of calcinations and sintering the fiber to get a dense membrane. The phase purity and composition is retained by the method as evidenced by the PXRD and EDS analysis.

5A.4. Summary and Conclusions

Dense ceramic hollow fiber membranes could be fabricated avoiding multiple steps including support fabrication, intermediate layer coating and dense separation layer coating by modified phase inversion technique. Dense ceramic fibers of $Sr_{0.7}Na_{0.3}Si_{0.95}Co_{0.05}O_{3-\delta}$ and brownmillerite $Ca_2FeCoO_{5\pm\delta}$ are fabricated successfully in dense form. The temperature of sintering is 1100°C and 1200°C respectively, which in comparison to the literature is low.

The cost of the process can be further reduced by the novel concept of direct spinning with the raw material mixture. Phase formation and sintering to form strong self standing fibers is achieved by a single step calcination at 1250°C. The phase formation is complete even at 1100°C, and the membrane densifies by 1200°C.

5A.5. References

1. Burggraaf, A. J.; Cot, L., Fundamentals of inorganic membrane science and technology. In *Membrane Science and Technology*, Burggraaf, A. J.; Cot, L., Eds. Elsevier: 1996; Vol. 4, p iii.
2. Wang, H.; Feldhoff, A.; Caro, J.; Schiestel, T.; Werth, S., Oxygen selective ceramic hollow fiber membranes for partial oxidation of methane. *AIChE Journal* **2009,** *55* (10), 2657-2664.
3. Shao, Z.; Dong, H.; Xiong, G.; Cong, Y.; Yang, W., Performance of a mixed-conducting ceramic membrane reactor with high oxygen permeability for methane conversion. *Journal of Membrane Science* **2001,** *183* (2), 181-192.
4. Balachandran, U.; Dusek, J. T.; Mieville, R. L.; Poeppel, R. B.; Kleefisch, M. S.; Pei, S.; Kobylinski, T. P.; Udovich, C. A.; Bose, A. C., Dense ceramic membranes for partial oxidation of methane to syngas. *Applied Catalysis A: General* **1995,** *133* (1), 19-29.
5. Balachandran, U.; Dusek, J. T.; Maiya, P. S.; Ma, B.; Mieville, R. L.; Kleefisch, M. S.; Udovich, C. A., Ceramic membrane reactor for converting methane to syngas. *Catalysis Today* **1997,** *36* (3), 265-272.
6. Yoon, H.; Oh, T.; Li, J.; Duncan, K. L.; Wachsman, E. D., Permeation Through $SrCe_{0.9}Eu_{0.1}O_{3-\delta}$ / Ni–$SrCeO_3$ Tubular Hydrogen Separation Membranes. *Journal of The Electrochemical Society* **2009,** *156* (7), B791-B794.
7. Zhu, X.; Wang, H.; Yang, W., Novel cobalt-free oxygen permeable membrane. *Chemical Communications* **2004,** (9), 1130-1131.

8. Saracco, G.; Vesteeg, G. F.; van Swaaij, W. P. M., Current hurdles to the success of high-temperature membrane reactors. *Journal of Membrane Science* **1994,***95* (2), 105-123.

9. Holmes, M. J.; Ohrn, T. R.; Chen, C. M.-P. Ion transport membrane module and vessel system with directed internal gas flow. 2010-02-09, 2010.

10. Luyten, J.; Buekenhoudt, A.; Adriansens, W.; Cooymans, J.; Weyten, H.; Servaes, F.; Leysen, R., Preparation of LaSrCoFeO_{3-x} membranes. *Solid State Ionics* **2000,***135* (1), 637-642.

11. Liu, S.; Li, K.; Hughes, R., Preparation of $SrCe_{0.95}Yb_{0.05}O_{3-\alpha}$ perovskite for use as a membrane material in hollow fibre fabrication. *Materials Research Bulletin* **2004,***39* (1), 119-133.

12. Tan, X.; Liu, S.; Li, K., Preparation and characterization of inorganic hollow fiber membranes. *Journal of Membrane Science* **2001,***188* (1), 87-95.

13. Tan, X.; Liu, Y.; Li, K., Mixed conducting ceramic hollow-fiber membranes for air separation. *AIChE Journal* **2005,***51* (7), 1991-2000.

14. Tan, X.; Liu, Y.; Li, K., Preparation of LSCF Ceramic Hollow-Fiber Membranes for Oxygen Production by a Phase-Inversion/Sintering Technique. *Industrial & Engineering Chemistry Research* **2005,***44* (1), 61-66.

15. Liu, S.; Li, K.; Hughes, R., Preparation of porous aluminium oxide (Al_2O_3) hollow fibre membranes by a combined phase-inversion and sintering method. *Ceramics International* **2003,***29* (8), 875-881.

16. Li, K.; Tan, X.; Liu, Y., Single-step fabrication of ceramic hollow fibers for oxygen permeation. *Journal of Membrane Science* **2006,***272* (1), 1-5.

17. Wei, C. C.; Chen, O. Y.; Liu, Y.; Li, K., Ceramic asymmetric hollow fibre membranes—One step fabrication process. *Journal of Membrane Science* **2008,***320* (1), 191-197.

Part A

Dense ceramc hollow fiber membrane as OTM candidate

Part B

SOFC application

5B.1. Introduction

Solid oxide fuel cell research is gaining increased attention due to the high power output and flexibility in fuel and oxidant[1, 2]. The reduction in operating temperature from ~900°C to ~500°C results in advantages like improved durability, suppression of degradation of components, better sealing of components and ultimately, reduced cost[3]. The material should exhibit better conductivity and catalytic activity to make intermediate temperature SOFC practical. The stability and compatibility of the electrode material with the electrolyte under operating conditions is also important[4]. Better adhesion and dispersion of the electrode on the dense electrolyte surface by a low temperature process also reduces the total cost of processing[5-7].

In this chapter, three materials viz., $Ca_2FeCoO_{5\pm\delta}$, $Ba_2InCe_{0.5}Co_{0.5}O_{5\pm\delta}$, and $Sr_{0.7}Na_{0.3}Si_{0.95}Co_{0.05}O_{3\pm\delta}$ are selected from three chapters on account of the room temperature and high temperature activity and projected as SOFC cathode catalyst materials. The goal of the chapter is to evaluate the electrode processing and conductivity of these materials.

5B.2. Experimental Section

The materials $Ca_2FeCoO_{5\pm\delta}$, $Ba_2InCeCoO_{5\pm\delta}$, and $Sr_{0.7}Na_{0.3}Si_{0.95}Co_{0.05}O_{3-\delta}$ are selected for the SOFC electrode evaluation study. Material synthesis is explained in chapter 2B, 3C and 4 respectively. Purchased $La_{0.6}Sr_{0.4}Fe_{0.8}Co_{0.2}O_{3\pm\delta}$ (<1 micron paticle, Spybusy Electronics Pvt Ltd, India) is used as a standard material for comparing the activity.

The reactivity of the materials with the electrolyte (CGO and YSZ) is tested by analysing phase formations at high temperatures. This is carried out by first grinding them together in 1:1 ratio by weight and then pressing to form a pellet. The pellet is subjected to heat treatment at 900°C for 48h. After cooling down to room temperature, the pellet is ground well and the phases formed are analysed by PXRD.

The dummy electrode fabrication is carried out in University of Lille1, France under Indo-French International Associated Laboratory (LIA) project. Dense membrane of electrolyte is made by pressing the material (CGO and YSZ) in to a pellet in uniaxial press at 1 bar pressure followed by isostatic press at 1800 bar pressure. The obtained membrane is densified by sintering at 1200°C for 2h in a bed of electrolyte powder.

Electrode ink is made by ball milling the material with ethanol at 400rpm with the electrolyte material in 1:1 ratio for 4h. The slurry is evaporated to get a fine powder and is mixed with 65 weight% of polyethylene glycol, followed by homogenisation by grinding in three cylinder system. The obtained cathode ink is screen printed on both sides of the dense electrode for further analysis. Adhesion of the cathode ink on the electrode surface is carried out at different temperatures and is tested for porosity and adhesion by SEM imaging.

The dummy electrode made is analysed by CH instrument for the conductivity as explained in chapter 2B.

5B.3. Results and Discussion

Phase stability of the electrode materials with conventionally used electrolyte materials is analysed by PXRD after high temperature treatment. Figure 5B.1 represents the PXRD pattern comparing the material, electrolyte CGO and YSZ and the mixture after temperature treatment separately. The material has no reactivity with CGO as evidenced by the absence of extra phases in the patterns. The materials $Sr_{0.7}Na_{0.3}Si_{0.95}Co_{0.05}O_{3-\delta}$ and $Ca_2FeCoO_{5\pm\delta}$ are nonreactive with both the conventional electrolytes. However an impurity phase of CeO_2 is observed after the temperature treatment of $Ba_2InCe_{0.5}Co_{0.5}O_{5\pm\delta}$ with YSZ.

The cathode slurry is screen printed on the dense electrolyte membrane and the adhesion temperature is optimised. The material showed better adhesion and porosity at temperature as low as 800°C. Normal adhesion temperature of the cathode materials on the electrodes is above 1000°C, and lowering of the temperature is advantageous to the overall processing of electrode. The dummy electrode morphology is analysed by SEM and the resultant image is represented in figure 5B.2, showing a porous deposition of the cathode material on the electrolyte membrane.

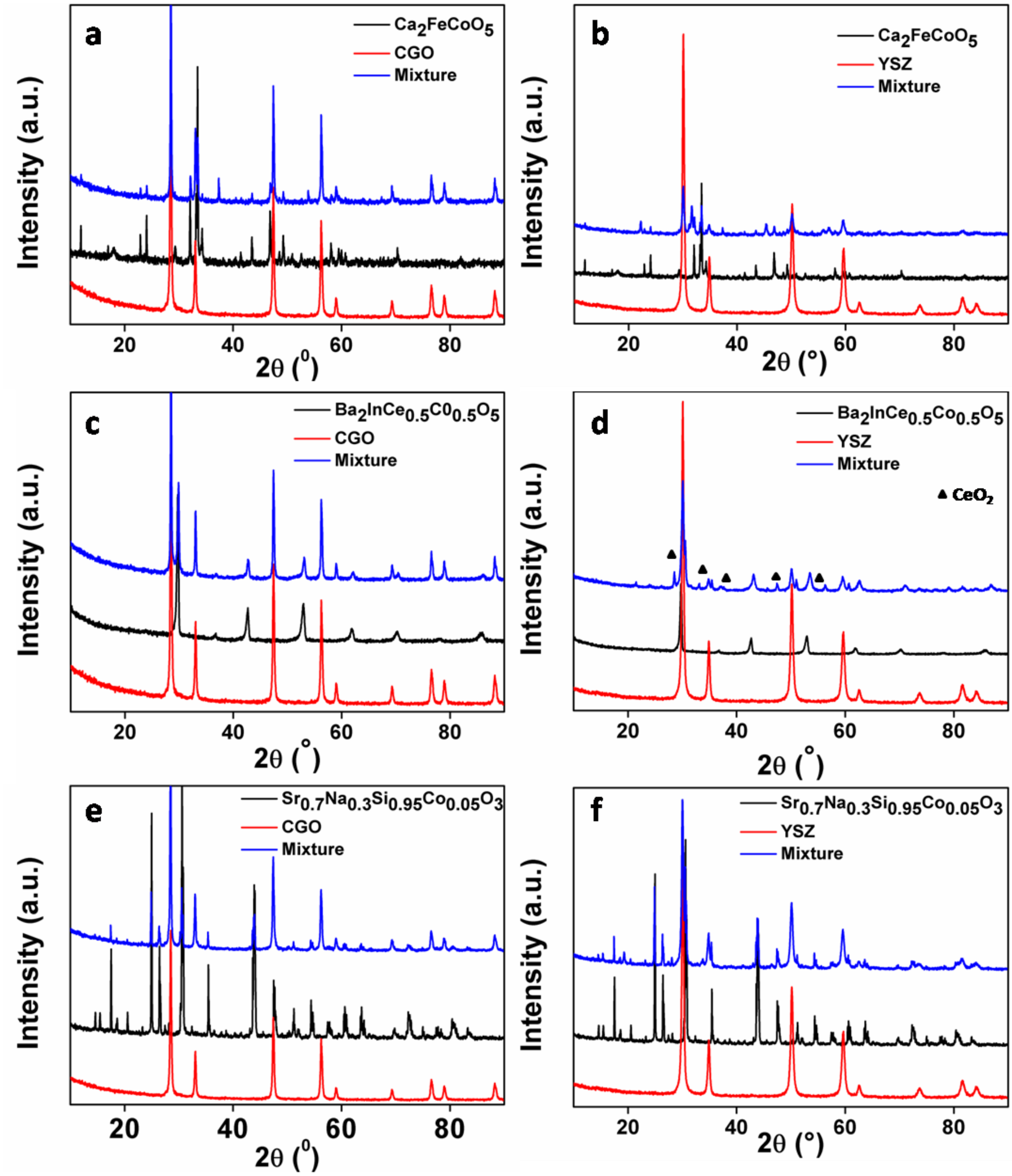

Figure 5B.1: PXRD pattern representing the reactivity of the material with conventional electrolytes CGO and YSZ, a) and b) $Ca_2FeCoO_{5\pm\delta}$ with CGO and YSZ respectively c) and d) $Ba_2InCe_{0.5}Co_{0.5}O_{5\pm\delta}$ with CGO and YSZ respectively and e) and f) $Sr_{0.7}Na_{0.3}Si_{0.95}Co_{0.05}O_{3-\delta}$ with CGO and YSZ respectively

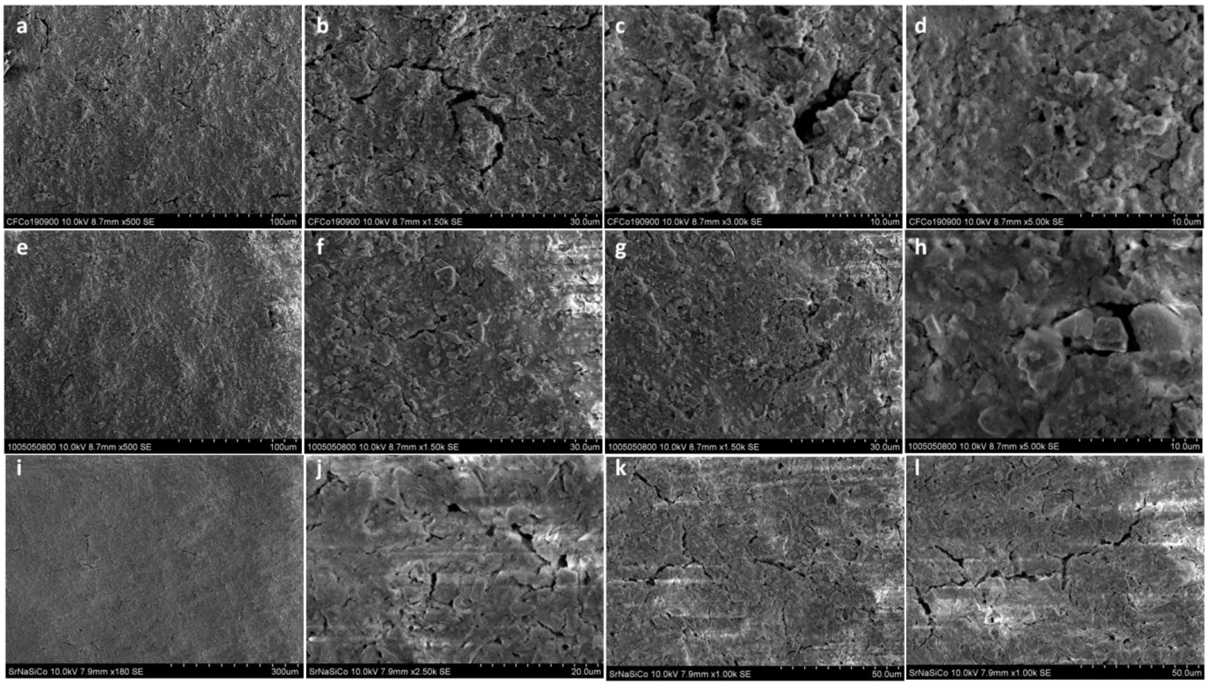

Figure 5B.2: SEM image showing the porous adhesion of material on the electrolyte surface. a) to d) $Ca_2FeCoO_{5\pm\delta}$, e) to h) $Ba_2InCe_{0.5}Co_{0.5}O_{5\pm\delta}$ and i) to l) $Sr_{0.7}Na_{0.3}Si_{0.95}Co_{0.05}O_{3-\delta}$

The coated dummy electrode is analysed for the conductivity by electrochemical impedance measurement using CH instrument. Figure 5B.3 shows the Nyquist plot representation of impedance data collected at 800°C in O_2 atmosphere. The data is fitted with the equivalent circuit as represented in the chapter 4 and the resistance data is represented in table 5B.1. $Ba_2InCe_{0.5}Co_{0.5}O_{5\pm\delta}$ exhibited higher conductivity than the conventional $La_{0.6}Sr_{0.4}Fe_{0.8}Co_{0.2}O_{3\pm\delta}$ electrode, and $Ca_2FeCoO_{5\pm\delta}$ electrode exhibited a comparable resistance value with the latter, however $Sr_{0.7}Na_{0.3}Si_{0.95}Co_{0.05}O_{3-\delta}$ electrode exhibited a lower conductivity compared to the rest. Hence $Ba_2InCe_{0.5}Co_{0.5}O_{5\pm\delta}$ and $Ca_2FeCoO_{5\pm\delta}$ materials can be projected as an alternative cathode material for SOFC application with an added advantage of low temperature electrode processing.

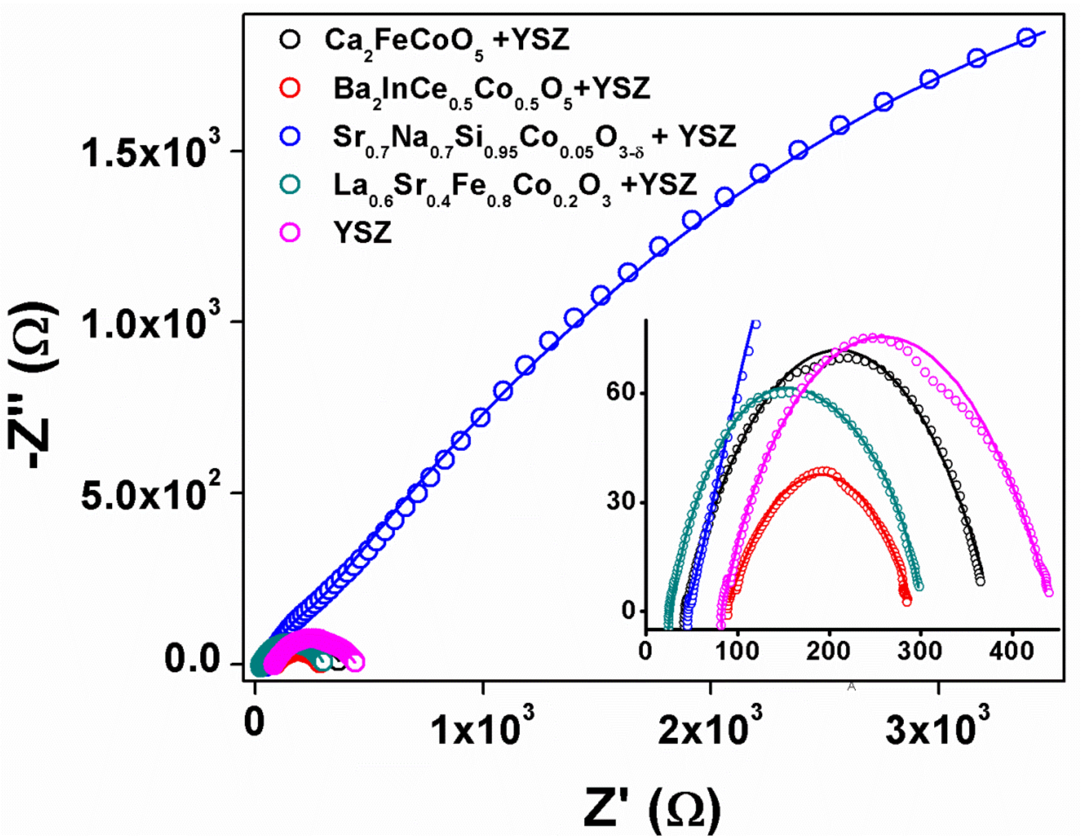

Figure5B.3: Impedance data of the dummy electrode at 800°C in O_2 atmosphere. The empty circles represent the data and the solid line represents the Z-fit of the data. Inset image indicates zoomed image representing semicircle portion.

Table 5B.1: Electrode impedance data

Electrode	Resitance (Ω cm^2)	Resistivity (Ω cm)
$Ca_2FeCoO_{5\pm\delta}$ + YSZ	501.5	4179.2
$Ba_2InCe_{0.5}Co_{0.5}O_{5\pm\delta}$ + YSZ	333.4	2778.3
$Sr_{0.7}Na_{0.3}Si_{0.95}Co_{0.05}O_{3-\delta}$ + YSZ	13700	114166.7
$La_{0.6}Sr_{0.4}Fe_{0.8}Co_{0.2}O_{3\pm\delta}$ + YSZ	377.4	3142.8

5B.4. Summary and Conclusions

The materials, $Ba_2InCe_{0.5}Co_{0.5}O_{5\pm\delta}$, $Ca_2FeCoO_{5\pm\delta}$ and $Sr_{0.7}Na_{0.3}Si_{0.95}Co_{0.05}O_{3\pm\delta}$ are tested for potential applicability as electrodes in SOFC. The materials are non-reactive with the conventional electrolytes at high temperatures. In the case of $Ba_2InCe_{0.5}Co_{0.5}O_{5\pm\delta}$, a phase of CeO_2 is observed after the heat treatment with YSZ electrolyte. The cathode ink is adhered as a porous layer on the top of the dense electrolyte at considerably lower temperature of 800°C than the conventional processes. Electrode impedance comparison with the standard cathode electrode shows that the material $Ba_2InCe_{0.5}Co_{0.5}O_{5\pm\delta}$ has superior conductivity and $Ca_2FeCoO_{5\pm\delta}$ electrode exhibits a comparable resistivity value when compared with the standard material. These properties make the material conducive to be used as electrode in SOFC applications.

5B.5. References

1. Sengodan, S.; Choi, S.; Jun, A.; Shin, T. H.; Ju, Y.-W.; Jeong, H. Y.; Shin, J.; Irvine, J. T. S.; Kim, G., Layered oxygen-deficient double perovskite as an efficient and stable anode for direct hydrocarbon solid oxide fuel cells. *Nature Materials* **2014,***14*, 205.
2. Liu, M.; Lynch, M. E.; Blinn, K.; Alamgir, F. M.; Choi, Y., Rational SOFC material design: new advances and tools. *Materials Today* **2011,***14* (11), 534-546.
3. Brett, D. J. L.; Atkinson, A.; Brandon, N. P.; Skinner, S. J., Intermediate temperature solid oxide fuel cells. *Chemical Society Reviews* **2008,***37* (8), 1568-1578.
4. Ma, Q.; Tietz, F., Comparison of Y and La-substituted SrTiO3 as the anode materials for SOFCs. *Solid State Ionics* **2012,***225*, 108-112.
5. Ivers-Tiffée, E.; Weber, A.; Herbstritt, D., Materials and technologies for SOFC-components. *Journal of the European Ceramic Society* **2001,***21* (10), 1805-1811.
6. Hildenbrand, N.; Boukamp, B. A.; Nammensma, P.; Blank, D. H. A., Improved cathode/electrolyte interface of SOFC. *Solid State Ionics* **2011,***192* (1), 12-15.
7. Boulfrad, S.; Cassidy, M.; Irvine, J. T. S., Adhesion and Percolation Parameters in Two Dimensional Pd–LSCM Composites for SOFC Anode Current Collection. *Advanced Functional Materials* **2010,***20* (5), 861-866.

Chapter 6

Summary and Conclusions

6.1. Summary

Chapter 1 introduces the need of alternative energy source on account of the increased pollution associated with the use of fossil fuels. Fuel cells can be a better alternative to generate energy. Unitised regenerative fuel cells operate in a cyclic manner with electrolyser converting water to H_2 and O_2 which is used in the fuel cell to form water again. SOFCs have the advantage of flexibility in fuels, but operates at high temperatures ~900°C. Reduction in operation temperature can results in wider deployment of the technique and for the same, the electrode materials have to be highly conducting and catalytically active. Oxygen kinetics is the rate determining step in the fuel cells since it involves a four electron process to create or break a strong double bond. State of the art materials for ORR and OER are Pt based materials and Ru or Ir oxides respectively, making the technique expensive. Perovskite related oxides reported to have stability in wide potential range, can be better alternatives for these materials. Both the metal sites, A and B, can be doped to introduce catalytic activity and oxygen vacancy. Brownmillerite oxides are related to perovskite structure with ordered oxygen vacancies and can be made into disordered form by proper doping strategy. The mechanism of perovskite related structure towards ORR and OER are also well studied. Pollution from the industries can be further reduced by using pure oxygen, by employing oxygen transport membranes, and perovskite based membranes with oxygen vacancy have been used for the application.

First part of the chapter 2 deals with 5atom% transition metal (Mn/ Co/Ni/Cu) doping in Fe site of $Ca_2Fe_2O_5$. The synthesis is carried out by citrate gel route at 1000°C and the materials crystallised in orthorhombic system. More than 5% doping was not successful with Ni and Cu, due to the formation of NiO and CuO phases as impurity and hence the stoichiometry $Ca_2Fe_{1.9}M_{0.1}O_{5\pm\delta}$ is selected for further analysis. Room temperature oxygen reduction and oxygen evolution studies suggests that Ni doped material is a better practical catalyst on account of better electron transfer number, less peroxide yield and better OER onset and current response. Correlation of activity to oxygen uptake and work function are also conducted by TGA and UPS analysis. In the second part role of increased Co doping in the Fe site is studied with the stoichiometry Ca_2Fe_{2-}

$_xCo_xO_{5\pm\delta}$ (x = 0, 0.25, 0.5). The structure exhibits interesting inter and intra layer ordering on 50atom% Co doping in the Fe position. There are two types of tetrahedral and two type of octahedral positions. Fe rich octahedral is connected to Co rich octahdera, and the same was case with tetrahedral layer, which forms the intralyer ordering. Interlayer ordering in occurs such a way that Fe rich octahedral are connected to Co rich tetrahedra only and vice versa. The room temperature activity is found to enhance by increasing the Co concentration. The high temperature conductivity is also found to enhance by the Co incorporation. The material tested is phase stable in O_2 rich and lean conditions at higher temperatures.

In the Chapter 3, $Ba_2In_2O_5$ is selected as the parent material. In the first part, role of transition metals (Mn/Fe/Co/Ni/Cu) towards the ORR and OER reactions are studied. Materials with stoichiometry $Ba_2In_{1.75}M_{0.25}O_5$ are synthesised. The orthorhombic brownmillerite structure with highly ordered oxygen vacancy is retained on transition metal doping, where as the parent material crystallised in disordered tetragonal structure. There was no considerable change in the activity with transition metal incorporation probably due to the retention of the ordered vacancy concentration in the lattice. In the second part a redox centre Ce is also incorporated in to the lattice along with 12.5atom% transition metal to have a stoichimetry $Ba_2InCe_{0.75}M_{0.25}O_{5\pm\delta}$ (M= Mn/Fe/Co/Ni/Cu). The room temperature activity is improved with Ce doping. The materials, except Fe doped variety, crystallised in the cubic structure with highly disordered oxygen vacancy even with 12.5atom% doping. In the third part, Co and Ce concentration is varied in $Ba_2In_{2-x+y}Ce_xCo_yO_{5\pm\delta}$ (x = 0.25, 0.5, 0.75, 1; y = 0.25, 0.5, 0.75). Room temperature ORR activity improves by increased Co doping and higher OER activity is obtained with optimum concentration of Co and Ce doping. The material selected shows excellent high temperature stability in O_2, N_2, and 5% H_2/Ar atmospheres and high temperature conductivity in O_2 and N_2 atmospheres.

Chapter 4 deals with the Na and transition metal ((Mn/Fe/Co/Ni/Cu)) doping in the A and B site of $SrSiO_3$ respectively to form $Sr_{0.7}Na_{0.3}Si_{0.95}M_{0.05}O_{3-\delta}$. The materials crystallises in the monoclinic crystal system with corner shared B_3O_9 units in a structure entirely different from the analogous perovskite family. Na doped material is reported to exist in multiple phases, which cannot be detected by PXRD. Upon recrystallistaion, evidence of phase segregation is observed by SEM and EDS analysis. The powder is analysed by solid state NMR, and found a clear evidence of phase separation in the as synthesised form also is observed. Room temperature activity is improved with the transition metal incorporation. The high temperature phase stability is analysed by HT-XRD in O_2, N_2 and 5% H_2/Ar atmosphere and the material exhibited exceptional stability in all the gas atmospheres. High temperature conductivity is also improved with doping.

Chapter 5 projects investigate the potential of the materials as oxygen transport membranes and electrodes in SOFC. In the first part, the feasibility of fabrication of dense hollow fiber membrane is analysed. The materials $Ca_2FeCoO_{5\pm\delta}$ and $Sr_{0.7}Na_{0.3}Si_{0.95}Co_{0.05}O_{3-\delta}$ are made in to dense fiber by sintering at 1250°C and 1100°C respectively. The low temperature single step densification can reduce the total cost of the process. A novel concept of fabrication of fiber directly from the carbonate precursor mixture is also introduced. The single step calcination densfication step which ensures phase formation can considerably reduce the overall cost of processing by reducing multiple calcination steps for material synthesis and sintering fiber. In the second part, dummy electrodes are made by coating the materials to YSZ dense electrolyte membrane and the adhesion temperature is optimised. Lower adhesion temperature of 800°C can be advantageous for the processing of electrode. Conductivity is compared with state of the art material $La_{0.6}Sr_{0.4}Fe_{0.8}Co_{0.2}O_{3\pm\delta}$. The conductivity of the electrode $Ba_2InCe_{0.5}Co_{0.5}O_{5\pm\delta}$ is superior and $Ca_2FeCoO_{5\pm\delta}$ is comparable to state of the art electrode projecting the material to be potential candidate SOFC application.

6.2. Conclusions

- Ni doping in the $Ca_2Fe_2O_{5\pm\delta}$ results in better bifunctional activity, however doping more than 5% is not successful.
- Increased cobalt doping in the $Ca_2Fe_2O_{5\pm\delta}$ enhances the room temperature bifunctional activity and high temperature conductivity. Interesting inter and intra layer ordering phenomenon is observed with 50atom% doping in the Fe site with Co.

- 12.5atom% transition metal doping in the In site in $Ba_2In_2O_{5\pm\delta}$ does not result in a considerable improvement in activity. The doped materials retain orthorhombic brownmillerite structure, where as the parent $Ba_2In_2O_{5\pm\delta}$ crystallised in disordered tetragonal structure.
- Cerium and transition metal co-doping improves the room temperature bifunctional activity. The phase changes to highly disordered cubic structure on incorporation of 12.5atom% transition metal and 37.5% Ce in the In site.
- ORR activity improved by increasing Co content in cobalt and cerium co-doped brownmillerite $Ba_2In_{2-x+y}Ce_xCo_yO_{5\pm\delta}$. OER activity is higher with optimum concentration of Ce and Co. Material crystallised in highly disordered cubic structure throughout the composition.
- $Ba_2InCe_{0.5}Co_{0.5}O_{5\pm\delta}$ retains the cubic phase, even at high temperature and oxidising and reducing atmospheres.
- A clear evidence of phase segregation in the compound is observed for $Sr_{0.7}Na_{0.3}Si_{0.95}M_{0.05}O_{3-\delta}$ from SEM and NMR. The room temperature bifunctional activity is improved by the incorporation of transition metal in the lattice.
- High temperature conductivity improved to a considerable extent by the Na and transition metal incorporation in the lattice.
- The materials are projected for their application in OTM and dense hollow fiber membranes of $Ca_2FeCoO_{5\pm\delta}$ and $Sr_{0.7}Na_{0.3}Si_{0.95}Co_{0.05}O_{3-\delta}$ are fabricated at relatively lower temperature
- One-step fabrication of hollow fiber directly from precursor carbonate mixture for the brownmillerite $Ca_2FeCoO_{5\pm\delta}$ has been carried out, which can considerably reduce overall cost of processing avoiding multiple steps of calcinations and sintering
- Dummy electrode conductivity of materials $Ba_2InCe_{0.5}Co_{0.5}O_{5\pm\delta}$ and $Ca_2FeCoO_{5\pm\delta}$ is comparable to the state of the art SOFC cathode $La_{0.6}Sr_{0.4}Fe_{0.8}Co_{0.2}O_{3\pm\delta}$, making them an alternative for SOFC cathode.

List of Publications

1. Bifunctional Oxygen Reduction andEvolution Activity in Brownmillerites $Ca_2Fe_{2-x}Co_xO_5$; **Shibin Thundiyil**, Sreekumar Kurungot, and R. Nandini Devi. *ACS Omega* **2019**, *4*, 31.
2. Role of B site ion in Bifunctional Oxyegn Electrocatalysis: A structure property Correlation Study on Doped $Ca_2Fe_2O_5$ Brownmillerites; **Shibin Thundiyil**, Vinod C Prabhakar, Kurungot Sreekumar, and R. Nandini Devi. *Phys. Chem. Chem. Phys., **2020**, 22, 15520*
3. Synergistic Effect of B Site Co-doping with Co and Ce in Bifunctional Oxygen Electrocatalysis By Oxygen Deficient Brownmillerite $Ba_2In_2O_5$; **Shibin Thundiyil**, Kurungot Sreekumar, and R. Nandini Devi. *Catal Today, **2020**, In press*
4. Photocatalytic H_2 evolution from water-methanol mixtures on $InGaO_3(ZnO)_m$ with an anisotropic layered structure modified with CuO and NiO catalysts; Soumya B. Narendranath, Saranya V. Thekkeparambil, Leena George, **Shibin Thundiyil**, and R. Nandini Devi. *J. Mol. Cat. A.*. **2016**, 4*15*, 82.

Contributions to Symposia/Conference

1. Oral presentation at ‘**ICRAMC-2020**’ held at Chennai, India during 19th to 21st February 2020
2. Poster presentation at **‘RTC2020’** held at NIT Calicut, India during 26th to 29th February 2020
3. Oral presentation at ‘**APCAT-8**’ held at Bangkok, Thailand during 4th to 7th August 2019
4. Oral presentation at ‘**CATSYMP-23’** held at Baglore, India during January 17-19, 2018
5. Oral presentation at Indo-French bilateral symposium **‘MATSUCAT-19’**, held at CSIR-NCL, Pune during 26th February to 2nd March 2019
6. Oral presentation NCL-RF 2nd annual students conference held at CSIR-NCL during 28-29 November 2019
7. Poster presentation at **‘Conference on Sustainable Catalytic Technologies’** during June 8-9 at CSIR-NCL, Pune

Annexure

A. Koutechy-Levich Plot

Koutechy Levich equation describes the relation between rotation speed and the disk current as represented as below[1],

$$\frac{1}{\mathrm{I_D}} = \frac{1}{\mathrm{I_k}} + \frac{1}{\mathrm{I_d}} = \frac{1}{\mathrm{I_k}} + \frac{1}{\mathrm{B}\omega^{\frac{1}{2}}}$$

$$\mathrm{B} = 062\mathrm{nFAC_O D_O}^{\frac{2}{3}}\upsilon^{\frac{-1}{6}}$$

$$\mathrm{I_k} = \mathrm{nAFKC_O}$$

where I_D is the disk voltammetric current which has the contribution of the kinetic current (I_k) and diffusion controlled current (I_d), ω is the rotation speed, n is the electron transfer number F is Faradays constant, A is the geometric area of the electrode, CO is the oxygen concentration in the oxygen saturated solution, DO is the diffusion coefficient of oxygen υ is the kinematic viscosity of the solution and k is the electron transfer rate constant. By plotting inverse of disk current against inverse of square root of rotation speed K-L plot is obtained, with B value as slope. For a direct 4 electron transfer reaction, the value of B is 0.46 $\mathrm{mAcm^{-2}S^{1/2.}}$

B. Tafel plot

Tafel equation represents the relation between overpotential η and the natural logarithm of current density j. For the reduction reaction, it can be expressed as

$$\eta_c = \frac{RT}{nF\alpha_c}\ln j_0 - \frac{RT}{nF\alpha_a}\ln j = a - b\ln j$$

where j_0 is the exchange current density, R is the gas constant, n is the number of electrons involved in the overall reaction, α is the charge transfer coefficient and a and c in the subscripts indicate anodic and cathodic parts. The plot of η against lnj gives -b as the slope, which gives an idea about mechanism of the reaction and electron transfer number involved in the reaction. The oxygen reduction reaction takes place through precise mechanism as explained below

$$\mathrm{O_2 \rightarrow O_{2(ads)}} \qquad (1)$$

$$\mathrm{O_{2(ads)} + e \rightarrow [O_{2(ads)}]^-} \qquad (2)$$

$$\mathrm{[O_{2(ads)}]^- \rightarrow O^-_{2(ads)}} \qquad (3)$$

$$\mathrm{O^-_{2(ads)} + H_2O \rightarrow HO_{2(ads)} + OH^-} \qquad (4)$$

$$\mathrm{HO_{2(ads)} + e \rightarrow HO^-_{2(ads)}} \qquad (5)$$

$$\mathrm{HO^-_{2(ads)} \rightarrow HO^-_2} \qquad (6)$$

Further charge transfer coefficient αa can be defined as given by Taylor and Humffray[2]

$$\mathrm{n\alpha_a = (\frac{n_f}{\upsilon} + n_r\beta)}$$

Where n_f is the number of electrons transferred before rate determining step (rds), nr is the number of electrons transferred in the rds, υ is the stoichiometric number of the reaction defined as the number of times the rds occurs for one repetition of the overall reaction and β is the symmetry factor of the rds which has a value near 0.5, the subscript a stands for anodic reaction and for the cathodic reaction, slope value will be of opposite sign. If the first electron reduction step is the rds, then the values obtained for n_f and n_r are 0 and 1 respectively, yielding Tafel slope (b) of -120 mV/decades[3]. However, if the rds involves the step subsequent to the first electron reduction, which is the migration of the superoxide ion , then n_f =1 and n_r = 0, resulting in a slope of -60 mV/decade, indicating a pseudo two electron transfer.

The oxygen reduction reaction takes place through abovesteps. Where subscript ‘ads’ stands for adsorbed species. The species formed in the step 2 is relatively inert intermediate, and the step subsequent to the first electron migration of the species to the active site[4].

Oxygen evolution reaction can also be considered to occur through a number of steps as with the ORR. The mechanism is explained by De Faria in acid solution as follows[5]

$$S + H_2O \rightarrow S - OH + H^+ + e \qquad (1)$$

$$S - OH \rightarrow S - O + H^+ + e \qquad (2)$$

$$S - OH + S - OH \rightarrow S - O + H_2O \quad (3)$$

$$S - O + S - O \rightarrow 2S + O_2 \quad (4)$$

Where S is the substrate, slope values are explained with the same explanation as in the ORR.

C. Electron transfer number and Peroxide Yield: RRDE technique

Further, electron transfer number was obtained from RRDE experiment. RRDE setup differs from RDE in that it has an additional coaxial ring electrode to collect the products from the disk, analysis of which indicates reduction pathway as well as electron count. The ring electrode was set with a potential value of 1.47 V vs RHE to detect the peroxides produced by the disk. Electron count of the electrochemical reaction and peroxide yield was calculated by RRDE experiment by equations 6 and 7[6-8]

$$\mathrm{n} = 4 * \frac{\mathrm{Id}}{\mathrm{I_d} + \mathrm{I_r}/\mathrm{N_C}}$$

where Id is the disk current, Ir is the ring current Nc is the collection efficiency, (collection efficiency in the present study is 0.37).

$$\mathrm{p} = 200 * \frac{\mathrm{I_r}/\mathrm{N_C}}{\mathrm{I_d} + \mathrm{I_r}/\mathrm{N_C}}$$

D. Arrhenius Plot

Arrhenius equation can be represented as

$$k = Ae^{-E_a/RT}$$

$$\ln k = -E_a/RT + \ln A$$

The equation is identical to the equation of straight line. Plot of ln k *vs* 1/T gives –Ea/R as the slope. Multiplying the slope with R gives the activation energy.

References

1. Bard, A. J.; Faulkner, L. R., *Electrochemical methods: fundamentals and applications*. Wiley: 1980.

2. Taylor, R. J.; Humffray, A. A., Electrochemical studies on glassy carbon electrodes: II. Oxygen reduction in solutions of high pH (pH>10). *J. Electroanal. Chem* **1975,** *64* (1), 63-84.
3. Ge, X.; Sumboja, A.; Wuu, D.; An, T.; Li, B.; Goh, F. W. T.; Hor, T. S. A.; Zong, Y.; Liu, Z., Oxygen Reduction in Alkaline Media: From Mechanisms to Recent Advances of Catalysts. *ACS Catal* **2015,** *5* (8), 4643-4667.
4. Hu, P.; Song, Y.; Chen, L.; Chen, S., Electrocatalytic activity of alkyne-functionalized AgAu alloy nanoparticles for oxygen reduction in alkaline media. *Nanoscale* **2015,** *7* (21), 9627-9636.
5. De Faria, L. A.; Boodts, J. F. C.; Trasatti, S., Electrocatalytic properties of ternary oxide mixtures of composition Ru0.3Ti(0.7−x)CexO2: oxygen evolution from acidic solution. *Journal of Applied Electrochemistry* **1996,** *26* (11), 1195-1199.
6. Paulus, U. A.; Schmidt, T. J.; Gasteiger, H. A.; Behm, R. J., Oxygen reduction on a high-surface area Pt/Vulcan carbon catalyst: a thin-film rotating ring-disk electrode study. *Journal of Electroanalytical Chemistry* **2001,** *495* (2), 134-145.
7. Zhou, R.; Zheng, Y.; Jaroniec, M.; Qiao, S.-Z., Determination of the Electron Transfer Number for the Oxygen Reduction Reaction: From Theory to Experiment. *ACS Catal.* **2016,** *6* (7), 4720-4728.
8. Tsai, Y.-L.; Huang, K.-L.; Yang, C.-C.; Ye, J.-S.; Pan, L.-S.; Lee, C.-L., Preparation and cyclic voltammetric dissolution of core‑shell‑shell Ag‑Pt‑Ag nanocubes and their comparison in oxygen reduction reaction in alkaline media. *International Journal of Hydrogen Energy* **2014,** *39* (11), 5528-5536.

Shibin Thundiyil

Material chemist with expertise in synthesis and structure property correlation of structured metal oxides, nitrides, oxy-nitrides and hydroxides; electrochemical analysis, and non ambient phase characterisation techniques

CSIR-National Chemical Laboratory, Pune E-mail: shibin.avera@gmail.com Mobile: +91-9809559753

Skills and Expertise

- Synthesis strategies for mixed metal oxides, oxynitrides and LDHs
- PXRD technique (Ambient and Non-ambient (XRK-900))
- Rietveld Refinement of PXRD patterns
- Electrochemical techniques (CV, LSV, EIS) and 4-probe instrument
- Electrode preparation in SOFC
- Dense/Porous ceramic membrane fabrication
- Experience with UV-Vis water splitting setup
- Data analysis and hands on experience with XRF, TGA, XPS-UPS, UV-Vis, IR, Raman spectrometer, ICP-MS, BET surface area, SEM-EDAX, GC, NMR, TPR/O
- Handling databanks: JCPDS, ICSD, Web of Science, Scopus
- Softwares: Origin, Diamond, Chemdraw
- Good communication skill: communicated results in number of national/international conferences

Education

Ph. D. Chemical Sciences Thesis title: Structural and Electrochemical Characterisation of Transition Metal Doped Perovskite Related Structures $ABO_{3-\delta}$,(A = Ca/Sr/Ba and B = Fe/Si/In) **01/2015-08/2020**	**CSIR-National Chemical Laboratory** affiliated to AcSIR	Defense date: 26/08/2020 Thesis submission: 06/01/2020
M. Sc. Chemistry (Material Sciences) **2011-2013** Thesis title: Synthesis and Characterization of Layered Hydroxides: Studies on Intercalation and Exfoliation	**Kannur University**, Kerala Thesis from: CSIR-National Chemical Laboratory	82.7% ('A' Grade) and University first position
B. Sc. Chemistry **2008-2011** Thesis title: Study on Water Quality near Padannapalam region, Kannur District, Kerala	**Kannur University**, Kerala (S.N College, Kannur)	84.4%

Certification

Higher Diploma in Software Engineering from NIIT, Experience in coding with C and C# language, database management (SQL), basics of JAVA.

Research Experience

Ph. D. Student **(01/2015- Present date)** CSIR- National Chemical Laboratory, Pune **Catalysis Division** Dr. R. Nandini Devi	Structure-property correlation of structured oxides, Structural studies with Rietveld refinement of PXRD pattern combined with other analytical techniques, Room temperature electrochemical analysis, SOFC testing and dense hollow fiber membrane fabrication as a candidate for Oxygen transport membrane and battery application, Reactor designing, Guiding Masters/ Engineering Thesis
Exchange Student, under **"CSIR-CNRS International Associated Laboratory (LIA)"** **(May-June 2015 and Nov-Dec 2017)** CNRS-University of Lille1, France Dr. Aurelie Rolle, Prof. Rose-Noelle Vannier	Materials for IT-SOFC applications. Materials analysed with various thermal techniques, Electrode analysis for SOFC, Stability analysis for SOFC application
Project Fellow **(01/2014- 01/2015)** CSIR- National Chemical Laboratory, Pune Catalysis Division Dr. R. Nandini Devi	Photocatalytic water splitting with layered hydroxide catalysts without sacrificial reagents, Design development of structured mixed metal oxides, Training Master students

Research Interests

- Synthesis of functional materials for photo and electrochemical energy applications
- Development and structure-property correlation of oxygen-deficient metal oxides like Perovskite, Brownmillerite, Pyrochlore etc, and fabrication of dense ceramic membranes for oxygen permeation

Patent

➢ Si Based Oxide Ion Conducting Composites its Process for Preparation and Applications thereof. IN201711022960

Publications

1. ***Shibin Thundiyil****, Vinod C Prabhakar, Kurungot Sreekumar, Nandini R Devi*,* Role of B site ion in bifunctional oxygen electrocatalysis: A structure property correlation study on doped $Ca_2Fe_2O_5$ brownmillerites, Phys Chem Chem Phys, 22, 15520-15527 (2020)

2. ***Shibin Thundiyil,*** *Kurungot Sreekumar, Nandini R Devi**, Synergistic effects in bifunctional oxygen electrocatalyis by oxygen deficient brownmillerite $Ba_2In_2O_5$ *(In Press) doi:* 10.1016/j.cattod.2020.05.046

3. ***Shibin Thundiyil****, Kurungot Sreekumar*, Nandini R Devi*,* Bifunctional oxygen reduction and evolution activity in brownmillerite $Ca_2Fe_{2-x}Co_xO_5$, ACS Omega, 4, 31-38 (2019)

4. Soumya B. Narendranath, Saranya V. Thekkeparambil, Leena George, ***Shibin Thundiyil*** *and R. Nandini Devi*, Photocatalytic H_2 evolution from water-methanol mixtures on $InGaO_3(ZnO)_m$ with an anisotropic layered structure modified with CuO and NiO co-catalysts, J. Mol. Cat. A., 415, 82 - 88 (2016)

5. ***Shibin Thundiyil****, Shunottara Jogdand, Nandini R Devi*,* One-step fabrication of Ca_2FeCoO_5 hollow fibers from the precursor mixture consisting of oxide synthesis starting materials (Under Revision)

6. ***Shibin Thundiyil,*** *Kurungot Sreekumar, Nandini R Devi*,* Transition metal doped silicate structure as efficient peroxide catalyst from electrochemical oxygen reduction (Manuscript completed)

7. ***Shibin Thundiyil,*** *Kurungot Sreekumar, Nandini R Devi*,* Brownmillerite peroxide catalysts: Electrochemical oxygen reduction in two electron pathway (Manuscript completed)

Conference Presentations

Oral Presentations

- ‘**ICRAMC2020**’, SRM University, Chennai during 19-21 February 2020
- NCL-RF Annual student conference during 28-29 November 2019
- ‘**APCAT-8**’, Bangkok, Thailand during August 4th -7th 2019
- Indo-French Bilateral Symposium ‘**MATSUCAT-19**’, CSIR-NCL, Pune, India during Feb 26-March 2, 2019
- ‘**CATSYMP-23**’, Bangalore, India, during January 17-19, 2018

Poster presentations

- International Conference on Recent Trends in Catalysis ‘**RTC2020**’, NIT Calicut, during February 26-29, 2020
- “Conference on Sustainable Catalytic Technologies” during June 8-9, 2017 at NCL, Pune
- Science day Posters at CSIR-NCL, Pune

References

Dr R. Nandini Devi
Principal Scientist
Catalysis and Inorganic Chemistry Division
CSIR-National Chemical Laboratory, Pune
Email: nr.devi@ncl.res.in

Prof. Rose-Noelle Vannier
Director
Ecole Nationale Superieure de Chemie de Lille
Villeneuve d’Ascq Cedex, Lille, France
Email: rose-noelle.vannier@ensc-lille.fr

shibinphdths

ORIGINALITY REPORT

5%

SIMILARITY INDEX

PRIMARY SOURCES

1	www.pdfsdocuments.com Internet	380 words — 1%
2	Chamundi P. Jijil, Indrajit M. Patil, Bhalchandra Kakade, R. Nandini Devi. " Cobalt-Doped Ba In O Brownmillerites: An Efficient Electrocatalyst for Oxygen Reduction in Alkaline Medium ", ACS Omega, 2018 Crossref	176 words — 1%
3	Chamundi P. Jijil, Siddheshwar N. Bhange, Sreekumar Kurungot, R. Nandini Devi. " Effect of B Site Coordination Environment in the ORR Activity in Disordered Brownmillerites Ba In Ce O ", ACS Applied Materials & Interfaces, 2015 Crossref	66 words — < 1%
4	Sébastien Royer, Daniel Duprez, Fabien Can, Xavier Courtois, Catherine Batiot-Dupeyrat, Said Laassiri, Houshang Alamdari. "Perovskites as Substitutes of Noble Metals for Heterogeneous Catalysis: Dream or Reality", Chemical Reviews, 2014 Crossref	62 words — < 1%
5	Xi Cheng, Emiliana Fabbri, Yuya Yamashita, Ivano E. Castelli et al. "Oxygen Evolution Reaction on Perovskites: A Multieffect Descriptor Study Combining Experimental and Theoretical Methods", ACS Catalysis, 2018 Crossref	47 words — < 1%
6	M. A. Peña, J. L. G. Fierro. "Chemical Structures and Performance of Perovskite Oxides", Chemical Reviews, 2001	42 words — < 1%

	Crossref	
7	Nian-Tzu Suen, Sung-Fu Hung, Quan Quan, Nan Zhang, Yi-Jun Xu, Hao Ming Chen. "Electrocatalysis for the oxygen evolution reaction: recent development and future perspectives", Chemical Society Reviews, 2017 Crossref	39 words — < 1%
8	Chamundi P. Jijil, Moorthi Lokanathan, Sundaresan Chithiravel, Chandrani Nayak et al. " Nitrogen Doping in Oxygen-Deficient Ca Fe O : A Strategy for Efficient Oxygen Reduction Oxide Catalysts ", ACS Applied Materials & Interfaces, 2016 Crossref	34 words — < 1%
9	etheses.bham.ac.uk Internet	29 words — < 1%
10	Chattopadhyay, J.. "Performance of tin doped titania hollow spheres as electrocatalysts for hydrogen and oxygen production in water electrolysis", International Journal of Hydrogen Energy, 200807 Crossref	24 words — < 1%
11	Wang, Li, Lingling Zhang, Lu Bai, Lei Han, and Shaojun Dong. "Nitrogen, cobalt-codoped carbon electrocatalyst for oxygen reduction reaction using soy milk and cobalt salts as precursors", Electrochemistry Communications, 2013. Crossref	21 words — < 1%
12	D. Carta, M. F. Casula, A. Falqui, D. Loche, G. Mountjoy, C. Sangregorio, A. Corrias. " A Structural and Magnetic Investigation of the Inversion Degree in Ferrite Nanocrystals MFe O (M = Mn, Co, Ni) ", The Journal of Physical Chemistry C, 2009 Crossref	20 words — < 1%
13	dspace-prod-lib.cc.uic.edu Internet	19 words — < 1%
14	Rajesh, Thattarathody, and R. Nandini Devi. "Role of Oxygen Vacancies in Water Gas Shift Reaction:	18 words — < 1%

Activity Study on BaCe0.98-xYxPt0.02O3-δ Perovskites", The Journal of Physical Chemistry C
Crossref

---

15 Hichour, M.. "Structural and elastic properties of antiperovskites XNBa"3 (X=As, Sb) under pressure effect", Physica B: Physics of Condensed Matter, 20091115 18 words — < 1%
Crossref

---

16 Microelectronics International, Volume 31, Issue 3 (2014-09-16) 18 words — < 1%
Publications

---

17 Lishan Peng, Jingjun Shen, Xingqun Zheng, Rui Xiang, Mingming Deng, Zhanxin Mao, Zhiping Feng, Ling Zhang, Li Li, Zidong Wei. "Rationally design of monometallic NiO-Ni3S2/NF heteronanosheets as bifunctional electrocatalysts for overall water splitting", Journal of Catalysis, 2019 17 words — < 1%
Crossref

---

18 Chunlei Ren, Hong Fang, Jianqiang Gu, Louis Winnubst, Chusheng Chen. "Preparation and characterization of hydrophobic alumina planar membranes for water desalination", Journal of the European Ceramic Society, 2015 17 words — < 1%
Crossref

---

19 Yinling Wang, Chengzhou Zhu, Shuo Feng, Qiurong Shi, Shaofang Fu, Dan Du, Qiang Zhang, Yuehe Lin. "Interconnected Fe, S, N-Codoped Hollow and Porous Carbon Nanorods as Efficient Electrocatalysts for the Oxygen Reduction Reaction", ACS Applied Materials & Interfaces, 2017 17 words — < 1%
Crossref

---

20 qspace.library.queensu.ca 16 words — < 1%
Internet

---

21 baadalsg.inflibnet.ac.in 16 words — < 1%
Internet

---

22 www.nature.com 14 words — < 1%
Internet

23 Joon Hyung Shim, Cheng-Chieh Chao, Hong Huang, Fritz B. Prinz. "Atomic Layer Deposition of Yttria-Stabilized Zirconia for Solid Oxide Fuel Cells", Chemistry of Materials, 2007
Crossref
14 words — < 1%

24 Dan Yue, YiKe Huang, Ling Zhang, Ke Jiang, Xin Zhang, Yuanjing Cui, Yang Yu, Guodong Qian. "Ratiometric luminescent sensing for ascorbic acid based on mixed Ce/Eu metal-organic framework", Journal of Materials Chemistry C, 2018
Crossref
13 words — < 1%

25 Guangyin Fan, Xiaojing Li, Yuling Ma, Yun Zhang, Jiangtao Wu, Bin Xu, Ting Sun, Daojiang Gao, Jian Bi. " Magnetic, recyclable Pt Co /Ti C X (X = O, F) catalyst: a facile synthesis and enhanced catalytic activity for hydrogen generation from the hydrolysis of ammonia borane ", New Journal of Chemistry, 2017
Crossref
13 words — < 1%

26 www.fuelcelltoday.com
Internet
13 words — < 1%

27 repository.ntu.edu.sg
Internet
12 words — < 1%

28 Dongsheng Xia, Ruozheng Wang, Yinping Wei, Lin Gan, Feiyu Kang. "Melamine-sponge-derived non-precious fuel cell electrocatalyst with hierarchical pores and tunable nitrogen chemical states for exceptional oxygen reduction reaction activity", Materials Today Energy, 2018
Crossref
12 words — < 1%

29 Gro Stakkestad, Sonia Faaland, Tove Sigvartsen. " Investigation of electrical conductivity and seebeck coefficient of Ca-and Sr-doped LaCrO ", Phase Transitions, 1996
Crossref
11 words — < 1%

30 tel.archives-ouvertes.fr
Internet
11 words — < 1%

31	pure.qub.ac.uk Internet	11 words — < 1%
32	S. B. Beale, S. V. Zhubrin. "A Distributed Resistance Analogy for Solid Oxide Fuel Cells", Numerical Heat Transfer, Part B: Fundamentals, 2007 Crossref	11 words — < 1%
33	research-repository.st-andrews.ac.uk Internet	10 words — < 1%
34	E. Teran-Salgado, D. Bahena-Uribe, P.A. Márquez-Aguilar, J.L. Reyes-Rodriguez, R. Cruz-Silva, O. Solorza-Feria. "Platinum nanoparticles supported on electrochemically oxidized and exfoliated graphite for the oxygen reduction reaction", Electrochimica Acta, 2018 Crossref	10 words — < 1%
35	V. A. Khomchenko, J. A. Paixão. " Spontaneous magnetization in the polar phase of Bi Ca FeO perovskites: The role of anion vacancies ", Journal of Applied Physics, 2014 Crossref	10 words — < 1%
36	www.spectroscopy-solutions.org Internet	10 words — < 1%
37	Jaka Sunarso, Siti Salwa Hashim, Na Zhu, Wei Zhou. "Perovskite oxides applications in high temperature oxygen separation, solid oxide fuel cell and membrane reactor: A review", Progress in Energy and Combustion Science, 2017 Crossref	10 words — < 1%
38	www.scribd.com Internet	10 words — < 1%
39	dyuthi.cusat.ac.in Internet	9 words — < 1%
40	creativecommons.org Internet	9 words — < 1%

41	Nan Wang, Tuanfeng Li, Ye Song, Jingjun Liu, Feng Wang. "Metal-free nitrogen-doped porous carbons derived from pomelo peel treated by hypersaline environments for oxygen reduction reaction", Carbon, 2018 Crossref	9 words — < 1%
42	www.mdpi.com Internet	9 words — < 1%
43	mdpi.com Internet	9 words — < 1%
44	www.aist.go.jp Internet	8 words — < 1%
45	J. M. Serra, V. B. Vert, O. Büchler, W. A. Meulenberg, H. P. Buchkremer. "IT-SOFC supported on Mixed Oxygen Ionic-Electronic Conducting Composites", Chemistry of Materials, 2008 Crossref	8 words — < 1%
46	thesis.library.caltech.edu Internet	8 words — < 1%
47	Liu, Shou-Heng, and Jyun-Ren Wu. "Influence of nitrogen and iron precursors on the synthesis of FeNx/carbons electrocatalysts toward oxygen reduction reaction in acid solution", Electrochimica Acta, 2014. Crossref	8 words — < 1%
48	Cong Liu, Fang Dong, Mingjie Wu, Yongxia Wang, Nengneng Xu, Xu Wang, Jinli Qiao, Penghui Shi, Haitao Huang. "Dual-active-sites design of CoSx anchored on nitrogen-doped carbon with tunable mesopore enables efficient Bi-Functional oxygen catalysis for ultra-stable zinc-air batteries", Journal of Power Sources, 2019 Crossref	8 words — < 1%
49	conservancy.umn.edu Internet	8 words — < 1%

50 biblio.ugent.be
Internet
8 words — < 1%

---

51 S. Escolástico, C. Solís, R. Haugsrud, A. Magrasó, J.M. Serra. "On the ionic character of H 2 separation through mixed conducting Nd 5.5 W 0.5 Mo 0.5 O 11.25−δ membrane", International Journal of Hydrogen Energy, 2017
Crossref
8 words — < 1%

---

52 S Linquette-Mailley. "Low-temperature oxygen electrode reaction on bismuth ruthenium oxides/stabilized zirconia", Solid State Ionics, 1998
Crossref
8 words — < 1%

---

53 Jiajia Wang, Xiyan Yue, Yanyan Yang, Suchada Sirisomboonchai, Peifen Wang, Xuli Ma, Abuliti Abudula, Guoqing Guan. "Earth-abundant transition-metal-based bifunctional catalysts for overall electrochemical water splitting: A review", Journal of Alloys and Compounds, 2020
Crossref
8 words — < 1%

---

54 Zou, Jing, Jungdeok Park, Heechul Yoon, Nigel Mark Sammes, and Jongshik Chung. "Effects of transition metal ion dopants on the performance of Ca2.9Bi0.1Co4O9−δ cathode", Journal of Alloys and Compounds, 2013.
Crossref
7 words — < 1%

---

55 Yuze Zeng, Jose F. Flores, Yu-Cheng Shao, Jinghua Guo, Yi-De Chuang, Jennifer Q. Lu. "Reproducibly creating hierarchical 3D carbon to study the effect of Si surface functionalization on the oxygen reduction reaction", Nanoscale, 2016
Crossref
7 words — < 1%

---

56 "Lead-Free Piezoelectrics", Springer Nature, 2012
Crossref
7 words — < 1%

---

57 Kateryna Artyushkova, Santiago Rojas-Carbonell, Carlo Santoro, Elizabeth Weiler et al. "Correlations between Synthesis and Performance of Fe-Based PGM-Free Catalysts in Acidic and Alkaline Media: Evolution of Surface Chemistry and Morphology", ACS Applied Energy Materials, 2019
7 words — < 1%

Crossref

---

58 Chamundi P. Jijil, Sreekuttan M. Unni, Kurungot Sreekumar, R. Nandini Devi. " Disordered Brownmillerite Ba InCeO with Enhanced Oxygen Reduction Activity ", Chemistry of Materials, 2012 — 6 words — < 1%

Crossref

EXCLUDE QUOTES	ON	EXCLUDE MATCHES	OFF
EXCLUDE BIBLIOGRAPHY	ON		